Towards Concussion Prevention in Ice Hockey: Mechanical Metamaterial Liners and Helmet Assessment

Daniel Matthias Haid

A thesis submitted in partial fulfilment of the requirements of
Sheffield Hallam University
for the degree of Doctor of Philosophy

October 2023

Candidate Declaration

I hereby declare that:

1. I have not been enrolled for another award of the University, or other academic or professional organisation, whilst undertaking my research degree.

2. None of the material contained in the thesis has been used in any other submission for an academic award.

3. I am aware of and understand the University's policy on plagiarism and certify that this thesis is my own work. The use of all published or other sources of material consulted have been properly and fully acknowledged.

4. The work undertaken towards the thesis has been conducted in accordance with the SHU Principles of Integrity in Research and the SHU Research Ethics Policy.

5. The word count of the thesis is 39,984.

Name	Daniel Matthias Haid
Award	PhD
Date of Submission	October 2023
Research Institute	Health Research Institute
Director(s) of Studies	Dr Leon Foster

Abstract

Ice hockey has one of the highest concussion rates in sport. During player-to-player collisions, the most common concussive scenario, helmets have been shown to offer limited protection. Helmet testing that is representative of the broad range of potential head impacts requires extensive specialist equipment, while certification standards are currently not assessing the impact scenario that most commonly causes concussions in ice hockey. Consequently, helmets protect well in the scenario they are certified and designed for – falls onto stiff surfaces – but provide limited protection during other commonly occurring impacts, especially impacts with more compliant bodies. Due to the wide range of injurious head impacts in ice hockey, it is challenging to develop a helmet that protects well in all scenarios. The aim of this programme of research was to develop a simplified test method, capable of replicating common ice hockey head impacts. Then, to investigate the capabilities of a mechanical metamaterial to enhance protection during collisions without compromising protection during more severe head impacts.

A novel test method, utilising laboratory equipment that is available to most researchers with an interest in impact protection, to replicate head impacts in ice hockey was developed and validated. It has been shown that a free-fall drop test method, with interchangeable impact surface orientation and compliance, can be used to create impact events that are representative of a range of common ice hockey head impacts. This newly developed test method can produce kinematic responses within less than 10% of key metrics obtained by current best practice methods to replicate ice hockey collisions and may facilitate widespread and more thorough testing in academic research and modifications to current test standard procedures.

A series of investigations were conducted to assess the potential of a mechanical metamaterial, comprising bi-beam structures, with an adaptive response to specific impact scenarios. Testing and modelling of individual bi-beams, unit cells, and cellular structures of bi-beams suggest a cellular structure, comprising bi-beams, can be developed by arranging unit cells relative to each other between two stiff sandwich plates. It has been shown that controlling the direction of buckling and the associated contact situations, can cause an abrupt switch in stiffness (~155 – 180%) in axial direction. Applied as a liner in an ice hockey helmet, this could achieve enhanced protection against an additional cause of injury – collisions – without compromising the performance in the scenario the helmets are currently designed for – falls. Dimensional scalability facilitates a wide range of possible designs and fields of application.

This programme of research contributes to the body of knowledge of head impact testing and helmet technologies to better protect players. Findings could help in developing better helmets that protect players against a wider range of head impacts which in turn would reduce concussions and make participation safer.

Acknowledgements

I would like to express my deepest thanks to my supervisors: Dr Oliver Duncan, Dr John Hart, and Dr Leon Foster for the countless things I learned from you and the guidance provided throughout this project. This PhD journey and my own professional development would not have been possible without your support. I would like to extend these thanks to all researchers and staff within the Sports Engineering Research Group at Sheffield Hallam University, in particular Terry Senior acting as my surrogate dad for the last four years.

Thank you, Jasmin. You were there any time I questioned myself, struggled with motivation to carry on, or just needed a reality check. I missed you and Max every day of this journey.

Finally, thank you to both my parents for your unconditional love, support, and belief in me. Everything I ever achieve is because you both worked so hard to provide me with the opportunities that you never had. For that, I am grateful every day.

Personal bibliography

Journal articles

Published:

Haid, D., Duncan, O., Hart, J., Foster, L. Free-fall drop test with interchangeable surfaces to recreate concussive ice hockey head impacts. *Sports Engineering* **26**,25 (2023). https://doi.org/10.1007/s12283-023-00416-6

Accepted for publication:

Haid, D., Foster, L., Hart, J., Greenwald, R., Allen, T., Sareh, P., Duncan, O. Mechanical metamaterials for sports helmets: structural mechanics, design optimisation, and performance. *Smart Materials and Structures.*

Conference proceedings:

Published:

Haid, D., Duncan, O., Hart, J., Foster, L. Feasibility of a free-fall drop test rig to replicate head impact scenarios in ice hockey. *16th International Conference on Advances in Experimental Mechanics, 6 – 8 September 2022.*

Haid, D., Duncan, O., Hart, J., Foster, L. Free-fall drop test rig to replicate head impacts in ice hockey. *ISEA 2022 – The Engineering of Sport 14, Purdue University, 6 – 10 June 2022.*

Haid, D., Duncan, O., Hart, J., Foster, L. Characterisation of thermoplastic polyurethane (TPU) for additive manufacturing. *Spinfortec2022: 14. Symposium der Sektion Sportinformatik und Sporttechnologie der Deutschen Vereinigung für Sportwissenschaft (dvs), Chemnitz, 29 – 30 September 2022.*

Accepted for publication:

Nickel, L., Duncan, O., Hart, J., Foster, L., Haid, D. Repeatability and Reproducibility of a Test Method to Assess Ice Hockey Head Impacts. *Special session on design for Sports Engineering at ADM 2023 International Conference, Florence, 6 – 8 September 2023.*

Haid, D., Duncan, O., Hart, J., Foster, L. Adaptable Mechanical Metamaterial for Ice Hockey Helmet Liners. *2023 IRCOBI Europe conference, Cambridge, 13 – 15 September 2023.*

Haid, D., Duncan, O., Hart, J., Foster, L. Proof-of-Concept of an adaptable mechanical Metamaterial for Ice Hockey Helmet Liners. *Special session on design for Sports Engineering at ADM 2023 International Conference, Florence, 6 – 8 September 2023*.

Contents

List of tables

List of figures

Nomenclature

Abbreviations

ABS	Acrylonitrile butadiene styrene
AE	Athletic Exposures
ATD	Anthropomorphic test device
ATP	Adenosine triphosphate
BrIC	Brain Injury Criterion
CI	Confidence interval
D	Impact duration
DIC	Digital image correlation
DTS	Diversified Technical Systems, Inc.
EPP	Expanded polypropylene
EPS	Expanded polystyrene
EVA	Ethylene-vinyl acetate
FE	Finite element
FFF	Fused filament fabrication
fps	Frames per second
GAMBIT	Generalized Acceleration Model for Brain Injury Tolerance
HIII	Hybrid III
HDPE	High-density polyethylene
HIC	Head Injury Criterion
HIP	Head Impact Power
ICC	Intraclass correlation coefficient
MEP Pad	Modular Elastomer Programmer Pad

MIPS	Multi-directional impact protection system
NOCSAE	National Operating Committee on Standards for Athletic Equipment
PAA	Peak angular acceleration
PAV	Peak angular velocity
PC	Polycarbonate
PLA	Peak linear acceleration
Q1	Lower quartile
Q3	Upper quartile
RIC	Rotational Injury Criterion
RT	Rebound time
SD	Standard deviation
SI	Severity Index
SIMon	Simulated injury monitor
SRD	Strain rate dependent
SRI	Strain rate independent
STP	Shear-thickening polymer
TDS	Technical data sheet
tPLA	Tough polylactic acid
TPU	Thermoplastic polyurethane
TTP	Time to peak
UCDBTM	University College Dublin Brain Trauma Model
VN	Vinyl nitrile
WSTC	Wayne State Tolerance Curve

Symbols

α	Angular acceleration [rad/s²]
Δh	Change in bi-beam length at critical load [mm]
ε	Engineering strain
μ	Initial shear modulus [Pa]
π	Ratio of circle circumference and diameter (3.142)
ρ	Density [kg/m³]
σ	Engineering stress [Pa]
v	Poisson's Ratio
φ	Half of the central angle of circular segment [°]
ω	Angular velocity [rad/s]
A	Area of bi-beam [mm²]
a	Linear acceleration [m/s²]
C	Relative injury sensitivity for a degree of freedom of the head
D1	Incompressibility parameter [Pa^{-1}]
d	Sagitta of circular segment [mm]
E	Young's Modulus [Pa]
g	Gravitational constant (9.81 m/s²)
h_0	Uncompressed length of bi-beam [mm]
h_c	Cord length of circular segment [mm]
I	Moment of Inertia [mm^4]
k	Column effective length factor
L	Length of bi-beam [mm]
n	End condition factor for buckling
P_{cr}	Critical buckling load

r	Radius of circular segment [mm]
t	Time [s]
t_{beam}	Thickness of bi-beam [mm]
W	Work per unit volume [J]
w_{beam}	Width of bi-beam [mm]

1. Chapter – Introduction

1.1 Introduction

This doctoral thesis documents an investigation of concussion risk assessment and prevention strategies in ice hockey. The project had two primary focuses; the development of a helmet test method that was representative of typical concussive impact scenarios; and the investigation of mechanical metamaterial solutions to the reduction of these concussive events. Each of these focuses aim to further concussion prevention in ice hockey, but also complement each other since the developed test method can be used to assess the effects of developed metamaterial structures in a helmet. This chapter outlines the motivation behind this research through a review of concussion incidences, commonly concussive head impacts, and the possible health implications of concussions. The aim, objectives, and thesis structure are given at the end of this chapter.

1.2 Motivation for the research

Concussions are a public health concern [1,2]. A concussion is a diffuse traumatic brain injury often induced by excessive head accelerations, that result in the temporary impairment of neurological functions [3]. Symptoms, such as headaches, sleep difficulties, and irritability, usually resolve within two weeks [1,4]; however, a history of clinically diagnosed concussions or sub-concussive head impacts is associated with an increased risk of long-term health implications [5–8]. The possibility of experiencing a concussion is an occupational hazard in most contact sports [9,10]. One such sport is ice hockey, a fast-paced and physical sport where injuries are common [11–13]. Within ice hockey, concussions can not only force players to take extended breaks for

recovery or even end their careers [14,15] but also place a financial burden on teams [16,17].

The use of protective equipment within ice hockey is mandatory, and certification to ensure a minimum level of protection that equipment provides has been introduced to the sport [18–21]. Innovations within the development of protective equipment, alongside rule changes, have further helped to reduce injury rates in the sport [22,23]. A certified helmet is one such item of equipment that is mandatory for participation in the sport. However, injuries to the head, especially concussions, remain common [14,24–26].

Within ice hockey, 14% of all recorded injuries on a professional level are concussions [14,24,26,27], though this is assumed to be an underestimation due to underreporting by players [28,29]. 93% of these concussions are attributable to collisions between players on the ice (i.e. shoulder, elbow, or glove-to-head impact) [30,31]. During collisions, the helmet impacts several layers of textiles, protective equipment, and the other player's body, which are typically less stiff than helmet liners [32,33]. Player-to-player collision head impacts are associated with lower magnitude, but longer duration, head accelerations in comparison to falls onto the ice or against the boards surrounding the ice rink [32,34,35]. Certification standards currently do not consider player-to-player collisions and helmets offer limited protection in this scenario [18–20].

Participating in ice hockey presents a wide range of scenarios in which concussive head impacts could occur, and a high risk of severe head injuries from falls [30,31]. Conventional helmet liner materials rely on compressive deformation to absorb impact energy [36–38]. Due to the requirement to protect well during falls, helmet liners have to be sufficiently stiff. Consequently, compression when impacting a more compliant

body is insufficient to efficiently absorb induced energy, leaving players susceptible to concussions [32,33,39]. Designs to protect against a wider range of head impacts, especially player-to-player collisions, such as multilayer foam or shear-thickening polymers, have been introduced with limited success [40–43].

Improving the breadth of protection provided by helmets could make ice hockey safer, and reduce injury breaks and hospitalisations, without affecting the high speed and physicality, which are characteristic of the sport. This will only be possible through the creation of increased knowledge around the mechanisms of concussion and understanding of the performance of helmet materials and designs. A representative and simple test method could facilitate extensive and widespread testing, which is necessary to further knowledge in the field, as well as modifications to certification standards. Furthermore, development of helmet designs that would offer an increased breadth of protection would be highly beneficial to the sport. It is believed this could be achieved through the incorporation of mechanical metamaterials within the liner that are capable of an adaptive response to specific impact scenarios. This could result in the creation of a helmet that both mitigates low energy longer duration (i.e. compliant) impacts, whilst preserving the current high impact energy absorbing properties that are required during falls against rigid surfaces.

1.3 Aim and Objectives

The aim of this programme of research was to develop a method to extend the assessment of ice hockey helmet performance to most common head impact scenarios; and to assess the potential of the use of mechanical metamaterials to enhance the breadth of protection provided. The objectives were to:

- Review published literature regarding concussions in ice hockey, designs and materials for helmets and impact protection, and helmet testing.
- Develop a method to replicate common head impacts in ice hockey for helmet testing.
- Investigate the potential of a mechanical metamaterial bi-beam design to create an adaptable response in deformation and stiffness to compression.
- Develop and critically evaluate a mechanical metamaterial sheet, comprising bi-beam structures, to be used as an adaptive helmet liner for ice hockey helmets.

1.4 Thesis structure

This programme of doctoral study will be presented as a traditional thesis, comprising six further chapters. These chapters are structured as follows:

- Chapter Two provides a critical review of literature relevant to the programme of doctoral study. The literature review examines concussions in ice hockey, the design of helmets and materials used in their construction, materials for impact protection and current test methodologies.
- Chapter Three details the development of a novel free-fall drop test method to replicate typical head impact scenarios observed in ice hockey. This includes an assessment of the protective properties of commercially available ice hockey helmets and a reliability assessment of the test method.
- Chapter Four introduces the concept of rate-dependent mechanical metamaterial bi-beams, as previously introduced by Janbaz et al. [44]. A material characterisation of 3D-printable thermoplastic polyurethane materials, used in the creation of bi-beam samples, is provided. Subsequently, uniaxial compression behaviour of individual bi-beams and bi-beam unit cells, that

comprise two individually orientated bi-beams, is evaluated to assess the potential of these structures to create a system with variable impact-specific stiffness properties. Finally, the potential to use the mechanical metamaterial as a helmet liner to protect more effectively against concussions is discussed critically.

- Chapter Five details the computational modelling of bi-beams to estimate deformation and stiffness during compression. An analytical and a numerical model are presented and their application to aid the development of bi-beam structures is discussed critically.
- Chapter Six details the experimental compression of cellular structures, comprising bi-beam unit cells, and findings are critically discussed. Further, a validation study to validate the buckling behaviour of bi-beams is presented.
- Chapter Seven discusses the main findings of this programme of doctoral study, followed by practical applications, limitations, potential areas for further research, and an overall conclusion of the research programme.

2. Chapter – Literature review

2.1 Introduction

This chapter presents a review of relevant literature to the programme of study. This is split into three sections:

- Concussions, injury mechanisms, and incidences in ice hockey
- Test methods and assessment criteria for head and helmet impact testing
- Materials and technologies for ice hockey helmets

2.2 Concussion in ice hockey

2.2.1 Introduction

A concussion is a diffuse traumatic brain injury often induced by excessive head accelerations, that result in the temporary impairment of neurological function [3,45]. Symptoms, affecting physical, cognitive, and emotional health, usually resolve within two weeks [4]. However, multiple concussions or repetitive sub-concussive head impact exposure is associated with an increased risk of long-term health problems [5].

Concussion rates in ice hockey, when compared to athletic exposures and occurrences per season, are among the top three highest concussion rates throughout sports [24,25]. Measures to reduce concussion risk, such as helmet developments and rule changes, have been introduced, with limited success [14,26,46,47]. As ice hockey is a fast-paced and physical sport, concussions are unlikely to be eliminated [12].

Understanding and replicating loading conditions of the head (and brain) during common ice hockey impacts is a vital step towards the improvement of current helmets. Accordingly, this section discusses; symptoms; injury mechanisms; incidences; and risk factors, of concussions in ice hockey.

2.2.2 Incidence

Ice hockey has one of the highest concussion rates in sports when compared to athletic exposures and occurrences per season [24,25]. Various measures, introduced to better protect players' heads have helped to reduce the overall number of head injuries but have not reduced concussion rates [14,46]. Indeed, concussion rates have been steadily rising and remain among the highest in sports [9,14,24,26,27,48].

Recent concussion rates in ice hockey have been reported at 7.87 concussions per 10,000 Athletic Exposures (AE) [25]. Further estimates, that correspond with this incidence, are an expected concussion in about 2% of all games [27], concussions accounting for up to 20% of all sustained injuries [10,14,24,27], and 22% of all athletes reporting at least one concussion [49]. These concussion incidences are prevalent throughout all skill and age levels [27,50,51] and across men's and women's ice hockey [47]. Due to inconsistencies in the definitions of injury and athletic exposure in published literature, some uncertainty remains regarding concussion incidence [48]. However, the collective evidence on concussion probability in ice hockey suggests a high risk for athletes compared to other sports.

A reason for the increase in concussions over the past 30 years is likely the increase in awareness and improved diagnostic methods [50]. Further factors are that ice hockey has become faster and players are taller and heavier [47]. However, 65.6% of players indicate they would continue to play if they believe they sustained a concussion [52]. This attitude results in underreporting of symptoms, inaccurate diagnosis, and eventually, in reported numbers being an underestimate of the actual total of sustained concussions [14,24,27,53].

2.2.2.1 Concussion risk factors

Contact between opposing players is the most common head impact scenario in ice hockey and causes about 88% of all concussions [14,30,31,47,54–56]. The initial points of contact of the head with an opponent during a concussive collision are a shoulder (55%), elbow (21%), glove (5%), stick, or knee [31]. The remaining 12% of concussions are caused by falls (7%) and contact with a team-mate (5%) [30].

Several factors influencing concussion risk have been identified. Protective equipment plays an important role as different helmet designs and fit can affect the provided protection [57]. Further, concussion risk is increased depending on player position (65% Forwards, 32% Defensemen, 3% Netminder) [26,27,30,58], in-game situations compared to training [12–14,26,47,59–61], gender (women higher than men) [47], and whether body checking is allowed [47]. Concussion risk is also increased for athletes that have already sustained one or more concussions in the past [14,56,59,60,62].

2.2.3 Concussion

A concussion is a diffuse traumatic brain injury often induced by excessive head accelerations, that result in the temporary impairment of neurological function. These accelerations may be caused by either a direct blow to the head, or, transmitted as an impulsive force to the head following an impact to the body. [3,63–66]. An absence of detectable structural damage to the brain is typical of concussion [3,67,68]. Instead, a complex sequence of metabolic events (Fig. 2.1), resulting in a neurochemical “energy crisis” (reduced adenosine triphosphate (ATP) generation – increased ATP usage) within the brain is triggered. These metabolic events are considered as the main cause of concussive symptoms [65,67]. As such, concussions are among the most complex injuries to diagnose, assess, and manage, encountered in sport.

A concussion typically results in the rapid onset of short-lived impairment of neurological function [3,4,63–65,67]. Symptoms are varied but can usually be categorised as; emotional, cognitive function, physical, and sleep disturbance (Table 2.1) [3,63,66]. These usually resolve within two weeks [3,4,65] but can persist beyond the typical recovery period [54,68].

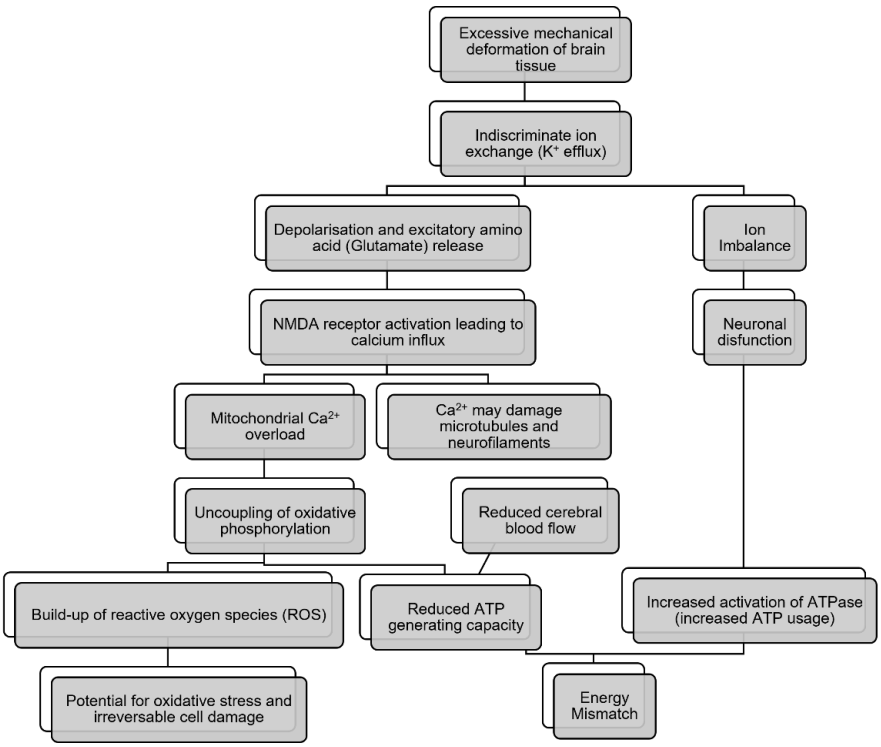

Fig. 2.1: The neurometabolic cascade of concussion [65].

A history of concussions is associated with microstructural changes in the brain and can cause lasting functional, physiological, and neurological changes [66,68,69]. Reported long-term consequences include reduced quality of life [70], increased risk of psychiatric disorders [4,6–8,64,71], increased risk of neurodegenerative disorders [4,6,64,72], and increased risk of suicide [73]. Repetitive exposure to sub-concussive head impacts, which can injure axonal and neuronal structures without associated symptoms, is associated with similar long-term changes in the brain [4,6,68]. Increased protection of the brain via helmet technology is an important part of the research community response.

Table 2.1: Signs and Symptoms of Concussion [66].

Domain	Symptom
Emotional	Irritable
	Sadness
	Nervousness
Cognitive	Feeling mentally “foggy”
	Feeling slowed down
	Difficulty concentrating
	Difficulty remembering
	Forgetful of recent information and conversations
	Confused about recent events
	Answers questions slowly
	Repeats questions
Physical	Headache
	Nausea
	Vomiting
	Balance problems
	Dizziness
	Visual problems
	Fatigue
	Sensitivity to light
	Sensitivity to noise
	Numbness/tingling
	Dazed
	Stunned
Sleep	Drowsiness
	Sleeping more than usual
	Sleeping less than usual
	Difficulty falling asleep

2.2.4 Concussion mechanism

Deformation of the brain cannot be directly measured; instead, indicative measures such as acceleration are used. Furthermore, the damage caused by a concussive blow spreads over large areas of the brain and is seldomly macroscopically detectable.

Consequently, there is some ongoing debate over concussion mechanisms [74–77]. Numerous, and sometimes conflicting, theories and mechanisms of brain injury have been proposed [78]. Despite some uncertainty, it is generally agreed that brain injury is related to excessive, or overly rapid, deformation of tissue [74].

2.2.4.1 Intracranial Pressure

During impact to the head, local pressures can exceed the injury threshold of brain tissue, causing damage [79]. It is assumed that two pressure mechanisms occur in the head during impact:

1. A transfer of energy from the skull to the brain, causing high coup (site of impact) pressure and low contrecoup (opposing side of impact site) pressure (Fig. 2.2).
2. A transfer of energy stored in the brain back to the skull, resulting in increased pressure throughout the skull [78,80].

Linear acceleration is the principal mechanism of high intracranial pressures (i.e., those inside the skull) [77]. However, tissue strains have also been correlated to angular acceleration and have been associated with increased pressure [81,82].

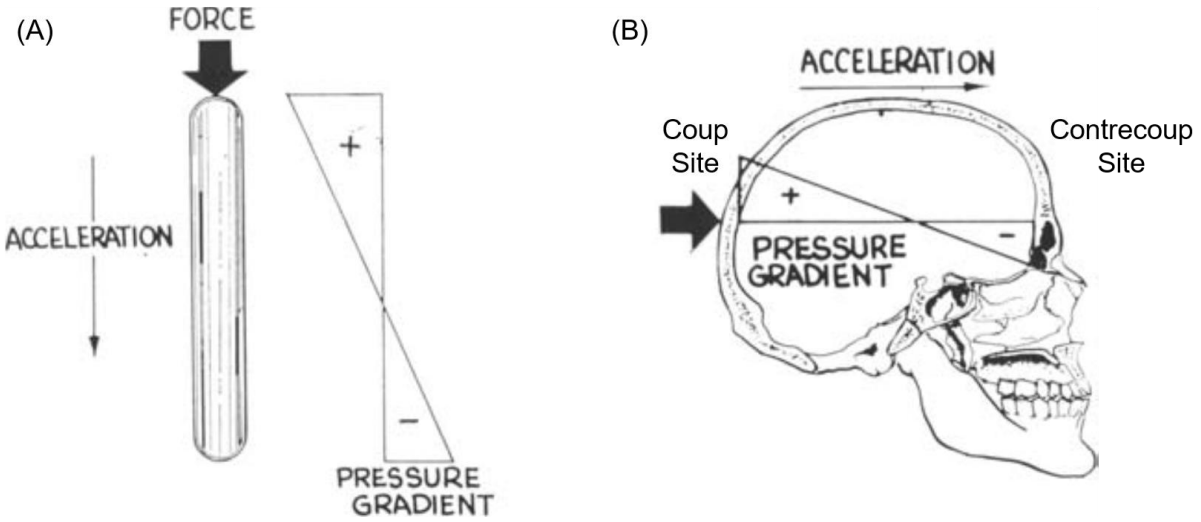

Fig. 2.2: Pressure gradients during impact in (**A**) a closed flask and (**B**) the cranium [83].

A primary factor in the development of various focal (localised) brain injuries are impact-induced intracranial pressure gradients [78,79,84,85]. Such pressure gradients are typically formed by high pressure at the coup site and areas of low pressure at the contrecoup site (Fig. 2.2) [86]. A reversal in the pressure gradient between coup and contrecoup sites is observed in falls; a result of the brain lagging the motion of the skull [74,79]. The principal sources for the emergence of intracranial pressure gradients are magnitude and duration of impact-induced linear accelerations [74,79]. It is, however, also necessary to consider skull deformation and compression as factors on the intracranial pressure response [78,79,85].

Localised deformation of brain tissue, and distortion of the brain stem, occur as a result of shear stresses attributable to pressure gradients. Subsequently, it has been concluded that coup and contrecoup brain injuries can both occur from intracranial pressure gradients [74,79,85–87].

2.2.4.2 Relative Motion of Head Structures

During impact, local brain tissue lags the motion of the skull [88]. Consequently, the brain is pushed up against the faster-moving skull causing injurious deformation [78,88] and bruising [89]. Similar relative movement occurs during rotation of the head. Loose coupling causes brain motion to lag that of the skull [89]. As head rotation slows, reaches a steady state, or changes direction, the brain will continue to move [76], causing (potentially injurious) loading of connective blood vessels and neurons [74,79]. Measurements of brain motion during impact suggest a relative displacement of 2 to 6 mm [80,88,90] and relative rotations of up to 5° [88].

Most kinds of brain injuries have been associated with relative motion between the brain and the skull. For example, direct brain contusion can be caused by movements

of the brain against the skull [79], intracranial bleeding by strained or ruptured blood vessels [74,91], and concussions by rapid deformation of brain matter [76].

2.2.4.3 External Loads

Most closed head injuries (non-fracture) follow accelerations, that cause damaging intracranial mechanisms [76,92]. Historically, two theories were accepted to explain the underlying mechanisms of head and brain injuries: Firstly, by direct impact causing linear acceleration, and secondly, by oblique (off-centre) impacts causing linear and angular acceleration [93]. Focal (localised) brain injuries are usually associated with linear acceleration, whereas diffuse (widespread) brain injuries are thought to be caused by angular acceleration of the head [35].

Early research on brain injury suggested that linear acceleration, caused by direct impact, was the most important injury mechanism. Linear acceleration has been linked to shear strains in brain tissue, increased pressure rate, and increased coup and contrecoup pressures [74,78,89].

Nearly all types of closed head injuries can be created by angular acceleration of the head following oblique impacts [77,94]. In 1943, Holbourn et al. suggested that angular acceleration has a critical influence on brain injury [95]. Various investigations have come to a similar conclusion [96,97] and suggest angular acceleration may be more damaging than linear, contributing more than 90% of brain strain [75,81,84]. Rotational velocity may also increase severity of brain injury when coupled with acceleration but is not considered high risk in isolation [98]. Rotation has been mainly associated with shear strains in the brain, leading to diffuse injuries [74]. The distribution of strains induced by angular loading decreases in magnitude from the surface to the centre of

the brain. Damaging strains only extend inwards to affect the core during increased pulse durations, causing the most severe levels of traumatic brain injuries [74,84].

Despite theories considering linear and angular acceleration as individual components, few head impact events outside of a laboratory setting will contain linear or rotational accelerations in isolation [74]. Despite uncertainty about the harmfulness of head acceleration components, both are generally present in any head impact and likely contribute to injurious loads on the brain [75,81,93,99].

Compressive deformation of the skull can also damage the brain. Direct impact on the head produces local stress areas, causing a slight in-bending of the skull bones that can slap the brain tissue directly underneath [74,86]. Depending on the amount of skull deformation, the damaged area may also spread laterally from the impact site. Inward bending of the skull has been associated with brain contusion [100] and intracerebral hematoma [74].

2.2.5 Summary

Concussions, causing short-term functional impairments and long-term health problems [4,5], are recognised as a public health concern. They are caused by biomechanical forces to the head where linear and angular kinematics can be injurious [75]. One of the highest concussion rates throughout sports is reported in ice hockey and concussions are one of the most common injuries within the sport [24,25]. Most concussions are caused during collisions with other players on the ice (~93%) and falls onto the ice or against the boards (~7%) [30,31]. Clearly, there are various head and brain deformation mechanisms that can contribute to concussion risk, making the design space for helmets complex. Helmets need to minimise multi-objective metrics in various types of impact.

2.3 Head Impact Testing

2.3.1 Introduction

Assessing helmets during representative impacts can help towards understanding and developing better head protection. Laboratory-based testing, designed to recreate real-world ice hockey head impacts, has been common practice since the introduction of the first ice hockey helmet standard in 1962 [21,22]. Test standards ensure minimum protective requirements, are a driving force for product improvement, and as a result, have helped to reduce the number of severe head injuries [23,101]. However, since their introduction, the standards have not been updated regularly to account for new developments and now, face substantial criticism [22,101,102]. Helmet testing in published research describes a wide range of test methods, often used in combination to assess multiple concussive loading conditions [22,23,32,33,103,104]. These protocols are often too complex for standard testing and the required equipment is often expensive or unavailable to research facilities [22] making representative helmet testing not widely available. Understanding helmet impact test protocols and how different factors can be modified to replicate different concussive events is essential to developing a suitable test method that may be used in standards and research. Therefore, this chapter critically discusses the state-of-the-art research and test standards for ice hockey helmets.

2.3.2 Anthropomorphic test devices

Instrumented anthropomorphic test device (ATD) headforms allow repeatable and controllable study of head impacts, unlike investigation with animal or cadaver skulls that have been used historically [22]. Three different headforms are commonly used in head impact tests: the EN 960 [105,106], the Hybrid III (Humanetics Innovative

Solutions, Inc.) [107], and the National Operating Committee on Standards for Athletic Equipment (NOCSAE) headform [108]. All three come with varying degrees of biofidelity and are used in test standards and research, depending on their advantages and limitations [22,109,110].

The EN 960 and ASTM F2220 headforms (Fig. 2.3 (A)), when used in helmet standards, are typically manufactured out of K1A- magnesium, or another appropriate metal. Both are based on the never published ISO DIS 6220 international standard and are used in all head impact testing standards prescribed by their respective institutions. Occasionally they are also used in test setups described in published literature [111–113]. They are specified in a range of sizes to allow helmet testing for all sizes of junior and senior helmets with respective masses from 1.97 to 6.1 kg [105,106]. The simplistic design of the EN 960 headform causes low biofidelity and the magnesium alloy possesses higher stiffness than a human head.

The Hybrid III (HIII) headform (Fig. 2.3 (B)), developed in 1974, is designed and optimised for use in frontal vehicle crash testing [108,114]. The headform comes in three size percentiles (5^{th} female, 50^{th} male, 95^{th} male) and is made from cast aluminium parts covered with a removable vinyl skin cover [108,110,114]. The 50^{th} male HIII is the most used headform in head impact research [22,32–35,103,111,112,114–141] and most injury risk estimates were developed with HIII test data [22]. The 5^{th} female HIII is also commonly used where helmets for children are tested [111,123,143,144]. Despite its popularity, the HIII has limited biofidelity and in some cases, the headform does not contact the helmet padding at the occipital bottom edge of helmets [22,108,109,145]. Some test setups use special skin covers or nylon stockings to improve biofidelity of the interface between headform and helmet [140,141,146,147].

The NOCSAE headform (Fig. 2.3 (C)) has been developed to accurately simulate human head response to impact for the certification of commercially produced sports helmets [108,145,148]. The headform is available in three sizes and consists of a urethane covering that is moulded to a headform [22,108,110]. It is used in all NOCSAE helmet standards [149–155] and commonly used in research [39,103,118,156–165]. Compared to the HIII, the NOCSAE headform better resembles human anatomical features, however, it was not designed to be used in combination with an anthropomorphic neckform limiting representative testing [108].

Anthropomorphic neckforms, attached to the headforms, are often used to achieve more realistic post-impact behaviour. The post-impact movement allows energy to be dissipated, resulting in a lower transfer of energy to the head and a longer duration impact event [104]. The HIII neckform is commonly used [112,131–140,144], however, its bending stiffness properties are only representative in anterior-posterior direction [22]. Alternative neck surrogates that overcome the limitation of directional sensitivity, such as the unbiased neckform, have been used increasingly in published research [22,32,34,39,104,120,125,143,162,163].

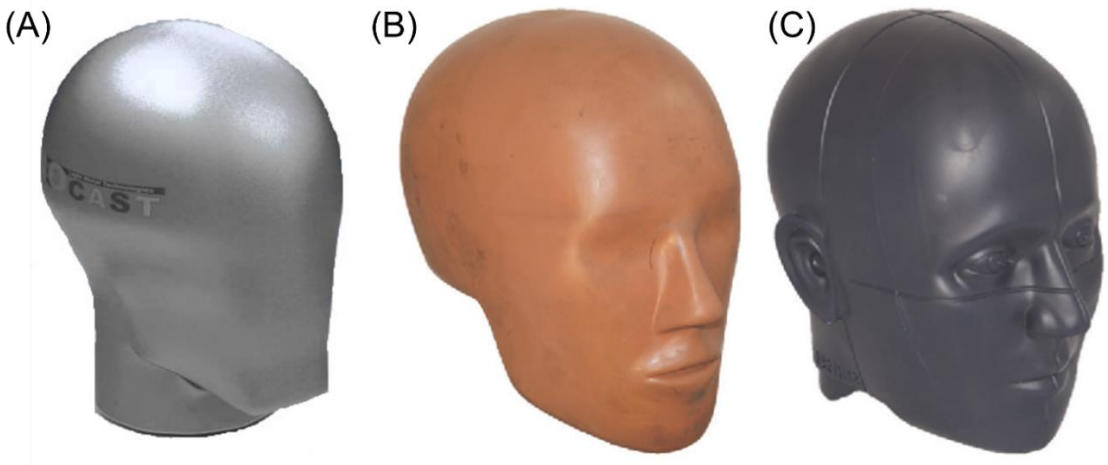

Fig. 2.3: (**A**) EN 960, (**B**) Hybrid III, and (**C**) NOCSAE headform.

2.3.3 Test Methods

Helmets ideally should provide protection throughout the anticipated range of impacts in their field of application. Therefore, helmet impact protocols are specific to the respective sport. In-field measurements [166,167] and video analysis [67,75,101,120, 124,136,142,143] can be used to characterise impacts. In ice hockey, the range of common head impacts and corresponding injury mechanisms is too broad to accurately replicate loading conditions with one test setup [22,23,32,104,168]. Methods described in test standards can be put into three categories: drop test, horizontal impactor test, and projectile impact test (Table 2.2). However, various considerations have to be made for all replicated impact scenarios.

The inbound loading vector, consisting of the impact site and the direction of the force, is an important consideration that depends on the helmet's field of application. Directional sensitivity [169] and increased angular kinematics due to non-centric impacts influence brain injury risk [132,134,135,170]. Standards typically either describe a test area (Fig. 2.4 (C)) that must be impacted [18,20,171–174] or precisely define locations (Fig. 2.4 (A & B)) [128–130,152,153, 158,159]. Most of the prescribed impact vectors in test standards are centric, with some exceptions [149,175]. Test protocols in published research typically use the same impact sites as prescribed in test standards [22], however, non-centric impact vectors are seen more often [32,116,121,134–136,156]. Multi-impact helmets, as used in ice hockey, are usually tested more than once (typically three times) for each impact vector to assess degradation effects [18–20,23,104,135,149,150,154,161,168].

Helmet padding temperature can range from ~0 °C to ~40 °C [176], depending on ambient temperature and the wearer's head temperature [160]. As some materials commonly used in helmets are temperature and moisture-dependent [177,178], testing

in different environmental conditions is necessary. Test standards for ice hockey helmets assess impact properties at ambient (20 °C), cold (-25 °C), and hot (30 °C) temperatures [18–20]. Test standards for helmets in other sports additionally include wet conditions [171,172,179–185] and artificial ageing of the helmet [172,174,184–187].

Table 2.2: Test methods in sports helmet standards.

Method	Required in	Reference
Drop test	Ice hockey	[18–20,149]
	American Football	[150]
	Bicycle	[171–173,179–181,188]
	Baseball & Softball	[151,152,189]
	Cricket	[187]
	Equestrian sports	[173,182,186,190]
	Lacrosse	[154]
	Motor Sports	[183,191–193]
	Skateboard	[194]
	Snow Sports	[184,195–197]
Horizontal impactor test	American Football	[150]
Projectile impact test	Ice hockey	[149]
	Baseball & Softball	[151,152,189]
	Cricket	[187]

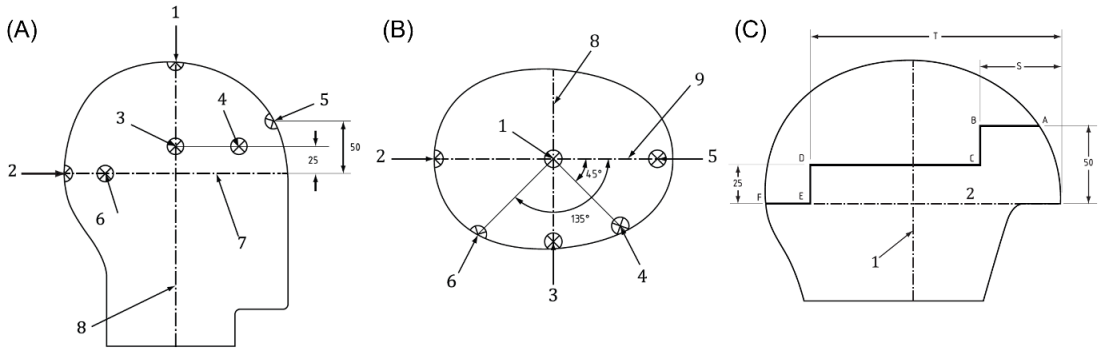

Fig. 2.4: (**A & B**) Prescribed impact sites (1: Crown, 2: Rear, 3: Side, 4: Front Boss, 5: Front, 6: Rear Boss) and (**C**) reference line for impact area [18].

2.3.3.1 Drop test

The most common method for helmet impact testing throughout test standards and research is a drop test (Fig. 2.5 (A)), as it is simple and consistently reproducible [22]. The headform is dropped, either guided [80–82,91,99,102,104,115,123,124,137,138, 141–143,145,182–184] or in free fall [201–204] onto a stationary high-mass anvil, topped with sport specific impact surfaces [22,23,133]. Drop tests typically replicate fall-type impacts; in ice hockey, these include the ground [142,205], ice [35,122], boards [35,122,143], or glass [35,143].

Test standards typically use a guided drop test onto sport-specific shaped anvils, such as a kerbstone [171,172,174,179–181,188,191,192], hemisphere [170,178,179,186, 187], or horseshoe [155,182,190]. Drop heights, impact surfaces, and impact locations are based on typical sport-specific impacts. Standards published by the NOCSAE generally use the NOCSAE headform [149–152,154,155,189], while all others use the EN960 [105] / ASTM F2220 [106] headform. All drop tests in ice hockey standards use a rigid Modular Elastomer Programmer (MEP) Pad as the impact surface and a drop height of 1 m, resulting in 4.5 m/s impact velocity. If the measured resultant peak linear acceleration does not exceed a threshold of 275 g, the helmet passes and is deemed suitable for use [18,20,149,206].

In published research, modifications to the standard test protocol are commonly made to tailor the test method for specific helmets. Many include angular kinematics in measurements, to account for the injurious effect rotation can have on the brain [3,22,23]. Wider ranges of impact velocities are commonly described in published literature than in test standards. Specifically, lower impact velocities and respective impact energies are tested to assess helmets throughout the range of impacts common in their field of application [22,111,118,142]. Additional test equipment, such as an ATD

neckform [32,120,137] or oblique impact surfaces [118,124,146,147,207], are often used to allow more realistic post-impact behaviour, and induce higher angular kinematics into the headform.

2.3.3.2 Horizontal impactor

The most common method to replicate a head impact caused by a collision between two ice hockey players is horizontal impacting of a stationary headform (Fig. 2.5 (B)) [22]. The impact is induced with either a pendulum rig [65,91,105,109,118,123,124, 192,193] or a pneumatic impactor [65,80–83,94,96,99,102,107,109,111,113–115,118, 119,124,136,139,142–146,149,151,191,192], while the headform is mounted onto a linear bearing track [112,165] or sliding system [103,116,120,130,163,208], to allow post-impact movement [104].

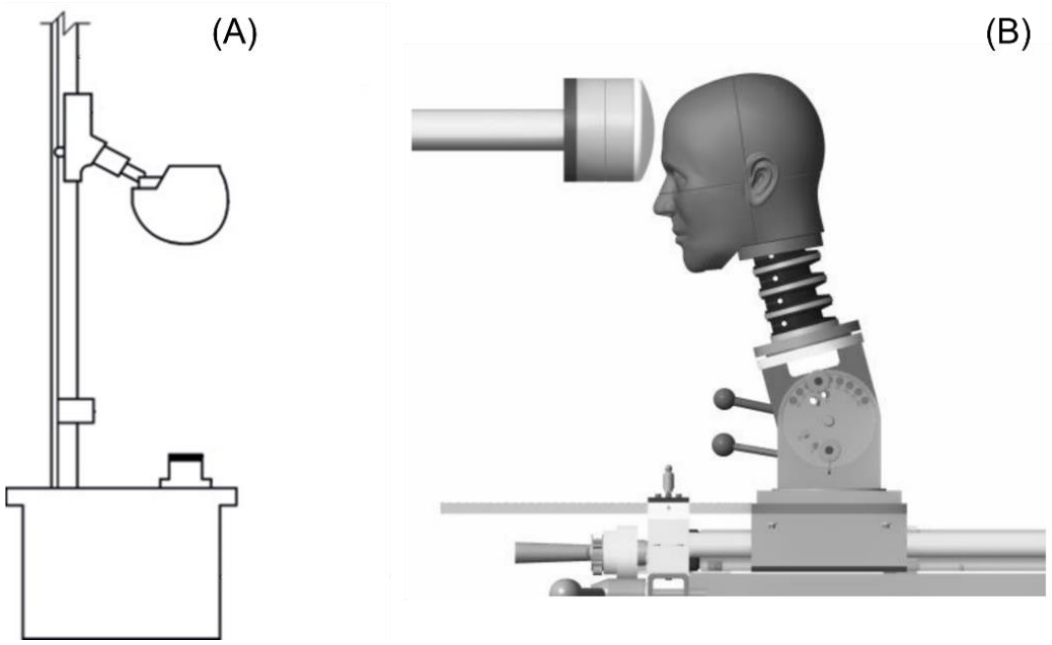

Fig. 2.5: (**A**) Guided drop test [18] and (**B**) horizontal impactor test setup [175].

The only test standard currently requiring a linear impacting system is the NOCSAE ND 002 for American Football helmets. The impacting system (15.5 kg) with a convex polyurethane impactor head impacts the helmeted headform at 6.0 m/s in six different

locations [150,175]. Modifications to this standard test setup are seen in published literature where reported impact velocities range from 2.0 m/s [112] to above 9.0 m/s [92,116,119,122,162,208]. The impactor shape [208] or stiffness [33,119,168,210] are commonly modified, and can be equipped with protective equipment that might impact the head, such as shoulder or elbow pads [32,122,144].

2.3.3.3 Projectile Impact

During projectile impacts, a low-mass object hits a stationary headform at high velocities [23]. They are used where athletes are more susceptible to being injured by a flying ball or puck. Hence, the impacting projectile is the ball or puck that the game is played with [149,151,152,189,211].

The NOCSAE ND 030, although not currently required by any legislation, is a projectile test standard for ice hockey helmets that tests at puck speeds of 28 m/s [149]. Similar protocols are described in published literature with impact velocities ranging from 19 to 45 m/s [23,32,39,103,111,125,126,129,138,162,163].

2.3.3.4 Other helmet impact tests

During more exploratory research or where standard protocols are not able to replicate the impact suitably, more complex test protocols have been described. Reported setups include full ATDs [92,212] colliding with sport-specific bodies such as headforms [92], other full-sized dummies [212], boards [213], or water [214]. Human interaction to induce impacts on the headform has also been reported [112,138,210]. Modifications to a drop test setup included horizontal motion of the impacting surface to simulate collisions with vehicles [131]. While generally too complex to be adopted as standard procedures, these exploratory test setups serve a vital role in defining head impact events.

2.3.4 Assessment criteria

To assess head impacts and helmet effectiveness, kinematics of the head must be quantified. Due to the complexity of head injuries and injury mechanisms, numerous measures have been developed [22]. Complexity ranges from peak accelerations to numerical simulations of the head and brain [215]. Each comes with different advantages and is designated for a specific kind of head injury with individual injury thresholds. Consequently, there is limited consensus on which kinematic measure is preferential, and careful consideration is required when choosing a head impact severity measure [22,137]. The most used measures are discussed below.

2.3.4.1 Linear acceleration

As mentioned previously (Section 2.2.4), linear acceleration of the brain is a mechanism of concussion. Several attempts have been made in defining a maximum tolerable threshold of peak linear acceleration (PLA) for head injuries such as skull fractures and concussions [92,96,99,216–219]. PLA is used as a measure of head impact severity throughout most head impact testing literature and helmet test standards [22].

The Wayne State Tolerance Curve (WSTC) (Fig. 2.6), derived from animal and cadaver impacts in 1953, was the first to associate linear acceleration with impact duration when assessing injury risk [220,221]. It describes tolerable average acceleration as a function of duration. Accelerations above the curve are assumed to be life-threatening while accelerations lower than the curve are assumed to be not life-threatening. Further threshold curves, based on the WSTC, have been developed to include different injuries or impact scenarios [219,222].

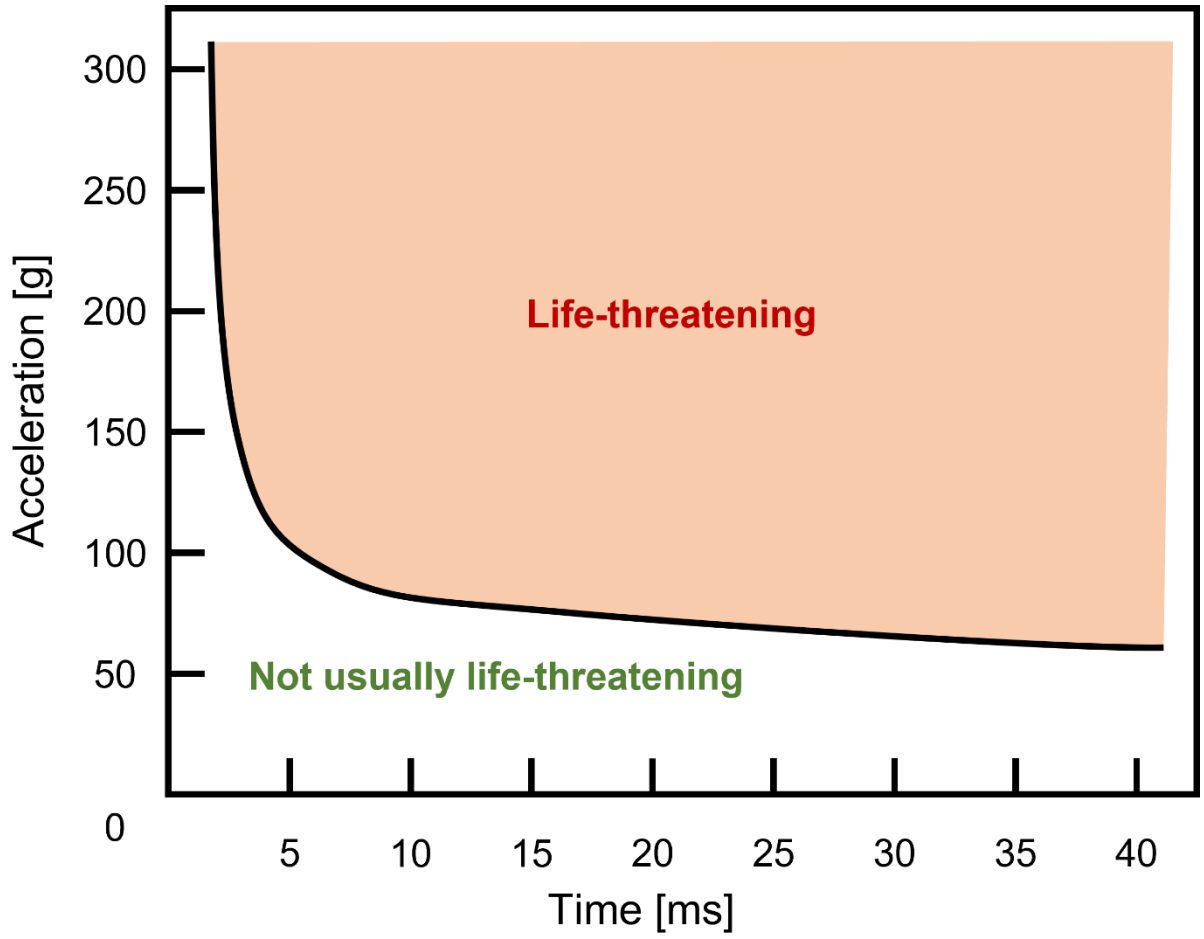

Fig. 2.6: The Wayne State Tolerance Curve. An impact with PLA and impact duration that results above the curve is considered life-threatening, while any impact below the curve is considered not life-threatening [218].

The Severity Index (SI) integrates the acceleration signal over the impact duration with a weighting factor (Equation (2.1)). SI allows for a comparison of head impacts of different pulse shape and impact duration. An SI of 1000 is described as the maximum pulse intensity without danger to life. SI is regularly used in head impact literature [22,92,117,141,157,158,161,200] and all NOCSAE test standards use SI threshold values (1200 – high-energy, 300 – low-energy) [149–152,154,155,189,223].

The Head Injury Criterion (HIC) (Equation 2.2), designed for frontal impacts in vehicle collisions, is a modification of the SI that only considers a pre-defined time interval (15 or 36 ms) [224,225]. HIC is a common measure for head impact severity in literature [124,141,212] but is not currently used in any helmet standards.

$$SI = \int_0^T a(t)^{2.5} dt \quad (2.1)$$

$$HIC = \left[\left(\frac{1}{t_2 - t_1} a_{res} dt \right)^{2.5} (t_2 - t_1) \right]_{max} \quad (2.2)$$

Where *a* is the resultant linear acceleration, T is the end of the impact, and values for t_1 and t_2 are chosen to maximise the HIC value.

2.3.4.2 Angular acceleration

Peak angular acceleration (PAA) and peak angular velocity (PAV) are commonly considered as injury probability measures in head impact literature [65,80,211,212,91, 99,101–103,110,118,140]. Various thresholds, up to ~200 krad/s², for different injuries have been suggested [219,228–231] and a PAA threshold (6 krad/s²) is defined in the NOCSAE 002 test standard for American Football helmets [150].

The Rotational Injury Criterion (RIC) (Equation 2.3), based on the assumption that injury risk from linear and angular acceleration are both inversely proportional to time duration, uses the resultant angular acceleration in the HIC equation (Equation 2.2). RIC was developed to be used complementary with HIC to assess all six degrees of freedom [232].

The Brain Injury Criterion (BrIC) (Equation 2.4) considers the angular velocity and the head's directional sensitivity to injuries caused by rotation [233,234]. RIC and BrIC are both designed to complement HIC to be able to capture skull fractures and brain injuries [232–234].

$$RIC = \left[\left(\frac{1}{t_2 - t_1} \alpha_{res} dt \right)^{2.5} (t_2 - t_1) \right]_{max} \quad (2.3)$$

$$BrIC = \sqrt{\left(\frac{\omega_x}{\omega_{xC}}\right)^2 + \left(\frac{\omega_y}{\omega_{yC}}\right)^2 + \left(\frac{\omega_z}{\omega_{zC}}\right)^2} \quad (2.4)$$

Where α_{res} is the resultant angular acceleration and ω is the angular velocity, while ω_{xC} is the threshold velocity around the x-axis (typically, ω_{xC} = 66.25 rad/s, ω_{yC} = 56.45 rad/s, ω_{zC} = 42.87 rad/s) [233,234].

2.3.4.3 Combined linear and angular acceleration

The Generalized Acceleration Model for Brain Injury Tolerance (GAMBIT) weights the effects of the two forms of motion (Equation 2.5). GAMBIT applies a classical material failure engineering approach [235]. Head Impact Power (HIP) uses the rate of change of kinetic energy of the head and compares it to critical injury threshold values (Equation 2.6) for each degree of freedom individually [236,237]. Both are used sparsely in published literature, however, HIP has been the most reliable in predicting concussions when compared with the other measures [236,238].

$$GAMBIT = \left[\left(\frac{a(t)}{a_c}\right)^m + \left(\frac{\alpha(t)}{\alpha_c}\right)^n\right]^{\frac{1}{s}} \quad (2.5)$$

$$HIP = C_{ii}a_{ii}\int a_{ii}dt + C_{jj}\alpha_{ii}\int \alpha_{ii}dt \quad (2.6)$$

Where a is the linear acceleration, a_c the threshold linear acceleration, α the angular acceleration, α_c the threshold angular acceleration, and C the relative sensitivity for each degree of freedom of the head (Due to a lack of knowledge on directional sensitivity, the coefficients are currently reflecting the mass and mass moments of inertia of the HIII headform: C_1, C_2, C_3 = 4.5 kg, C_4 = 0.016 Nms², C_5 = 0.024 Nms², C_6 = 0.022 Nms²) [236].

2.3.4.4 Numerical

Numerical simulations use measured kinematics as input variables to compute deformation metrics such as principal strain, cumulative strain damage measure, or pressure in the brain as injury prediction tools [102]. Predicted strain in the corpus callosum and thalamus (both located in the centre of the brain) showed strong correlation with clinical diagnosis of concussion [239–244]. Different numerical brain trauma models have been developed and used in published literature over time such as the University College Dublin Brain Trauma Model (UCDBTM) [89,245,246] or the Simulated Injury Monitor (SIMon) [129,137]. Despite increased complexity and computational effort, the use of predicted brain deformation metrics has been recommended over kinematic measures as higher correlations with occurring concussions have been shown [122,135].

2.3.5 Summary

Helmet tests replicate real-world head impacts in a laboratory setting. Standard procedures for ice hockey helmets prescribe a guided drop test onto a rigid surface, simulating falls onto the ice. This helped to nearly eliminate catastrophic head injuries, however, common impact scenarios that are thought to cause concussions, including angular kinematics or more compliant impact surfaces, are currently not considered. In published literature, a wide range of test methods and impactors are described. There is limited consensus on the ideal way to replicate head impacts and extensive laboratory equipment is currently required.

2.4 Ice hockey helmets

2.4.1 Introduction

One of the earliest documentations of a helmet worn in sports was during an American Football Game in 1893 [247]. Early helmets, using pieces of leather lined with felt padding and held together by straps, were not effective in injury prevention [21,247,248]. The first test standard for ice hockey helmets, introduced in Sweden in 1963 [249], and the mandatory use of helmets in 1979 [21], created pressure on manufacturers and boosted developments. Innovations in manufacturing and materials such as injection-moulded shells and foam materials [21] have helped to reduce number and severity of head injuries in ice hockey, despite a great increase in hours of play [249]. More recent innovations in helmet technology include new materials, such as shear-thickening polymers [250] or cellular structures [251,252], as well as designated systems to reduce head rotations [253,254]. This section provides an understanding of helmet design, energy absorption mechanisms, and currently available materials and systems which is essential to addressing limitations in current helmets.

2.4.2 Helmet design

The broad goal of all impact protective equipment is to absorb all foreseeable induced impact energies while minimising metrics associated with injury risk. For a predictable and consistent impact scenario, the optimisation process for an energy-absorbing material, described below, is effective and well understood. The challenge with helmets, especially in sports such as ice hockey, is the variety of different impact scenarios. These can range from rigid surfaces to compliant bodies or projectiles, and the helmet should ideally protect effectively during all of them. Consequently, the range

of different helmet designs is as wide as the range of different fields of applications [21,23,40]. However, any sports helmet can typically be classified as one of two designs.

- Crash helmets: Crush under impact and are in use where the head is likely to be impacted once at high energy, such as motorsports, bicycling, and alpine sports. After an impact, these single-impact helmets lack much of their original ability to offer protection and need replacement [21,23].
- Multi-impact helmets: Designed to maintain their impact performance during many impacts over long durations and return to their original shape after each impact. Typical sports are American Football, ice hockey, and lacrosse [21,23].

Despite differences in design and additional impact attenuation systems applied commonly, helmet designs in most applications consist of a minimum of two layers. A stiff outer shell (Fig. 2.7 (A)) prevents penetration and spreads loads over a larger area, while a compressible liner (Fig. 2.7 (B)) absorbs energy through deformation [23,255].

Fig. 2.7: Ice hockey helmet with (**A**) HDPE outer shell and (**B**) dual-density foam liner.

2.4.3 Energy absorption of cellular structures

The principal idea of impact protection is converting kinetic energy into another form of energy, while keeping forces and accelerations to a minimum [36]. Through bending, fracturing, hinging, and buckling of cell walls, cellular structures exhibit a higher capacity to absorb energy than solid materials under the same stress conditions [256]. Foams, historically the most common helmet liner material, are such a cellular structure, and can be tailored to specific impact loads by controlling (relative) density and thickness [36,255]. Specifically, increasing foam relative density (foam density/density of the constituent material), without modifying cellular structure, increases foam stiffness and plateau stress [257]. To make design choices for any impact protection structure, an understanding of energy-absorption mechanisms is essential.

Energy absorption diagrams provide a systematic approach to choosing a suitable material for impact protection and energy absorption. They are based on compression stress (σ) vs. strain (ε) curves (Fig. 2.8 (A)), where the area under the curve is the work per unit volume (W) [36]. The stress vs. strain curves of cellular materials such as foams can often be divided into three sections. (i) linear elasticity: Up to about 3 to 5% strain; (ii) Plateau: Depending on the material, either elastic buckling, plastic collapse, or ductile failure of the cell walls; (iii) Densification: Cells undergo self-contact, cell walls are completely collapsed, opposing cell walls are crushed together, and the constituent material is compressed [36].

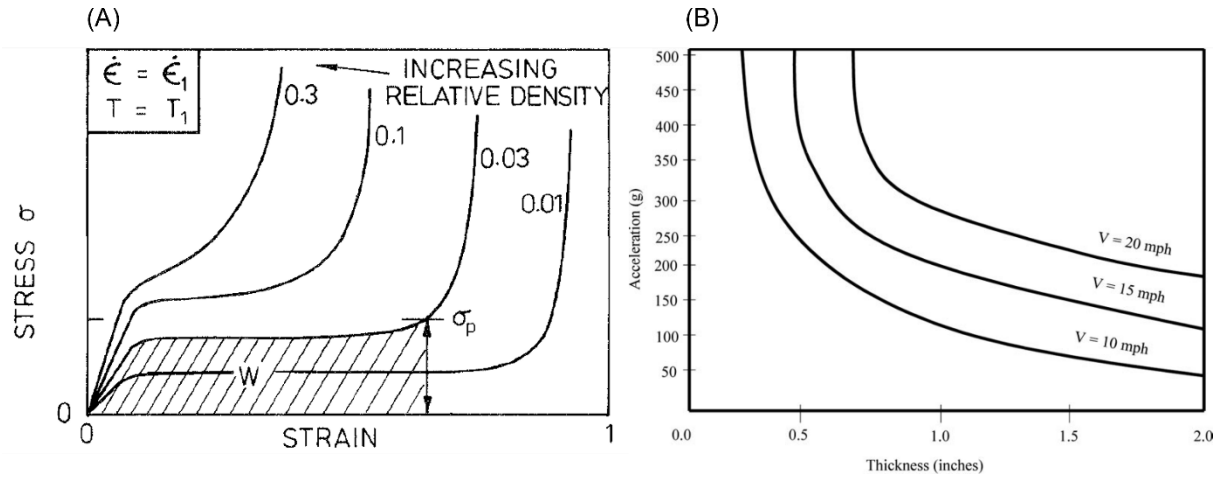

Fig. 2.8: (**A**) Compression stress-strain curves for different relative densities of a foam material at identical strain rates. Area W under the curve illustrates the absorbed energy. (**B**) Minimum acceleration achievable for a given thickness [36].

Energy absorption efficiency is highest during the plateau region. The level of this plateau can be tailored by material, respective density, and layer thickness [36]. To maximise the area under a stress vs. strain, or force vs. displacement curve, and therefore absorb a maximum amount of energy before the material densifies, the material should be chosen based on the expected impact energy, impactor, and impacted body [36]. Possible scenarios of material compression upon impact are shown in Fig. 2.8 (A). An overly stiff material (Curve 0.3 and 0.1) with a high plateau stress will not densify upon impact. Due to the low compressive deformation, large forces are required to absorb the applied impact energy, causing greater accelerations. If the material is too soft (Curve 0.01), it will densify before most of the energy is absorbed, meaning high forces are required to absorb the applied energy over the small remaining distance, once again causing high accelerations. An ideal impact material (Curve 0.03) absorbs the induced energy, without densifying, during the plateau region and keeps transmitted forces and accelerations to a minimum [21,36]. The above trend provides an intuitive explanation of foam selection but neglects the effects of impactor/helmet shape or stiffness, anisotropy, visco-elasticity, and dynamic

wave propagation, which are not only reliant upon stress vs. strain curves. So, such a selection process should be seen as an approximate rule of thumb only, while further testing is often used while designing or modifying a helmet.

Energy absorption and therefore provided impact protection increases with increasing thickness. While high densification strain results in an increase in absorbable impact energy before the onset of high accelerations, increasing compressive displacement by increasing thickness also decreases acceleration (Fig. 2.8 (B)). However, increased thickness comes at the expense of helmet size which has been associated with increased angular accelerations, comfort, and aerodynamics. Another limiting factor is athletes' willingness to wear the helmet. An overly bulky or inaesthetic helmet could be rejected by athletes, so is not feasible even if it provides better protection [21,36].

2.4.4 Helmet materials

Shell materials

The stiff outer shell of the helmet serves multiple purposes. Upon impact, the shell prevents penetration of the helmet to protect the head from sharp objects [258], and is intended to spread the impact over a larger area to avoid concentrated loads and engage more liner material [21,23,40,255,258,259]. The helmet shell also absorbs energy and serves as the first layer of protection. Shell deformation, which depends on material and geometry [21,260], accounts for about a third of the overall absorbed energy [255,261]. Lastly, the shell provides a structure for the helmet liner to be secured to [258].

Helmet shells are usually injection moulded, semirigid thermoplastics [40]. The most common shell material for ice hockey helmets is high-density polyethylene (HDPE) (Fig. 2.7 (A)). HDPE is inexpensive, dimensionally stable, easily moulded, chemical

resistant, and notch-insensitive, making it suitable for mass-produced helmet shells. Polycarbonate (PC) offers high impact strength and possesses many desirable characteristics for helmet shells. PC is, however, also more expensive, and sensitive to notches or cracks than HDPE, so is less commonly used. Acrylonitrile butadiene styrene (ABS) provides reduced cost, notch-sensitivity, and chemical resistance, but lower impact strength compared to PC. ABS is commonly seen as shell material for ice hockey, baseball, and lacrosse helmets [40].

Integrated systems

A low-friction layer, placed between the head and the helmet, between the helmet's liner and shell, or between layers of helmet foam [262] allows the components to rotate relative to each other, which can reduce angular kinematics [203,263–265]. The most well-known example of this technology is the multi-directional impact protection system (MIPS) (Fig. 2.9). The 1 mm thick plastic sheet is elastically suspended and allows 10 – 15 mm motion of the helmet relative to the head [266]. Low-friction layers can reduce angular kinematics during oblique impacts [146,147,203,204,263,267] and are applied in various helmets throughout different sports (Fig. 2.9 (B)) [266].

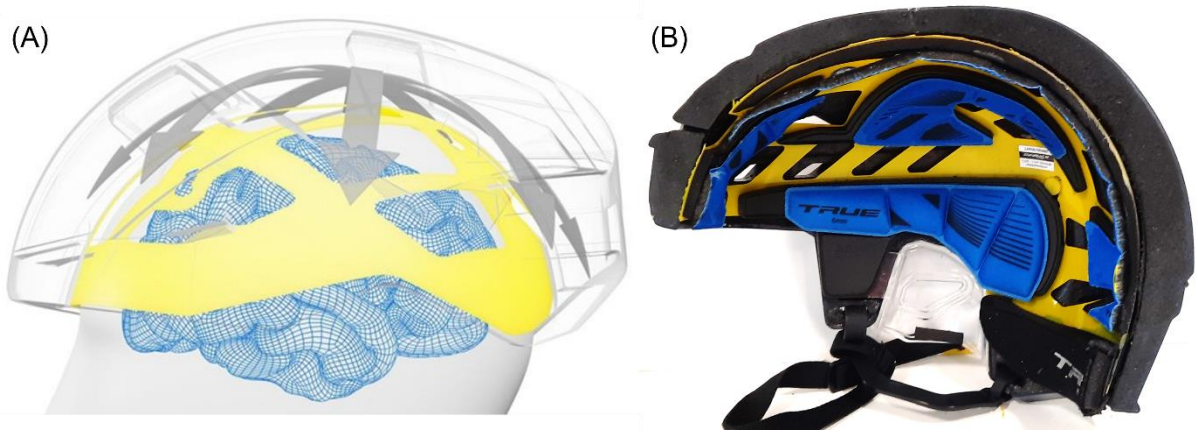

Fig. 2.9: (**A**) MIPS system acting as a low-friction layer between the head and the helmet and (**B**) MIPS system integrated into a commercially available ice hockey helmet.

Liner materials

A conventional foam, as used in the example in section 2.4.3, is only ideal for one impact energy [36–38]. However, as described previously (section 2.2.2), ice hockey has a wide range of common head impacts [30,31], and a helmet should protect during all of them. Certification standards – designed to replicate falls - are the only barrier for a helmet to be allowed in competition. Hence, helmet liners are optimised for the specific impact energy prescribed in the standards [21,23,32]. During impacts with more compliant bodies, such as a padded shoulder, traditional helmet liners are typically too stiff. Therefore, they exhibit only a small amount of deformation, causing little reduction in peak acceleration [32,33]. Consequently, head injury rates in ice hockey caused during falls have decreased, while those caused during collisions remain high [30,31].

Different approaches to make helmet liners more effective over a wider range of impacts have been made. Multilayer foam, where a soft foam is paired with a harder foam (Fig. 2.7 (A)) can achieve a wider range of manageable impacts by producing more than one plateau region (Fig. 2.10) [40,41]. Shear-thickening polymers gradually increase in stiffness with increasing loading rate, providing adaptation to the occurring impact [42,43]. Designing a helmet that can manage the range of common head impacts in ice hockey requires an understanding of what materials and systems are currently available and used in helmets or other impact applications.

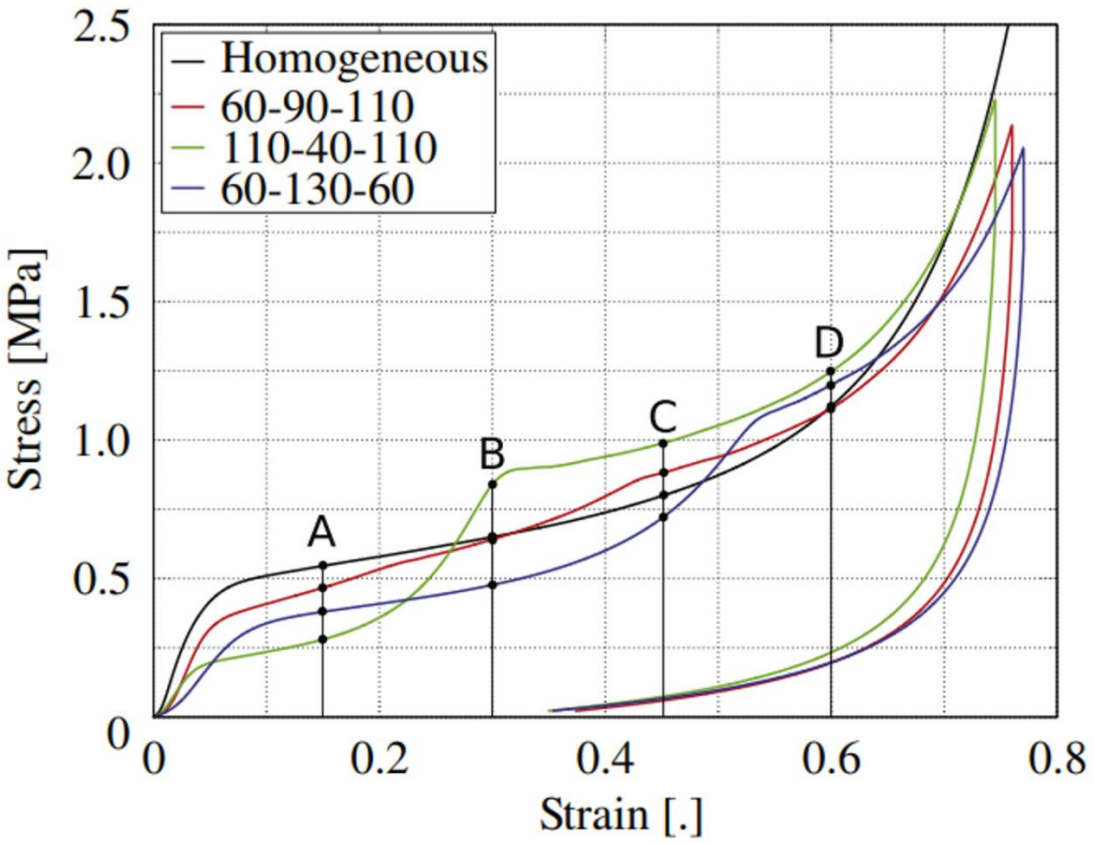

Fig. 2.10: Stress vs. strain curves for (A) homogenous and (B - D) multi-layered foams (numbers in legend describe foam density) under quasi-static compression [268].

Foam

The predominant liner material for single-use crash helmets is expanded polystyrene (EPS). Energy absorption of EPS relies on crushing (plastic deformation and fracturing), causing most of the original protection to be compromised after one impact [40,269]. Ice hockey helmets, which must withstand multiple impacts, require liner materials to recover after an impact. Vinyl nitrile (VN) (Fig. 2.11 (A)) and expanded polypropylene (EPP) (Fig. 2.11 (B)), the most common foams in ice hockey helmets, can be compressed with limited structural damage and efficiently absorb energy during impact [21,37,226,270,271]. Both are low cost and easy to process by cutting from a larger sheet or moulding, respectively [226]. While VN and EPP show small differences in provided protection from angular motion [226], conventional foams are not effective in reducing angular kinematics.

Fig. 2.11: (**A**) VN foam, (**B**) EPP foam, and (**C**) a shear-thickening polymer pad as parts of an ice hockey helmet liner.

Shear-thickening polymers

Conventional fluids are nearly Newtonian, meaning that their viscosity does not change with shear strain rate (Fig. 2.12). Newton's approximation does not always apply [272]. Shear-thickening polymers (STP) are a non-Newtonian material, with viscosity increasing with the rate of applied shear strain, meaning they are flexible during quasi-static loading, but appear to harden under dynamic loads (Fig. 2.12) [273]. Viscosity returns to the quasi-static value after the external load is removed [272], and the material may recover. This reversible transition of viscosity has been shown to increase energy absorption through dissipation into heat energy and can improve the performance of protective equipment [274,275].

During impact tests, STP sheets have been shown to reduce accelerations and peak forces more effectively than conventional foam materials [42,272]. This difference in impact performance increases progressively the higher the strain-rate [42,43]. The flexibility of STPs under low shear strain rates allows for increased comfort when worn as protective equipment [274,275]. STPs are used for impact protection in a variety of applications such as sports and the military (Fig. 2.11 (C)) [250].

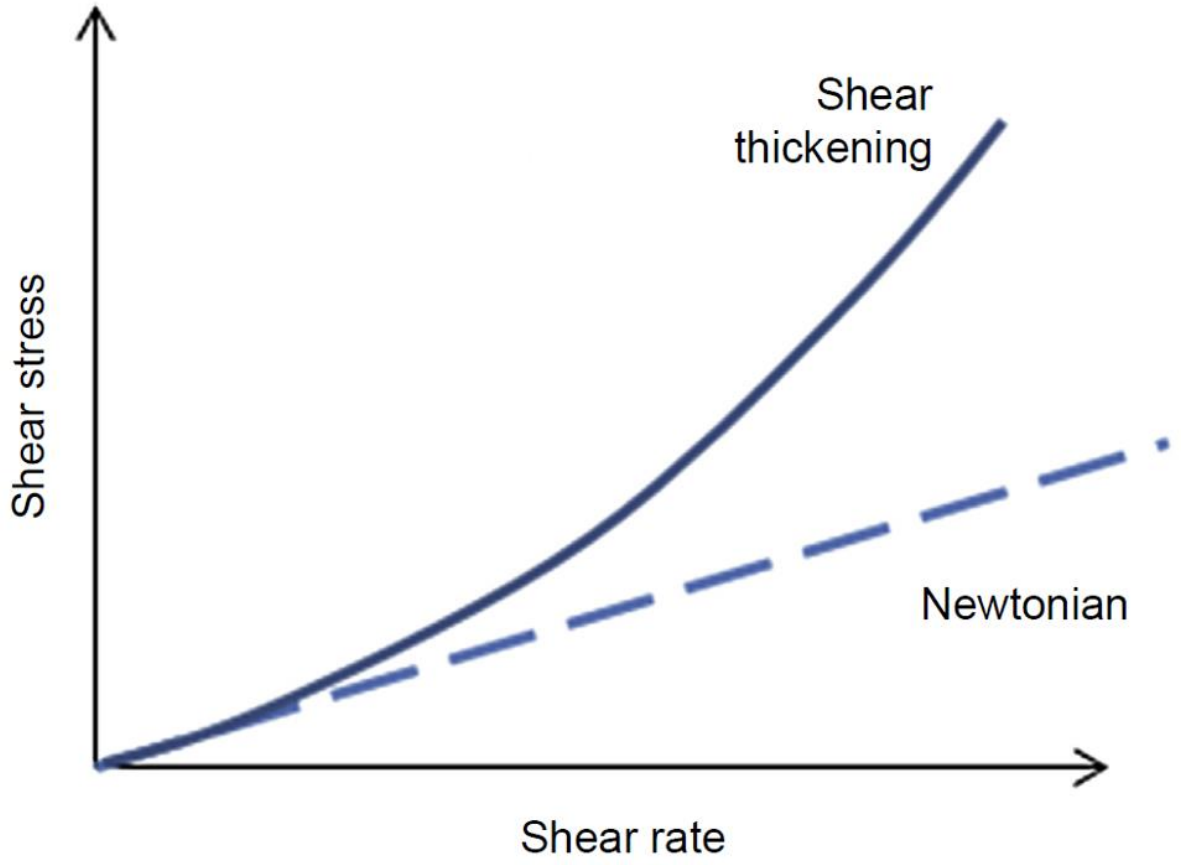

Fig. 2.12: Behaviour of Newtonian and shear-thickening fluids.

2.4.5 Mechanical metamaterials

Mechanical metamaterials are designed structures with a micro/nano-architecture to achieve properties that usually cannot be found in natural materials [276–279]. They can be fabricated from conventional materials such as foam [280] or designed as periodical cellular structures [278]. Some mechanical metamaterials have shown desirable properties for impact protection [201].

Auxetics

Auxetic materials have a negative Poisson's Ratio [267]. Poisson's Ratio is the negative product of the ratio of lateral to axial strain; auxetic materials expand laterally when stretched axially and contract (laterally) in compression (Fig. 2.13) [267]. Auxetic open-cell foam can be fabricated from conventional thermo-plastic foam by thermo-

mechanical conversion [280–282], while steam or pressure vessel processes can be used for closed-cell foam [283–285]. In comparison to their conventional parent foams, which are currently used in some helmet systems, auxetic foams can have altered properties such as increased density [281], indentation resistance [286,287], and stiffness [281,288]. Impact tests based on sporting standards have shown lower peak forces for auxetic foams than conventional ones, when conventional foams ‘bottomed out’ [289]. Conventional and auxetic foams often show similar peak forces during low-energy impacts but differ above a critical impact energy [201].

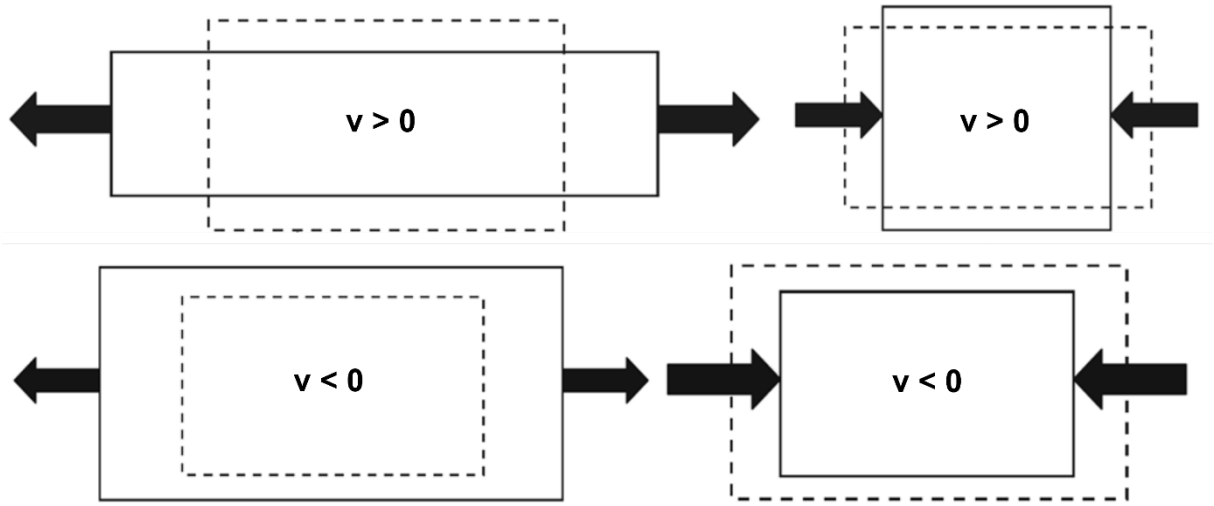

Fig. 2.13: Deformation due to positive and negative Poisson's ratio during tensile and compressive loading.

Designed cellular structures

Advancements in additive manufacturing and moulding methods, allowing fabrication of complex geometries, increased the possibilities to design and produce periodic cellular structures such as honeycombs and lattices [290–293]. Topology, base material properties, and relative density can be optimised to tailor impact behaviour and mass [294–296] using numerical analysis methods [294,295,297–303]. Further advantages include the possibility to laterally spread impact energy more efficiently

than conventional foams [294,304] or progressive layer-by-layer failure under dynamic loading, widening the range in which impacts can be managed [297,303].

2D periodic cellular structures, such as honeycomb and tubular structures (Fig. 2.14), periodically repeat in two directions [305] and have high in-plane stiffness while being low mass [297,306–309]. The structural response during impacts in the extruded direction includes crumpling and buckling of cell walls [308] with densification occurring at ~75% strain [307]. Design choices like cell size, wall thickness, and depth can be used to tailor macro-scale properties of honeycomb and tubular structures. Further modifications such as graded or hierarchical honeycomb structures can improve the range of manageable impacts and out-of-plane impact behaviour [307,310–312]. Honeycomb and tubular structures as impact absorbing elements in sports equipment and helmets (Fig. 2.14 (B) are commonly described in literature [307,310,313–316] and are commercially available [251,252,317,318].

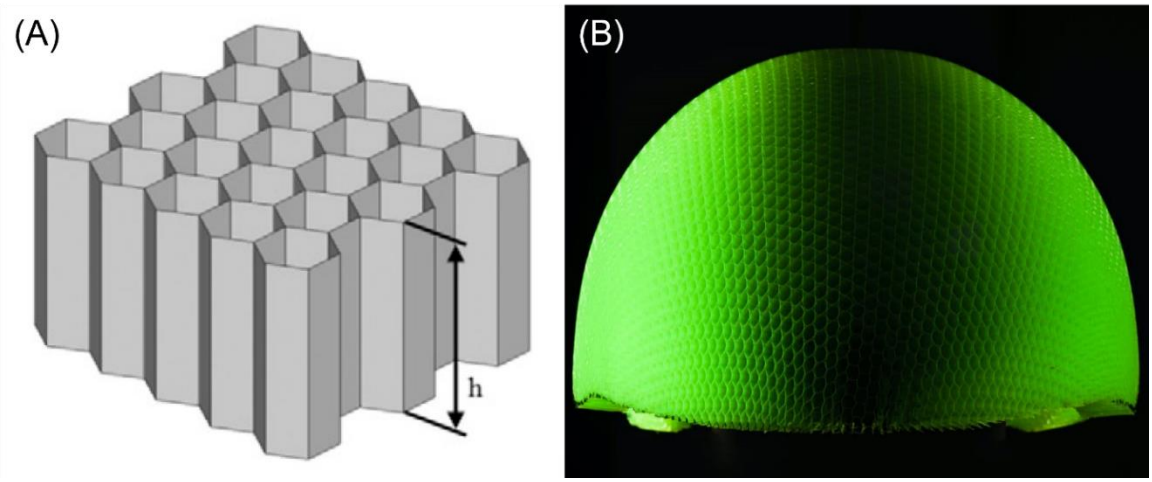

Fig. 2.14: (**A**) Honeycomb structure [312] and (**B**) tubular structure (Koroyd) [251] draped into an oval shape to serve as a helmet liner.

3D periodic cellular structures, such as lattices, consist of unit cells periodically repeating in three directions [303,305,319,320]. While properties of conventional materials degrade with reduced density, lattices maintain nearly constant stiffness when relative density is decreased [293]. When unit cell size is sufficiently small

compared to the contacting body, lattices can be viewed as homogeneous materials and heterogeneous structures [290,293,296,302]. This allows to create new materials with previously unattainable macro-scale properties [319,321].

Many different unit cell geometries for lattices in impact applications have been proposed and analysed throughout published literature. Exemplary unit cell designs include square/cubic- (Fig. 2.15 (A)) [322] or octet (Fig. 2.15 (B)) [290] truss lattice configurations, chiral (Fig. 2.15 (C)) [323–326] or anti-chiral (Fig. 2.15 (D)) [327] structures, Miura-ori (Fig. 2.15 (E)) [328,329], and re-entrant structures (Fig. 2.15 (F)) [330,331]. All the above-mentioned structures can have low mass, and additional potentially beneficial characteristics, such as auxeticity for re-entrant or chiral structures [323,331]. 3D periodic cellular structures can already be found in certified and commercially available helmets (e.g. ice hockey (Fig. 2.16 (A)) [317] and American Football [332]).

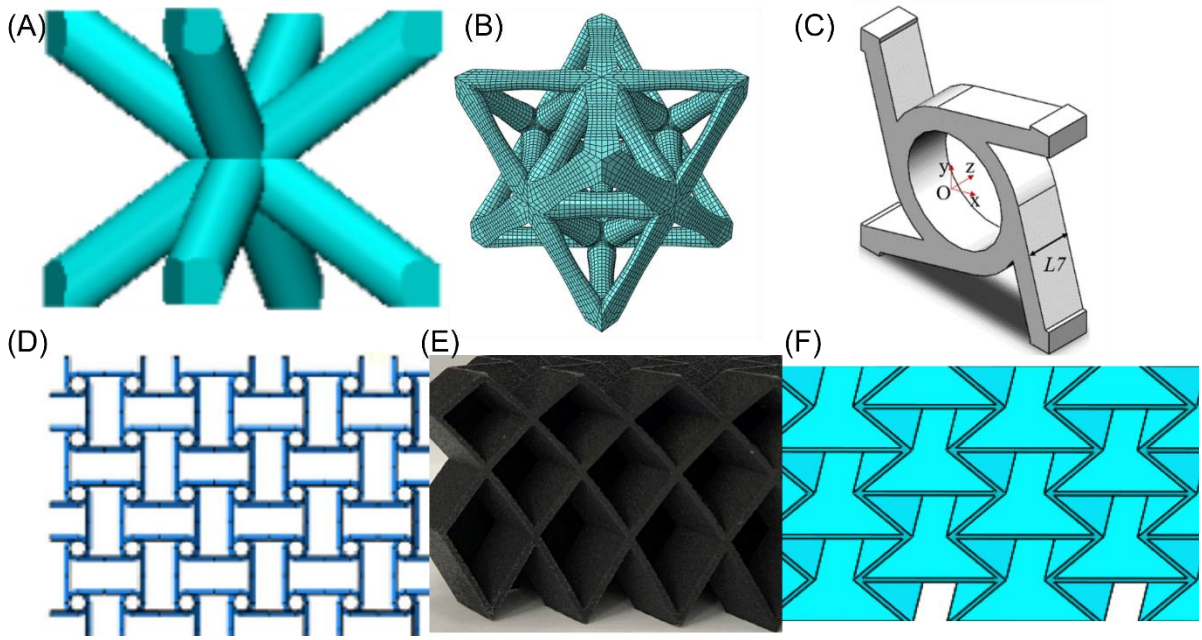

Fig. 2.15: Unit cell geometries for different 3D periodic cellular structures: (**A**) cubic truss lattice, (**B**) octet truss lattice, (**C**) chiral, (**D**) anti-chiral, (**E**) Miura-ori, and (**F**) reentrant.

Foldable (origami) structures are produced from a flat sheet by a simple folding process [333]. Geometries include zigzag [333,334] dome [335–337], tubular [338], or truncated structures [337–339]. High energy absorption, low initial crushing peak forces, large densification strain, and low strain rate sensitivity can be achieved, depending on geometry [335–337,339–341]. Foldable impact absorption elements are used in some helmets (Fig. 2.16 (B)) [342] as well as blast and shock mitigation systems [343].

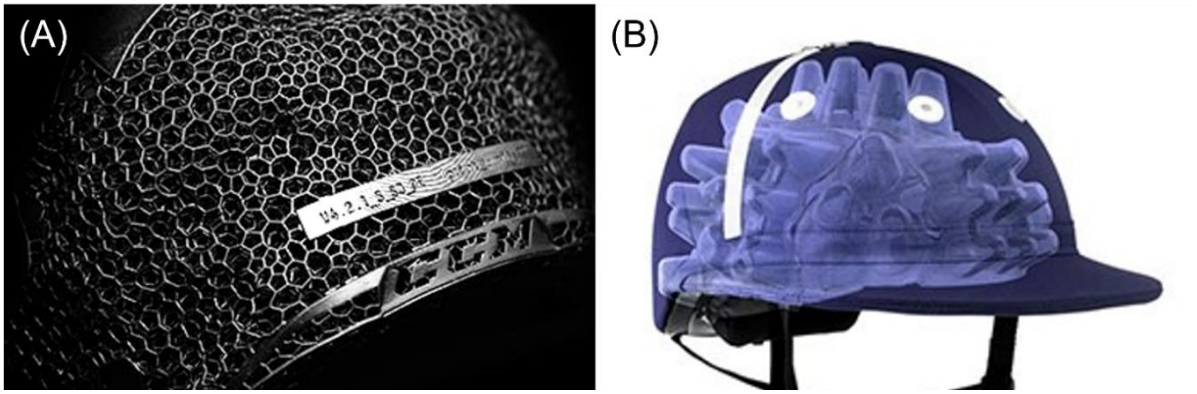

Fig. 2.16: (**A**) Hexagonal lattice structure as ice hockey helmet liner and [317] (**B**) truncated (Viconic) structures as equestrian helmet liner [344].

Negative stiffness

Snap through elements cause negative stiffness behaviour, resulting in a drop in force as applied deformation increases [345–351]. Negative stiffness can be achieved by buckling an end constrained beam (Fig. 2.17 (A)). The beam snaps from one state of equilibrium to the next during the application of perpendicular load (often via a connecting rib) [345,346,351]. Negative stiffness is present for a segment of the force vs. compression relationship, corresponding to when the beam snaps through (Fig. 2.17 (B)). The onset and length of the segment and the critical buckling load can be tailored by changing the diagonal angle of the symmetric beam and the second moment area of the beam, respectively [349]. Negative stiffness has been shown to

improve protection during impacts [352], balancing positive stiffness of neighbouring unit cells to flatten and elongate the stress plateau (Fig. 2.17 (B)).

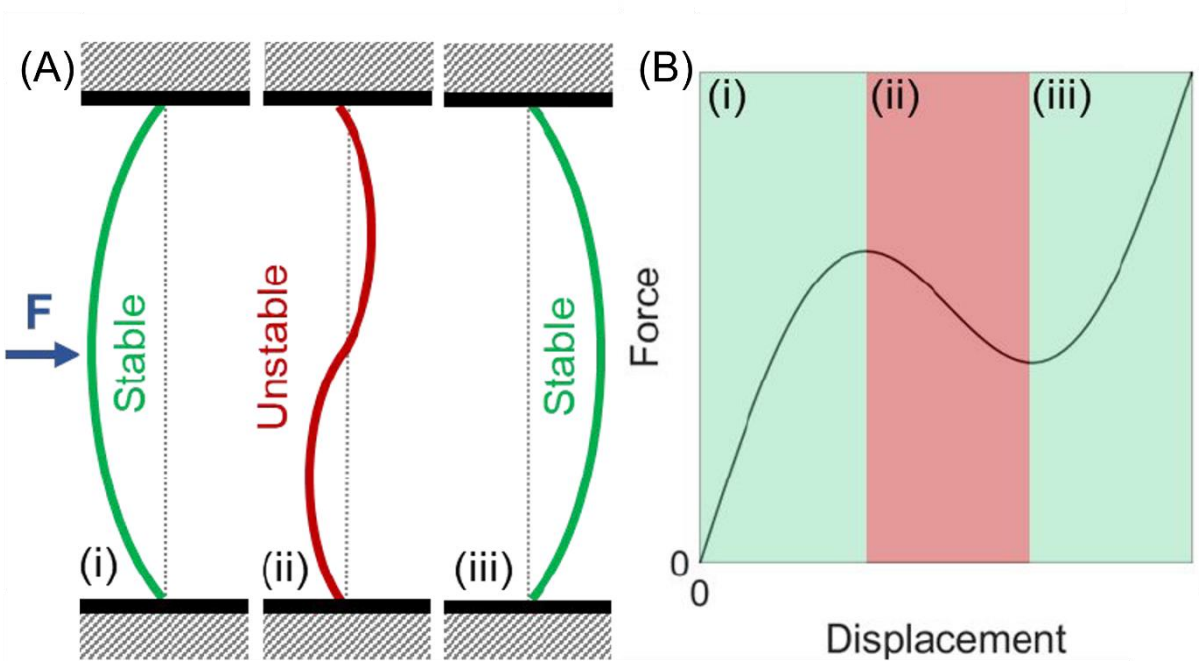

Fig. 2.17: (**A**) Stages of snap through in a buckling beam, and direction of applied force; (**B**) Example force vs. displacement, including stages from (A).

Adaptive metamaterials

Janbaz et al. presented a mechanical bi-beam metamaterial with rate-dependent buckling behaviour that achieved negative viscoelasticity [44]. Presented compression test results suggest (Fig. 2.18 (B)), that a shear-thickening response that is more tailorable than that of a shear-thickening polymer alone, could be achieved. Further, switching the orientation would achieve high stiffness at high strain-rates and lower stiffness at lower strain-rates. This behaviour could be desirable for helmet liners in sports that experience a wide range of different head impacts [44].

When two laterally connected beams (i.e. bi-beams) are compressed (Fig. 2.18 (A)), the stiffer beam drives the buckling direction while the softer beam provides support; buckling is towards the unsupported side of the stiff beam. So, buckling direction can be controlled with the use of a low elastic modulus but highly viscoelastic, strain rate

dependent (SRD) beam laterally connected to a higher elastic modulus, strain rate independent (SRI) beam (Fig. 2.18) [44]. At low compression rates, the SRD material possesses a lower stiffness than the SRI material – meaning the bi-beams buckle towards the SRI beam (Fig. 2.18 (A)). Exceeding a threshold strain rate switches the order of stiffness and the direction of buckling (Fig. 2.18 (A)) [44].

A unit cell of this metamaterial consists of two bi-beams, positioned at a small distance from each other and with opposite orientations. Depending on strain rate, the bi-beams bend either towards or away from each other (Fig. 2.18 (B)). Bending towards each other prevents or limits buckling, whereas bending away from each other allows buckling (Fig. 2.18 (B)). A sheet layer consisting of bi-beam unit cells could be scaled and draped into a helmet liner to create an adaptive helmet system [44].

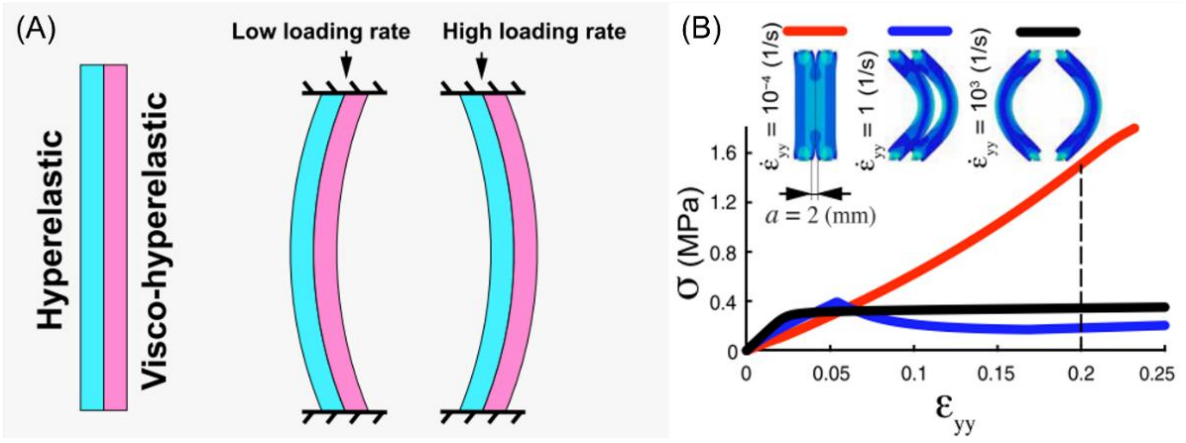

Fig. 2.18: (**A**) Single bi-beam design and buckling direction for different axial strain rates and (**B**) stress-strain curves for different loading conditions [44].

The dominant deformation mode in hexagonal honeycombs and lattices is cell rib flexure [353,354] (Fig. 2.19). This flexure reduces the distance of neighbouring junctions, reducing the magnitude of positive compressive Poisson's ratio, or increasing that of negative Poisson's ratio. Introducing viscoelastic material in the cell ribs may switch the dominant mode, increasing the magnitude of Poisson's ratio, and hardness, during more severe impacts (Fig. 2.19). Introducing viscoelastic material in

the junction of auxetic, re-entrant honeycombs or lattices may have a similar effect, through amplification of the dominance of rib flexure to draw neighbouring junctions inward. These concepts have been shown in structures with dual materials of different stiffness [355,356], but not viscoelastic materials. Designed to fit into a helmet, these structures may provide an adaptive response to impacts.

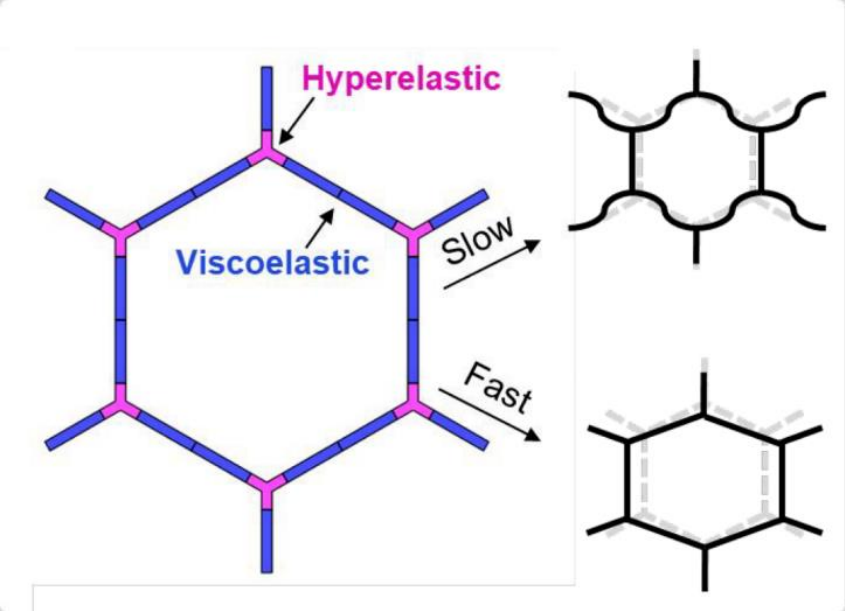

Fig. 2.19: Multi-material hexagonal cell causing a switch in the dominant deformation mode.

2.4.5 Summary

Ice hockey helmets, as a minimum, consist of a stiff outer shell and an energy absorbing liner. In applications where multiple impacts are sustained, as with ice hockey, the liner must recover quickly and without losing its impact protection properties. Conventional helmet materials absorb energy through compression, limiting their effectiveness to protect from rotation and the manageable range of impacts. Various approaches, involving novel materials and integrated systems, have been made to improve helmets - so far with limited success.

2.5 Chapter summary

Due to a lack of structural damage, concussions are difficult to diagnose and treat. However, it is generally agreed upon that the cause of concussions is excessive or overly rapid deformation of brain tissue, due to high accelerations of the head. Ice hockey has one of the highest concussion rates in sports. Most reported concussions (~93%) in professional ice hockey are caused during collisions with other players on the ice.

Ice hockey helmet certification standards prescribe a guided drop test onto a rigid surface, replicating falls onto the ice. This protocol does not consider more compliant impact bodies or angular kinematics of the head, hence, leaving uncertainty about helmets' capabilities to protect wearers during head impacts that are not falls. More thorough helmet assessments, as described in published research, require extensive laboratory equipment that is unavailable to most research facilities, limiting the work that is carried out in the field.

Currently, available ice hockey helmets are effective within the range of impact energies they are designed and tested for - falls. This does not cover the range of commonly concussive head impacts in ice hockey, leaving wearers susceptible to concussions. Various approaches in design and material choices can be seen throughout the range of commercially available helmets. So far, with limited success in preventing concussion during the most commonly concussive head impacts (collisions), as protection during falls must not be compromised and no current helmet liner provides sufficient protection during both kinds of impacts.

3. Chapter - Free-fall drop test to replicate head impacts in ice hockey

3.1 Introduction

The literature review highlighted that most concussions in ice hockey (~93%) result from a collision between players on the ice [30,31]. During collisions, a player's head impacts several layers of textiles, protective equipment, and the other player's body, which are typically less stiff than the MEP Pad impacted in test standards. Consequently, helmet performance during the most common concussion scenario is currently not assessed during certification. A deep understanding of helmets and their energy-absorbing components during impact is essential to improve helmets to better protect against concussions without compromising other aspects. Widespread and in-depth helmet testing could inform and drive helmet development and innovations.

An adaptable test method, requiring less laboratory equipment, that can replicate a range of head impacts could facilitate modifications to certification standards and testing by more researchers. The presented test method was developed to recreate commonly concussive head impacts in ice hockey using interchangeable impact surface compliance and orientation.

The objectives of this chapter were to:

- Assess the feasibility of a free-fall drop test method with interchangeable impact surface compliance and orientation to replicate headform kinematic responses typical for ice hockey head impacts.
- Assess the protective capabilities of a range of commercially available ice hockey helmets during impact.
- Assess the reliability of the developed test method.

3.2 Methods

3.2.1 Materials

An adult 50th percentile male Hybrid III headform (mass: 4.54 kg; JASTI Co. Ltd), equipped with a sensor system (Slice Nano, Diversified Technical Systems, Inc. (DTS)) with three linear accelerometers (ACCEL SLICE, DTS) and three angular rate sensors (ARS3 PRO, DTS) in its centre of mass, was used for all impacts (Fig. 3.1 (A)). The drop mechanism was an “energise to release” electromagnet, attached to a wall-mounted drop rig (Fig. 3.1 (B)). Before each drop, the headform was positioned in the required orientation and height using strings attached to the electromagnet. For unhelmeted impacts, the strings were used as slings (Fig. 3.1 (C)) while for helmeted impacts the strings were attached to the helmets’ ventilation openings (Fig. 3.1 (D)). The anvil for all impacts was a high-mass (~700 kg) steel table (Fig. 3.1 (B)). A high-speed video camera (Phantom Miro R311, Vision Research Ltd., Bedford, UK) was set up at a distance of 1 m from the impact location, with the field of view perpendicular to the impact surface (Fig. 3.1 (B)).

For flat (perpendicular) impacts, impact surfaces were attached directly to the steel table (Fig. 3.1 (B)). For oblique impacts, impact surfaces were attached to a 45° angled wedge that was clamped to the table (Fig. 3.3). During flat impacts, five different surfaces were used; MEP Pad (1-inch height, CadexInc) and layered Ethylene-vinyl acetate (EVA) foam (EVAZOTE-50, algeos.com) sheets bonded with double-sided tape giving 24, 48, 72, and 96 mm overall thickness, providing increasing compliance during impacts. During impacts onto the oblique anvil, three layered EVA foam thicknesses (24, 48, and 72 mm) were used.

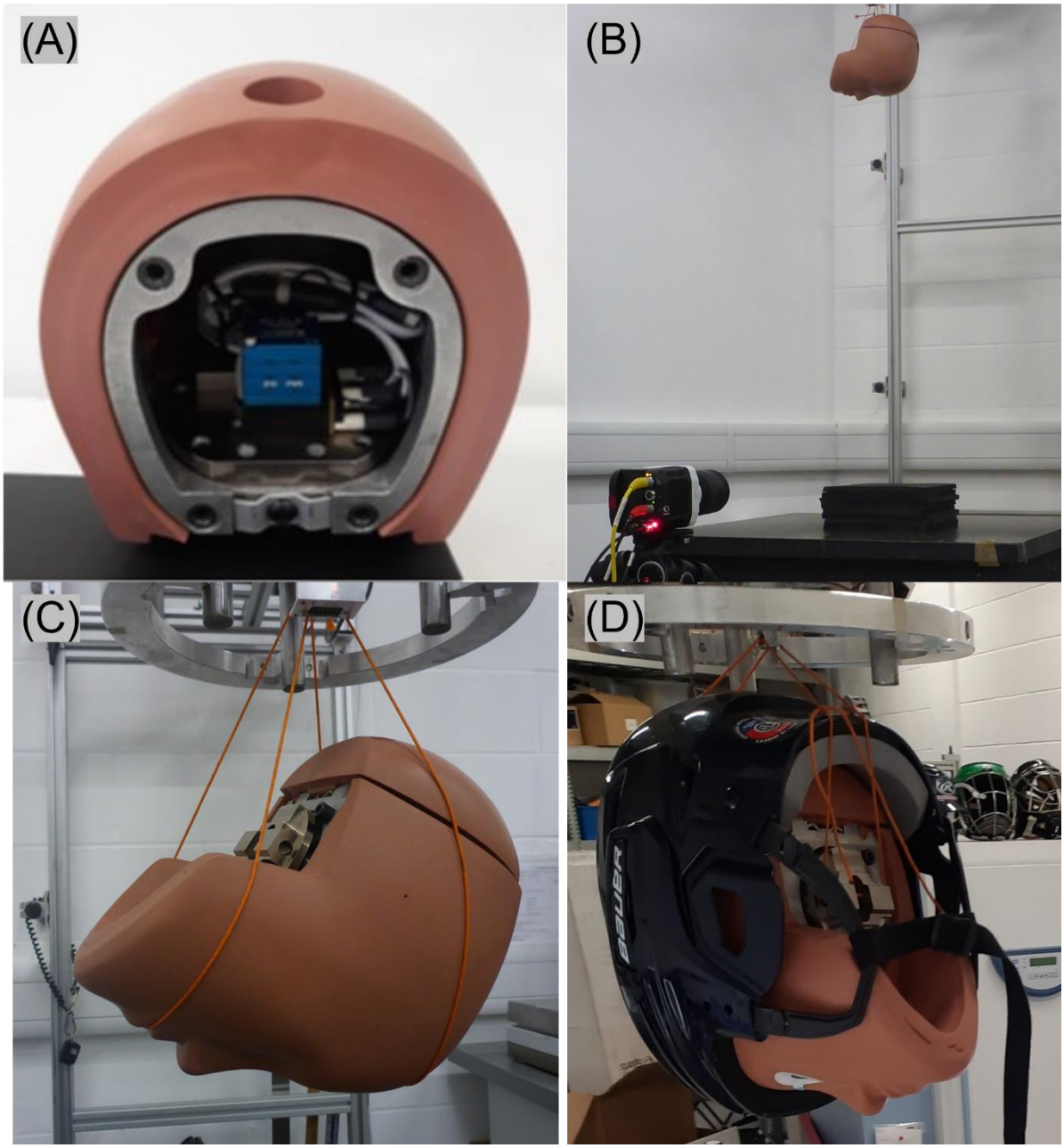

Fig. 3.1: **(A)** DTS system mounted inside the HIII headform. **(B)** Setup used for free-fall drop test onto the flat 96 mm foam (8 layered sheets) surface with a high-speed camera at 1 m distance from the impact location. **(C)** HIII headform held over the impact surface by strings. **(D)** Helmeted HIII headform held over the impact surface by strings attached to the helmet's ventilation openings.

Five different certified and commercially available ice hockey helmets (Fig. 3.2) were fitted to the headform. Five helmets of each model were used, and all helmets were a medium size. The helmets represented various price ranges, liner materials, and helmet designs:

- Helmet 1: The Bauer Hockey IMS 5.0 helmet (Fig. 3.2 (A–C)) represented the low end of the price range (44.99 US$), and the recommended level of play is “Recreational”. The shell is a two-piece adjustable design made from HDPE. The liner is a dual-density foam layer made from VN. The overall mass is 498 grams.
- Helmet 2: The Bauer Hockey 5100 helmet (Fig. 3.2 (D–F)) is at the lower end of the price range (89.99 US$), and the recommended level of play is “Performance”. The shell is a two-piece adjustable design made from HDPE. The liner is a triple-density foam layer where the top and bottom layers are made from VN, and the middle layer is an HX-SORB® high-density honeycomb structured foam. The overall mass is 549 grams.
- Helmet 3: The CCM Hockey FitLite 90 helmet (Fig. 3.2 (G–I)) is in the middle of the price range (179.99 US$), and the recommended level of play is “Performance”. The shell is a two-piece adjustable design made from HDPE. The liner consists of shear-thickening polymer pads (D3O®), dual-density VN foam, a hexagon matrix foam, and an open-cell foam (i.Q.SHION®) comfort layer. The overall mass is 558 grams.
- Helmet 4: The TRUE Dynamic 9 Pro Helmet (Fig. 3.2 (J-L) is at the higher end of the price range (259.99 US$), and the recommended level of play is “Elite”. The shell is a one-piece design made from PC. The liner is made from EPP foam and fitted with the MIPS® system. The overall mass is 543 grams.
- Helmet 5: The Bauer Hockey Re-Akt 200 helmet (Fig. 3.2 (M–O)) represents the top end of the price range (299.99 US$), and the recommended level of play is “Elite”. The shell is a two-piece design made from HDPE. The liner consists

of shear-thickening polymer pads (XRD® Impact), multi-density foams, and is fitted with a low-friction layer (Suspend-Tech®). The overall mass is 747 grams.

Fig. 3.2: **(A, D, G, J & M)** Front and **(B, E, H, K & N)** side view of the helmet shell and **(C, F, I, L & O)** liner system for all five helmets. **(A – C)** Bauer IMS 5.0, **(D – F)** Bauer 5100, **(G – I)** CCM FitLite, **(J – L)** TRUE Dynamic, **(M – O)** Bauer Re-Akt 200.

3.2.2 Test method

The headform was impacted either unhelmeted or fitted with one of the five helmets. The drop height for all impacts was 1 m, resulting in an impact velocity of 4.5 m/s and energy of 51.3 – 53.8 J, varying with helmet mass. The height was checked before every drop using a laser distance measure (Leica Disto D210, accuracy ±1 mm). The helmets' chin straps were closed, and a tight fit, following manufacturer and retailer recommendations, was checked before every impact.

Three centric sites (force vector passing through headform centre of mass) on the outer shell of the headform or helmet were impacted for the five flat impact surfaces; Front, Side, and Rear (Fig. 3.3 (A–C)). Two centric sites (Front, Rear) and three non-centric sites (force vector not passing through headform centre of mass) were impacted for the three oblique impact surfaces; Front, Rear and FrontBoss, Side, RearBoss, respectively (Fig. 3.3 (D–H)). A new helmet was used for each flat impact surface. The three helmets used to impact the three most compliant surfaces (48, 72, and 96 mm) during the flat surface impacts were used again for the oblique impacts. For every impact configuration, three trials were carried out resulting in a total of 540 impacts.

Linear acceleration and angular velocity were measured with a sampling frequency of 100 kHz for 70 ms (20 ms pre-trigger and 50 ms post-trigger), triggered when a 5 g threshold was exceeded in any axis. High-speed video footage was captured at 2,000 frames per second (fps) (resolution, 1024 x 768 pixels, 0.5 mm/pixel; exposure, 500 µs). High-speed video footage was used to calculate impact velocities.

For an inter-rater reliability study, a proportion of the data collection was repeated by a second appraiser with no previous involvement or experience in developing or using the test method. A Bauer 5100 helmet was dropped onto the same impact surfaces as

described previously. For flat surface impacts the Front site was chosen and for oblique surface impacts Front and FrontBoss sites were impacted.

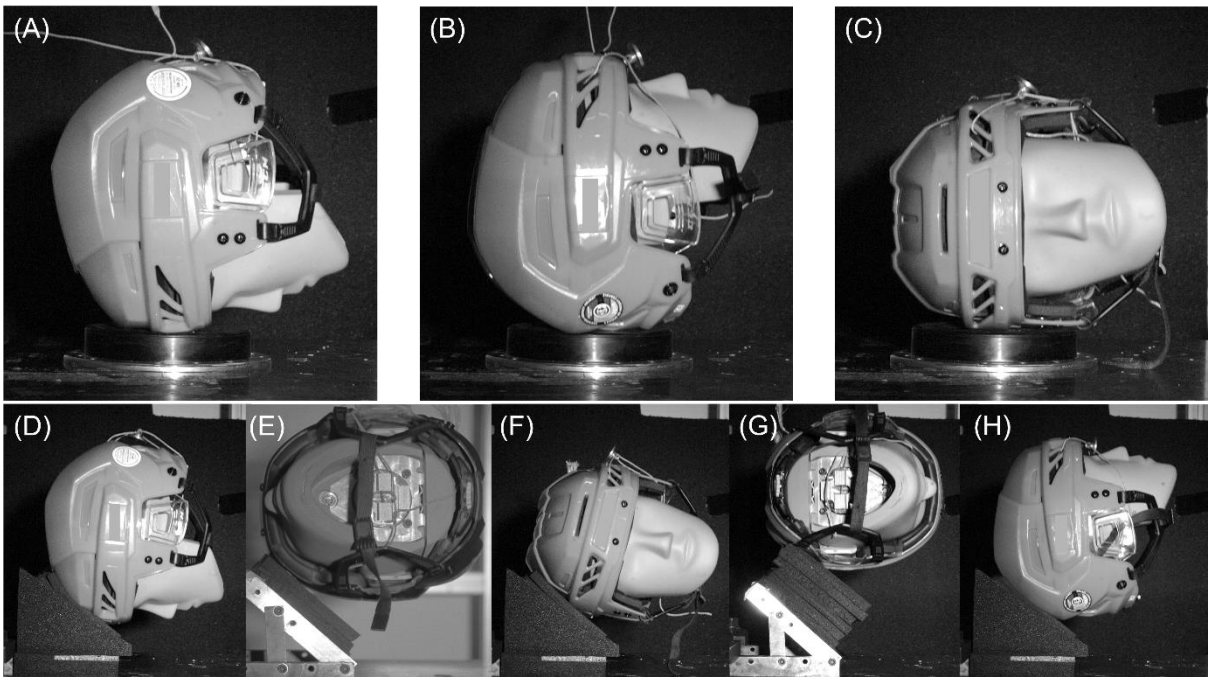

Fig. 3.3: Impacts onto the (**A - C**) Flat and (**D - H**) 45° oblique anvil; (**A & D**) Front, (**E**) FrontBoss, (**B & F**) Side, (**G**) RearBoss, and (**C & H**) Rear impact location.

3.2.3 Data analysis

A CFC 1000 filter, as recommended by Post et al. [125], was applied to each linear accelerometer axis using DTS SLICEWARE (Version 1.08.0868). A 4-pole Butterworth low pass filter with a cut-off frequency of 200 Hz was applied to each angular velocity axis, chosen based on a frequency analysis using a Fast Fourier Transform [357]. After filtering, the angular velocity data were differentiated to obtain angular acceleration. Peak linear (PLA) and peak angular acceleration (PAA), impact duration (D), time to peak (TTP), and rebound time (RT) were obtained from filtered data using MATLAB (R2018a). These values were compared quantitatively while the acceleration vs. time trace shapes were compared qualitatively to reference values from concussive head impacts (Table 3.1), recreated in a laboratory setting. To assess the intra-rater reliability of repeated measurements, two-way mixed model intraclass correlation coefficients

(ICC (3,1)) with absolute agreement definition and their respective 95% confidence intervals (CI) were calculated for PLA, PRA, and D [358,359]. To assess inter-rater reliability of repeated measurements, a two-way random effects model with absolute agreement between multiple raters (ICC (2,k)) and the respective 95% CIs were calculated (IBM SPSS 26) [358,359].

To enhance visualisation, a pairwise distance function, normalised to measured maximum values (linear acceleration / 350 g, angular acceleration / 11 krad/s², and duration / 35 ms) was added to Fig. 3.5 & Fig. 3.6 as a shaded area using a colormap function in MATLAB. A 10% pairwise distance corresponded to 35 g, 1.1 krad/s², 3.5 m/s, or the Pythagorean equivalent distance from a reference value (i.e., $\sqrt{(\Delta PLA^2 + \Delta D^2)}$ or $\sqrt{(\Delta PRA^2 + \Delta D^2)}$).

Two measures to assess head impact severity, the Head Injury Criterion (HIC, Equation 2.2 [224], chapter 2.3.4.1) and the Rotational Injury Criterion (RIC, Equation 2.3 [232], chapter 2.3.4.2), were calculated. HIC was chosen to allow comparison with other head impact data as it is commonly used in published research. RIC was chosen to allow consideration of angular kinematics and to complement the use of HIC. All obtained values were compared between tested helmets and the unhelmeted impacts to assess the helmets' impact performance.

Table 3.1: Statistical characteristics of the reference dataset.

	PLA [g]	PAA [krad/s²]	D [ms]
Mean (± SD)	28.8 (± 11.8)	3.44 (± 1.40)	26.2 (± 3.2)
Minimum	7.7	0.69	18.0
Lower quartile (Q1)	20.9	2.58	24.6
Median	26.8	3.55	25.5
Upper quartile (Q3)	35.3	4.00	28.6
Maximum	67.8	7.85	35.8

3.3 Results

Linear acceleration vs. time data shows a single peak (Fig. 3.4 & Appendix 1). This shape is similar for flat and oblique surface impacts and characteristic of collisions between players. Acceleration vs. time traces for Front site impacts (Fig. 3.4) are similar in shape to other tested impact sites for flat and oblique surface impacts. The highest accelerations (highest obtained peak values: 325 g, 15.5 krad/s²), and shortest durations (5.5 ms), were produced during impacts onto stiff surfaces (i.e. MEP Pad and 24 mm foam layer). Peak accelerations decreased (lowest obtained peak values: 21 g, 0.5 krad/s²) with increasing impact surface compliance, while impact duration increased (37.4 ms) (Fig. 3.4 & Appendix 1).

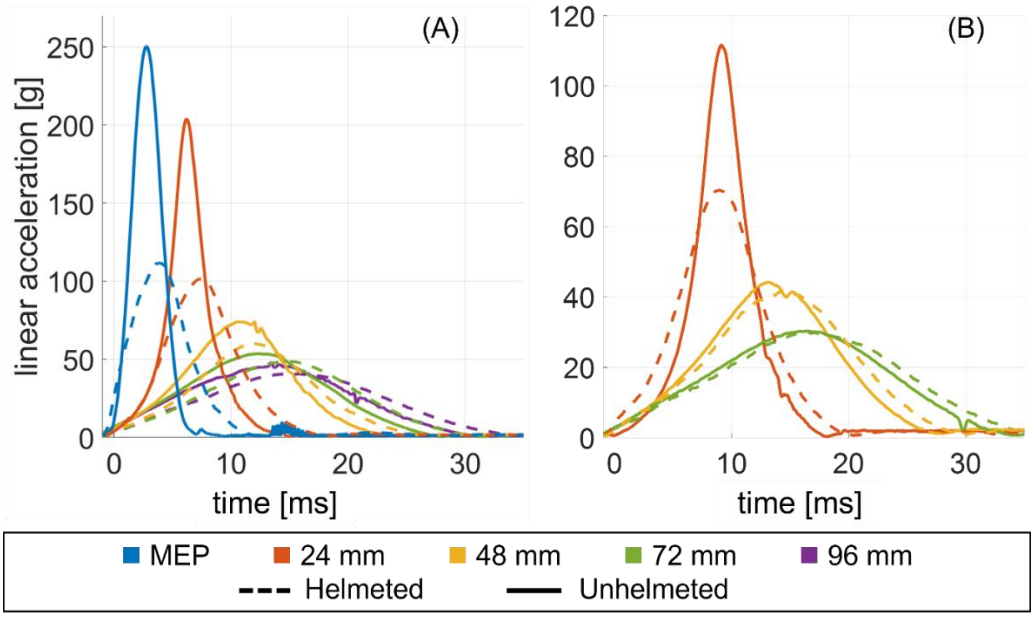

Fig. 3.4: Helmeted (dashed line) and unhelmeted (solid line) linear acceleration vs. time traces for (**A**) flat and (**B**) oblique surface, Front site impacts onto the range of impact surfaces. Helmet 2 data is shown, representative of other helmets.

For the flat surface, most helmeted impacts were within 10% of the reference values, according to the pairwise distance function, normalised to maximum values, shown as shaded areas. All impacts on foam thicknesses of 48 mm and thicker, were within the 10% range (Fig. 3.5). Similarly, most impacts were within the 10% range for oblique surface impacts for linear as well as angular acceleration, and all impacts onto the 48

mm foam layer were within the 10% range (Fig. 3.6). The 10% pairwise distance corresponded to 35 g, 3.5 ms, or the Pythagorean equivalent distance for the flat surface and 35 g, 1.1 krad/s^2, 4 ms, or the Pythagorean equivalent distance for the oblique surface.

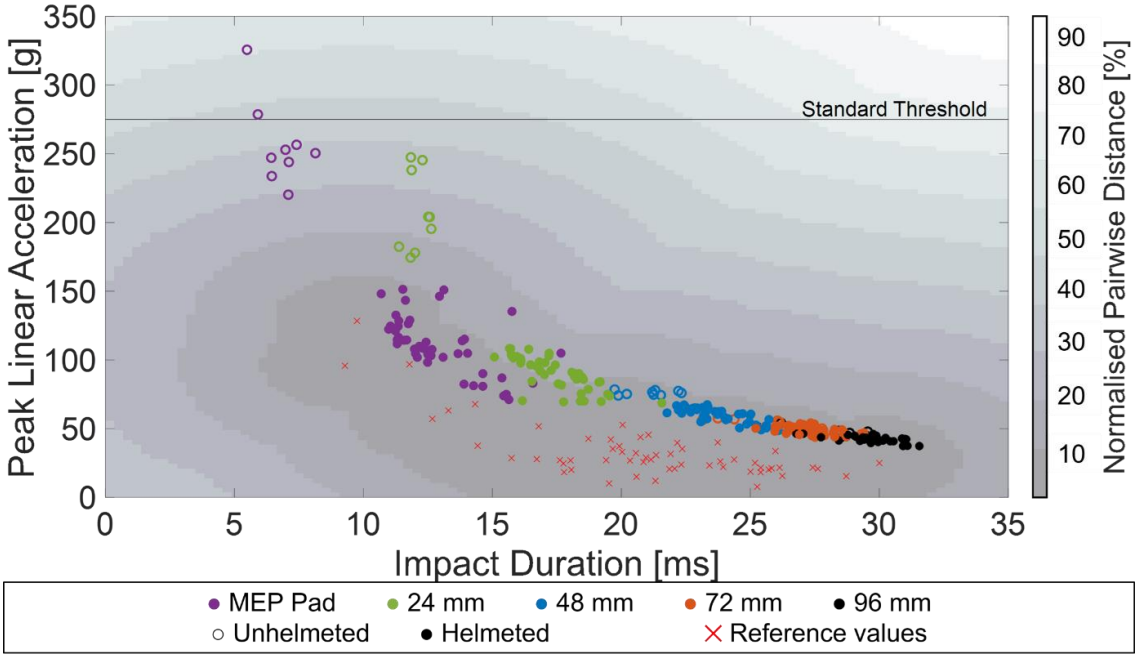

Fig. 3.5: Peak linear acceleration vs. impact duration for all impacts onto the flat surface; filled markers represent helmeted impacts and unfilled markers represent unhelmeted impacts. Shaded areas represent a normalised (acceleration / 350 g and duration / 35 ms) pairwise distance from the reference values in percent. Reference values of concussive impacts, recreated in a laboratory environment, obtained from [104].

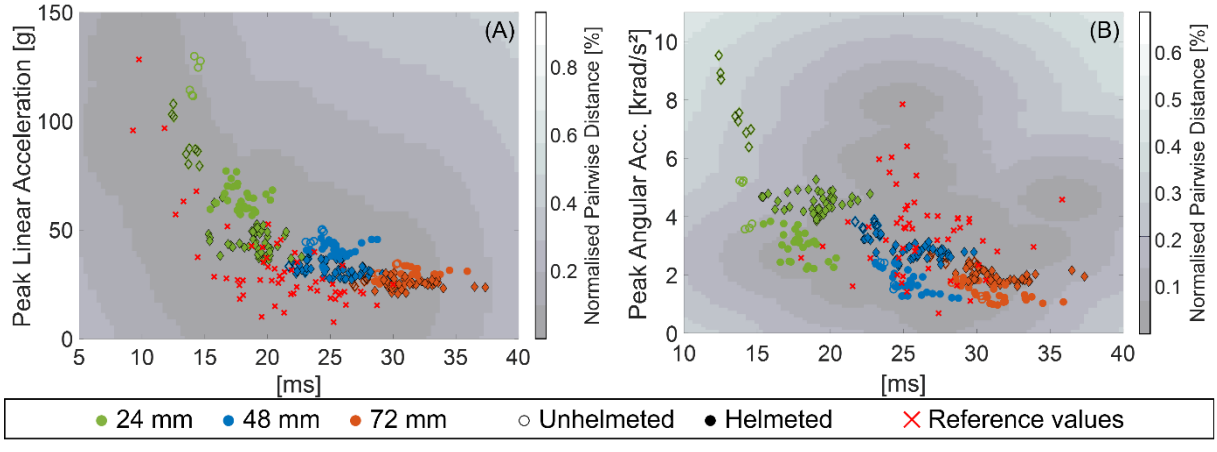

Fig. 3.6: Peak (**A**) linear and (**B**) angular acceleration vs. impact duration for all impacts onto the oblique surface; filled markers represent helmeted impacts and unfilled markers represent unhelmeted impacts, circles represent centric impacts, and diamonds with a black outline represent non-centric impacts. Shaded areas represent a normalised (linear acceleration / 350 g, angular acceleration / 1.1 krad/s², and duration / 35 ms) pairwise distance from the reference values in percent. Reference values of concussive impacts, recreated in a laboratory environment, obtained from [104].

On average, helmets reduced peak accelerations and increased impact durations for all impacts when compared to unhelmeted impacts. The influence of a helmet on measured accelerations and durations decreased with increasing impact surface compliance (Fig. 3.5, Fig. 3.6, Fig. 3.7, Fig. 3.8, Table 3.2 & Appendix 1). For impacts onto perpendicular impact surfaces, helmets reduced peak linear acceleration by up to 71% and increased the impact duration by up to 161%. For stiff surface impacts (i.e. 24 mm foam layer) onto the oblique anvil, helmets reduced peak linear and angular acceleration by up to 64 and 53%, respectively, while increasing impact durations by up to 66%. For some compliant surface impacts (i.e. 72 mm and 96 mm foam layer), mean PLA was reduced by only 3% and mean D was not consistently increased, compared to unhelmeted impacts.

Table 3.2: Mean unhelmeted (UH) and helmeted (H) PLA & D for flat surface impacts and PLA, PAA, and D for oblique surface impacts with the percentual increase/decrease the helmet had on the headform's kinematic response when compared to unhelmeted impacts (%).

		Flat		Oblique		
		PLA [g]	D [ms]	PLA [g]	PAA [krad/s²]	D [ms]
MEP						
-	UH	257 (±29)	6.8 (±0.8)	-	-	-
-	H	111 (±20)	12.9 (±1.7)	-	-	-
-	%	- 57	90	-	-	-
24 mm						
-	UH	208 (±27)	12.1 (±0.4)	103 (±17)	6.4 (±1.9)	13.8 (±0.7)
-	H	90 (±12)	17.5 (±1.3)	57 (±14)	3.9 (±0.8)	22.0 (±6.9)
-	%	- 57	45	- 45	- 39	59
48 mm						
-	UH	76 (±2)	21.1 (±0.9)	40 (±7)	3.0 (±0.9)	23.2 (±0.8)
-	H	60 (±5)	23.7 (±1.1)	38 (±9)	2.4 (±0.6)	29.3 (±7.0)
-	%	- 21	12	- 5	- 20	26
72 mm						
-	UH	54 (±3)	25.5 (±1.4)	29 (±3)	2.1 (±0.5)	28.9 (±1.2)
-	H	49 (±3)	27.2 (±1)	27 (±3)	1.7 (±0.4)	34.4 (±6.8)
-	%	- 9	7	- 7	- 19	19
96 mm						
-	UH	48 (±3)	28.1 (±1.6)	-	-	-
-	H	43 (±2)	29.4 (±1.2)	-	-	-
-	%	- 10	5	-	-	-

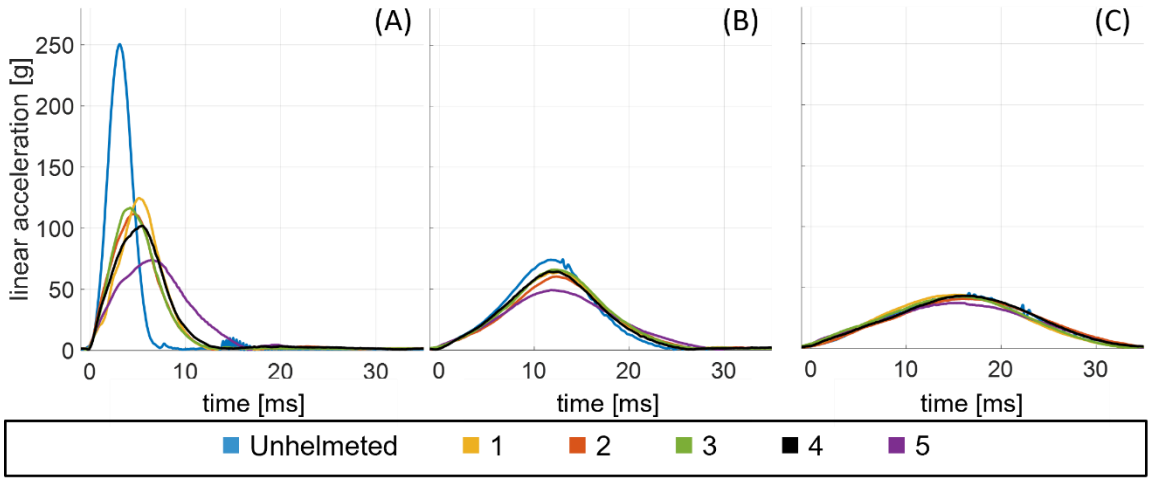

Fig. 3.7: Linear acceleration vs. time traces for flat surface, Front site impacts onto the (**A**) MEP Pad, (**B**) 48 mm foam layer, and (**C**) 96 mm foam layer.

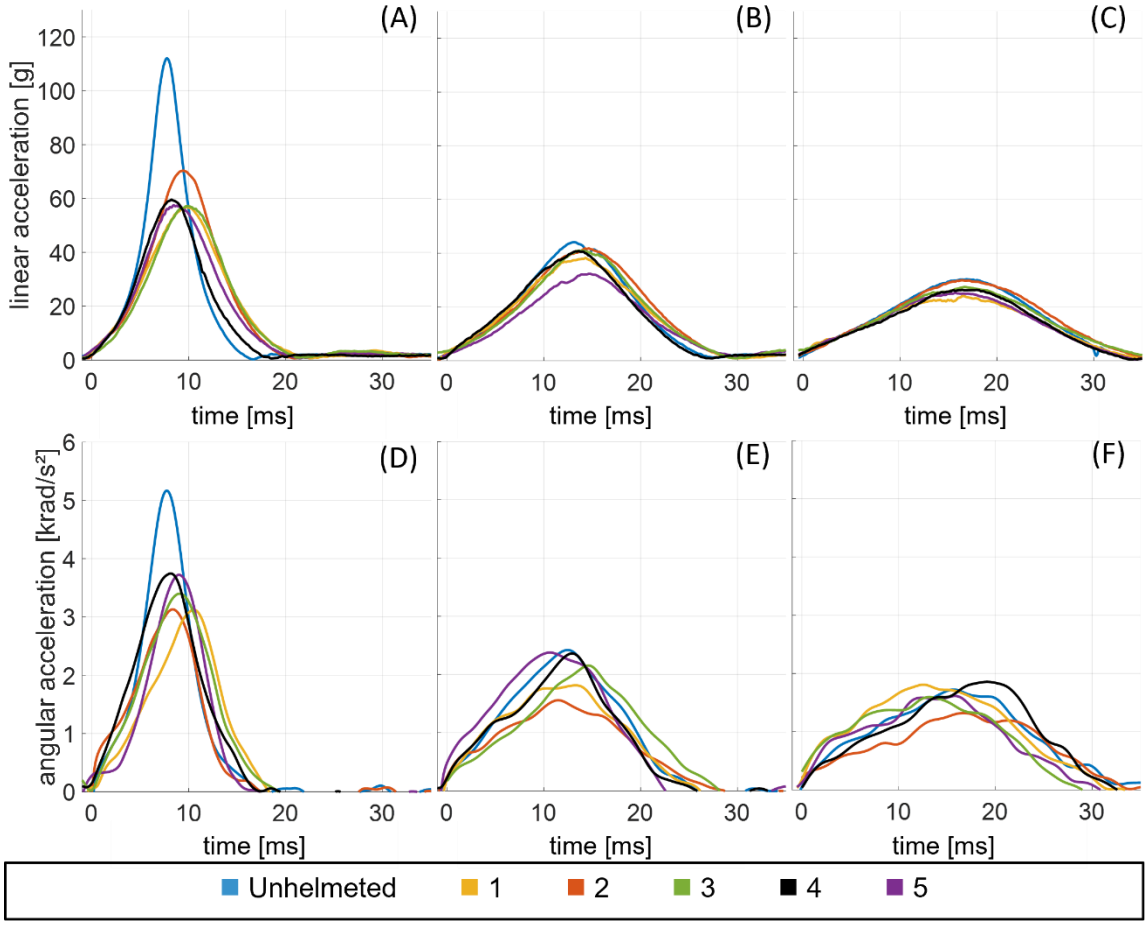

Fig. 3.8: (**A - C**) Linear and (**D - F**) angular acceleration vs. time traces for oblique surface, Front site impacts onto the (**A & D**) 24 mm foam layer, (**B & E**) 48 mm foam layer, and (**C & F**) 72 mm foam layer.

During oblique impacts, centric impact sites produced higher linear accelerations and lower angular accelerations than non-centric impact sites (Fig. 3.6). For non-centric impact sites angular accelerations were higher than linear accelerations. Impact durations and the difference between unhelmeted and helmeted tests were typically smaller for centric impact sites (Fig. 3.6). Across all helmeted impacts, mean PLA ranged from 27 to 111g and mean PAA from 1.7 to 3.9 krad/s² (Table 3.2), corresponding to an estimated risk of concussion below 5% for all impact scenarios [216,360]. The highest mean PLA (257 g), obtained from unhelmeted impacts onto the MEP Pad corresponds to an estimated risk of concussion of ~50% [216]. For 48-mm foam, non-centric impacts, mean PLA (31.5 ± 2.8 g) is between the median and Q3, mean PAA (2.8 ± 0.3 krad/s²) is between Q1 and the median, and mean D (25.8 ±1.8 ms) is between Q1 and Q3 of the reference data (Table 3.1), respectively.

Differences in linear (Fig. 3.9 (A) & Appendix 2) and angular (Fig. 3.9 (B) & Appendix 2) peak accelerations between tested helmets were seen in some impacts. No trend of a helmet producing lower peak accelerations compared to other helmets was observed. Helmets increased mean impact durations for all impact surface compliances. The proportion of time to peak (TTP) and rebound time (RT) increased from 48% to 52% with increasing surface compliance (Fig. 3.10 & Appendix 2). Observable differences between helmets were obtained for the HIC and the RIC (Fig. 3.11 & Appendix 2). Throughout all impacts, the highest obtained HIC was 347.1 (unhelmeted, 24 mm, Front site) and the highest RIC was $2.26*10^6$ (unhelmeted, 24 mm, Side site), corresponding to an estimated risk of concussion of under 10% [216] and under 5%[232], respectively. Values for additional assessment criteria are shown in Appendix 2.

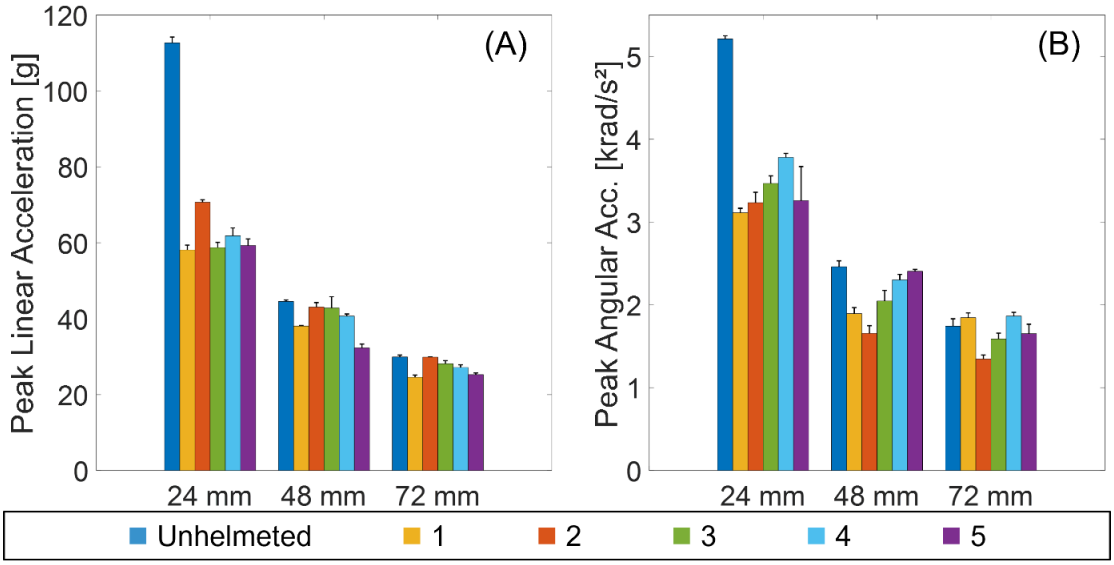

Fig. 3.9: Mean peak (**A**) linear and (**B**) angular accelerations of oblique, Front site impacts for unhelmeted and helmeted events with each helmet individually.

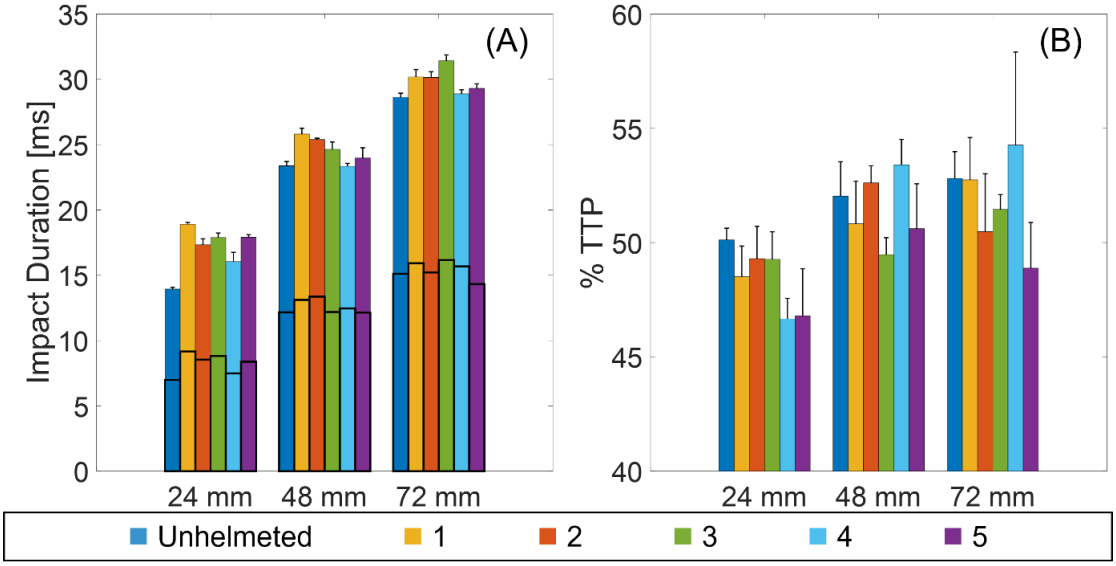

Fig. 3.10: Mean (**A**) impact durations with horizontal bars indicating the proportion of time to peak (bottom half) and rebound time (top half), and (**B**) percentage of time to peak of the total impact duration from oblique, Front site impacts for unhelmeted and helmeted events with each helmet individually.

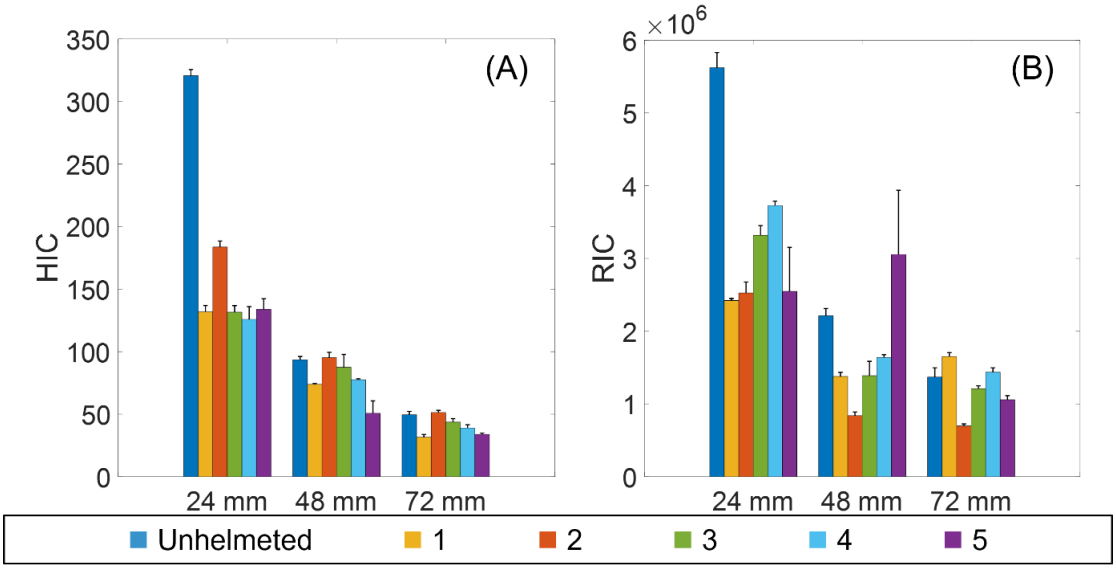

Fig. 3.11: Mean (**A**) HIC and (**B**) RIC from oblique, Front site impacts for unhelmeted and helmeted events with each helmet individually.

ICCs and their respective 95% CIs suggest excellent intra and inter-rater reliability (Table 3.3). To mitigate the effect of the large true score variance in the dataset, additional ICCs, where data were grouped by impacted surface and where unhelmeted impacts were excluded, were calculated. The lowest obtained ICC for intra-rater reliability was 0.838 with lower and upper limits of a 95% CI of 0.619 and 0.941, respectively. The lowest obtained ICC for inter-rater reliability was 0.887 with lower and upper limits of a 95% CI of 0.813 and 0.931.

Table 3.3: Intra and Inter-rater reliability ICCs and their respective 95% CIs for flat surface and oblique surface impacts. Unhelmeted impacts were excluded in the calculations of the ICC values shown.

	Intra-rater		Inter-rater	
	ICC	95% CI	ICC	95% CI
Flat, PLA [g]	0.995	0.991 → 0.997	0.967	0.929 → 0.984
Flat, D [ms]	0.996	0.994 → 0.997	-	-
Oblique, PLA [g]	0.991	0.987 → 0.994	0.980	0.958 → 0.990
Oblique, PAA [krad/s²]	0.997	0.995 → 0.998	0.952	0.897 → 0.977
Oblique, D [ms]	0.990	0.984 → 0.993	-	-

3.4 Discussion

A broad range of headform kinematic responses, expressed in PLA, PAA, and impact duration, was obtained for comparison with a reference dataset and assess the feasibility of interchangeable impact surface compliance in a free-fall drop test. Additional two commonly used head injury criteria (HIC and RIC) were calculated for helmet comparison. Some impact scenarios achieved a good match with the reference data. As expected, peak accelerations decreased (Fig. 3.9) while impact durations increased (Fig. 3.10) with increasing surface compliance (Fig. 3.5 & Fig. 3.6) [32,33,121]. Obtained linear and angular acceleration vs. time traces show a single peak shape (Fig. 3.4, Fig. 3.7 & Fig. 3.8), similar to reported shoulder to head collisions [23]. Commonly used guided drop tests [22] produce acceleration vs. time traces with an initial high, short-duration peak followed by a longer duration, lower magnitude peak similar to falls [23]. In head impact research, the single peak shape, characteristic of collisions, is generally achieved using a horizontal impactor [22,23,104]. This test setup produced a collision type acceleration vs. time trace shape with a drop test.

Comparing impacts with reference values published by Post et al. [104], the closest representation was achieved with oblique, 48-mm foam, non-centric impacts (Fig. 3.6). Flat surface impacts generally produced higher linear accelerations than the reference data (Fig. 3.5). Impacting foam layers of 72 mm, or thicker, produced longer duration impacts than the reference data. Impact surfaces that were stiffer than the 48 mm foam layer resulted in linear accelerations being too high and impact durations too short to match the reference data (Fig. 3.5 & Fig. 3.6).

Increasing surface compliance had a greater effect on the unhelmeted headform than the helmeted one, as expected [32,33,121,162]. As such, the difference between

helmeted and unhelmeted impacts decreased up to a point where a fitted helmet made no consistently measurable difference to peak accelerations, but impact durations were still increased (Fig. 3.5 & Fig. 3.6). No assessment on the representativeness of layered EVA foam to represent real-world impact bodies in ice hockey was carried out. However, this effect of decreasing helmet effectiveness with increasing surface compliance, also shown previously, suggests that the free-fall drop test with interchangeable surfaces can replicate ice hockey shoulder and elbow to head impacts [32,33].

Impacting centric impact sites during oblique impacts resulted in higher linear accelerations and lower angular accelerations than the reference data (Fig. 3.6). Impacting non-centric locations produced magnitudes within the range of the reference data (mean difference < 3 g & 0.62 krad/s²). Due to the spread and skew in the reference data, and the lower variation and relatively normal distribution in the data we collected, this free-fall drop test can only replicate a proportion of the dataset. For 48-mm foam, non-centric impacts mean PLA (31.5 ± 2.8 g) is between the median and Q3, mean PAA (2.8 ± 0.3 krad/s²) is between Q1 and the median, and mean D (25.8 ±1.8 ms) is within interquartile range of the reference data, respectively (Table 3.1). Hence, the presented results lie in a range of potentially concussive real-world ice hockey collision head impacts (Fig. 3.6, [104]), and while they do not cover the whole range within the dataset, they are more precise (less variable).

Comparing measured peak accelerations between helmets shows differences in some impacts. Most (538 of the 540) impacts produced lower peak accelerations than the 275 g threshold used in the standards [18–20], with two unhelmeted tests onto the MEP pad exceeding the threshold (Fig. 3.5). We used a different test setup – a free-fall drop test – and a different headform so the pass/fail threshold should only be

indicatively applied. No helmet consistently produced lower peak accelerations compared to the other helmets (Fig. 3.9). Greater differences between helmets were found for the calculated Head Injury Criterion and the Rotational Injury Criterion, which both consider a maximum time interval (Fig. 3.11, [224,232]). Helmets that produced high linear acceleration (or HIC) generally produced low angular acceleration (or RIC), and vice versa. However, no conclusions can be made about which materials or design features are preferential in an ice hockey helmet based on the obtained data. The proportion of time to peak of the total impact duration increased with increasing surface compliance, which is likely caused by the compressed surface and not the helmet (Fig. 3.10).

Intra and inter-rater ICCs and SDs (Fig. 3.9, Fig. 3.10, Fig. 3.11 & Table 3.3) suggest excellent reliability of repeated measures. Due to the large true score variance in the dataset, ICC should be considered cautiously [359]. However, due to the ICC still suggesting excellent reliability when measures were grouped by surface and when unhelmeted impacts were not considered, the test method (within-subjects) appears to have high reliability [358].

3.4.1 Limitations

The reference dataset was obtained from laboratory-recreated head impacts [104], as an in-field head injury data set is not publicly available. Despite being considered the best available estimate, a dataset of measured concussive impacts in ice hockey could increase confidence in head impact research, including this study.

Analysis of the high-speed video footage shows that it is difficult to precisely hit the predefined impact site consistently. Even though variations in measurement data are small and ICCs (within and between-subject) suggest excellent reliability (Table 3.3),

future work could modify the test setup to use a drop carriage similar to Meehan et al. [168], carry out more repeated measures per impact scenario, and test at different impact energies.

It is possible that the EVA foam, used to produce different impact surface compliances, degraded between tests. Future testing could consider the durability of the impacted surface. An anthropomorphic headform such as the 50th percentile Hybrid III used here has limited biofidelity and only partially represents head geometry, helmet fit, and friction between head and helmet [110,361]. The Hybrid III headform is, however, widely accepted and used in head impact research and provides reliable comparability to other published head impact research [22]. Further work could include additional materials described in the literature review, such as different headforms or an anthropomorphic neckform. Brain stresses and -strains, predicted using a finite element model, could further assess loads on the brain and injury probability. The five different helmets fitted onto the headform in this study were chosen to represent the range of helmet designs and the price range of commercially available helmets. In future work, adding additional helmets could increase confidence in the dataset and would give further insights into the effectiveness of different helmet designs.

3.5 Conclusion

This study demonstrated that by modifying the impacted surface, a free-fall drop test can produce kinematic responses similar to the method currently used to replicate ice hockey collisions. A wide range of head impact scenarios, representative of falls onto ice and collisions with other players, can be replicated using this method by adjusting compliance and orientation of the impacted surface. A drop height of one metre onto a 48 mm layered EVA foam surface, aligned at 45°, gave peak linear and angular

accelerations, and impact durations, within 10% of those obtained by current best practice methods. These findings facilitate a simpler test protocol for ice hockey helmets, either for adoption in certification standards or research.

4. Chapter – Compressive behaviour of bi-beams

4.1 Introduction

The presented literature review (chapter 2) and results of chapter 3 highlighted limitations of current ice hockey helmets, not reducing peak linear and angular accelerations effectively throughout the whole range of common head impacts in ice hockey [32,33,39]. Player-to-player collisions, where the impacting body possesses lower stiffness than the helmet liner, is commonly associated with clinical diagnosis of concussion [30,31]. Typically used helmet liner materials are relatively stiff, as they are usually selected to pass certification requirements and protect well during the most severe impacts – falls onto the ice. During player-to-player collisions, compression and crushing, the primary energy absorbing mechanism of a helmet [36], does not always occur sufficiently due to the deformation of the impacting body [32,33]. Consequently, helmet performance is limited, leaving players susceptible to injury. Due to the severity of injuries caused by rigid surface impacts (i.e. the ice and boards), helmets need to work well in these impacts, so using lower stiffness liners, which would be more effective during collisions, is not feasible.

A helmet liner with adaptable stiffness, could improve helmet performance during impacts with more compliant bodies, while maintaining the required high stiffness during rigid surface impacts. This chapter explores strain rate-dependent bi-beam structures, previously introduced by Janbaz et al. [44], with tailorable buckling behaviour. A bi-beam consists of two laterally attached beams, each with the same geometry, made from two different materials (Fig. 4.1). One of the materials is highly deformable and stiffens at high strain rates (i.e., visco-hyperelastic), while the other is highly deformable, largely strain rate-independent (i.e., hyperelastic), and stiffer than

the visco-hyperelastic beam under quasi-static conditions. Beams typically buckle when they are compressed beyond a critical load [362]. The softer side acts as a support – so both beams buckle toward the unsupported, stiffer side of the bi-beam. Consequently, these bi-beams should buckle towards the stiffer (hyperelastic) side at low compression rates. Exceeding a threshold strain rate switches the order of stiffness and the direction of buckling (Fig. 4.1) [44].

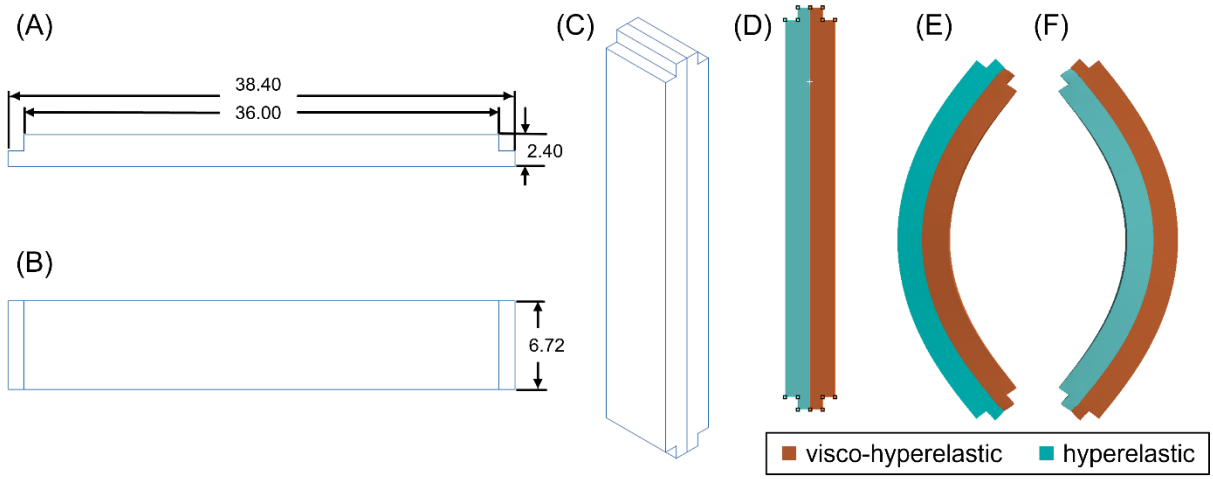

Fig. 4.1: (**A**) Side view and (**B**) top view of beam geometry [mm]. (**C**) Bi-beam. (**D**) A bi-beam made of a visco-hyperelastic and a hyperelastic beam. (**E**) Buckling towards the hyperelastic side (i.e. at low strain rates), and (**F**) buckling towards the visco-hyperelastic side (i.e. at high strain rates).

A unit cell of the mechanical metamaterial consists of two bi-beams, positioned at a small distance from each other and with opposite orientations (Fig. 4.2). Due to the positioning of the two bi-beams relative to each other, and the switch of buckling direction depending on compression rate, two different loading conditions can occur.

1. At low compression rates, both bi-beams buckle in opposite directions and thus do not restrict each other's buckling motion, causing a relatively compliant response (Fig. 4.2 (B)).
2. At high compression rates, both bi-beams buckle towards each other. Contact between the two beams prevents further buckling, causing an increase in stiffness (Fig. 4.2 (C)).

The strain rate dependant switching of buckling direction increases the stiffness abruptly, and allows a tuneable response to loading conditions, such as stiff or compliant surface impacts. Buckling behaviour has been shown to be reliable and predictable, while the design was scalable in size [44]. Nonetheless, a rigorous analysis of the effect of beam stiffness on buckling direction is required before application in a helmet, where reliability is critical. So, this chapter first characterises a range of polymers, and then uses these to demonstrate repeatability of bi-beam response.

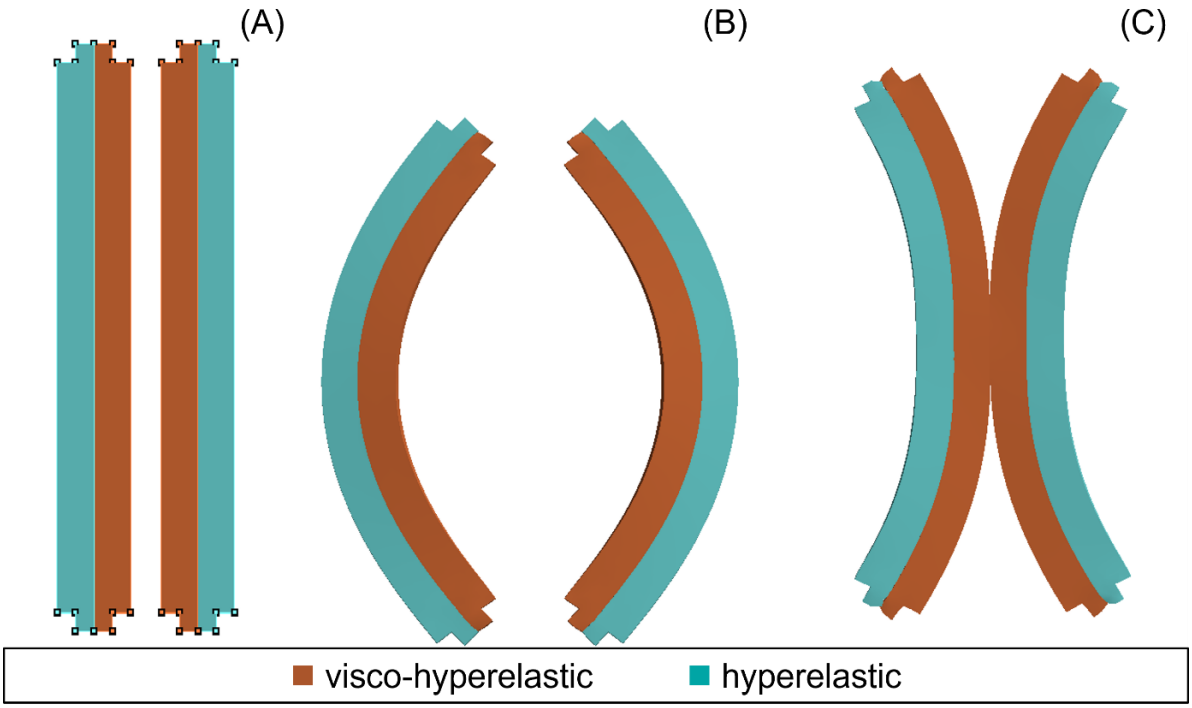

Fig. 4.2: Bi-beam unit cell (**A**) uncompressed, (**B**) buckling out, and (**C**) buckling in.

Firstly, materials for the fabrication of beams were characterised as properties of 3D printed materials are often not openly available or can be unsuitable due to material properties changing with printing parameters [363]. Additive manufacturing was used for the fabrication of all bi-beam samples. Consistent quality of samples, understanding of material behaviour, and knowledge of material parameters, were obtained for the planning of experimental testing and the creation of material models for numerical

simulations. A material characterisation following a previously suggested protocol for finite element (FE) modelling of mechanical metamaterials for sports applications, was carried out for four 3D printable thermoplastic polyurethane (TPU) materials for defined print parameters [364].

Secondly, bi-beam prototypes were produced and experimentally tested individually and as unit cells. Results from experimental testing and numerical simulations, presented by Janbaz et al. [44], suggest an adaptive reaction to different compression rates, however, testing was carried out at low speeds (maximum of 500 mm/min, 8.3 s^{-1}). Building on insights on material properties from the material characterisation, mechanical testing of bi-beams to gain an understanding of buckling behaviour at increased strain rates and to further assess the potential of a bi-beam metamaterial structure for impact applications was undertaken. Individual bi-beams and unit cells, consisting of two bi-beams orientated to each other, were compressed uniaxially using a mechanical test machine. Rate-dependence was not considered as the order of stiffness of chosen constituent materials remained unchanged for all compression rates. Insights gained were used to inform the subsequent design of a metamaterial structure consisting of bi-beam unit cells and testing at velocities and energies representative for impact events.

The objectives of this chapter were to:

- Define print settings for each material to consistently achieve successful prints.
- Measure material parameters required for the planning of experimental studies and the creation of material models for numerical simulations.
- Rigorously demonstrate the effect of beam stiffness on bi-beam buckling direction, under quasi-static and dynamic loading.

- Understand buckling behaviour of bi-beams and the switching of compressive stiffness of unit cells depending on the contact situation.

4.2 Methods

4.2.1 Material characterisation

4.2.1.1 Sample fabrication

UltiMaker S5 fused filament fabrication (FFF) 3D printers with a Bowden extruder and 0.4 mm nozzle were used for the fabrication of all test samples. Four commercially available TPU filaments (Table 4.1) with a diameter of 2.85 mm were selected to represent a range of common flexible materials. All samples were printed with a 0.12 mm layer height, and with 100% infill. All other print settings were determined through an iterative refinement of the print process for each material (Table 4.2). Twelve type 1 dog-bone samples, as specified in BS ISO 37:2017 [365], and 27 cubic (compression) samples (side length 10 mm), were produced and tested for each material (Fig. 4.3).

Table 4.1: TPU material parameters according to manufacturer's technical data sheet (TDS).

Material	Density [kg/m³]	Shore Hardness	Tensile Modulus [MPa]
Flex Medium, Extrudr, AT [366]	1190	98 A	40
MD Flex, Copper 3D, CHL [367]	1160	98 A	150
TPU 95A, Ultimaker, NLD [368]	1220	95 A	26
NinjaFlex, Ninjatek, USA [369]	1190	85 A	12

Table 4.2: Material-specific 3D print settings.

Material	Print temp. [°C]	Bed temp. [°C]	Print speed [mm/s]	Flow
Flex Medium	210	30	30	110%
MD Flex	235	60	75	100%
TPU 95A	223	60	25	106%
NinjaFlex	235	50	20	100%

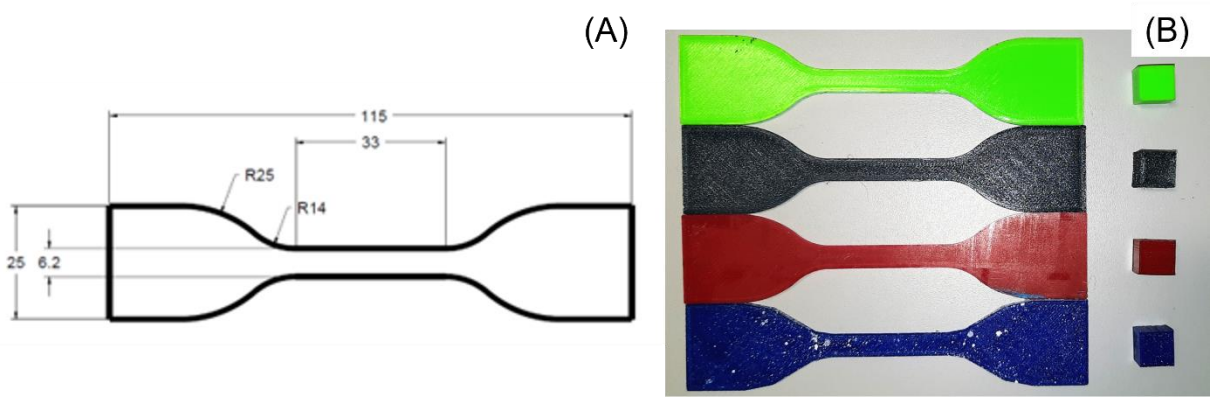

Fig. 4.3: (**A**) Dog-bone tensile test sample geometry [mm], thickness: 2 mm [365] and (**B**) tensile and compression test samples (from top to bottom: Flex Medium (neon green) [366], MD Flex (grey blue) [367], TPU 95A (red) [368], and NinjaFlex (sapphire blue) [369]).

4.2.1.2 Test procedure

Material characterisation was carried out using an Instron Electropuls E3000 dynamic testing instrument (Illinois Tool Works Inc., US) equipped with a 5 kN load cell (Fig. 4.4 (A)). Quasi-static tensile tests were undertaken for the “dog-bone” samples, with a grip distance of 70 mm, to an engineering strain of 0.5 (35 mm), with strain rate set to 0.006 s^{-1} (0.42 mm/s). The cubes were compression tested to an engineering strain of 0.5 (5 mm) at a strain rate of 0.008 s^{-1} (5 mm/min) with a pre-load of 10 N. Machine force, displacement data, and sample dimensions were used to compute engineering stress (σ) and strain (ε). A linear trend line was fitted between strains of 0 and 0.1 to obtain Young’s Modulus (E). To assess the effects of print layer building direction on final mechanical properties, cubic samples were compressed in their building direction (Z-direction) and perpendicular to building direction (X-direction), with each test repeated three times. For full-field strain measurements using Digital Image Correlation (DIC), a spray paint speckle pattern was applied to the narrow portion of all tensile samples (Fig. 4.4 (B)) and to one face of all cubic samples (undercoat: matt white acrylic, speckles: matt black acrylic). A camera (Phantom Miro R311, Vision Research Ltd., UK; resolution 1280 x 800 pixels, sample rate 24 fps; lens, Nikon AF Nikkor 24 – 85 mm), positioned 500 mm from the test sample, and with the field of view perpendicular

to the speckled surface, filmed all the tests (Fig. 4.4 (A)). Lateral and axial engineering strains were obtained by 2D DIC using GOM Correlate (2019 Hotfix 7, Rev. 128764, Build 2020-06-18). Poisson's Ratio (v) was obtained by fitting a linear trendline to the lateral vs. axial strain data [370] up to an axial strain of 0.1.

Additional tests were carried out to assess rate dependence. Firstly, tensile tests to an engineering strain of 0.4 (28 mm) were undertaken, at applied strain rates of 1, 2, 3 s^{-1} (70, 140, 210 mm/s); with the camera filming at 210 fps. Secondly, compression tests to an engineering strain of 0.4 (4 mm) were undertaken, at applied strain rates of 1, 2, 4, 8, 16 s^{-1} (10, 20, 40, 80, 160 mm/s), with the camera filming at 1600 fps. These compression tests were only performed in the Z-axis, with each test repeated three times. Stress, strain, and Young's modulus were obtained using the same method as the quasi-static tests. Viscoelastic material data were obtained through stress relaxation testing. Three cubic samples of each material were compressed to an engineering strain of either 0.2 (2 mm) or 0.4 (4 mm) at a rate of 0.005 s^{-1} (0.05 mm/s). Force was measured while compression was held for 600 s.

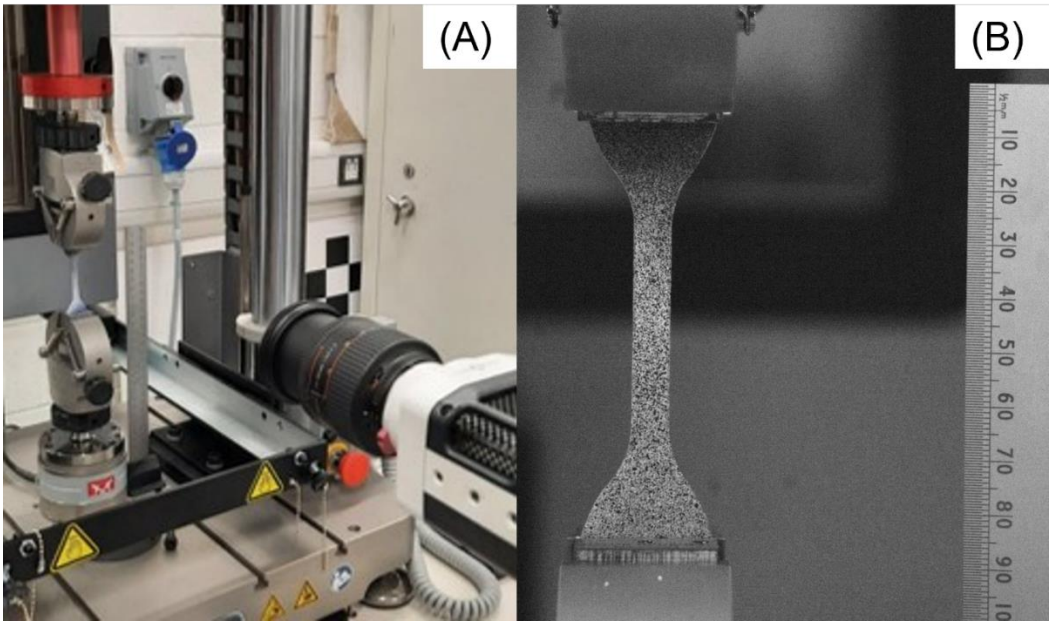

Fig. 4.4: (**A**) Tensile test setup and (**B**) still from video footage for DIC analysis, showing a sample with applied speckle pattern.

4.2.2 Experimental compression of bi-beams

4.2.2.1 Sample fabrication

The two materials chosen to fabricate bi-beam samples for testing were TPU 95A (red) and NinjaFlex (blue) (Fig. 4.5), for their difference in stiffness. Both materials can be considered hyperelastic and do not have notably different rate dependence properties (Fig. 4.9 & Fig. 4.10). They were chosen to obtain a rigorous and controlled assessment of the system; bi-beams are expected to buckle towards the stiffer TPU 95A beam at all compression rates. Print settings were similar to the ones described previously (Chapter 4.3.2). TPU 95A and NinjaFlex beams were bonded using an epoxy adhesive (Metalset A4, Smooth On) and left to cure at room temperature for at least 24 hours.

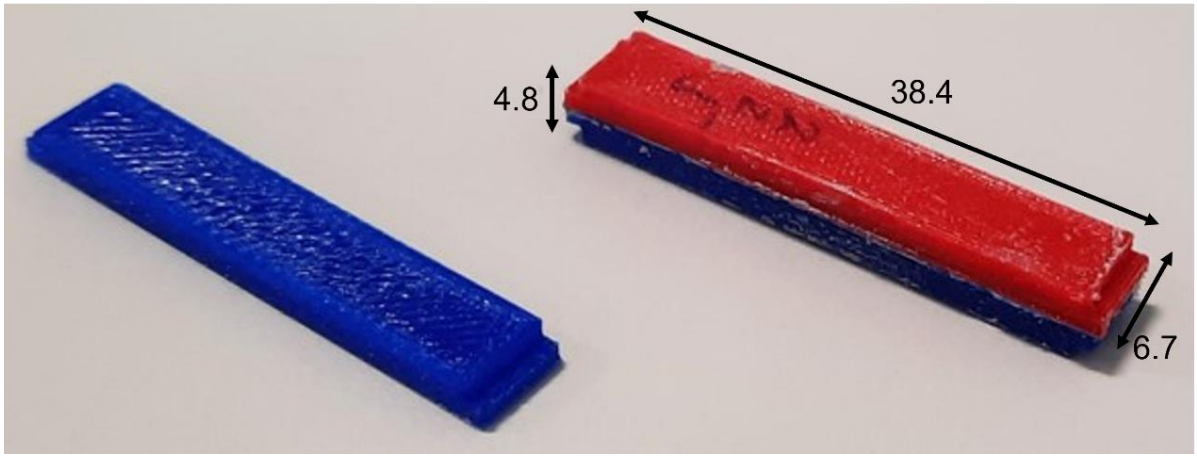

Fig. 4.5: Beam (left) made from Ninjaflex (blue) and bi-beam (right) with dimensions [mm] made from TPU 95A (red) and Ninjaflex (blue).

4.2.2.2 Test procedure

To assess their effective stiffness, bi-beams were compressed using the Instron Universal Test machine (Electropuls E3000, 5kN load cell). Bi-beams were tested individually (Fig. 4.7 (A)) and in three different unit cell configurations (2 mm gap – orientated to buckle away from each other (known as “out” herein Fig. 4.7 (B)), 2 mm gap – orientated to buckle towards each other (known as “in” herein Fig. 4.7 (C)), 10

mm gap – in (Fig. 4.7 (D)). Gap sizes were selected based on pilot testing, so that bi-beams underwent a second buckling, at the unit cell level when 2 mm apart, and did not when 10 mm apart. To position the bi-beams and prevent slipping during compression, 3D-printed plates (tough polylactic acid (tPLA), PLA Pro+, RS PRO [371]) with rectangular slots (Fig. 4.6) were clamped into the test machine for all testing (Fig. 4.7).

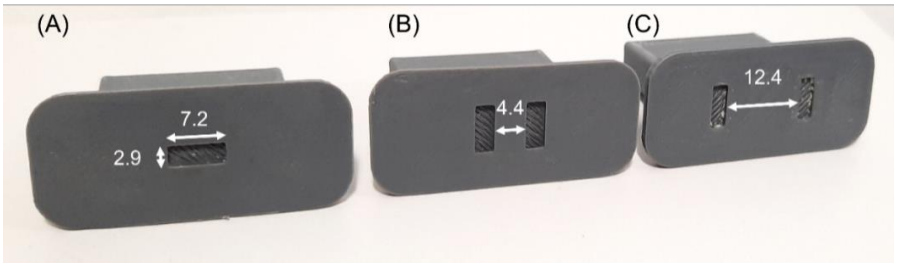

Fig. 4.6: Plates with rectangular (2.9 x 7.2 mm) cavities for clamping into the Instron test machine to position and test (**A**) an individual beam, (**B**) a unit cell with a 2 mm gap between bi-beams, and (**C**) a unit cell with 10 mm between bi-beams.

Bi-beams were compressed in axial direction to a strain of 0.15 (5.76 mm displacement) at a strain rate of 8.3 s^{-1} (5.31 mm/s), similar to the original work on bi-beam structures presented by Janbaz et al. [44]. Additional tests with compression rates of 0.83 s^{-1} (0.53 mm/s) and 83.3 s^{-1} (53.12 mm/s, close to Instron machine maximum) were carried out. For each configuration, five tests were carried out, resulting in a total of 60 uniaxial compression tests. Force vs. displacement raw data was obtained from the Instron machine and all tests were filmed (Phantom Miro R311, Vision Research Ltd., Bedford, UK).

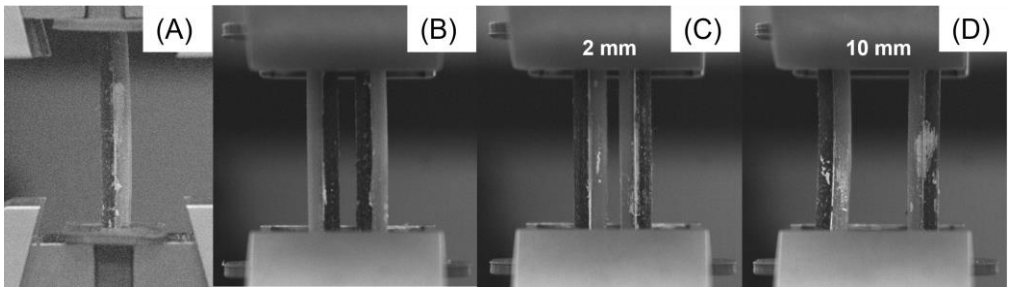

Fig. 4.7: Uncompressed (**A**) individual bi-beam, (**B**) unit cell in buckling “out” configuration, (**C**) unit cell in buckling “in” configuration with a 2 mm gap, and (**D**) unit cell in buckling “in” configuration with a 10 mm gap.

4.3 Results

4.3.1 Material characterisation

Mean Poisson's ratio were all ~0.4 (Table 4.3 & Fig. 4.8). Tensile moduli was up to 3.9 times greater than stated on the respective TDS (Table 4.3) [366,368]. For Flex Medium and TPU 95A, compressive modulus did not change depending on the direction relative to layer orientation. For MD Flex and NinjaFlex, lower compression moduli were found when compressed perpendicular to layer orientation (Table 4.3).

Table 4.3: Poisson's Ratio, Tensile Modulus, deviation from TDS [366–369], and directional sensitivity for all four TPU materials obtained from quasi-static testing.

Material	ν_{zx}	E_z – Tensile [MPa]	E_z/E_{TDS}	E_z/E_x
Flex Medium	0.38 ± 0.01	147.2 ± 14.3	3.7	0.99
MD Flex	0.37 ± 0.01	130.9 ± 6.3	0.9	0.89
TPU 95A	0.40 ± 0.01	101.2 ± 6.8	3.9	1.0
NinjaFlex	0.36 ± 0.02	24.4 ± 8.9	2.0	0.78

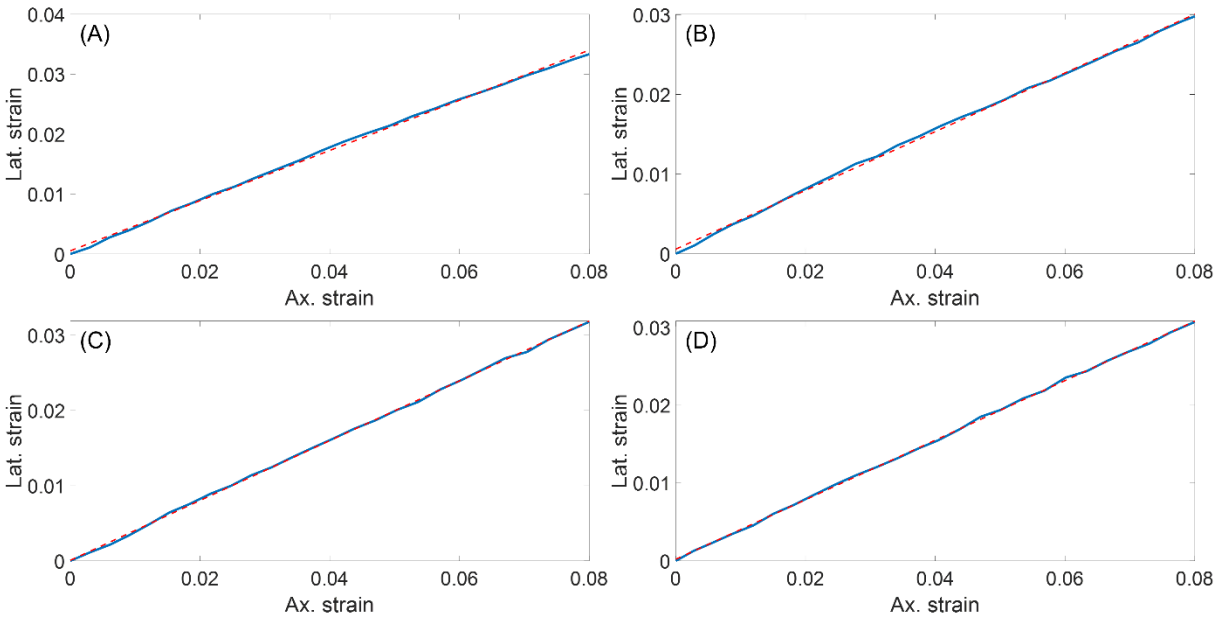

Fig. 4.8: Lateral vs. axial strain during tensile tests with plotted linear trendline and respective equation obtained from DIC for (**A**) Flex Medium, (**B**) MD Flex, (**C**) TPU 95A, and (**D**) NinjaFlex.

Increased strain rates showed all four TPUs to be rate dependant. For both, tensile (Fig. 4.9) and compression tests (Fig. 4.10), stiffness increased with increasing strain rate. During stress relaxation tests, shear modulus decayed over time. After 600 s holding time, measured forces decreased to ~75% of the initial magnitude for all four characterised materials (Fig. 4.11).

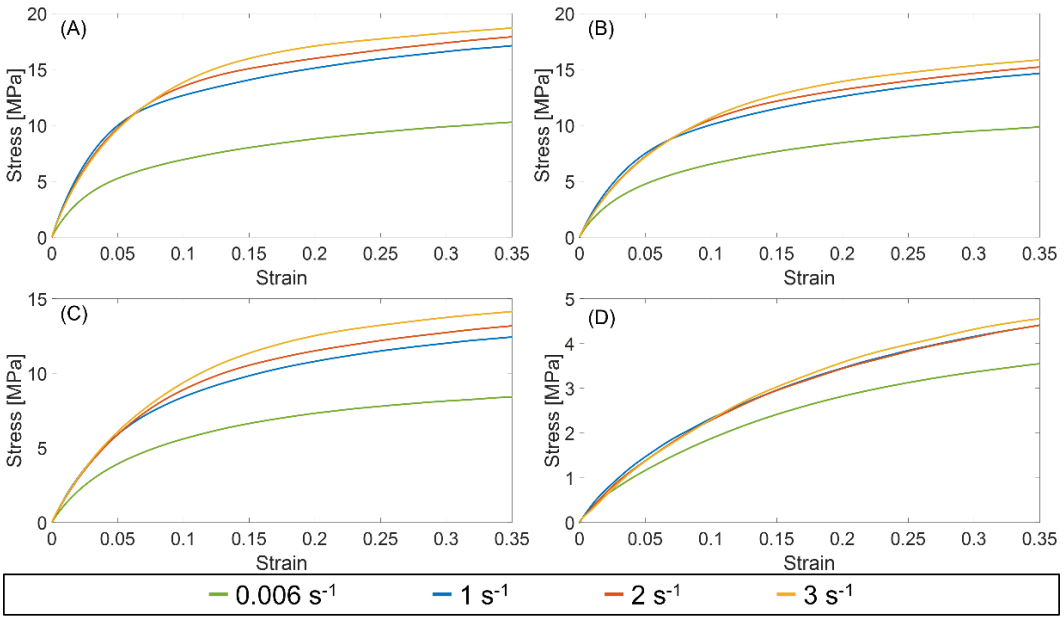

Fig. 4.9: Tensile stress vs. strain data at four different strain rates for (**A**) Flex Medium, (**B**) MD Flex, (**C**) TPU 95A, and (**D**) NinjaFlex (note y-axis variation to ensure all data was visible).

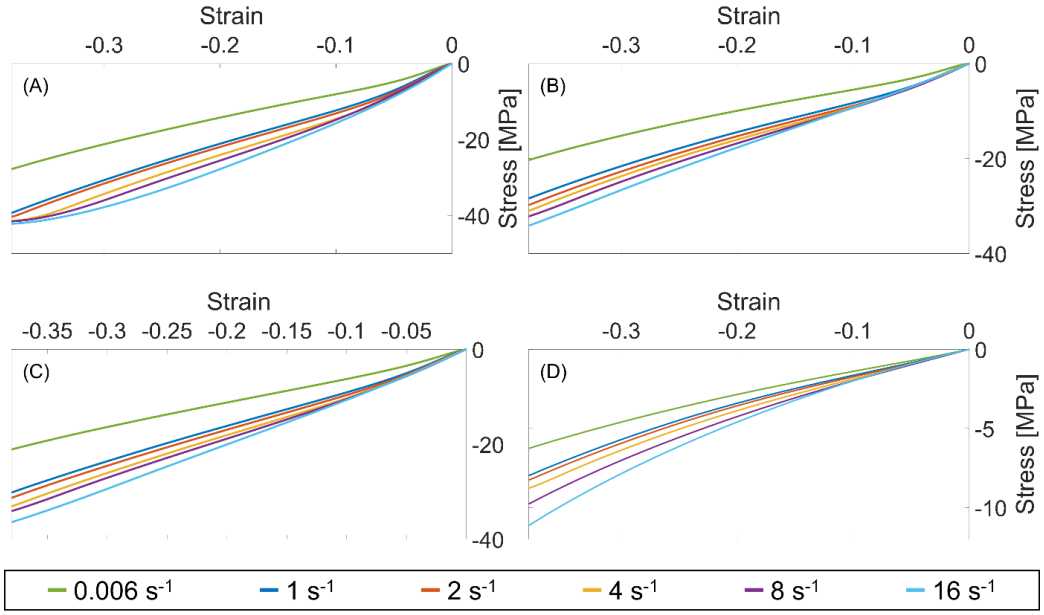

Fig. 4.10: Compression stress vs. strain data at six different strain rates for (**A**) Flex Medium, (**B**) MD Flex, (**C**) TPU 95A, and (**D**) NinjaFlex (note y-axis variation to ensure all data was visible).

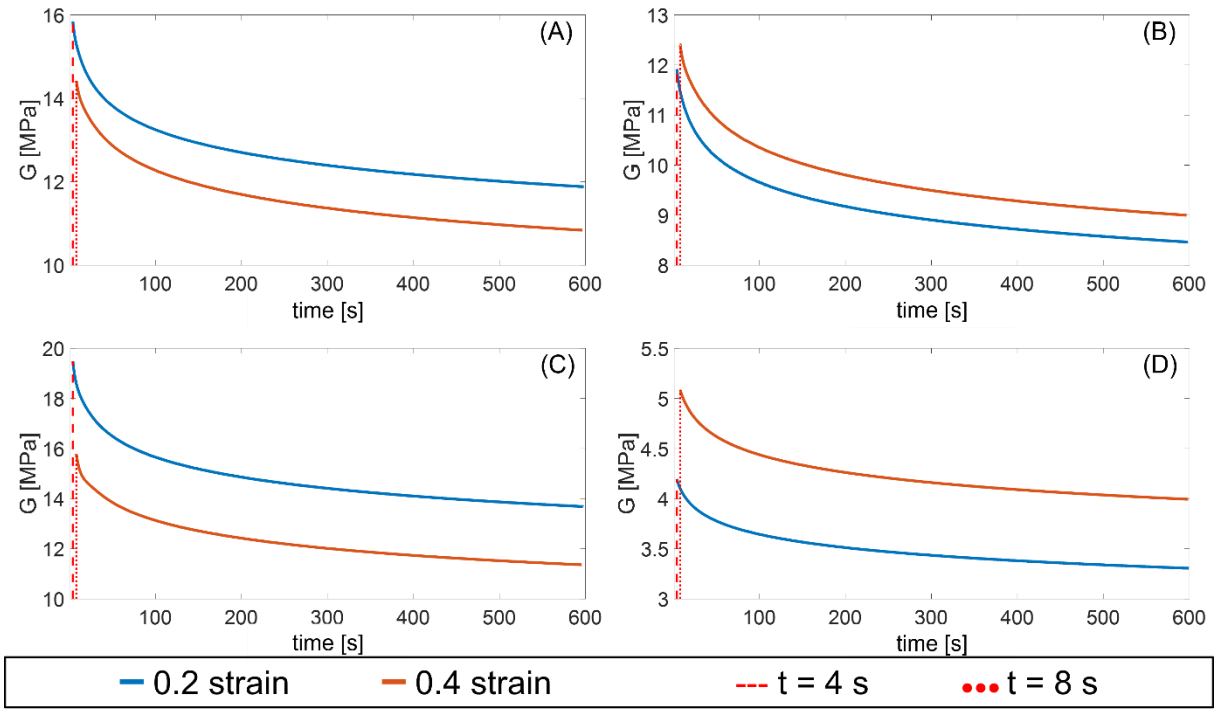

Fig. 4.11: Stress relaxation shear modulus vs. time curve with a holding time of 600 s for (**A**) Flex Medium, (**B**) MD Flex, (**C**) TPU 95A, and (**D**) NinjaFlex.

4.3.2 Experimental compression of bi-beams

In 4 out of the 60 tests carried out, one of the bi-beams did not buckle in the predicted direction. The data from these tests is not included in the results below, but indicates there is some potential uncertainty in the system. With increasing strain rate, the mean peak force increased in most cases (Table 4.4). Mean peak forces increased by up to 48% when comparing the lowest to the highest compression rate. For an individual bi-beam in uniaxial compression, mean peak forces increased (34%) from a 0.83 s^{-1} to an 8.3 s^{-1} strain rate, but not from an 8.3 s^{-1} to an 83.3 s^{-1} strain rate. The standard deviation from the mean peak forces was above ~20% for 8.3 s^{-1} strain rate tests (Table 4.4). Buckling “in” with a larger gap (10 mm) between the beams, preventing a “pushing away” and subsequent change in on bi-beams buckling direction, increased mean peak forces 2 to 3-fold compared to the buckling out scenario (Table 4.4).

Peak forces were measured between 0.03 and 0.04 compressive strain (1 – 1.5 mm compressive displacement). The buckling deformation of the bi-beam takes place after reaching the peak force, from which point the force constantly decreases. At the maximum compression of 0.15 strain (5.76 mm), force is at a level of about two thirds of the maximum value (Fig. 4.12 & Appendix 3 for all sample results).

Table 4.4: Mean (± SD) peak force [N] for all four test configurations at three strain rates.

	0.83s^{-1} (0.53 mm/s)	**8.3 s^{-1} (5.3 mm/s)**	**83.3 s^{-1} (53 mm/s)**
Individual	30.64 (± 2.82)	41.06 (± 9.18)	41.06 (± 4.93)
Out	65.12 (± 4.36)	73.5 (± 6.21)	96.54 (± 6.04)
In – 2 mm gap	106.52 (± 13.96)	125.45 (± 19.3)	119.38 (± 10.12)
In – 10 mm gap	167.4 (± 4.71)	204.28 (± 20.38)	247.4 (± 31.83)

During uniaxial compression of a unit cell, when both bi-beams buckled out, mean peak forces increased (12.8% and 31.3% respectively) with increasing compression rate (Table 4.4). Peak forces were measured between 0.05 and 0.065 compressive strain (2 – 2.5 mm). At maximum compression, measured force dropped to ~60% of the obtained maximum value (Fig. 4.13 & Appendix 3).

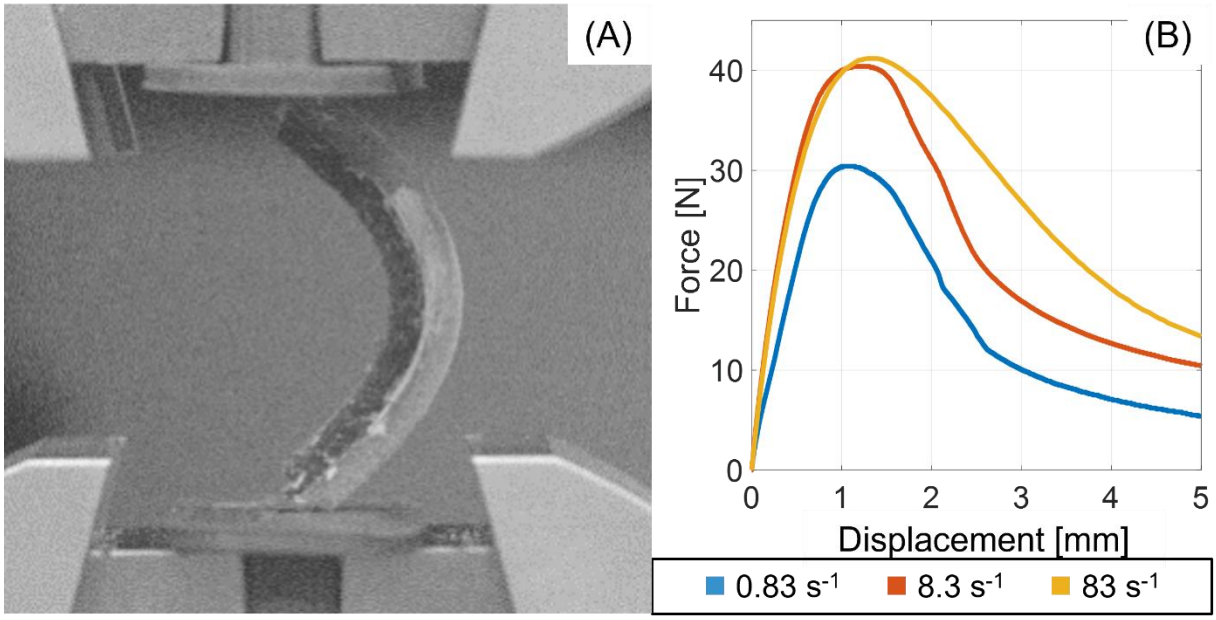

Fig. 4.12: Uniaxial compression test of representative individual bi-beam (dark: NinjaFlex, light: TPU 95A) in (**A**) maximal (0.15 engineering strain) compression and (**B**) Force [N] vs. displacement [mm] traces for all three strain rates.

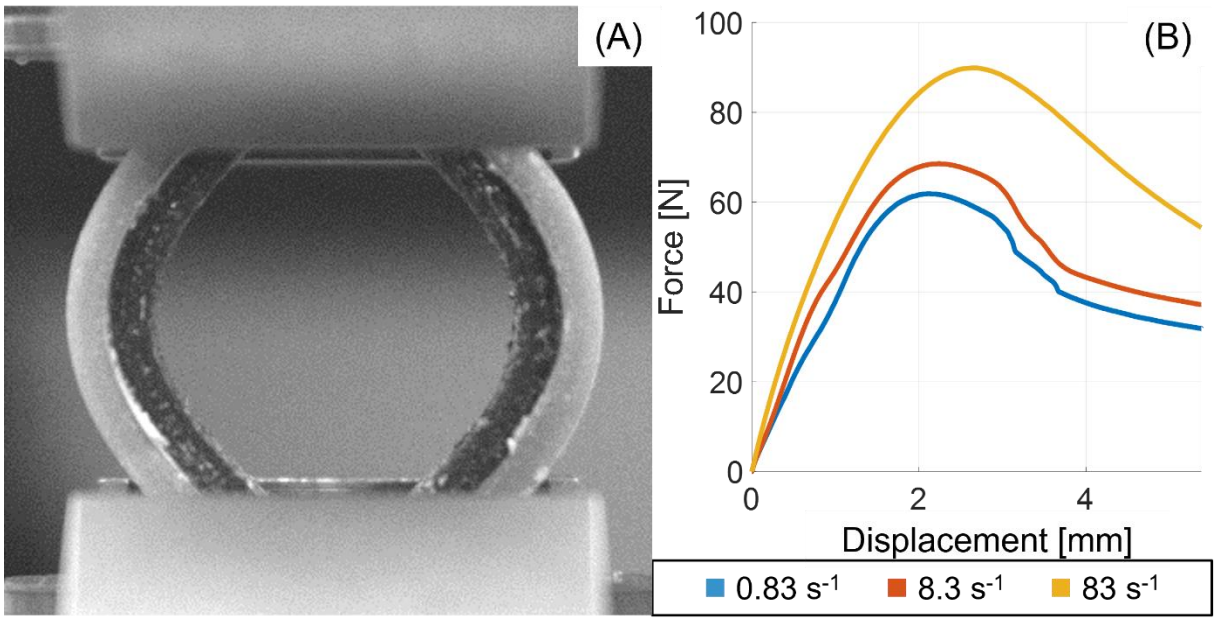

Fig. 4.13: Uniaxial compression test of a representative bi-beam unit cell buckling “out” in (**A**) maximal (0.15 engineering strain) compression and (**B**) Force [N] vs. displacement [mm] traces for all four strain rates.

During uniaxial compression of a unit cell, when bi-beams were positioned 2 mm apart and both bi-beams buckled “in”, mean peak forces increased from 0.83 s^{-1} to 8.3 s^{-1} strain rate (17.8%) but not from 8.3 s^{-1} to 83 s^{-1} (- 4.8%) (Table 4.4). After an initial buckling towards each other and making contact, one bi-beam would push the other

one back to change its initial buckling direction, resulting in both beams buckling into the same direction. Maximum forces varied more than during the buckling out scenario as the interaction between bi-beams affects the deformation. Peak forces, corresponding to maximum compressive strength, were measured between 0.04 and 0.065 compressive strain (1.5 - 2 mm). At maximum compression, measured forces dropped to ~30 – 40% of measured maximum values (Fig. 4.14 & Appendix 3).

During uniaxial compression of a bi-beam unit cell, when bi-beams were positioned at 10 mm distance and both bi-beams buckled “in”, the highest peak forces were measured and mean peak forces increased (22% and 21.1% respectively) with increasing strain rate (Table 4.4). The shape of the force vs. displacement trace differs from the other configurations. Rather than declining after the initial peak (0.05 – 0.065 strain), the force increases again to a second, higher peak around 0.1 to 0.12 compressive strain (4 – 4.5 mm), due to the bi-beams restricting each other’s buckling deformation. The higher the compression rate, the less pronounced the transition area after the initial peak (Fig. 4.15 & Appendix 3).

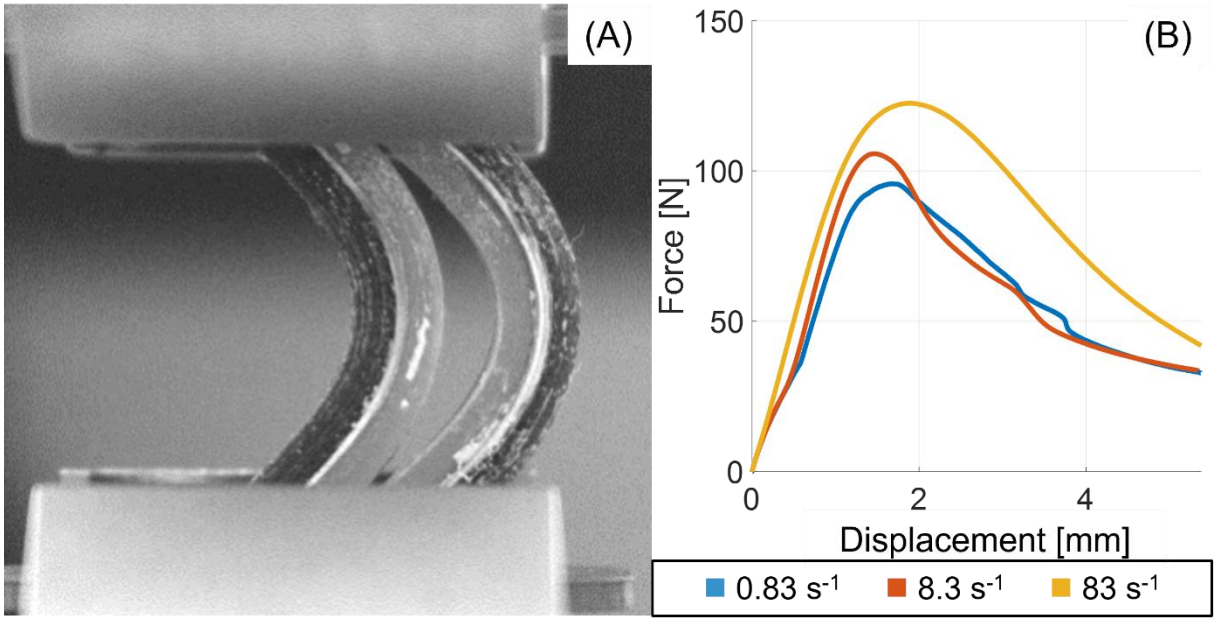

Fig. 4.14: Uniaxial compression test of a representative bi-beam unit cell buckling "in" with the bi-beams positioned at a distance of 2 mm from each other in (**A**) maximal (0.15 engineering strain) compression and (**B**) Force [N] vs. displacement [mm] traces for all four strain rates.

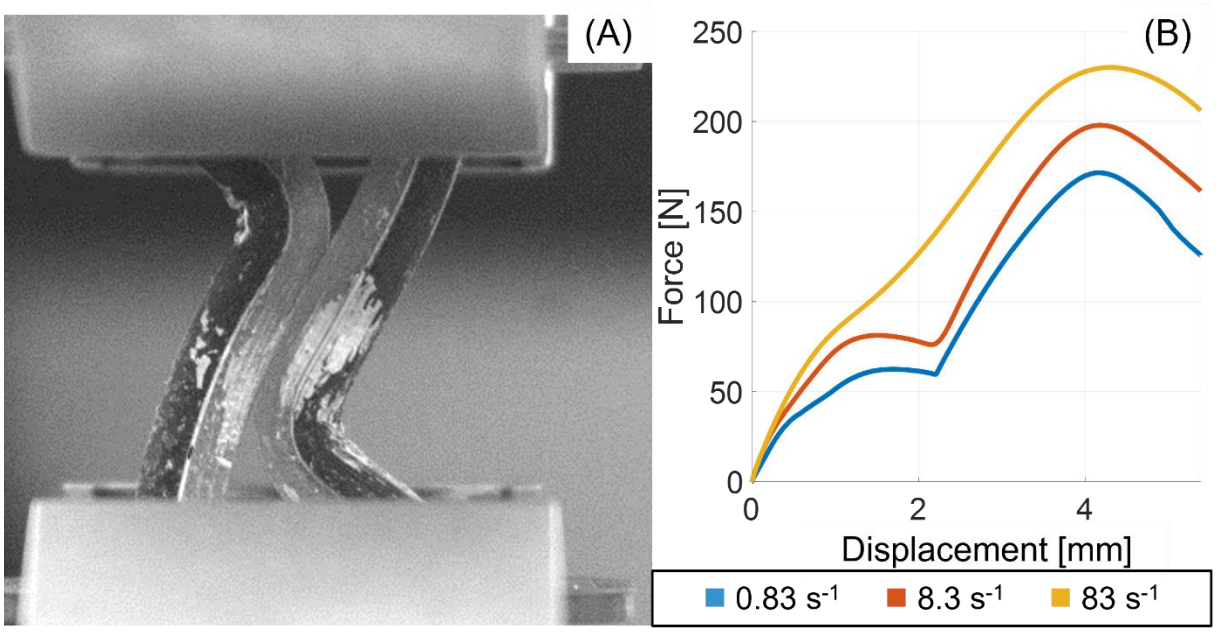

Fig. 4.15: Uniaxial compression test of a representative bi-beam unit cell buckling "in" with the bi-beams positioned at a distance of 10 mm from each other in (**A**) maximal (0.15 engineering strain) compression and (**B**) Force [N] vs. displacement [mm] traces for all four strain rates.

Comparing the three compression scenarios for the bi-beam unit cell with each other, the two desired compression scenarios – buckling "out" and buckling "in" with a 10 mm gap – occurred consistently and predictably at all strain rates (Fig. 4.16). Bi-beams buckling against each other, restricting each other's deformation, increased the

compressive strength of a unit cell. Maximum forces were 157%, 178%, and 156% higher for 0.83, 8.3, and 83 s^{-1} strain rate, respectively (Table 4.4 & Fig. 4.16).

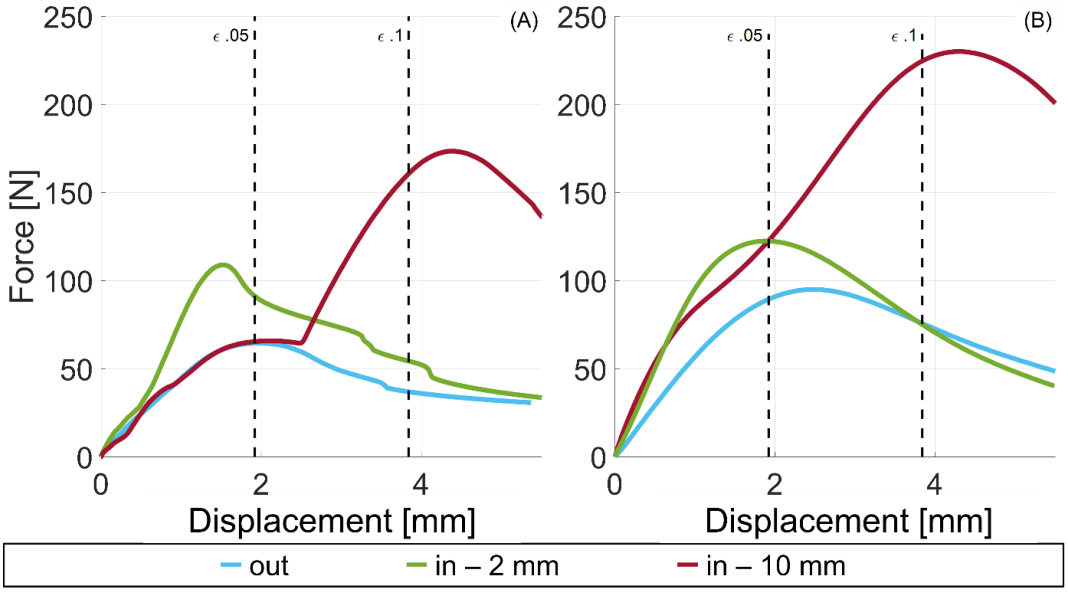

Fig. 4.16: Force vs. Displacement trace for buckling conditions of the bi-beam unit cell at (**A**) 0.83 s^{-1} and (**B**) 83 s^{-1} compression rates.

4.4 Discussion

Obtained material data allows for modelling of all four TPU materials in numerical simulations. The properties can also be used by other researchers without the need to do a separate characterisation. However, as material properties of additively manufactured materials always depend on the printer settings [363], the same settings as described in section 4.2.1.1 must be used when using provided material parameters. Consistency in prints and availability of parameters for simulations can facilitate developments in sports equipment and other fields.

Poisson's Ratio of NinjaFlex (0.36) was below the value of 0.45 measured previously [364]. Directional sensitivity was observed for two (MD Flex and NinjaFlex) of the four TPUs (Table 4.3). The obtained material data are suitable for obtaining coefficients for non-linear hyperelastic material models via a curve fitting procedure. Similarly, the stress relaxation data can be used to obtain coefficients to model viscoelastic material

behaviour. Material properties (Table 4.3) and model coefficients allow for a realistic representation of materials in numerical simulations, described in chapter 5.

The buckling direction of bi-beams during uniaxial compression was consistently predictable. Despite sources of variation on bi-beam properties, such as the 3D printing, the bonding, and the manual loading into the test machine, beams buckled the intended way 95% of the time. Hence, a sufficient number of bi-beams would be required in a cellular structure to ensure incorrect buckling would not notably increase injury risk. The two buckling scenarios required for the intended switch in uniaxial compressive strength were achieved by both bi-beams buckling “out” and by both bi-beams buckling “in” with a larger (10 mm) gap between them.

As expected, mean peak forces of the unit cell buckling out were about double the mean peak forces of an individual beam. Peak forces occurred at higher strains for unit cell compression which is likely due to the bi-beams buckling at different times. For the buckling “in” with the smaller (2 mm) gap, the buckling direction after the initial contact of both bi-beams was not predictable. The interaction between the two bi-beams also introduced higher variations in measurements.

Increasing compression rate increased mean peak forces by ~10 – 30% due to the rate dependence of both TPUs. The tested compression rates were below compression rates expected in a real-world impact. However, the tested range provides insights on the effect of compression rate. A switch in buckling behaviour increased mean peak forces by ~155 – 180%. The higher the compression rate, the smoother the transition between the first and the second peak of the buckling “in” force vs. displacement trace was. This drastic increase in compressive strength of one unit cell, based on buckling behaviour and rate-dependence, suggests that a similar effect

is possible for a cellular sheet structure consisting of multiple unit cells. Expanding to a cellular structure and tailoring the buckling direction threshold, determined by strain rate, may create a mechanical metamaterial sheet layer with large potential in impact applications, such as ice hockey helmets.

Further work could explore alternative interfaces between bi-beams and sandwich plates and friction effects between bi-beams. Further, a strain rate-dependent switch in buckling direction as described in chapter 2.4.5 and section 4.1 would provide further insights into the structures feasibility in impact applications.

4.5 Conclusion

Consistent buckling in the predicted direction and no observable signs of damage or material failure to test samples suggests that the fabricated bi-beams are suitable for subsequent testing. Depending on the contact situation of a unit cell, a clear difference in the compressive response (i.e., increased compressive strength and no drop in force after initial buckling) can be observed. Due to the controlled stiffness of samples (i.e., eliminating strain-rate dependent switch in buckling direction), a rigorous demonstration of the effect of contact situation in a unit cell on compressive strength was achieved. Two different responses to compressive deformation from two identical structures suggests potential for bi-beam cellular structures for use in applications where a wide range of different impact events is expected, such as sports helmets.

4.6 Chapter summary

This chapter detailed the concept of bi-beams, tailorable buckling behaviour depending on compression rate, and an associated switch in order of stiffness depending on the resulting contact situation. This effect can be used in a unit cell to create different contact situations during compression which result in an increase in compressive

strength. This effect could be used in impact applications, such as ice hockey helmets, where a wide range of different impacts are common.

Optimal print settings for four different 3D printable TPU materials were determined. Subsequently, a material characterisation was carried out. Results informed decisions on bi-beam sample materials and fabrication parameters. Further, obtained material parameters are suitable to create hyperelastic material models to be used in numerical simulations.

Bi-beams and unit cells were compressed axially at different compression rates. Buckling deformation and the effect of different contact situations within unit cells were assessed to further develop the bi-beam structures into a cellular structure. Predictability in buckling direction towards the side of higher instantaneous stiffness and an abrupt increase in compressive strength were shown.

Findings of this chapter suggest potential for bi-beam structures to be further developed into a cellular mechanical metamaterial with an adaptable compressive response that can be fitted into a helmet or similar impact protection application. The shown abrupt switch in compression behaviour may facilitate increased protection throughout a wider range of impacts or increased protection during impact events where helmet protection is currently limited, without compromising protection during impacts where helmets already work well.

5. Chapter – Modelling of bi-beams

5.1 Introduction

The experimental results described in chapter 4 highlighted the potential of bi-beam structures for an adaptive response to impacts. Gaining further insights on bi-beam behaviour during compression, via fabrication and experimental testing of a large number of bi-beams, would require time and material expenditure. Predictive models of bi-beam deformation and stiffness, depending on constituent materials and design choices, could provide an efficient method to develop bi-beams for expected impact scenarios. In this chapter, insights gained from chapter 4 were utilised to develop predictive models of bi-beam compression.

Firstly, deriving an analytical model, using material properties (chapter 4.3) and bi-beam geometries, could provide an efficient way to estimate bi-beam behaviour and inform design choices. The ability to estimate forces and deformations with the developed model could save time and material cost compared to experimental testing, and does not require specialist software and computation time such as a numerical model. Secondly, a numerical model using FE analysis could facilitate the testing of scenarios and designs computationally. All required material parameters to create material models, representative of TPU materials, were obtained in chapter 4.3. Experimental testing results, described in chapter 4.4, provide a dataset that can be used to validate FE models.

The objectives were to:

- Derive an analytical model to predict critical loads and buckling deformation.
- Create material models for bi-beam constituent materials to be used in FE simulations.

- FE simulation of bi-beam compression scenarios
- Validate obtained results from models against results from chapter 4
- Assess the potential of created models to simulate and inform the development of bi-beam structures.

5.2 Methods

5.2.1 Analytical model

The critical load at which a bi-beam (slenderness ratio = 33.3), compressed axially, would buckle was calculated using Euler's critical load formula [362].

$$P_{cr} = \frac{n^2 \times \pi^2 \times E \times I}{L_0^2} \quad (5.1)$$

Where E = 63.3 MPa (mean of E_{NF} and E_{TPU} (chapter 4.3.3, Table 4.3) for simplicity of the presented model), beam length L_0 = 38.4 mm, and end condition n = 1.2. The end condition was approximated to represent a pinned condition and account for the initially restricting effect of the slot configuration during the pivoting of the bi-beams' ends. The bi-beam moment of inertia was calculated using:

$$I_x = \frac{w \times t^3}{12} \quad (5.2)$$

where width w_{beam} = 6.72 mm and thickness t_{beam} = 4.8 mm. Change in length at critical load P_{cr} was calculated using Hooke's law equation:

$$\Delta h = \frac{P_{cr} * h_0}{E * A} \quad (5.3)$$

where the bi-beam cross-sectional area is:

$$A = w_{beam} * t_{beam} \quad (5.4)$$

For the calculation of bi-beam deflection during buckling, it is assumed that the buckled shape can be approximated as a circular section. Firstly, half of the central angle φ is approximated numerically using the Newton-Raphson method [372]:

$$\varphi_{n+1} = \varphi_n + \frac{f(\varphi_n)}{f\prime(\varphi_n)} \quad (5.5)$$

where:

$$f(\varphi) = \sin(\varphi) - \frac{h_c}{h_0} * \varphi = 0 \quad (5.6)$$

$$f'(\varphi) = \cos(\varphi) - \frac{h_c}{h_0} \quad (5.7)$$

And the cord length h_c, representing the distance between the endpoints of the beam.

$$h_c = h_0 - \Delta h \quad (5.8)$$

Based on the assumed circular segment representing the shape of the buckled bi-beam, the radius was calculated using:

$$r = \frac{h_c}{2+\sin(\varphi)} \quad (5.9)$$

The sagitta of the circular segment, representing the lateral deflection of the neutral axis of the bi-beams was calculated using:

$$d = r * (1 - \cos(\varphi)) \quad (5.10)$$

Angle φ, radius r, and lateral deflection d were calculated for 13 increments of 1 mm axial compression to estimate bi-beam deformation during buckling. Calculated values were compared to values obtained from video analysis of the experimental compression tests, described in chapter 4.

5.2.2 Numerical model

Bi-beams and plate geometries with the same dimensions as samples used in the experimental testing (chapter 4.4), were created in Creo Parametric (V 9.0.0.0). Ansys Mechanical (via. Workbench, 2020 R2) was used for all further steps of the numerical simulations. Three scenarios (Individual beam, unit cell buckling “out”, and unit cell buckling “in” with a 10 mm gap) of 5.76 mm uniaxial compression (0.15 engineering strain) over 0.109 s (0.83 s^{-1}), 1.09 s (8.3 s^{-1}), and 10.9 s (83 s^{-1}), similar to experimental testing (chapter 4), were simulated. Simulated compression rates were chosen to be similar to compression rates during experimental testing to allow for validation of the numerical model. A static structural solver was set to 200 iterative sub-steps for all simulations. Based on a mesh convergence study, 6 hexahedral elements were seeded through the width of the bi-beams, resulting in 800 elements and 5242 nodes in the meshed model for the individual beam with plates (Fig. 5.1 (A)), and 1600 elements and 3036 nodes for the unit cell with plates (Fig. 5.1 (B)).

Material models for TPU 95A and NinjaFlex, the same materials used for experimental testing, were developed and applied to each side of the simulated bi-beams. Density (ρ), obtained from the materials technical datasheets [368,369], and v, obtained from quasi-static material tests (chapter 4.3), were put in the material model. Multiple material models were trialled, including Linear-elastic, Neo-Hookean, Mooney-Rivlin 5 parameter, and Ogden. A linear-elastic model (Table 5.1) gave the most realistic representation of stiffness at low strain rates, considered most important for buckling behaviour, while keeping computation times manageable.

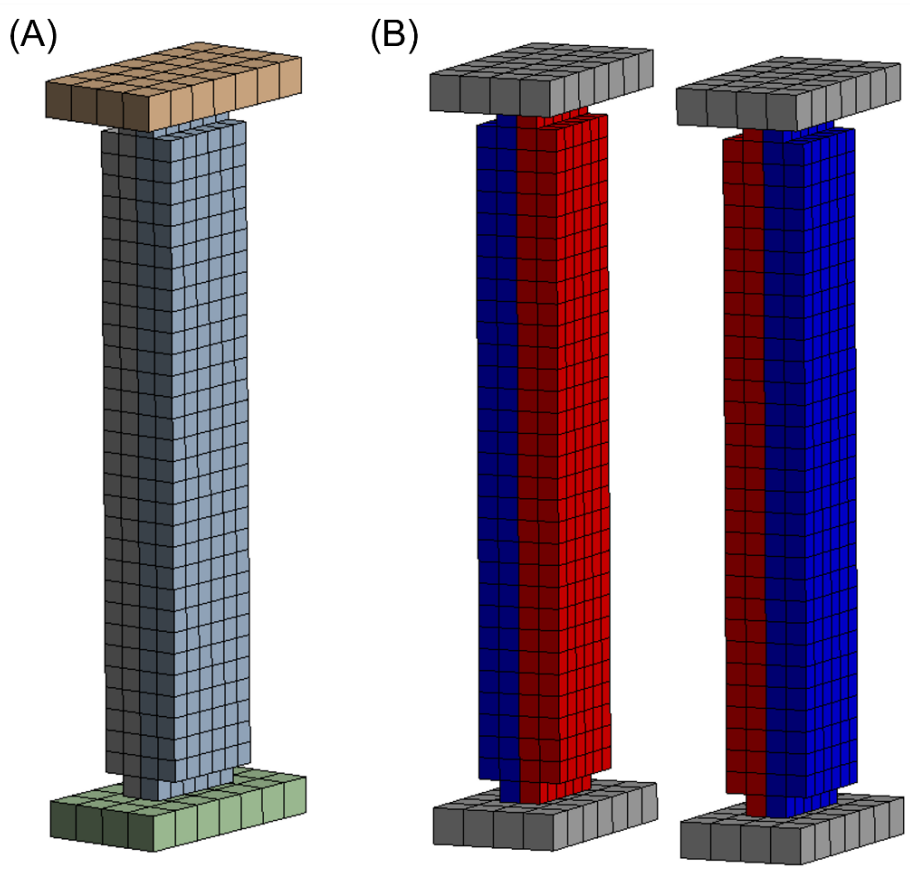

Fig. 5.1: Meshed geometries for (**A**) individual beam and (**B**) unit cell FEA simulations.

Additionally, each material's stress relaxation data was curve fitted to a 6-term Prony series to describe the materials' full viscoelastic response (Fig. 5.2 (C) & (D) & Table 5.2). To ensure the plates had much higher stiffness than the beams and would not deform during simulations, properties of structural steel were assigned.

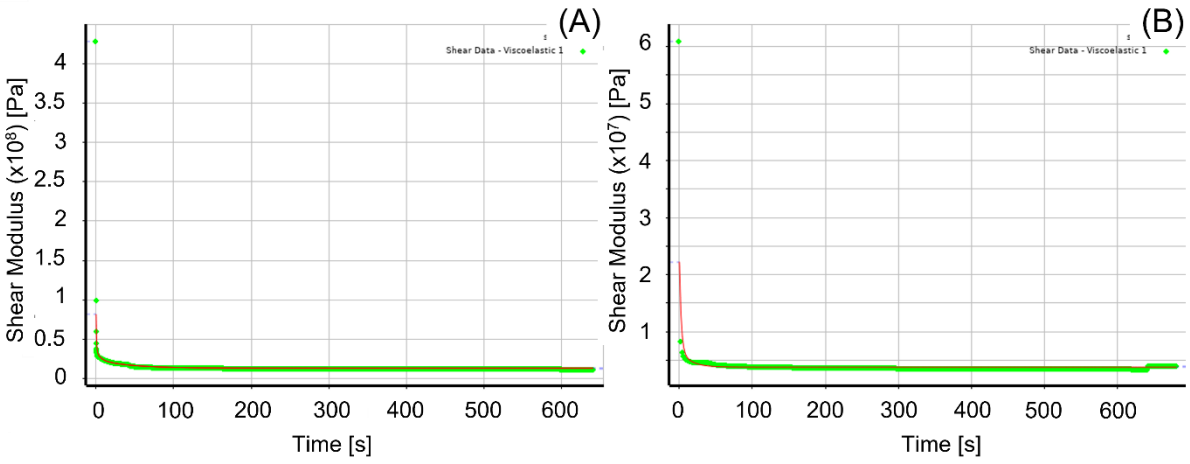

Fig. 5.2: Curve fit for stress relaxation data for (**A**) TPU 95A and (**B**) NinjaFlex. A linear scale time axis was chosen to visualise the curve fitted to relaxation data.

Table 5.1: Linear elastic material parameters used in FEA simulations.

Material	TPU 95A	NinjaFlex
Young's Modulus [MPa]	101.2	24.4
Poisson's ratio v	0.40	0.36

Contact information for all structures was assigned. Individual sides of the bi-beams and all contacts between plates and beams were assigned bonded, to ensure reliable convergence of the model. For the unit cell buckling "in" configuration, contact between the bi-beams was assigned frictional with a friction coefficient of 0.5. Additionally, a pinball radius of 0.2 mm was specified for the touching surfaces of the bi-beams.

Table 5.2: Parameters of the 6-term Prony series for both material models.

	TPU 95A		NinjaFlex	
	Relative Moduli	**Relaxation Time [s]**	**Relative Moduli**	**Relaxation Time [s]**
1	0.03263	347.95	0.10876	3.82
2	0.05213	25.82	0.10817	3.82
3	0.05207	26.10	0.10886	3.82
4	0.05207	25.82	0.10037	3.86
5	0.60623	0.60	0.09322	32.10
6	0.05212	25.82	0.09451	108.30

5.3 Results

5.3.1 Analytical model

Predicted Euler's critical buckling load was 31.5 N. Predicted cord length h_c, central angle φ, radius, and lateral deflection of the neutral axis are shown in Table 5.3 and illustrated in Fig. 5.3. Based on the predicted lateral deflection when a unit cell buckles "in", contact between bi-beams occurs between 0.6 mm and 1.6 mm axial compression. Compared to results from chapter 4, predicted contact occurs at lower compression than what was obtained experimentally.

Comparing lateral deflections predicted by the analytical model to lateral deflections obtained from video analysis (Table 5.4 & Fig. 5.4) shows good agreement between the model and experimental results. However, lateral deflections are slightly overestimated at small compressions and slightly underestimated at higher strains.

Table 5.3: Cord length h_c [mm], half the central angle φ [°], radius [mm], and maximum lateral deflection of the bi-beam neutral axis [mm] as predicted by the analytical model.

h_c [mm]	φ [°]	Radius [mm]	Lat. Deflection [mm]
37.8	17.5	63.0	3.0
36.8	28.8	38.3	4.7
35.8	36.8	29.9	6.0
34.8	43.6	25.3	7.0
33.8	49.5	22.2	7.8
32.8	54.8	20.1	8.5
31.8	59.8	18.4	9.1
30.8	64.4	17.1	9.7
29.8	68.8	16.0	10.2
28.8	73.1	15.1	10.7
27.8	77.1	14.3	11.1
26.8	81.1	13.6	11.5
25.8	84.9	13.0	11.8

Table 5.4: Modelled and measured maximum lateral deflection [mm] for compressive displacement of 0.6 mm to 5.6 mm.

h_c [mm]	Deflection (model) [mm]	Deflection (measured) [mm]
37.8	3.0	1.3
36.8	4.7	3.6
35.8	6.0	6.7
34.8	7.0	8.3
33.8	7.8	9.1
32.8	8.5	9.9

Fig. 5.3: Predicted beam shape based on analytically predicted values.

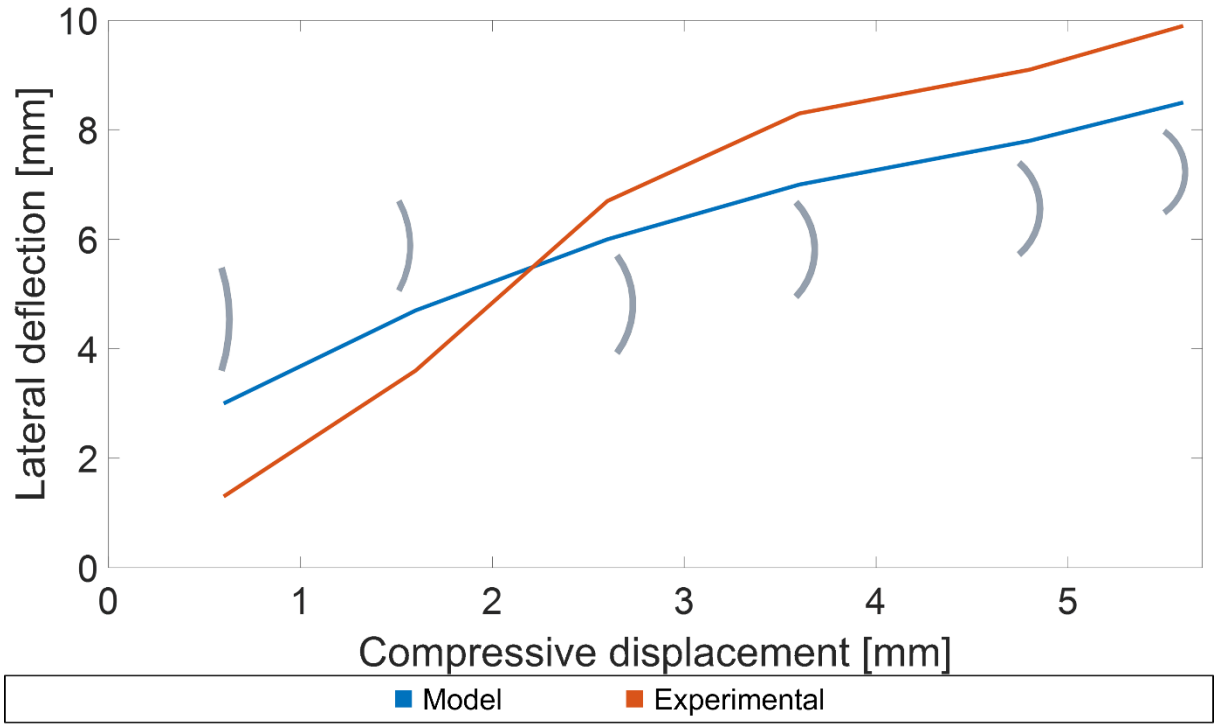

Fig. 5.4: Lateral deflection [mm] vs. compressive displacement [mm] of bi-beams during uniaxial compression obtained from the analytical model and from DIC of test video footage.

5.3.1 Numerical model

Simulations of individual bi-beams show a stark increase in forces up to an axial compression of 1.3 mm (~0.3 engineering strain), which is where the beam started buckling. Exceeding 1.3 mm compression, the force levels of the buckling beam started plateauing until the maximum compression of 5.76 mm (0.15 engineering strain) was reached (Fig. 5.5 & Fig. 5.6). Maximum forces were increased by 22 - 35% in no-contact scenarios and increased by 43 – 64% for buckling “in” scenarios. Work was increased by 32 – 43% in no-contact scenarios and increased by 37 – 52% for buckling “in” scenarios (Table 5.5). Maximum forces were similar to the maximum forces measured during the experimental compression testing (Section 4.4.3, Table 4.4). Despite bi-beams bonded to the compression plates in simulations, a similar buckling mode as during the experimental testing was obtained (Fig. 5.5) due to the 1.2 mm cut-outs at both ends of a bi-beam.

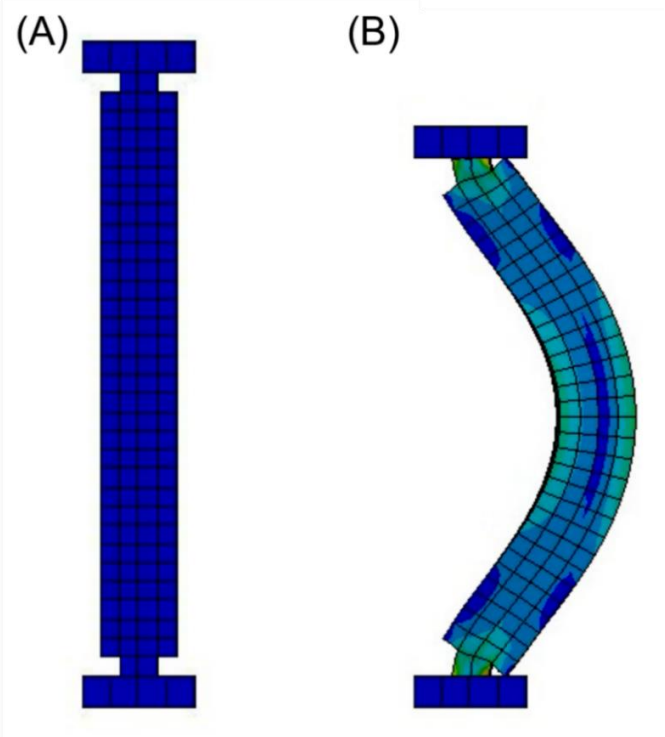

Fig. 5.5: Simulated deformation of an individual bi-beam compressed axially to an engineering strain of 0.15 (5.76 mm) (**A**) before compression and (**B**) at maximum strain.

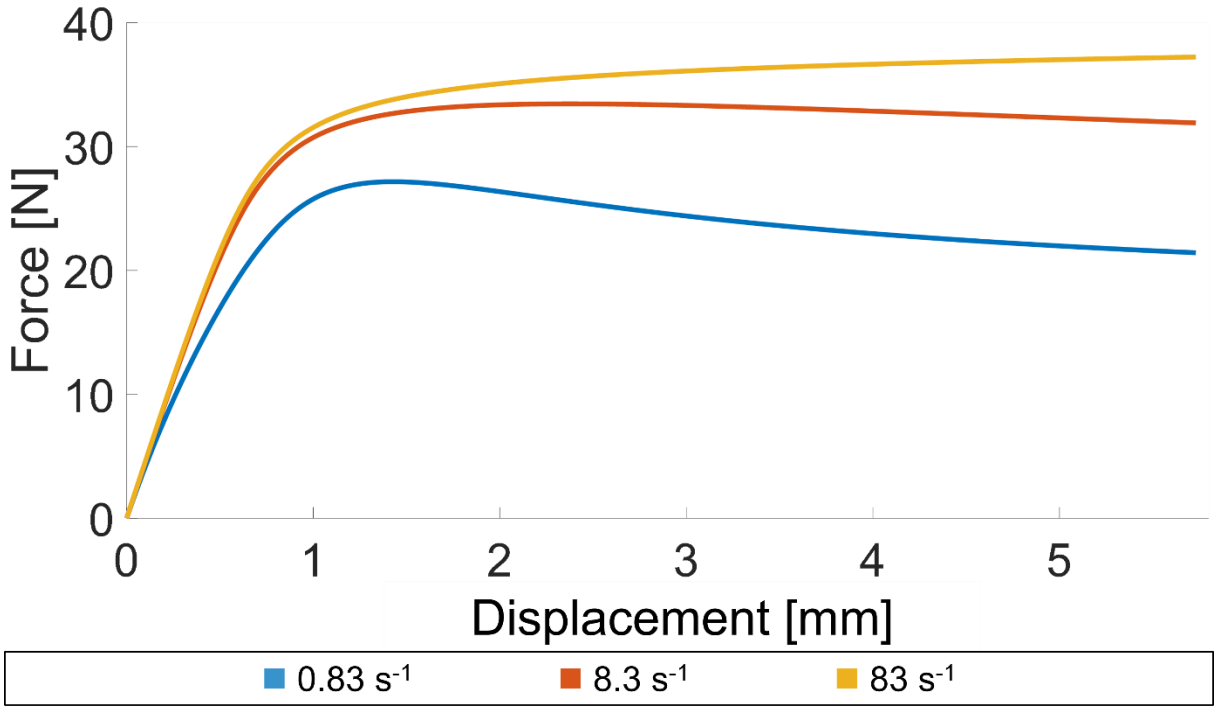

Fig. 5.6: Force [N] vs. displacement [mm] traces for numerical simulations of an individual bi-beam compressed axially to an engineering strain of 0.15 (5.76 mm) at 0.83 s^{-1}, 8.3 s^{-1}, and 83 s^{-1}.

Table 5.5: Maximum force [N] and work done [mJ] for all scenarios simulating 5.76 mm axial compression.

	Strain rate	**Maximum force [N]**	**Work [mJ]**
Individual beam	0.83 s^{-1}	28.47	137.2
	8.3 s^{-1}	34.77	181.8
	83 s^{-1}	38.56	196.9
Unit cell - Out	0.83 s^{-1}	56.93	274.5
	8.3 s^{-1}	69.55	363.5
	83 s^{-1}	77.11	393.8
Unit cell - In	0.83 s^{-1}	180.18	498.5
	8.3 s^{-1}	258.58	685.3
	83 s^{-1}	295.28	759.8

Simulations of bi-beam unit cells (Fig. 5.7) show rate dependence (i.e., lower strain rate results in lower forces), similar to the individual bi-beam simulations. As there was no interaction between bi-beams of a unit cell when bi-beams buckled “out” (Fig. 5.7 (B)), simulated forces and deformations of one bi-beam are identical to the individual bi-beam simulations. Maximum forces were similar to the maximum forces obtained

during experimental testing (Fig. 5.8, Fig. 5.9 (A) & Table 5.5), however, the observed drop in forces after buckling during experimental testing is not seen in the simulated results (Fig. 5.9 (A)).

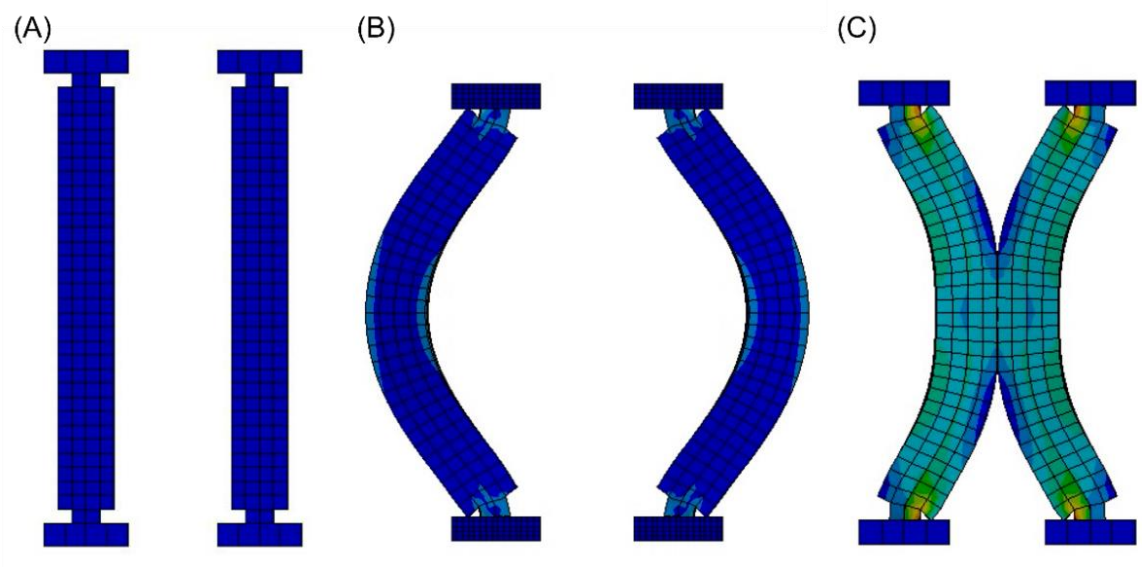

Fig. 5.7: Simulated deformation of a bi-beam unit cell compressed axially to an engineering strain of 0.15 (5.76 mm) (**A**) before compression, (**B**) buckling "out", and (**C**) buckling "in".

When bi-beams buckled “in” (Fig. 5.7 (C)), axial forces started increasing further when contact was made between the bi-beams (Fig. 5.8) around 2.75 mm compression (0.07 engineering strain). At maximum compression of 5.76 mm (0.15 engineering strain), the force vs. displacement trace did not yet reach a peak, in contrast to experimental results where forces decreased after reaching a second peak (Fig. 5.9 (B)). After initial contact, the deformation of bi-beams was symmetrical (Fig. 5.7 (C)) and did not result in deformations seen in experimental testing.

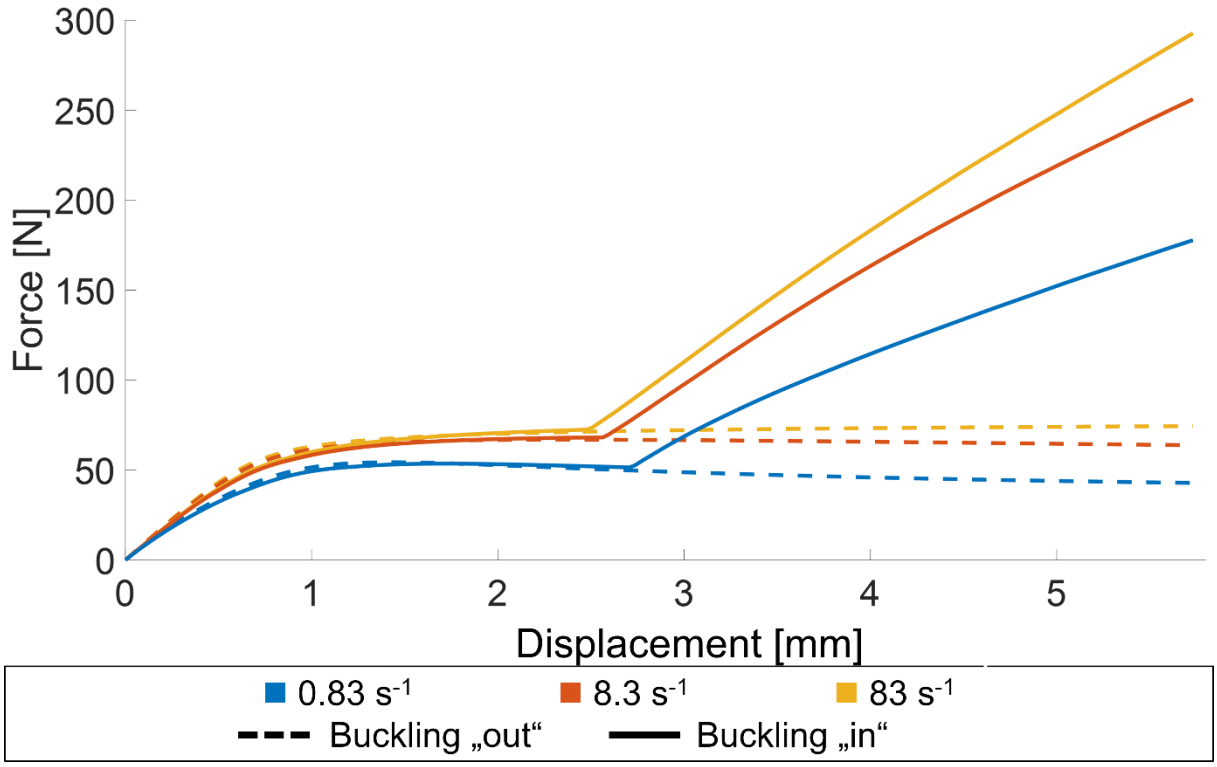

Fig. 5.8: Force [N] vs. displacement [mm] traces from numerical simulations of bi-beam unit cells buckling "out" (dashed lined) and "in" (solid line) during axial compression to an engineering strain of 0.15 (5.76 mm) at 0.83 s^{-1}, 8.3 s^{-1}, and 83 s^{-1}.

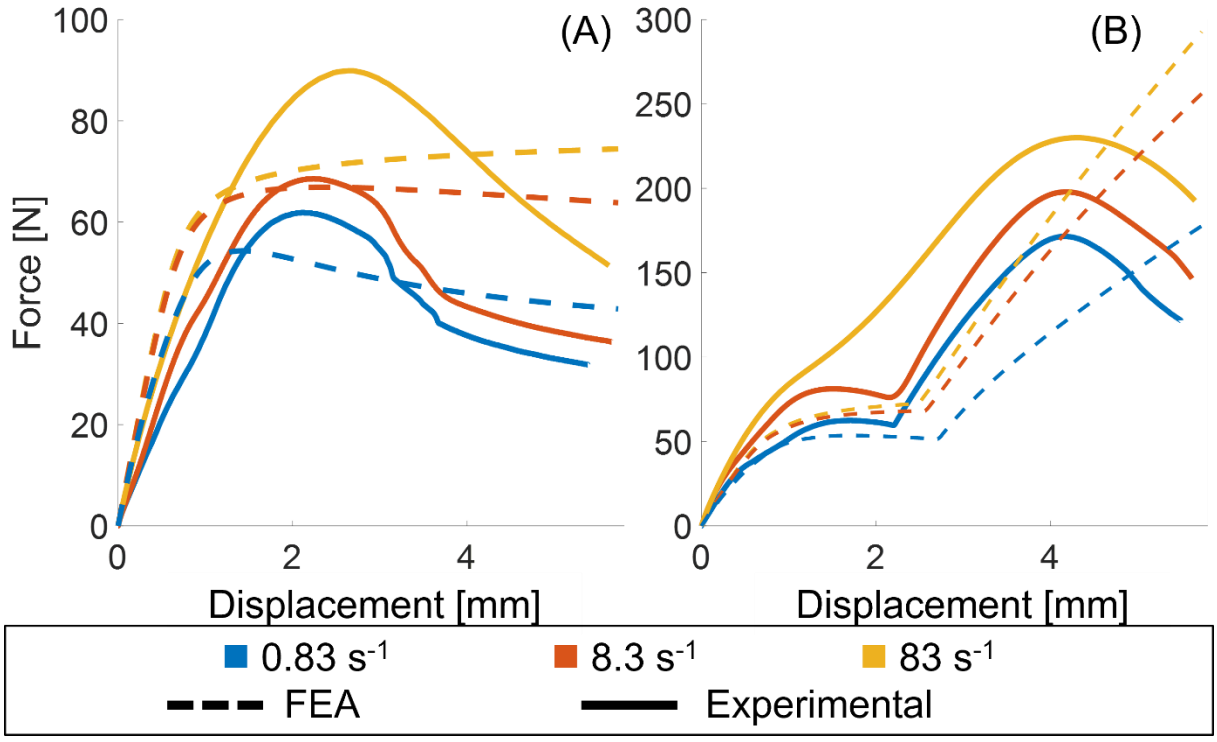

Fig. 5.9: Force [N] vs. displacement [mm] traces from numerical simulations (dashed line) and experimental testing (solid line) (**A**) buckling “out” and (**B**) buckling “in” during axial compression to an engineering strain of 0.15 (5.76 mm) at 0.83 s^{-1}, 8.3 s^{-1}, and 83 s^{-1}.

5.3 Discussion

Estimating the behaviour of a bi-beam structure prior to experimental testing can inform design choices depending on the expected impact scenarios. Calculated Euler's critical load gave a realistic force level for buckling (Difference of 0.9 N (2.8%) and 3 N (10.5%) when compared to experimental and numerical results, respectively). It can provide an estimate for maximum stiffness of a bi-beam as forces decrease once the bi-beam is buckling. Further, it provides an understanding of the forces required to initiate buckling deformation. However, due to the slenderness ratio of the bi-beam, the use of the Rankine-Gordon formula should be considered. Predicting the lateral deflection allows to estimate at what compressive displacement the bi-beams in a unit cell buckling "in" make contact, leading to a further increase in stiffness. The gap between bi-beams in a unit cell is determining the point of compression at which stiffness is abruptly increased. Hence, estimating the compression at which bi-beams make contact can aid the design and development process.

Characteristics, such as compressive displacement at peak force and curve shape, of force vs. displacement traces of the numerical simulations of all three loading conditions are similar in shape to the ones obtained from experimental testing (chapter 4.4, Fig. 5.9). Obtained forces are similar to the forces obtained from experimental uniaxial compression tests.

The linear elastic material models were based on the results of the material characterisation described in chapter 4.3. Various material models, meshes, solvers, and numbers of iteration steps have been trialled. A linear elastic model was chosen because it achieved a good fit with the experimental results, while hyperelastic material models underestimated stiffness at low strains by a factor of 2 – 3. Bonding the bi-

beams to the compression plates was required to ensure consistent convergence of the numerical model. Restricting the bi-beams from pivoting, as seen during experimental testing, could have an influence on obtained results. When unit cells were designed to buckle “in” and compress towards each other, contacts and deformations were symmetrical between the two bi-beams. Contact between bi-beams during experimental testing resulted in each bi-beam buckling in two points and a folding-like, large contact area situation. Further work on a numerical model could include solutions to simulate this kind of deformation.

5.4 Conclusion

An analytical model to predict bi-beam behaviour during compression can be used to inform design choices for bi-beam metamaterial structures, while requiring no material expenses or computational time. Further, this chapter demonstrates the potential for numerical analysis to further understanding and predict the behaviour of the bi-beam metamaterial structure.

5.5 Chapter summary

This chapter utilised insights gained from chapter 4 to model uniaxial compression tests of bi-beams and unit cells. Firstly, an analytical model to calculate critical buckling load and lateral deflection during compression was derived and compared to experimental results. Secondly, numerical models were created and compared to experimental results.

The analytical model, described above, estimates Euler's critical buckling load and lateral deflection of bi-beams during buckling. These parameters can be used to inform design choices, such as constituent material stiffness and the gap between two bi-

beams, before conducting more time-consuming mechanical testing or numerical simulations.

Created FE models, detailed in this chapter, produced force vs. displacement traces and axial forces similar to the ones obtained from experimental testing. Presented models can be used for further assessing and developing bi-beam structures, and to trial different designs and material properties.

6. Chapter – Bi-beam cellular structure for impact applications

6.1 Introduction

Chapters 4 and 5 highlighted an abrupt switch in stiffness, based on bi-beam buckling direction and resulting contact situation, within a unit cell. This response to axial compression suggests potential of bi-beam structures to create an adaptable response to impact events and be further developed into a cellular mechanical metamaterial structure for impact protection. Insights on bi-beam structures, gained from experimental testing and modelling, can be used to inform design decisions such as the dimensions, constituent material stiffness, and the gap between bi-beams. A cellular sheet structure, as would be required for impact applications, can be constructed by multiple unit cells, orientated to each other. There are some uncertainties around buckling behaviour of multiple unit cells within one structure, as post-buckling effects are often a-periodic and assumptions from a single unit cell cannot be applied to a whole sheet structure. This section describes compression tests of cellular structures of bi-beams.

All testing of bi-beams described previously (chapter 4.4) was carried out using an Instron universal testing machine (Electropuls E3000, 5kN load cell). While allowing for consistently repeatable test conditions, this also restricted displacement speeds to machine limits. Further, out-of-plane motion was not possible. To assess the potential of bi-beam cellular structures to be used in impact protection, insights on compressive behaviour during strain rates representative of impacts are required. This section details how multiple unit cells, orientated to each other to form a cellular sheet

structure, were impacted at various speeds (and energies) ranging up to strain rates representative of impact scenarios.

A controllable buckling reaction is required for the material to be efficient in impact applications. Bi-beam buckling direction, in some test conditions, was inconsistent and not predictable. Various factors such as glueing bi-beam samples to plates, increased strain rates, and shelf life of filaments and adhesives could have had an influence on the impact response of the bi-beams. An investigation, similar to the testing described in chapter 4.4, could provide insights into potentially influencing factors of inconsistent buckling behaviour.

The objectives of this chapter were to:

- Assess compression behaviour of cellular structures compared to unit cells.
- Test cellular structures at compression rates representative of impact scenarios and without restricting out-of-plane deformations.
- Investigate the influence of bi-beam and study design choices on the buckling direction during compression.

6.2 Methods

6.2.1 Uniaxial compression of bi-beam cellular structures

Two different configurations (Fig. 6.1 (A)) of multiple bi-beam unit cells (4) were tested in uniaxial compression. 3D-printed sandwich plates with slots for the bi-beams in different locations, made from tPLA, were clamped to the Instron machine's compression plates (Fig. 6.1 (B)). No new bi-beams were produced for this testing and the bi-beams used were previously tested in chapter 4.4.

Configurations of the cellular structure testing were either all bi-beams buckling “out”, for a compliant response during compression, or all bi-beams buckling “in” with a 10 mm gap, for a high-stiffness response during compression. Bi-beam structures were compressed to 0.15 engineering strain (5.76 mm displacement) at strain rates of 0.83 and 83 s^{-1} (0.53 and 53 mm/s), similar to the experimental testing of individual unit cells.

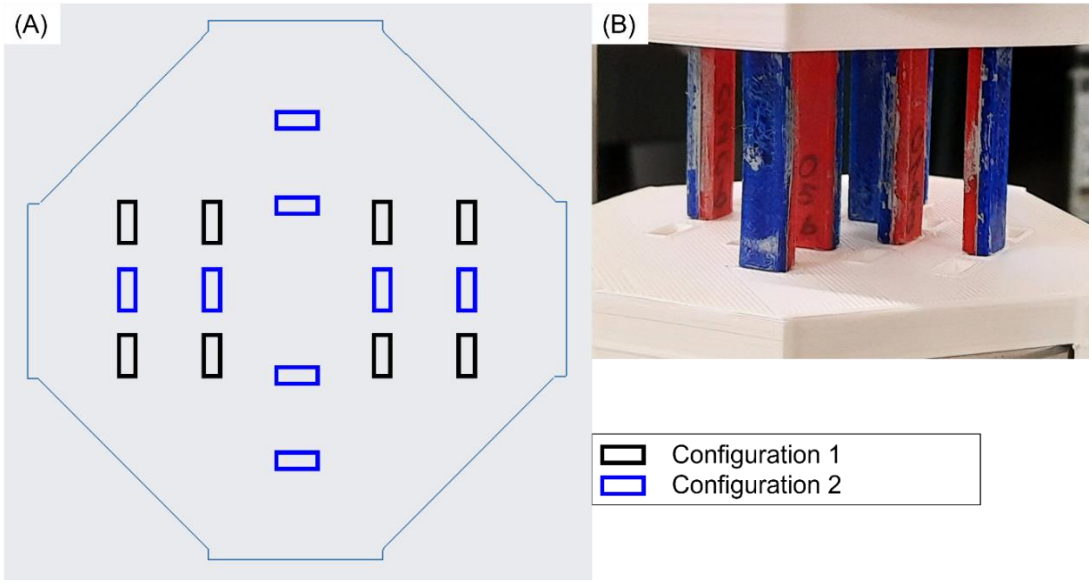

Fig. 6.1: (**A**) Bi-beam unit cell configurations (config. 1 - black, config. 2 - blue) on the sandwich plate and (**B**) configuration 2, buckling “in”, loaded into the Instron test machine.

6.2.2 Impact tests of cellular structures

Cellular sheet structures consisting of 4 bi-beam unit cells (Fig. 6.2 (B)), similar to configuration 2 (Fig. 6.1 (A)) were fabricated for impact tests. Bi-beams were glued to additively manufactured sandwich plates (tPLA, thickness 2 mm) using a silicone adhesive (Sil-Poxy™, Smooth-On, Inc.) and arranged for buckling “in” and “out” scenarios, respectively. The top plate of the sheet structure was attached to an impactor mass of 2136 g and dropped onto a force plate (Kistler Type 9257BA) (Fig. 6.2 (A)) measuring force in vertical direction at 20,000 Hz. Informed by the results from section 4.4, drop heights were 20, 40, and 60 cm resulting in impact velocities of 1.98,

2.8, and 3.43 m/s and impact energies of 4.27, 8.55, and 12.82 J, respectively. Each impact scenario was repeated 5 times resulting in 30 impacts using a total of 240 newly manufactured bi-beams. A high-speed camera (Phantom Miro R311, Vision Research Ltd., Bedford, UK) filming at 2,000 fps was set up at a distance of 60 cm from the impacted sample. Vertical force [N] and time [s] were obtained from force plate data. Compressive displacement [mm] of the top plate was obtained using digital image correlation (GOM Correlate, 2019 Hotfix 7, Rev. 128764, Build 2020-06-18).

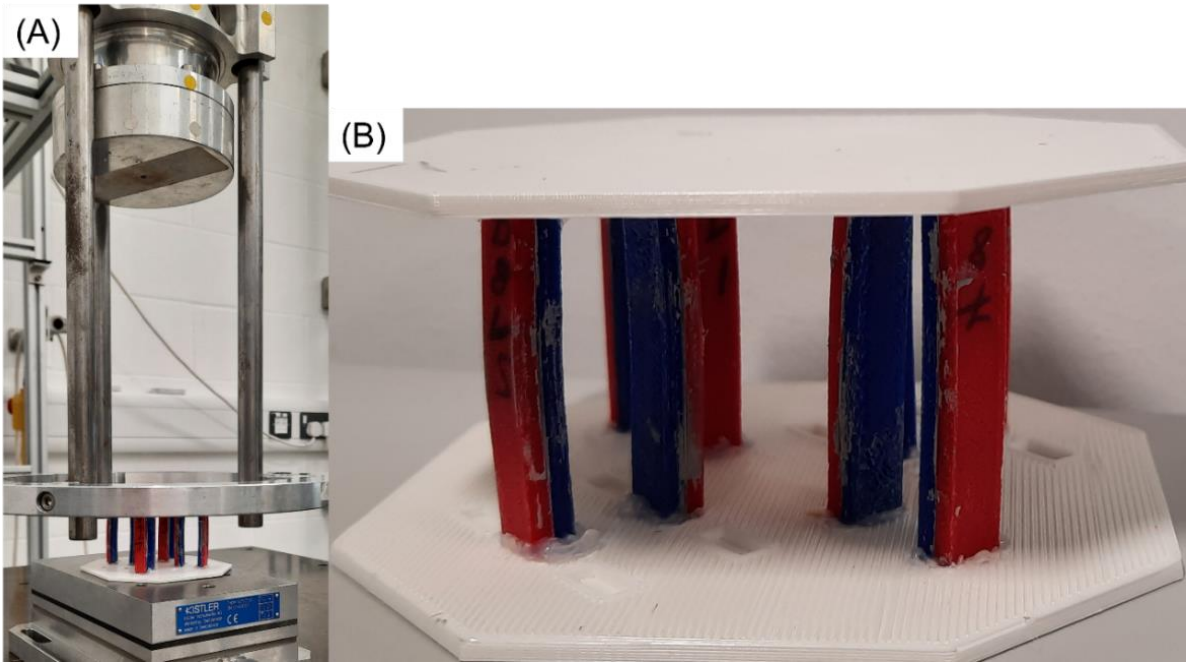

Fig. 6.2: (**A**) Drop test setup and (**B**) cellular structure in buckling "Out" configuration.

6.2.3 Validation of bi-beam buckling direction

Ten bi-beams that were previously buckled during the impact testing described in section 6.2 were chosen for additional compression testing. Selected bi-beams were axially compressed between plates clamped into an Instron universal testing machine (Electropuls E3000, 5kN load cell) to an engineering strain of 0.15 (5.76 mm), similar to testing in section 4.4. Compression rates of 0.83 s^{-1}, 8.3 s^{-1}, and 83 s^{-1} (0.53, 5.3, and 53 mm/s) were tested and bi-beam orientation was switched after each test, resulting in 6 trials for each sample. 60 axial compression tests were carried out in

total, and the order of test parameters was randomised for each bi-beam. A camera (Phantom Miro R311, Vision Research Ltd., UK; resolution 1280 x 800 pixels; lens, Nikon AF Nikkor 24 – 85 mm) was set up at 500 mm from compressed bi-beams. Buckling direction during all trials was recorded and force vs. displacement data was obtained from the Instron machine.

6.3 Results

6.3.1 Uniaxial compression of bi-beam cellular structure

Uniaxial compression of a sheet structure, consisting of four bi-beam unit cells, did result in a similar switch in material stiffness as observed for an individual unit cell (Fig. 6.3). All bi-beams buckled in the predicted direction for all four test scenarios (Fig. 6.4). When buckling “out”, forces at 0.15 engineering strain were reduced to 40 to 50% of the peak force (Table 6.1 & Fig. 6.3). When buckling “in”, a second increase can be seen in the force vs. displacement trace (Fig. 6.3) and peak forces are increased by 68 to 125% (Table 6.1). Increasing compression rate increased compressive stiffness and, hence, measured forces by 30 to 70%. Similar to the individual unit cell, the transition to the second increase in force when bi-beams buckled “in” was less pronounced at a higher compression rate (Fig. 6.3). No consistent difference between peak forces was found between the two tested unit cell configurations and differences in peak forces were below 9% for all four test scenarios (Table 6.1).

Table 6.1: Peak force [N] for both unit cell configurations and buckling conditions for 0.83 s^{-1} and 83 s^{-1} compression rates.

	0.83s^{-1} (0.53 mm/s)	**83 s^{-1} (53 mm/s)**
Config. 1 – Out	477.7	559.4
Config. 1 – In	801.3	1244.9
Config. 2 – Out	441.3	600.4
Config. 2 – In	787.3	1349.3

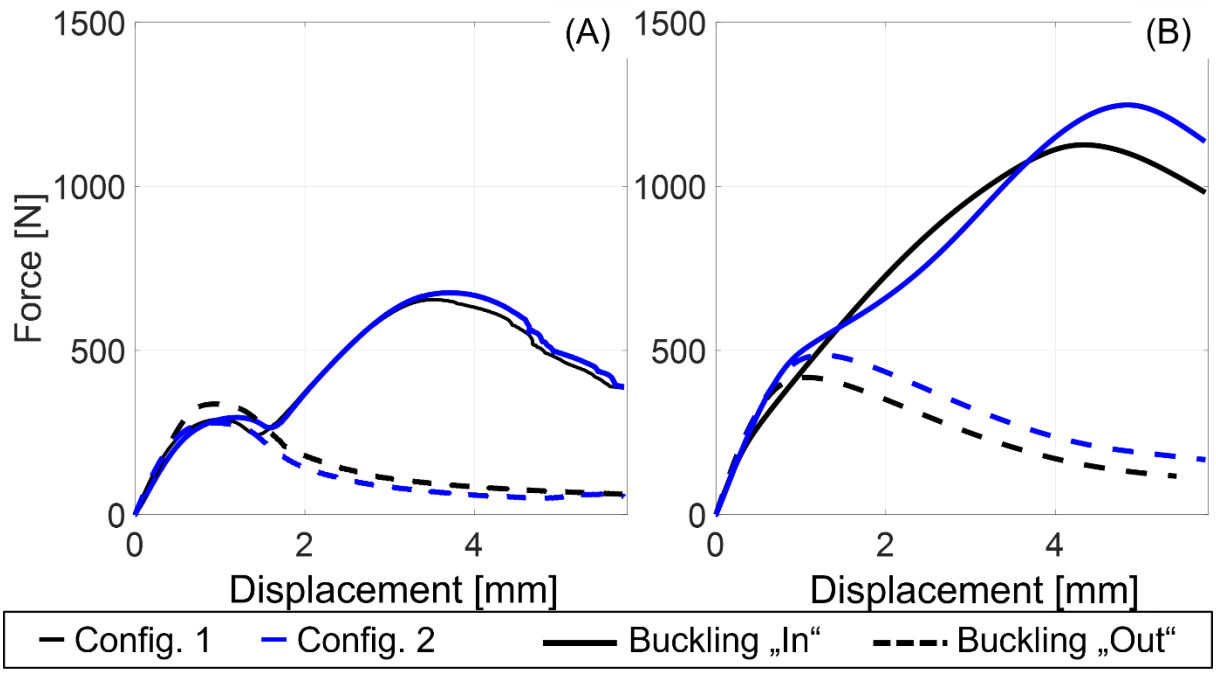

Fig. 6.3: Force [N] vs. displacement [mm] traces for both unit cell configurations and buckling conditions for (**A**) 0.83 s^{-1} and (**B**) 83 s^{-1} compression rates.

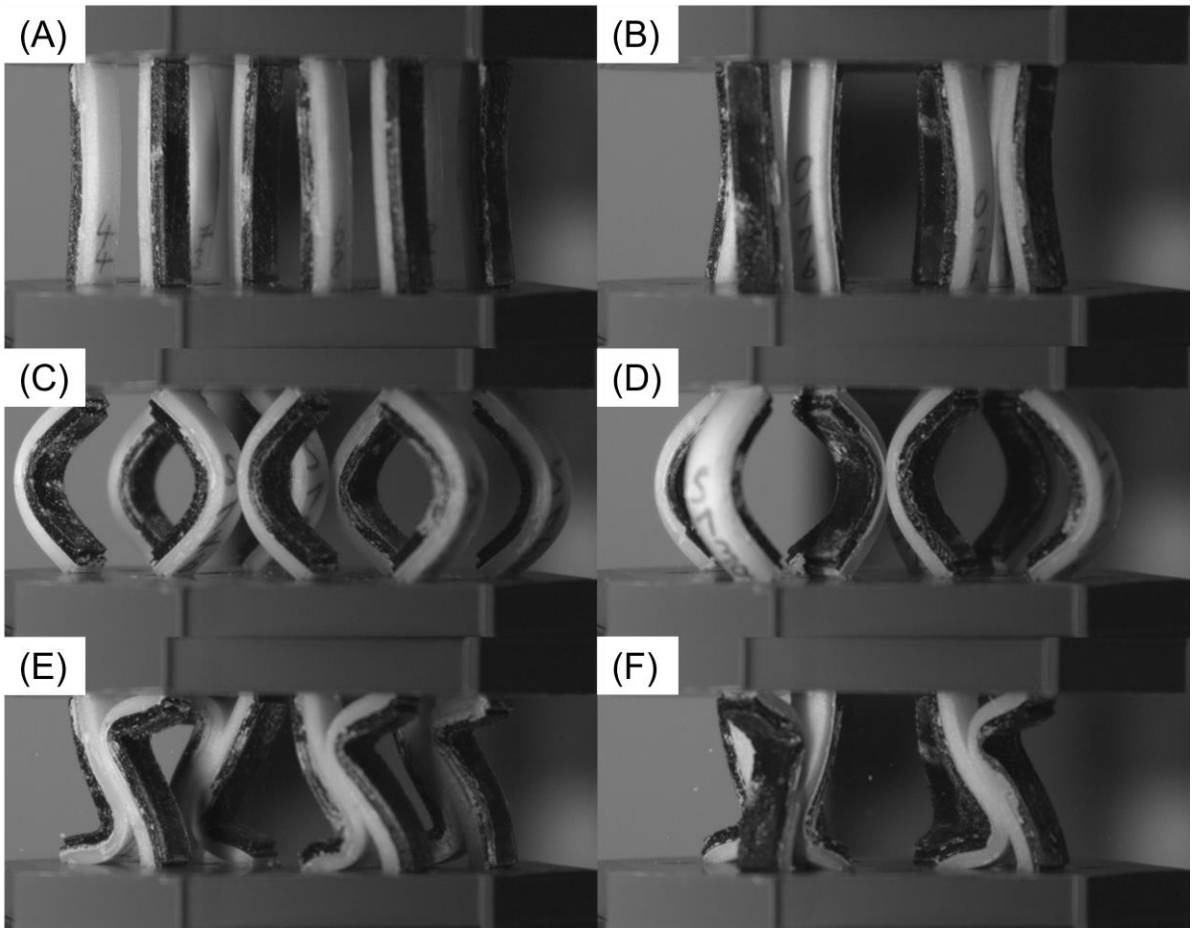

Fig. 6.4: (**A, C & E**) Configuration 1 and (**B, D & F**) configuration 2 sheet structures consisting of four bi-beam unit cells while (**A & B**) uncompressed, (**C & D**) at 0.15 compressive strain while buckling “out” and (**E & F**) at 0.15 compressive strain while buckling “in”.

6.3.2 Impact tests of cellular structures

Resulting contact situations for individual unit cells were as predicted in only 30% of scenarios for 20 cm, 37.5% for 40 cm, and 10% for 60 cm. With increasing drop height and respective impact energy, the direction of buckling became more consistent, however, in the opposite direction as predicted (towards NinjaFlex beam).

During these impacts, the contact situation in each unit cell appears random. So, the post buckling response is described based on the number of contacting unit cells (Fig. 6.5). The shape of force vs. time traces changes depending on the number of contacting unit cells. No-contact scenarios (Fig. 6.5 (B)) show an initial peak, followed by a 10-15 ms period of increased forces, resulting in 20 – 25 ms impact durations (Fig. 6.6 & Appendix 4). Unit cells contacting during impact (Fig. 6.5 (C) & (D)) causes a second increase in forces after the initial peak (Fig. 6.6 & Appendix 4). Maximum forces, compressive displacement, and impact durations increased with an increasing drop height of the impactor. Maximum forces increased while compressive displacement and impact duration decreased with an increasing number of contacting unit cells (Fig. 6.6, Table 6.2 & Appendix 4).

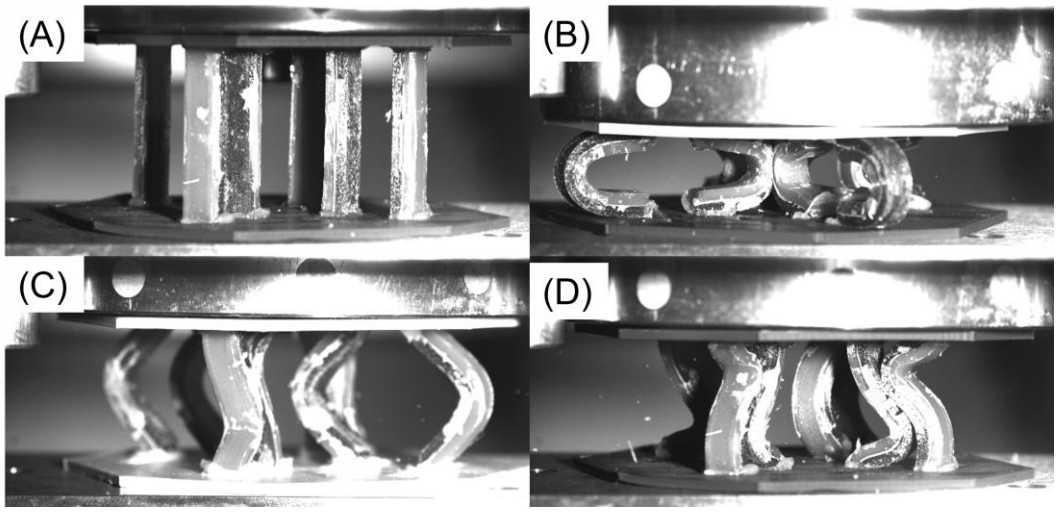

Fig. 6.5: Structures consisting of four unit cells during impact (**A**) uncompressed and in maximum compression for (**B**) all four unit cells buckling “out”, (**C**) both contact situations, and (**D**) all four unit cells buckling “in”.

Table 6.2: Maximum force, maximum displacement, and impact duration for all three drop heights and grouped based on the amount of contacting unit cells during impact.

		Max. Force [N]	Max. Displacement [mm]	Impact duration [ms]
20 cm	< 2	1830.8 (± 76.1)	4.4 (± 0.4)	10.3 (± 0.8)
	> 2	1822.5 (± 49.9)	4.0 (± 0.2)	8.9 (± 0.5)
40 cm	< 2	2167.9 (± 138.9)	9.8 (± 1.4)	21.3 (± 4.1)
	> 2	2202.3 (± 330.7)	8.0 (± 2.6)	12.8 (± 3.8)
60 cm	< 2	2261.2 (± 83.0)	20.13 (± 2.2)	28.4 (± 0.8)
	> 2	2721.2 (± 738.2)	7.9 (± 0.6)	13.0 (± 1.4)

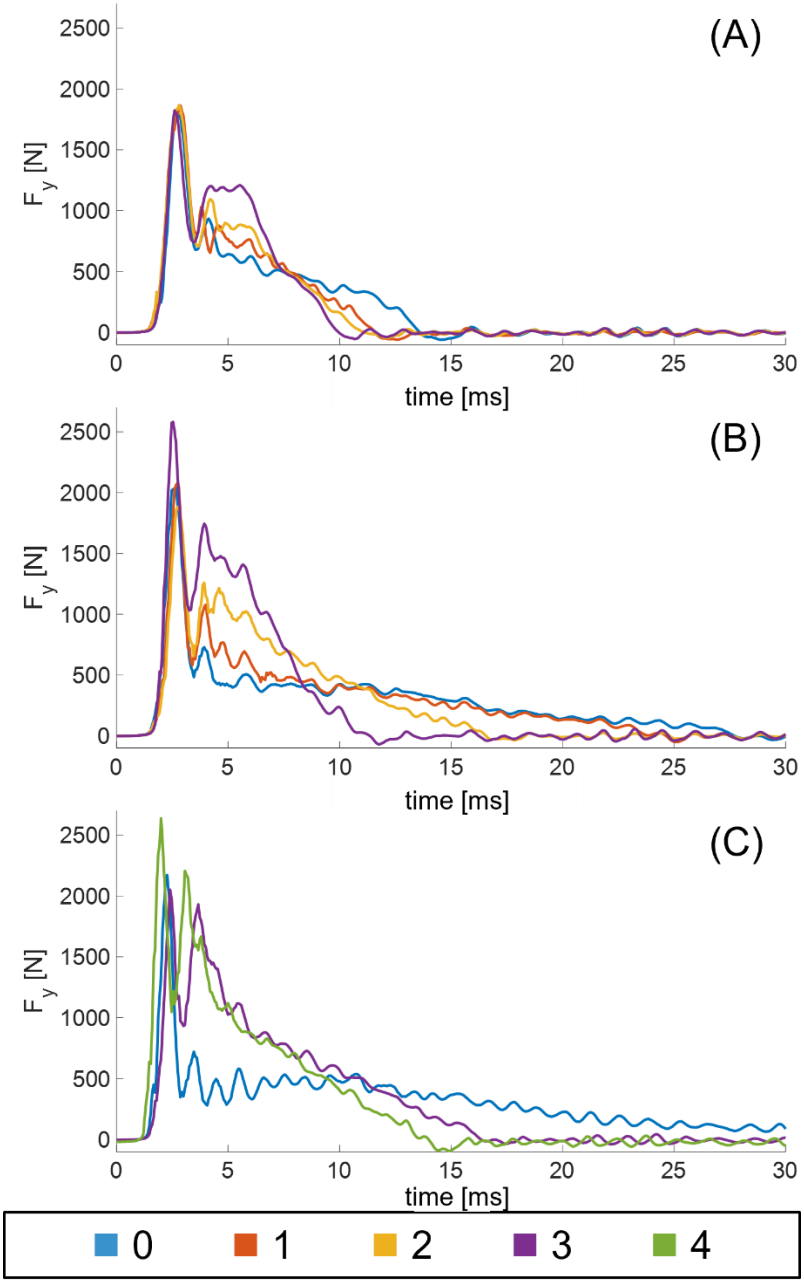

Fig. 6.6: Force [N] vs. time [ms] traces for impacts onto cellular structures consisting of four bi-beam unit cells from a drop height of (**A**) 20 cm, (**B**) 40 cm, and (**C**) 60 cm. Line colour represents the number of unit cells making contact during compression.

6.3.3 Validation of bi-beam buckling direction

Bi-beams buckled towards the TPU 95A beam in 58 out of 60 tests (~ 97%). The two occasions of buckling towards the NinjaFlex beam were for the same bi-beam, compressed at a strain rate of 83 s^{-1} (53 mm/s) at both orientations. Initial deformation during compression is shown in Fig. 6.7 for the individual beam compressed by the Instron machine (Fig. 6.7 (A – C)) and during impact tests (Fig. 6.7 (D – F)). Compression rate had a similar effect on the force vs. displacement curve as described in chapter 4.4.3. Force vs. displacement traces were similar in magnitude and shape to the results shown in chapter 4.4.3 (Appendix 5).

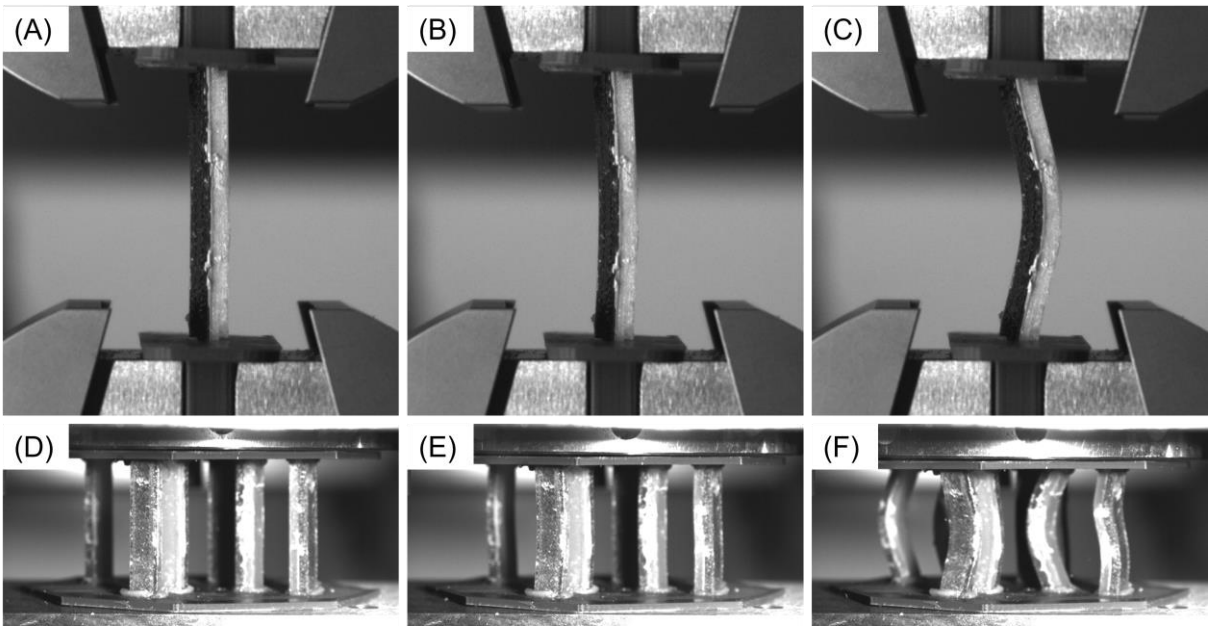

Fig. 6.7: Stills of initial deformation during compression of (**A - C**) individual bi-beam, compressed using the Instron test machine, and (**D - E**) a bi-beam cellular structure during impact tests.

6.4 Discussion

After reaching the critical buckling load, the buckling direction of bi-beams was as predicted during all uniaxial compression tests. However, the beams were buckled in previous testing (chapter 4.4) which could have affected subsequent buckling. Changes in stiffness due to strain rate that were observable in the compression test

data of individual bi-beams can also be seen in the compression test data of bi-beam cellular structures (i.e. increasing stiffness with changing buckling behaviour and increasing compression rate). The configuration of bi-beam unit cells did not make a notable difference in compression behaviour, suggesting that increasing the number of unit cells and various configurations are feasible. However, only one compression test for each of the two configurations and strain rates was carried out and results should be considered cautiously.

During impact testing the buckling direction of bi-beams was not predictable. Some changes were required to the experimental set up, to facilitate the impact testing, (i.e., glueing bi-beams to plates). While Bi-beams could still pivot in place for similar deformation, these changes introduced an influence on buckling direction that may have been larger than the difference in material stiffness. Consequently, the described test setup is not feasible to ensure desired buckling directions in impact applications and further design work is required. This inconsistency in buckling direction was unexpected since Janbaz et al. [44] achieved reliable buckling despite material imperfections and out-of-plane compression, and testing described in chapter 4.4 and chapter 6.2.1 (Fig. 6.4) were consistent and predictable.

Analysing collected data, based on the occurring contact situations during impact, shows differences in force vs. time traces (Fig. 6.6). The first, buckling, peak in force was generally the same for all samples. No contact within bi-beam unit cells then generally created a compliant material response to compression, whereby force reduced after buckling. Between ~5 and 10 ms, impact force was lower for the non-contacting than the self-contacting samples, resulting in lower energy absorption for the non-contacting samples during the first ~10ms. When self-contact occurred, a second force increase was seen. So, after ~10 ms, force was then higher for the non-

contacting samples, because less of the impact energy had been absorbed. Presented results and force vs. time curves suggest that a change in impact response occurs when the contact situation of bi-beam unit cells changes. Designing the bi-beam metamaterial structure to be applied as a helmet liner and tested according to the method described in chapter 3 could give further insights into the efficacy of each buckling scenario for head injury prevention.

During testing in the Instron machine, the buckling direction of bi-beams, which buckled unpredictably during testing described in chapter 6.2.2, was again predictable (~ 97%). Differences in initial deformation can be seen when visually comparing the initial deformation of bi-beams during machine testing with impact testing (Fig. 6.7). Impacted (glued) beams start a bending deformation from the onset (Fig. 6.7 (D – F)) rather than compressing prior to reaching Euler's critical buckling load, as seen for the machine compressed (non-glued) bi-beams (Fig. 6.7 (A – C)). Further, during impact testing the buckling mode for some of the glued beams is different (i.e. fixed end condition – initially no pivoting) (Fig. 6.7 (F)). This suggests a change in end conditions for the buckling bi-beam, caused by the glueing. These observations and the consistency in buckling behaviour suggest that neither filament, adhesive shelf life, nor imperfections due to the manufacturing process were influencing buckling behaviour during impact tests. While the Instron test machine cannot produce displacement speeds high enough to replicate impact scenarios (maximum speed ~55 mm/s, while all impacts were > 2,000 mm/s), findings described in chapter 4.3 suggest that no increase in strain rate would switch the order of stiffness between the two constituent materials. So, the silicone adhesive used to attach the bi-beams to the top and bottom plates (and needed to hold the unit cell together before the drop tests), is the most likely cause of the unpredictable buckling direction.

6.5 Conclusion

Unit cell deformation during compression remains similar when they are periodically arranged as a larger cellular structure, suggesting an increase in stiffness proportional to the increasing number of unit cells. Inconsistency in buckling direction requires further investigation, and must be addressed before a bi-beam cellular structure can be used in a real-world impact application. No contact between constituent bi-beams resulted in a relatively compliant response, while stiffness increased with an increasing number of unit cells buckling in, suggesting that the desired effect of adaptable stiffness is still present at impact strain rates.

Inconsistency in buckling direction of bi-beams during impact testing is likely caused by the assembly method. When compressing bi-beams axially, without pre-loading and additional adhesives, buckling behaviour is predictable. Future work requires alternative methods for the assembly of the cellular structure.

6.6 Chapter summary

This chapter utilised insights gained from chapters 4 and 5 to gain further understanding of cellular structures comprising bi-beam unit cells and their potential for application in impact protection. Cellular structures were fabricated and compressed mechanically at various strain rates. Further, a follow-up study, investigating inconsistencies in buckling behaviour, was conducted to explain findings.

Compression tests of cellular structures show that the stiffness of a cellular structure scales proportionally to the number of unit cells it comprises. When tested at strain rates representative of impact events, system stiffness changes depending on the number of unit cells buckling towards each other (i.e., increasing stiffness and decreasing impact duration), suggesting an adaptable response to compression during

impact. Buckling behaviour was inconsistent and not predictable during impact testing. A validation study, compressing bi-beams used during impact tests in a mechanical test machine, suggests that inconsistencies in buckling behaviour were caused by the adhesive that was necessary for the assembly of the cellular structure.

7. Chapter – Overall Discussion

7.1 Introduction

The aim of this programme of research was to contribute to the prevention of concussions from head impacts in ice hockey. The developed free-fall drop test method (Chapter 3) replicates common head impacts in ice hockey, and requires less laboratory equipment than other test methodologies in peer-reviewed literature [104]. This facilitates improved access to representative testing and may form a prerequisite to certification standards [18–20]. The investigated mechanical metamaterial (Chapters 4 – 6), with adaptable stiffness properties, may improve protection during compliant collisions without compromising protection during the most severe head impacts – falls onto the ice.

This research was motivated by peer-reviewed literature (Chapter 2) which suggests that concussion rates in ice hockey are high [24–26,46], and symptoms commonly persist beyond the typical time for recovery [4,5]. The most common cause for clinical concussions is collisions between players on the ice where the head hits a relatively compliant body [30,31]. Certification standards currently do not consider compliant surface impacts [18–20] and helmets are not designed for that kind of impact scenario [32,33]. Consequently, players are susceptible and concussion rates remain high while most other head injuries are currently less common [12,25,47].

This chapter summarises the findings of this programme of research in relation to each specified objective, as well as the primary contributions to knowledge, practical implications, limitations, potential areas for further research and overall conclusions.

7.2 Research objectives outcomes

7.2.1 Objective One: Review published literature regarding concussions in ice hockey, designs and materials for helmets and impact protection, and helmet testing.

This was achieved in Chapter Two through a review of peer-reviewed literature within the field of concussions and injury mechanisms, helmet and head impact testing, and designs and materials for helmets and impact protection.

Peer-reviewed literature suggests that concussion rates in ice hockey are still at a high level despite a general decline in head injuries [14,24–26]. Most concussions are caused by player-to-player collisions, with the head impacting a compliant structure, rather than in a severe fall onto the ice where the head impacts this rigid surface [30,31]. Currently, certification standards do not consider impact scenarios other than falls [18–20], and other test protocols, described in peer-reviewed literature, require extensive laboratory equipment [104,168]. Further, helmets offer only limited protection during collisions, due to limited helmet liner compression [32,33]. Conventional materials can only absorb energy effectively within a defined range respective to the material [36]. The range of commonly injurious head impacts in ice hockey is too wide for one conventional material to protect effectively. Engineered materials, in particular the investigated rate-dependent bi-beam mechanical metamaterial with adaptable buckling behaviour [44], may offer energy absorption properties that could enhance helmets during collisions without compromising protection during falls.

Further research into test methods that allow a representative but simplified characterisation of a helmet's impact protection could facilitate widespread testing. This would in turn expand the knowledge on helmets and allow further developments.

A mechanical metamaterial with adaptable stiffness behaviour depending on the occurring impact [44], which has not been tested for impact applications, may help in reducing concussion rates in ice hockey and other sports without risking more serious injuries from more severe impacts. Consequently, work in described fields to protect players better and reduce injury rates was warranted.

7.2.2 Objective Two: Develop a method to replicate common head impacts in ice hockey for helmet testing.

Work undertaken in achieving this is described in Chapter Three, which details the development of a free-fall drop test method with interchangeable impact surfaces to replicate concussive head impacts in ice hockey.

This included dropping an instrumented headform, helmeted and unhelmeted, from a height of 1 m onto impact surfaces of different compliance and orientation. The obtained kinematic responses of the headform were used to assess helmet performance during different impacts and compared to a representative dataset of concussive head impacts in ice hockey [104]. A test configuration (45° anvil and 48 mm of EVA foam layer) was determined to replicate kinematics which are typical of a concussive collision type head impact in ice hockey. All commercially available helmets tested in this study provided decreased protection during more compliant surface impacts and differences were found between different helmets. A subsequent reliability study of the test method suggests excellent reliability (ICCs > 0.95).

This study suggests that a free-fall drop test method can produce kinematic responses similar to the method currently used in academic research [104,168]. The simplified test setup may facilitate a test protocol to assess ice hockey helmets that can be adopted by a wider range of research facilities. Further, the use of different compliance

impact surfaces may facilitate modifications to current certification standard test protocols.

7.2.3 Objective Three: Investigate the potential of a bi-beam design to create an adaptable response in deformation and stiffness to compression.

This was achieved in Chapter Four, which details the principle of a rate-dependent mechanical metamaterial with adaptable stiffness properties that are dependent on the impact scenario [44], and Chapter Five, detailing the modelling of these bi-beam structures. The metamaterial is comprised of bi-beam structures that exhibit a variable buckling behaviour as determined by the initial deformation rate.

This included a material characterisation of additively manufactured TPU materials that were used to fabricate prototype samples for further testing. Optimal print settings were determined in an iterative process, while material parameters, required to design bi-beams and create material models for simulations, were obtained through various material tests. Further, bi-beams and unit cells (comprising two bi-beams orientated to each other) were compressed uniaxially at different strain rates. Occurring buckling deformations and contact situations within unit cells suggest an adaptable response to different compression rates and the metamaterials' potential to be used in impact applications.

Further, bi-beam stiffness and deformation were modelled using an analytical and numerical approach. Both models were validated against results from experimental testing. These models are a time and cost-effective method to aid the design and evaluation of bi-beam structures.

Findings suggest that bi-beam prototype samples could be additively manufactured, however, strain rate-dependence was not considered. Further, the abrupt switch in stiffness, based on buckling behaviour, and consequential either stiff or compliant response to compression may be beneficial in impact applications where a wide range of impacts is expected, such as ice hockey helmets.

7.2.4 Objective Four: Develop and critically evaluate a mechanical metamaterial sheet, comprising bi-beam structures, to be used as an adaptive helmet liner for ice hockey helmets.

This was achieved in Chapter Six, which details the mechanical testing of cellular structures, comprising bi-beam unit cells, at various strain rates.

Cellular structures were compressed in a universal test machine, and subsequently positioned on a force plate and impacted using a drop rig. Due to inconsistent buckling behaviour during impact tests, where the assembly method had to be modified, a validation study was carried out. Impacted bi-beams were compressed in a test machine where consistent buckling was observed again.

Findings suggest that a cellular structure, comprising bi-beams, can be developed by arranging unit cells relative to each other between two stiff sandwich plates. Sheet stiffness increases proportionally to the number of unit cells.

7.3 Contribution to knowledge

This programme of research makes several contributions to the body of knowledge within the field of impact protection and concussion prevention through helmets in sports, specifically ice hockey.

First, a novel test method to replicate common head impacts in ice hockey has been developed. This method, as described in Chapter 3, comprises an instrumented

headform dropped from a height of 1 m onto impact surfaces of different compliance and with different orientations. It has been shown that by adapting the compliance and orientation of the impacted surface, kinematic responses representative of various commonly injurious head impacts (i.e., falls and collisions) can be replicated. Previously, extensive laboratory equipment and a designated test rig for each impact scenario were required [104,168].

This programme of research has also contributed to the body of knowledge regarding a mechanical metamaterial, comprising bi-beam structures, that provides an adaptable compression response depending on the impact scenario (Chapters 4 – 6). Through elimination of rate dependence on buckling direction, described in Chapter 4, it has been shown that the associated contact situation within a unit cell, can cause an abrupt switch in stiffness in axial direction. The same effect was observed in Chapter 6 when multiple unit cells were orientated to each other between two stiff sandwich plates to deform simultaneously during compression without making contact with each other, suggesting that the metamaterial can be scaled to create a sheet layer that can react differently to different impact scenarios. Further, the analytical and the numerical model described in Chapter 5 obtained similar results as mechanical testing, suggesting that future design steps can be carried out computationally, reducing time and material expenditure.

7.4 Practical applications

The primary contributions to knowledge of this programme of research offer practical applications in a range of fields, including head impact and helmet testing, and design of personal protective equipment such as ice hockey helmets.

7.4.1 Head impact and helmet testing

Current ice hockey helmet certification standards test “shock absorption” of helmets with a linear guided drop test onto a rigid polymer surface – representing falls onto the ice [18–20]. While this test protocol helped in nearly eliminating catastrophic injuries from the sport, it does not consider the whole range of commonly injurious head impacts in ice hockey. As discussed in Chapter 2.3, helmet testing described in peer-reviewed literature is inconsistent and a thorough analysis of a helmet’s impact protection capabilities requires extensive laboratory equipment [104,168], which is often not available to researchers. The findings outlined in Chapter 3 suggest that it is possible to replicate various head impact scenarios with a drop-test method by adapting the compliance and orientation of the impacted surface.

Interchangeable surface compliance may facilitate modifications to certification standards. Test protocols could remain mostly unchanged with the exception of the orientation and the compliance of the impacted surface. This simple and feasible adaptation could allow certification standards to incorporate a wider range of head impact scenarios without affecting the repeatability of tests, required for certification testing. More thorough certification procedures would also put pressure on manufacturers to design and produce helmets that provide protection for a wider range of impacts.

Increased helmet testing carried out in academic research generates increased insights and understanding of helmet design, the efficacy of materials and material combinations, and prevention strategies for head injuries. The developed test method utilises laboratory equipment which is available to most researchers with an interest in impact protection. Enabling more researchers to carry out representative head impact

and helmet testing opens up the field, facilitates more testing, that in turn will increase understanding.

7.4.2 Impact protection and injury prevention

Currently, commercially available ice hockey helmets protect well against the impacts that they are designed for – falls onto the ice and against the surrounding boards. However, protection during the most common concussive scenario (~93% player-to-player collisions), has been shown to be limited [32,33]. Impact energy absorption of cellular solids, which are typically used for helmet liners, relies on material compression [36]. Ice hockey helmet liners are designed to be stiff to allow for compressive deformation without bottoming out during the most severe impacts. Consequently, they don't compress sufficiently to absorb energy when a more compliant body is impacted [32,33]. Conventional liner materials can only be effective within a certain impact range. This range is insufficient to protect against all commonly injurious head impacts in ice hockey [32,33]. Multilayer foam [40,41] and shear-thickening polymers [42,43] are typically used in current helmets to increase impact protection but with limited success. This programme of research investigated the potential of a strain rate-dependent mechanical metamaterial (Chapters 4 – 6). The adaptable stiffness properties [44] of this engineered material structure has potential to provide enhanced protection during compliant surface impacts without compromising protection during rigid surface impacts.

The investigated sheet structure, comprising bi-beam unit cells, can achieve an abrupt switch in axial stiffness dependent on the bi-beam buckling direction and resulting contact situation within unit cells, as described in Chapter 4. This effect can be utilised to achieve optimised compressive properties for two different impact scenarios. Consequently, impact protection for applications where a wide range of impacts is

expected, such as ice hockey, could achieve enhanced protection against an additional cause of injury – collisions – without compromising the performance in the scenario the helmets are currently designed for – falls. An analytical and a numerical model of the bi-beam design have both obtained similar results as mechanical testing. These findings, depicted in Chapter 5, suggest that it is possible to utilise computational approaches to design and further develop the investigated bi-beam metamaterial.

Obtained results from testing of cellular bi-beam structures (Chapter 6) show that axial stiffness increases proportionally to the number of unit cells when sandwich plates possess high stiffness. Further, bi-beam dimensions are scalable in size provided the geometric aspect ratio is maintained. This suggests that adaptable stiffness properties are achievable for a wide range of shapes and sizes. Consequently, sheet layers of the investigated bi-beam metamaterial, assessed for their potential as helmet liners, can be developed for a wide range of impact protection equipment.

7.5 Limitations

Several limitations have been identified in each chapter of this programme of research. Four aspects warrant further consideration which are discussed in this section.

Firstly, the test method developed during this programme of research and described in Chapter 3 includes several limitations. The headform's kinematic responses were validated against a dataset of laboratory-recreated head impacts [104], as in-field head injury data is not publicly available. Despite being considered the best available estimate, a dataset of in-field measured concussive head impacts in ice hockey would increase confidence in findings. Further, possible degradation of the EVA foam, which was used to produce increasingly compliant impact surfaces, over time or after multiple impacts was not controlled. It is assumed that the material recovered between impacts

and no degradation effect influenced measurements, however, this is an aspect of the test method that could be controlled in future work. Using an anthropomorphic headform always includes limited biofidelity. Even though the Hybrid III headform is widely used and accepted, additional anthropomorphic headforms or a skin surrogate to increase the helmet-headform interface's biofidelity could be considered when using the method.

Second, the design of bi-beams, as detailed in Chapter 4, included limitations due to time and material constraints. The two constituent materials did not switch order of stiffness at any of the tested strain rates. While a proof-of-concept was achieved in this programme of research, the investigated mechanical metamaterial relies on a rate-dependent switch of buckling direction to enable real-world application. Further, the positioning of bi-beams between sandwich plates, while suitable for this programme of research, is not feasible for application in protective equipment. During the machine testing, the thin end of the bi-beams was fitted into rectangular cavities on the sandwich plates, which were held in position by the Instron machine. During the subsequent impact testing (Chapter 6), bi-beams were glued into the sandwich plate's cavities so the structure would not collapse. Neither method of assembly is feasible for a system that will have to endure multiple impacts or cannot be set up individually before every impact.

Third, the mechanical testing of Chapter 4 and 6 (Bi-beams, unit cells, and cellular structures) with the Instron machine was carried out to an axial compressive engineering strain of 0.15. This strain was chosen to replicate the experimental testing from previous work [44]. However, during impact testing of cellular structures, the compressive strain exceeded 0.15 in all tests of medium and high impact energy. Applied into a piece of protective equipment, compressive strains are likely to also

exceed the 0.15 engineering strain during more severe impacts. Consequently, not having test data from the experimental axial compression of bi-beams beyond an engineering strain of 0.15 is a limitation of this programme of research.

Finally, the FE model, informed by findings and results detailed in Chapter 4 and described in Chapter 5, obtained similar forces and a similar abrupt switch in stiffness as the experimental testing. However, the linear-elastic material model only represents the constituent materials' stiffness at low strains. Further, in the FE model, the bi-beams were bonded to the sandwich plates. This was necessary to ensure consistent convergence of the model, however, it did not allow the bi-beams to pivot in the same way that was seen in the mechanical testing of Chapters 4 and 6.

7.6 Future research

Several areas of further research have been highlighted through this programme of research.

First, the presented drop test method uses a free-fall drop test rig (Chapter 3). A reliability study suggests excellent reliability; however, an analysis of high-speed video footage suggests that it is difficult to consistently impact the same location at the same orientation. A guided drop test rig, equipped with a cradle to hold the headform, may increase repeatability and consistency of impacts. A guided drop test is also used in certification standards, and using similar equipment would increase the feasibility of modifications to standard procedures. Future research, assessing if a guided drop test obtains similar results when impacting a compliant surface, could make the test method adoptable more widely.

Second, the bi-beams, introduced in Chapter 4, tested in this programme of research were prototypes, designed specifically for the conducted studies. As discussed in the

previous section, introducing strain rate-dependence as the mechanism to switch buckling direction is an essential step towards using the mechanical metamaterial in impact protection equipment. Further, the connection between bi-beams and stiff sandwich plates requires more development for a connection that recovers to its original state after compression while still allowing the bi-beams to pivot and maintain the desired mode of buckling. Further work may focus on the design of bi-beams to create a structure that could be applied to a multi-impact piece of protective equipment.

Third, the bi-beam testing carried out in this programme of research (Chapters 4 and 6) assessed only one material combination and axially compressed the structure to a strain of 0.15 to obtain a proof-of-principle. Further, no out-of-plane testing or assessment of angular acceleration attenuation was done. Testing a wider range of material combinations and the effect on axial stiffness, shear behaviour, as well as compressing bi-beams further to assess whether a buckling-out effect occurs during the most severe impacts could provide a wider understanding of the structure's response to different impacts. Further research may focus on more extensive testing to fully understand behaviour in all potentially occurring impact scenarios. As presented in Chapter 5, these investigations could be aided by using FE analysis to save on time and material expenditure. Furthermore, implementing the metamaterial structure in a helmet system and following the test protocol detailed in Chapter 3, could provide further evidence that a bi-beam metamaterial could be used within ice hockey helmets.

Finally, the FE analysis in this programme of research (Chapter 5) suggests that it is feasible to utilise numerical analysis for the development and design of the bi-beam metamaterial. Further research could expand the work that was carried out with FE analysis to assess cellular structures of multiple unit cells, create material models from

testing with higher strain rates, and analyse impact scenarios that are more representative of ice hockey head impacts.

7.7 Conclusions

The findings of this programme of research demonstrate an improved test method which could make helmet testing more widely available and advance current understanding of head impacts. In addition, this programme of research contributes to improvements in helmet performance, as well as the creation of a metamaterial structure that may protect effectively against a wider range of impacts. It has been shown that a simplified test setup can be used to create head impact scenarios that are representative of real-world injurious head impacts in ice hockey. Further, a proof-of-concept for a mechanical metamaterial with adaptable stiffness response, dependent on strain rate, has been obtained. This programme of research contributes to pathways that may help to obtain a better understanding of helmet technologies and to better protect players against a wider range of common head impacts. Both are assumed to contribute to reducing concussion incidences and making participation safer without altering how the game is played.

8. Chapter – References

1. Langlois JA, Rutland-Brown W, Wald MM. The epidemiology and impact of traumatic brain injury: A brief overview. J Head Trauma Rehabil. 2006;21(5).

2. Sussman ES, Pendharkar A V., Ho AL, Ghajar J. Mild traumatic brain injury and concussion: terminology and classification. 1st ed. Vol. 158, Handbook of Clinical Neurology. Elsevier B.V.; 2018. 21–24 p.

3. McCrory P, Meeuwisse W, Dvořák J, Aubry M, Bailes J, Broglio S, et al. Consensus statement on concussion in sport—the 5th international conference on concussion in sport held in Berlin, October 2016. Br J Sports Med. 2017;51(11).

4. McAllister T, McCrea M. Long-Term cognitive and neuropsychiatric consequences of repetitive concussion and head-impact exposure. J Athl Train. 2017;52(3).

5. Bailes JE, Petraglia A I., Omalu B i., Nauman E, Talavage T. Role of subconcussion in repetitve mild brain injury. J Neurosurg. 2013;119(November).

6. Manley G, Gardner AJ, Schneider KJ, Guskiewicz KM, Bailes J, Cantu RC, et al. A systematic review of potential long-term effects of sport-related concussion. Br J Sports Med. 2017;51(12).

7. Guskiewicz KM, Marshall SW, Bailes J, Mccrea M, Harding HP, Matthews A, et al. Recurrent concussion and risk of depression in retired professional football players. Med Sci Sports Exerc. 2007;39(6).

8. Chrisman SPD, Richardson LP. Prevalence of diagnosed depression in adolescents with history of concussion. J Adolesc Heal. 2014;54(5).

9. Prien A, Grafe A, Rössler R, Junge A, Verhagen E. Epidemiology of Head Injuries Focusing on Concussions in Team Contact Sports: A Systematic Review. Sport Med. 2018;48(4).

10. A. Shaw J. A Review of the Incidence of Head Injuries in Football, Baseball, Ice Hockey, and Cycling. Am J Sport Sci. 2019;7(1).

11. Elaison P, Black A, Richmond S, Babul S, Pike I. Evidence Summary: Ice

Hockey. Act Safe Cent BC Inj Res Prev Unit Vancouver. 2018;(February).

12. Benson BW, Meeuwisse WH. Ice Hockey Injuries. Epidemiol Pediatr Sport Inj. 2005;49.

13. McKay CD, Tufts RJ, Shaffer B, Meeuwisse WH. The epidemiology of professional ice hockey injuries: A prospective report of six NHL seasons. Br J Sports Med. 2014;48(1).

14. Pauelsen M, Nyberg G, Tegner C, Tegner Y. Concussion in ice hockey - A cohort study across 29 seasons. Clin J Sport Med. 2017;27(3).

15. Caron JG, Bloom GA, Johnston KM, Sabiston CM. Effects of multiple concussions on retired national hockey league players. J Sport Exerc Psychol. 2013;35(2).

16. Hiploylee C, Wennberg R, Tator CH. The financial toll of career-ending concussions in professional hockey. Concussion. 2016;1(4).

17. Donaldson L, Li B, Cusimano MD. Economic burden of time lost due to injury in NHL hockey players. Inj Prev. 2014;20(5).

18. EN ISO 10256 - 2:2018, 2018, “Protective equipment for use in ice hockey - Part 2: Head protection for skaters”, BSI Standards Publication.

19. ASTM Standard F1045 - 22, “Standard Performance Specification for Ice Hockey Helmets”, ASTM International, West Conshohocken, PA, 2022, DOI:10.1520/F1045-22, www.astm.org.

20. Canadian Standards Association. (2009). Casques de hockey sur glace (CAN/CSA Standard No. Z262.1-09).

21. Hoshizaki TB, Brien SE, Bailes JE, Maroon JC, Kaye AH, Cantu RC. The science and design of head protection in sport. Neurosurgery. 2004;55(4).

22. Whyte T, Stuart CA, Mallory A, Ghajari M, Plant DJ, Siegmund GP, et al. A review of impact testing methods for headgear in sports: Considerations for improved prevention of head injury through research and standards. J Biomech Eng. 2019;141(7).

23. Hoshizaki TB, Post A, Oeur RA, Brien SE. Current and future concepts in helmet

and sports injury prevention. Neurosurgery. 2014;75(4).

24. Nezwek TA, Lee CS. Concussion in the NHL : Where Do We Stand ? J Orthop Res Ther. 2016;2016(2).

25. Van Pelt KL, Puetz T, Swallow J, Lapointe AP, Broglio SP. Data-Driven Risk Classification of Concussion Rates: A Systematic Review and Meta-Analysis. Sport Med. 2021;51(6).

26. Kuhn AW, Solomon GS. Concussion in the National Hockey League: a systematic review of the literature. Concussion. 2016;1(1).

27. Adams R, Li AY, Dai JB, Haider S, Lau GK, Cheung KP, et al. Modifying Factors for Concussion Incidence and Severity in the 2013-2017 National Hockey League Seasons. Cureus. 2018;10(10).

28. Wennberg RA, Tator CH. Concussion incidence and time lost from play in the NHL during the past ten years. Can J Neurol Sci. 2008;35(5).

29. Izraelski J. Concussions in the NHL: A narrative review of the literature. J Can Chiropr Assoc. 2014;58(4).

30. Hutchison MG, Comper P, Meeuwisse WH, Echemendia RJ. A systematic video analysis of National Hockey League (NHL) concussions, part I: Who, when, where and what? Br J Sports Med. 2015;49(8).

31. Hutchison MG, Comper P, Meeuwisse WH, Echemendia RJ. A systematic video analysis of National Hockey League (NHL) concussions, part II: How concussions occur in the NHL. Br J Sports Med. 2015;49(8).

32. Clark JM, Post A, Hoshizaki TB, Gilchrist MD. Protective Capacity of Ice Hockey Helmets against Different Impact Events. Ann Biomed Eng. 2016;44(12).

33. de Grau S, Post A, Meehan A, Champoux L, Hoshizaki TB, Gilchrist MD. Protective capacity of ice hockey helmets at different levels of striking compliance. Sport Eng. 2020;23(1).

34. Clark JM, Connor TA, Post A, Hoshizaki TB, Gilchrist MD. The influence of impact surface on head kinematics and brain tissue response during impacts with equestrian helmets. Sport Biomech. 2019;00(00).

35. Post A, Hoshizaki TB, Karton C, Clark JM, Dawson L, Cournoyer J, et al. The biomechanics of concussion for ice hockey head impact events. Comput Methods Biomech Biomed Engin. 2019;22(6).

36. Gibson LJ, Ashby MF. Energy absorption in cellular materials. Cellular Solids. 2014. 309–344 p.

37. Gimbel G, Hoshizaki T. Compressive properties of helmet materials subjected to dynamic impact loading of various energies. Eur J Sport Sci. 2008;8(6).

38. Bird ET, Bowden AE, Seeley MK, Fullwood DT. Materials selection of flexible open-cell foams in energy absorption applications. Mater Des. 2018;137.

39. Clark JM, Hoshizaki TB, Gilchrist MD. Protective capacity of an ice hockey goaltender helmet for three events associated with concussion. Comput Methods Biomech Biomed Engin. 2017;20(12).

40. Piland SG, Gould TE, Jesunathadas M, Wiggins JS, McNair O, Caswell S V. Protective helmets in sports [Internet]. Materials in Sports Equipment. Elsevier Ltd; 2019. 71–121 p.

41. Mustafa H, Pang TY, Ellena T, Nasir SH. Impact attenuation of user-centred bicycle helmet design with different foam densities. J Phys Conf Ser. 2019;1150(1).

42. Fowler JN, Pallanta AA, Swanik CB, Wagner NJ. The Use of Shear Thickening Nanocomposites in Impact Resistant Materials. J Biomech Eng. 2015;137(5).

43. Soutrenon M, Michaud V. Impact properties of shear thickening fluid impregnated foams. Smart Mater Struct. 2014;23(3).

44. Janbaz S, Narooei K, Van Manen T, Zadpoor AA. Strain rate-dependent mechanical metamaterials. Sci Adv. 2020;6(25).

45. Carroll LJ, Cassidy JD, Holm L, Kraus J, Coronado VG. Methodological issues and research recommendations for mild traumatic brain injury: The WHO Collaborating Centre Task Force on Mild Traumatic Brain Injury. J Rehabil Med Suppl. 2004;(43).

46. Beaver W. Concussion in the NHL: A Case Study. J Contemp Athl. 2018;12(2).

47. Anderson GR, Melugin HP, Stuart MJ. Epidemiology of Injuries in Ice Hockey. Sports Health. 2019;11(6).

48. Donskov AS, Humphreys D, Dickey JP. What is injury in ice hockey: An integrative literature review on injury rates, injury definition, and athlete exposure in men's elite ice hockey. Sports. 2019;7(11).

49. Renton T, Howitt S, Marshall C. Lifetime prevalence of concussion among Canadian ice hockey players aged 10 to 25 years old, 2014 to 2017. J Can Chiropr Assoc. 2019;63(2).

50. Wennberg RA, Tator CH. National Hockey League reported concussions, 1986-87 to 2001-02. Can J Neurol Sci. 2003;30(3).

51. Schneider KJ, Nettel-Aguirre A, Palacios-Derflingher L, Mrazik M, Brooks BL, Woollings K, et al. Concussion Burden, Recovery, and Risk Factors in Elite Youth Ice Hockey Players. Clin J Sport Med. 2021;31(1).

52. Hutchinson S, Ellison P, Levy A, Marchant D. Knowledge and attitudes towards concussion in UK-based male ice hockey players: A need for attitude change? Int J Sport Sci Coach. 2019;14(2).

53. Williamson IJS, Goodman D. Converging evidence for the under-reporting of concussions in youth ice hockey. Br J Sports Med. 2006;40(2).

54. Tator CH, Blanchet V, Ma J. Persisting Concussion Symptoms from Bodychecking: Unrecognized Toll in Boys' Ice Hockey. Can J Neurol Sci. 2022;

55. Robidoux MA, Kendall M, Laflamme Y, Post A, Karton C, Hoshizaki TB. Comparing concussion rates as reported by hockey Canada with head contact events as observed across minor ice-hockey age categories. J Concussion. 2020;4.

56. Van Pelt KL, Caccese JB, Eckner JT, Putukian M, Brooks MA, Cameron KL, et al. Detailed description of Division I ice hockey concussions: Findings from the NCAA and Department of Defense CARE Consortium. J Sport Heal Sci. 2021;10(2).

57. Gamble ASD, Bigg JL, Sick S, Krolikowski M, Patton DA, Hagel BE, et al. Helmet fit assessment and concussion risk in youth ice hockey players: A nested case-

control study. J Athl Train. 2021;56(8).

58. Ornon G, Ziltener JL, Fritschy D, Menetrey J. Epidemiology of injuries in professional ice hockey: a prospective study over seven years. J Exp Orthop. 2020;7(1).

59. Emery CA, Meeuwisse WH. Injury rates, risk factors, and mechanisms of injury in minor hockey. Am J Sports Med. 2006;34(12).

60. Emery CA, Hagel B, Decloe M, Carly M. Risk factors for injury and severe injury in youth ice hockey: A systematic review of the literature. Inj Prev. 2010;16(2).

61. Black AM, Macpherson AK, Hagel BE, Romiti MA, Palacios-Derflingher L, Kang J, et al. Policy change eliminating body checking in non-elite ice hockey leads to a threefold reduction in injury and concussion risk in 11- and 12-year-old players. Br J Sports Med. 2016;50(1).

62. Guskiewicz KM, McCrea M, Marshall SW, Cantu RC, Randolph C, Barr W, et al. Cumulative Effects Associated with Recurrent Concussion in Collegiate Football Players: The NCAA Concussion Study. J Am Med Assoc. 2003;290(19).

63. Ferry B, Alexei D. Concussion. NCBI Bookshelf. 2022. p. 1–8.

64. Jordan BD. The clinical spectrum of sport-related traumatic brain injury. Nat Rev Neurol. 2013;9(4).

65. Marshall CM. Sports-related concussion: A narrative review of the literature. J Can Chiropr Assoc. 2012;56(4).

66. Harmon KG, Clugston JR, Dec K, Hainline B, Herring SA, Kane S, et al. American Medical Society for Sports Medicine Position Statement on Concussion in Sport. Clin J Sport Med. 2019;29(2).

67. Signoretti S, Lazzarino G, Tavazzi B, Vagnozzi R. The pathophysiology of concussion. PM R. 2011;3(10 SUPPL. 2).

68. Choe MC. The Pathophysiology of Concussion. Curr Pain Headache Rep. 2016;20(6).

69. Mainwaring L, Ferdinand Pennock KM, Mylabathula S, Alavie BZ. Subconcussive head impacts in sport: A systematic review of the evidence. Int

J Psychophysiol. 2018;132(January).

70. Gard A, Lehto N, Engström Å, Shahim P, Zetterberg H, Blennow K, et al. Quality of life of ice hockey players after retirement due to concussions. Concussion. 2020;5(3).

71. Gouttebarge V, Kerkhoffs GMMJ. Sports career-related concussion and mental health symptoms in former elite athletes. Neurochirurgie. 2021;67(3).

72. Mez J, Daneshvar DH, Kiernan PT, Abdolmohammadi B, Alvarez VE, Huber BR, et al. Clinicopathological evaluation of chronic traumatic encephalopathy in players of American football. JAMA - J Am Med Assoc. 2017;318(4).

73. Fralick M, Thiruchelvam D, Tien H, Redelmeier D. Risk of suicide after a concussion. C 2016. 2016;188(7).

74. Post A, Hoshizaki TB. Mechanisms of brain impact injuries and their prediction: A review. Trauma. 2012;14(4).

75. King AI, Yang KH, Zhang L, Hardy W. Is head injury caused by linear or angular acceleration? Proc Int Res Conf Biomech Impacts. 2003;(September).

76. Bayly P V., Cohen TS, Leister EP, Ajo D, Leuthardt EC, Genin GM. Deformation of the human brain induced by mild acceleration. J Neurotrauma. 2005;22(8).

77. Zhang L, Yang KH, King AI. Biomechanics of neurotrauma. Neurol Res. 2001;23(2–3).

78. Hardy WN, Mason MJ, Foster CD, Shah CS, Kopacz JM, Yang KH, et al. A study of the response of the human cadaver head to impact. Stapp Car Crash J. 2007;51.

79. Hardy WN, Khalil TB, King AI. Literature review of head injury biomechanics. Int J Impact Eng. 1994;15(4).

80. Nusholtz GS, Lux P, Kaiker P, Janicki MA. Head impact response - Skull deformation and angular accelerations. SAE Tech Pap. 1984;93(1984).

81. Zhang J, Yoganandan N, Pintar FA, Gennarelli TA. Role of translational and rotational accelerations on brain strain in lateral head impact. Tech Pap ISA. 2006;464(May 2014).

82. Thomas LM, Roberts VL, Gurdjian ES. Experimental intracranial pressure gradients in the human skull. J Neurol Neurosurg Psychiatry. 1966;29(5).

83. Gross AG. A New Theory on the Dynamics of Brain Concussion and Brain Injury. 1957;

84. Ommaya AK, Gennarelli TA. Cerebral concussion and traumatic unconsciousness: Correlation of experimental and clinical observations on blunt head injuries. Brain. 1974;97(4).

85. Thomas LM, Roberts VL, Gurdjian ES. Impact-induced pressure gradients along three orthogonal axes in the human skull. J Neurosurg. 1967;26(3).

86. Gurdjian ES, Lissner HR. Mechanism of Head Injury as Studied by the Cathode Ray Oscilloscope. J Nerv Ment Dis. 1945;102(4).

87. Hodgson VR, Thomas LM, Gurdjian ES, Fernando OU, Greenberg SW, Chason JL. Advances in understanding of experimental concussion mechanisms. SAE Tech Pap. 1969;

88. Hardy WN, Foster CD, Mason MJ, Yang KH, King A, Tashman S. Investigation of Head Injury Mechanisms Using Neutral Density Technology and. Stapp Car Crash J. 2001;45(November).

89. Gilchrist MD, O'Donoghue D. Simulation of the development of frontal head impact injury. Comput Mech. 2000;26(3).

90. Shatsky SA, Evans DE, Miller F, Martins AN. High speed angiography of experimental head injury. J Neurosurg. 1974;41(5).

91. Kleiven S. Influence of impact direction on the human head in prediction of subdural hematoma. J Neurotrauma. 2003;20(4).

92. Pellman EJ, Viano DC, Withnall C, Shewchenko N, Bir CA, Halstead PD. Concussion in professional football: Helmet testing to assess impact performance - Part 11. Neurosurgery. 2006;58(1).

93. Bandak FA, Eppinger RH. A three-dimensional finite element analysis of the human brain under combined rotational and translational accelerations. SAE Tech Pap. 1994;103.

94. Gennarelli TA, Thibault LE, Ommaya AK. Pathophysiologic responses to rotational and translational accelerations of the head. SAE Tech Pap. 1972;

95. Holbourn AHS. Mechanics of Head Injury. Lancet. 1943;242(2).

96. Ommaya AK, Hirsch AE, Flamm ES, Mahone RH. Cerebral Concussion in the Monkey: An Experinental Model. Science (80-). 1966;153(3732).

97. Margulies SS, Thibault LE. A proposed tolerance criterion for diffuse axonal injury in man. J Biomech. 1992;25(8).

98. Hernandez F, Camarillo DB. Voluntary Head Rotational Velocity and Implications for Brain Injury Risk Metrics. J Neurotrauma. 2019;36(7).

99. Zhang L, Yang KH, King AI. A Proposed Injury Threshold for Mild Traumatic Brain Injury. J Biomech Eng. 2004;126(2).

100. Viano DC, King AI, Melvin JW, Weber K. Injury biomechanics research: An essential element in the prevention of trauma. J Biomech. 1989;22(5).

101. Halstead PD, Alexander CF, Cook EM, Drew RC. Hockey Headgear and the Adequacy of Current Designs and Standards. Saf Ice Hockey, ASTM STP 1341. 1998;

102. Willinger R, Deck C, Halldin P, Otte D. Towards advanced bicycle helmet test methods. Int Cycl Saf Conf. 2014;(November).

103. Clark JM, Hoshizaki TB, Gilchrist MD. Event-specific impact test protocol for ice hockey goaltender masks. Sport Biomech. 2018;00(00).

104. Post A, Dawson L, Hoshizaki TB, Gilchrist MD, Cusimano MD. Development of a test method for adult ice hockey helmet evaluation. Comput Methods Biomech Biomed Engin. 2020;23(11).

105. British Standards Institution (2006), BS EN 960:2006, Headforms for use in the testing of protective helmets.

106. ASTM Standard F2220-2015, 2015, “Standard Specification for Headforms”, ASTM International, West Conshohocken, PA, 2015, DOI:10.1520/F2220-15, www.astm.org.

107. Solutions HI. Hybrid III 50th Male [Internet]. 2020.

108. MacAlister A. Surrogate Head Forms for the Evaluation of Head Injury Risk. Brain Inj Biomech Symp. 2013;

109. Post A, Oeur A, Hoshizaki B, Gilchrist MD. An examination of American football helmets using brain deformation metrics associated with concussion. Mater Des. 2013;45.

110. Kendall M, Walsh ES, Hoshizaki TB. Comparison between Hybrid III and Hodgson-WSU headforms by linear and angular dynamic impact response. Proc Inst Mech Eng Part P J Sport Eng Technol. 2012;226(3–4).

111. McIntosh AS, Janda D. Evaluation of cricket helmet performance and comparison with baseball and ice hockey helmets. Br J Sports Med. 2003;37(4).

112. Giacomazzi A, Smith T, Kersey R. Analysis of the impact performance of ICE hockey helmets using two different test methodologies. J ASTM Int. 2009;6(4).

113. McIntosh AS, McCrory P. Impact energy attenuation performance of football headgear. Br J Sports Med. 2000;34(5).

114. Humanetics2022. humaneticsgroup Hybrid III 50th Male [Internet]. 2022.

115. Rousseau P, Walsh ES, Foreman S, Hoshizaki TB. The effect of impact condition on the relationship between linear and angular acceleration. 2009;53.

116. Rousseau P, Post A, Hoshizaki TB. A comparison of peak linear and angular headform accelerations using ice hockey helmets. J ASTM Int. 2009;6(1).

117. Rousseau P, Hoshizaki TB. The influence of deflection and neck compliance on the impact dynamics of a Hybrid III headform. Proc Inst Mech Eng Part P J Sport Eng Technol. 2009;223(3).

118. Bland ML, McNally C, Rowson S. Differences in Impact Performance of Bicycle Helmets during Oblique Impacts. J Biomech Eng. 2018;140(9).

119. Post A, Karton C, Hoshizaki TB, Gilchrist MD. Analysis of the protective capacity of ice hockey helmets in a concussion injury reconstruction. 2014 IRCOBI Conf Proc - Int Res Counc Biomech Inj. 2014;

120. Clark JM, Post A, Hoshizaki TB, Gilchrist MD. Determining the relationship between linear and rotational acceleration and MPS for different magnitudes of

classified brain injury risk in ice hockey. In: 2015 IRCOBI Conference Proceedings. 2015.

121. de Grau S, Post A, Hoshizaki TB, Gilchrist MD. Effects of surface compliance on the dynamic response and strains sustained by a player's helmeted head during ice hockey impacts. Proc Inst Mech Eng Part P J Sport Eng Technol. 2019;234(1).

122. Post A, Dawson L, Hoshizaki TB, Gilchrist MD, Cusimano MD. The influence of impact source on variables associated with strain for impacts in ice hockey. Comput Methods Biomech Biomed Engin. 2019;22(7).

123. Post A, De Grau S, Ignacy T, Meehan A, Zemek R, Hoshizaki B, et al. Comparison of helmeted head impact in youth and adult ice hockey. 2016 IRCOBI Conf Proc - Int Res Counc Biomech Inj. 2016;

124. Jorgensen JK, Thoreson AR, Stuart MB, Loyd A, Smith AM, Twardowski C, et al. Interpreting oblique impact data from an accelerometer-instrumented ice hockey helmet. Proc Inst Mech Eng Part P J Sport Eng Technol. 2017;231(4).

125. Post A, Clark JM, Robertson DGE, Hoshizaki TB, Gilchrist MD. The effect of acceleration signal processing for head impact numeric simulations. Sport Eng. 2017;20(2).

126. Nur S, Kendall M, Clark JM, Hoshizaki TB. A comparison of the capacity of ice hockey goaltender masks for the protection from puck impacts. Sport Biomech. 2015;14(4).

127. Oeur RA, Zanetti K, Hoshizaki TB. Angular acceleration responses of American football, lacrosse and ice hockey helmets subject to low-energy impacts. 2014 IRCOBI Conf Proc - Int Res Counc Biomech Inj. 2014;

128. Kendall M, Post A, Rousseau P, Hoshizaki TB. The effect of shoulder pad design on reducing peak resultant linear and rotational acceleration in shoulder-to-head impacts. Mech Concussion Sport. 2014;

129. Ouckama R, Pearsall DJ. Projectile impact testing of ice hockey helmets: Headform kinematics and dynamic measurement of localized pressure distribution. 2014 IRCOBI Conf Proc - Int Res Counc Biomech Inj.

2014;(September).

130. Walsh ES, Rousseau P, Hoshizaki TB. The influence of impact location and angle on the dynamic impact response of a Hybrid III headform. Sport Eng. 2011;13(3).

131. McIntosh AS, Lai A, Schilter E. Bicycle Helmets: Head Impact Dynamics in Helmeted and Unhelmeted Oblique Impact Tests. Traffic Inj Prev. 2013;14(5).

132. Walsh ES, Hoshizaki TB. Poster Session III, July 15th 2010 — Abstracts Sensitivity analysis of a Hybrid III head- and neckform to impact angle variations. Procedia Eng. 2010;2(2).

133. Oeur RA, Hoshizaki TB. The effect of impact compliance, velocity, and location in predicting brain trauma for falls in sport. 2016 IRCOBI Conf Proc - Int Res Counc Biomech Inj. 2016;

134. Walsh ES, Post A, Rousseau P, Kendall M, Karton C, Oeur A, et al. Dynamic impact response characteristics of a helmeted Hybrid III headform using a centric and non-centric impact protocol. Proc Inst Mech Eng Part P J Sport Eng Technol. 2012;226(3–4).

135. Post A, Oeur A, Hoshizaki B, Gilchrist MD. Examination of the relationship between peak linear and angular accelerations to brain deformation metrics in hockey helmet impacts. Comput Methods Biomech Biomed Engin. 2013;16(5).

136. Kendall M, Post A, Gilchrist MD. A Comparison of dynamic impact response and brain deformation metrics within the cerebrum of head impact reconstructions representing three mechanisms of head injury in ice hockey. IRCOBI Conf 2012. 2012;

137. Knowles BM, Dennison CR. Predicting Cumulative and Maximum Brain Strain Measures From HybridIII Head Kinematics: A Combined Laboratory Study and Post-Hoc Regression Analysis. Ann Biomed Eng. 2017;45(9).

138. Rousseau P, Hoshizaki TB. Defining the effective impact mass of elbow and shoulder strikes in ice hockey. Sport Biomech. 2015;14(1).

139. Allison MA, Kang YS, Bolte IV JH, Maltese MR, Arbogast KB. Validation of a Helmet-based system to measure head impact biomechanics in ice hockey. Med

Sci Sports Exerc. 2014;46(1).

140. Allison MA, Kang YS, Maltese MR, Bolte JH, Arbogast KB. Measurement of Hybrid III Head Impact Kinematics Using an Accelerometer and Gyroscope System in Ice Hockey Helmets. Ann Biomed Eng. 2015;43(8).

141. Pellman EJ, Viano DC, Tucker AM, Casson IR, Waeckerle JF. Concussion in Professional Football: Reconstruction of Game Impacts and Injuries. Neurosurgery. 2003;53(4).

142. Michio Clark J, Connor TA, Post A, Blaine Hoshizaki T, Ní Annaidh A, Gilchrist MD. Could a Compliant Foam Anvil Characterize the Biofidelic Impact Response of Equestrian Helmets? J Biomech Eng. 2020;142(6).

143. Chen W, Post A, Karton C, Gilchrist MD, Robidoux M, Hoshizaki TB. A comparison of frequency and magnitude of head impacts between Pee Wee And Bantam youth ice hockey. Sport Biomech. 2020;00(00).

144. Post A, Karton C, Robidoux M, Gilchrist MD, Hoshizaki TB. An examination of the brain trauma in Novice and Midget ice hockey : Implications for helmet innovation. 2019;

145. Cobb BR, Macalister A, Young TJ, Kemper AR, Rowson S, Duma SM. Quantitative comparison of Hybrid III and National Operating Committee on Standards for Athletic Equipment headform shape characteristics and implications on football helmet fit. Proc Inst Mech Eng Part P J Sport Eng Technol. 2015;229(1).

146. Bottlang M, Rouhier A, Tsai S, Gregoire J, Madey SM. Impact Performance Comparison of Advanced Bicycle Helmets with Dedicated Rotation-Damping Systems. Ann Biomed Eng. 2020;48(1).

147. Bliven E, Rouhier A, Tsai S, Willinger R, Bourdet N, Deck C, et al. Evaluation of a novel bicycle helmet concept in oblique impact testing. Accid Anal Prev. 2019;124(December 2018).

148. NOCSAE DOC (ND) 001-17m19, 2019, “Standard Test Method and Equipment Used in Evaluating the Performance Characteristics of Headgear/Equipment”, National Operating Committee on Standards for Atletic Equipment.

149. NOCSAE DOC (ND) 030 - 11m16, 2016, “Standard Performance Specification for Newly Manufactured Ice Hockey Helmets”, National Operating Committee on Standards for Athletic Equipment.

150. NOCSAE DOC (ND) 002-17m19a, 2019, “Standard Performance Specification for Newly Manufactured Football Helmets”, National Operating Committee on Standards for Athletic Equipment.

151. NOCSAE DOC (ND) 022-21,2021, “Standard Performance Specification for Newly Manufactured Baseball/Softball Batter’s Helmets”, National Operating Committee on Standards for Athletic Equipment.

152. NOCSAE DOC (ND) 029-21, 2021, “Standard Performance Specification for Newly Manufactured Baseball/Softball Fielder’s Headgear”, National Operating Committee on Standards for Athletic Equipment.

153. NOCSAE DOC (ND) 021-18m19a, 2019, “Standard Projectile Impact Test Method and Equipment Used in Evaluating the Performance Characteristics of Protective Headgear, Faceguards, or Projectiles”, National Operating Committee on Standards for Athletic Equipmen.

154. NOCSAE DOC (ND) 041- 15m18, 2018, “Standard Performance Specification for Newly Manufactures Lacrosse Helmets With Faceguard”, National Operating Committee on Standards for Athletic Equipment.

155. NOCSAE DOC (ND) 050-11m19, 2019, “Standard Performance Specification for Newly Manufactured Polo Helmets”, National Operating Committee on Standards for Atletic Equipment.

156. Levy Y, Gallone MB, Bian K, McDougall K, Ouckama R, Mao H. Using a Strain-Based Computational Approach for Ice Hockey Helmet Performance Evaluation. 2020;

157. Pennock B, Kivi D, Zerpa C. Effect of Neck Strength on Simulated Head Impacts During Falls in Female Ice Hockey Players. Int J Exerc Sci. 2021;14(1).

158. Zerpa C, Carlson S, Przysucha E, Liu M, Sanzo P. Evaluating the Performance of a Hockey Helmet in Mitigating Concussion Risk Using Measures of Acceleration and Energy During Simulated Free Fall. Int J Extrem Autom

Connect Healthc. 2021;3(2).

159. Kis M, Saunders FW, Irrcher I, Tator CH, Bishop PJ, Hove MWT. A method of evaluating helmet rotational acceleration protection using the kingston impact simulator (KIS Unit). Clin J Sport Med. 2013;23(6).

160. Rowson B, Rowson S, Duma SM. Hockey STAR: A Methodology for Assessing the Biomechanical Performance of Hockey Helmets. Ann Biomed Eng. 2015;43(10).

161. Carlson S, Zerpa C, Pryzsucha E, Liu M, Sanzo P, Bay T. Energy Measures Across Hockey Helmet Impact Locations. In: ISBS Proceedings Archive 371. 2019. p. 443–6.

162. Clark JM, Taylor K, Post A, Hoshizaki TB, Gilchrist MD. Comparison of Ice Hockey Goaltender Helmets for Concussion Type Impacts. Ann Biomed Eng. 2018;46(7).

163. Michio Clark J, Post A, Blaine Hoshizaki T, Gilchrist MD. Distribution of brain strain in the cerebrum for laboratory impacts to ice hockey goaltender masks. J Biomech Eng. 2018;140(12).

164. Jeffries L, Zerpa C, Przysucha E, Sanzo P, Bay T. the Influence of Full Facial Protection on Headform Peak Linear Acceleration At Different Helmet Impact Locations. In: Conference of the International Society of Biomechanics in Sports. 2018. p. 864–8.

165. Jeffries L, Zerpa C, Przysucha E, Sanzo P, Carlson S. The Use of a Pneumatic Horizontal Impact System for Helmet Testing. J Saf Eng. 2017;6(1).

166. O'Connor KL, Rowson S, Duma SM, Broglio SP. Head-impact-measurement devices: A systematic review. J Athl Train. 2017;52(3).

167. Bartsch AJ, Hedin DS, Gibson PL, Miele VJ, Benzel EC, Alberts JL, et al. Laboratory and On-field Data Collected by a Head Impact Monitoring Mouthguard. Proc Annu Int Conf IEEE Eng Med Biol Soc EMBS. 2019;(Imm).

168. Meehan A, Post A, Hoshizaki TB, Gilchrist MD. Investigation of an Ice Hockey Helmet Test Protocol Representing Three Concussion Event Types. J Test Eval. 2022;50(1).

169. Zhang L, Ramesh D, Yang KH, King AI. EFFECTIVENESS OF THE FOOTBALL HELMET ASSESSED BY FINITE ELEMENT MODELING AND IMPACT TESTING. In: IRCOBI Conference 2003. 2003. p. 27–38.

170. Walsh ES, Rousseau P, Foreman S, Hoshizaki TB. The Determination of Novel Impact Conditions for the Assessment of Linear and Angular Headform Accelerations. 2005;42(1943).

171. ASTM Standard F1952 - 22, “Standard Specification for Helmets Used for Downhill Mountain Bicycle Racing”, ASTM International, West Conshohocken, PA, 2015, DOI:10.1520/F1952-22, www.astm.org.

172. EN 1078:2012+A1:2012, 2014, “Helmets for pedal cyclists and for users of skateboards and roller skates”, DIN Deutsches Institut für Normung e. V.

173. ASTM Standard F1446 - 20, “Standard Test Methods for Equipment and Procedures Used in Evaluating the Performance Characteristics of Protective Headgear”, ASTM International, West Conshohocken, PA, 2020, DOI:10.1520/F1446-20, www.astm.org.

174. EN 966:2012+A1:2012, 2013, “Helmets for airborne sports”, DIN Deutsches Institut für Normung e. V.

175. NOCSAE DOC (ND) 081-18am19a, 2019, "Standard Pneumatic Ram Test Method and Equipment Used in Evaluating the Performance Characteristics of Protective Headgear and Face Guards, National Operating Committee on Standards for Athletic Equipment.

176. Rowson S, Duma SM. The temperature inside football helmets during head impact: A fiveyear study of collegiate football games. Proc Inst Mech Eng Part P J Sport Eng Technol. 2013;227(1).

177. Sabelli J, Morehouse CA. Comparison of Ice Hockey Helmet Impact Attenuation Tests on Steel and Elastomeric Surfaces. Saf Ice Hockey ASTM STP 1341. 2000;3.

178. Saczalski KJ, West MN, Saczalski TK, Frausto L, Pozzi MC. Test Analysis of Youth and Adult Football Helmet Head Injury Risk Resulting From Repear Impacts In High Humidity And Temperature. Proc ASME 2017 Int Mech Eng

Congr Expo. 2017;

179. ASTM Standard F1447, 2018, “Standard Specification for Helmets Used in Recreational Bicycling or Roller Skating”, ASTM International, West Conshohocken, PA, 2018, DOI:10.1520/F1447-18, www.astm.org.

180. 16 CFR Part 1203, 1998, “Safety Standard for Bicycle Helmets; Final Rule”, Consumer Product Safety Commission.

181. Snell B-95A, 1998, “1995 Standard for Protectice Headgear For Use In Bicycling”, Snell Memorial Foundation Inc.

182. ASTM Standard F1163-15, 2015, “Standard Specification for Protective Headgear Used in Horse Sports and Horseback Riding”, ASTM International, West Conshohocken, PA, 2018, DOI:10.1520/F1163-15, www.astm.org.

183. Federation Internationale de l’Automobile. Norme Fia 8860-2018 Et 8860-2018-Abp Fia Standard 8860-2018 and 8860-2018-Abp Casque Haute Performance. 2018;

184. Deutsche Norm. EN 1077:2007, 2007, “Helmets for alpine skiers and snowboarders”, Deutsches Institut für Normung.

185. DIN EN 1385:2012, 2012, “Helme für den Kanu- und Wildwassersport”, DIN Deutsches Institut für Normung e. V.

186. EN 1384:2017, 2017, “Helmets for equestrian activities”, DIN Deutsches Institut für Normung e. V.

187. BS 7928:2013+A1:2019, “Specification for head protectors for cricketers”, BSI Standards Publication.

188. Snell B-90A B-90C, 1998, “Standard for Protectice Headgear For Use In Bicycling”, Snell Memorial Foundation Inc.

189. NOCSAE DOC (ND) 024-21, “Standard Performance Specification for Newly Manufactured Baseball/Softball Catcher’s Helmets with Faceguard”, National Operating Committee on Standards for Athletic Equipmen.

190. Snell E2016, 2016, “Standard for Protectice Headgear For Use in Horseback Riding”, Snell Memorial Foundation Inc.

191. Snell foundation SPFH. Snell SA2015, “Standard for Protectice Headgear For Use in Competitive Automotive Sports”, Snell Memorial Foundation Inc. 2020.

192. Snell SA20, 2019, “2020 Special Applications Standard for Protective Headgear”, Snell Memorial Foundation Inc.

193. Snell EA2016, 2016, “Standard for Protective Headgear For Use in Elite Automotive Sports”, Snell Memorial Foundation Inc.

194. Used P. ASTM Standard F1492 - 22, “Standard Specification for Helmets Used in Skateboarding and Trick Roller Skating”, ASTM International, West Conshohocken, PA, 2022, DOI:10.1520/F1492-22, www.astm.org. 2001;i.

195. ASTM Standard F2040, 2018, “Standard Specification for Helmets Used for Recreational Snow Sports”, ASTM International, West Conshohocken, PA, 2003, DOI:10.1520/F2040-18, www.astm.org.

196. Snell RS-98, 1998, “1998 Standard for Protectice Headgear For Use In Recreational Skiing and Snowboarding”, Snell Memorial Foundation Inc.

197. Snell S-98, 1998, “1998 Standard for Protectice Headgear For Skiing and Other Winter Activities”, Snell Memorial Foundation Inc.

198. Sarvghad Moghaddam H, Kwok W. Role of Helmet Fit on Angular and Linear Accelerations of Head in Ice Hockey. Int J Biomed Sci Eng. 2019;7(2).

199. Koncan DA, Zemek R, Gilchrist MD, Hoshizaki TB. Helmet Construction Influences Brain Strain Patterns for Events Causing Concussion in Youth Ice Hockey. 2017;

200. Johnson GI. A comparison of results on helmet impact testing. J Test Eval. 2003;31(1).

201. Foster L, Peketi P, Allen T, Senior T, Duncan O, Alderson A. Application of auxetic foam in sports helmets. Appl Sci. 2018;8(3).

202. Mills NJ, Gilchrist A. Oblique impact testing of bicycle helmets. Int J Impact Eng. 2008;35(9).

203. Aare M, Halldin P. A new laboratory rig for evaluating helmets subject to oblique impacts. Traffic Inj Prev. 2003;4(3).

204. Halldin P, Gilchrist A, Mills NJ. A new oblique impacttest for motorcycle helmets. Int J Crashworthiness. 2001;6(1).

205. Viano DC, Withnall C, Wonnacott M. Football helmet drop tests on different fields using an instrumented hybrid III head. Ann Biomed Eng. 2012;40(1).

206. ASTM Standard F1045, 2016, “Standard Performance Specification for Ice Hockey Helmets”, ASTM International, West Conshohocken, PA, 2016, DOI: 10.1520/F1045-16, www.astm.org.

207. Stigson H, Rizzi M, Ydenius A, Engström E, Kullgren A. Consumer Testing of Bicycle Helmets. In: IRCOBI Conference 2017. 2017. p. 173–81.

208. Rowson B, Rowson S, Duma SM. Hockey STAR: A Methodology for Assessing the Biomechanical Performance of Hockey Helmets. Ann Biomed Eng. 2015;43(10).

209. Tyson AM, Rowson S. Adult Football STAR Methodology. Virginia Tech Helmet Lab. 2018;(540).

210. Withnall C, Wonnacott M, Searle J. Developing a linear impactor test method for ice hockey. ASTM Spec Tech Publ. 2020;STP 1625.

211. British Standards Institution (2013), BS 7928:2013, Specification for head protectors for cricketers.

212. Richards D, Ivarsson BJ, Scher I, Hoover R, Rodowicz K, Cripton P. Ice hockey shoulder pad design and the effect on head response during shoulder-to-head impacts. Sport Biomech. 2016;15(4).

213. Schmitt KU, Muser MH, Thueler H, Bruegger O. Crash-test dummy and pendulum impact tests of ice hockey boards: Greater displacement does not reduce impact. Br J Sports Med. 2018;52(1).

214. Scher IS, Stepan LL, Hoover RW. Head and neck injury potential during water sports falls: examining the effects of helmets. Sport Eng. 2020;23(1).

215. Horgan TJ, Gilchrist MD. The creation of three-dimensional finite element models for simulating head impact biomechanics. Int J Crashworthiness. 2003;8(4).

216. Funk JR, Duma SM, Manoogian SJ, Rowson S. Biomechanical Risk Estimates for Mild Traumatic Brain Injury. 51st Annu Proc Assoc Adv Automot Med. 2007;1(1).

217. Denny-Brown D, R. RW. Experimental Cerebral Concussion. Brain. 1941;64(2).

218. Gurdjian ES, Roberts VL, Thomas M. Tolerance Curves of Acceleration and Intracranial Pressure and Protective Index in Experimental Head Injury. J Trauma. 1966;6(5).

219. Ono K, Kikuchi A, Nakamura M, Kobayashi H, Nakamura N. Human head tolerance to sagittal impact reliable estimation deduced from experimental head injury using subhuman primates and human cadaver skulls. SAE Tech Pap. 1980;

220. Lissner HR, Lebow M, Evans FG. Experimental studies on the relation between acceleration and intracranial pressure changes in man. Surgery, Gynecol Obstet. 1960;111.

221. Gurdjian ES, Lissner HR, Latimer FR, Haddad BF, Webster JE. Quantitative determination of acceleration and intracranial pressure in experimental head injury; preliminary report. Neurology. 1953;3(6).

222. Hoshizaki TB, Post A, Kendall M, Cournoyer J, Rousseau P, Gilchrist MD, et al. The development of a threshold curve for the understanding of concussion in sport. Trauma (United Kingdom). 2017;19(3).

223. NOCSAE DOC (ND) 022-20, 2020, “Standard Performance Specification for Newly Manufactured Baseball/Softball Batter’s Helmets”, National Operating Committee on Standards for Athletic Equipment.

224. Hutchinson J, Kaiser MJ, Lankarani HM. The Head Injury Criterion (HIC) functional. Appl Math Comput. 1998;96(1).

225. Versace J. A Review of the Severity Index. SAE Tech Pap - 15th Stapp Car Crash Conf. 1971;

226. Rousseau P, Post A, Hoshizaki TB. The effects of impact management materials in ice hockey helmets on head injury criteria. Proc Inst Mech Eng Part P J Sport Eng Technol. 2009;223(4).

227. Rousseau P, Hoshizaki TB, Gilchrist MD. For ASTM F-08: Protective capacity of ice hockey player helmets against puck impacts. Mech Concussion Sport. 2014;

228. Ommaya AK, Hirsch AE, Martinez JL. The Role of Whiplash in Cerebral Concussion. SAE Tech Pap. 1966;

229. Gennarelli TA, Thibault LE. Biomechanics of acute subdural hematoma. J Trauma. 1982;22(8).

230. Unterharnscheidt FJ. Translational versus Rotational Acceleration-Animal Experiments with Measured Input. Scand J Rehabil Med. 1971;4.

231. Pincemaille Y, Trosseille X, MacK P, Tarrière C, Breton F, Renault B. Some new data related to human tolerance obtained from volunteer boxers. SAE Tech Pap. 1989;98.

232. Kimpara H, Iwamoto M. Mild traumatic brain injury predictors based on angular accelerations during impacts. Ann Biomed Eng. 2012;40(1).

233. Takhounts EG, Hasija V, Ridella SA, Rowson S, Duma SM. Kinematic Rotational Brain Injury Criterion (BRIC). In: Proceedings of the 22nd enhanced safety of vehicles conference Paper no 11-0263. 2011.

234. Takhounts EG, Craig MJ, Moorhouse K, McFadden J, Hasija V. Development of Brain Injury Criteria (BrIC). SAE Tech Pap. 2013;2013-Novem(November).

235. Newman JA. A generalized acceleration model for brain injury threshold (GAMBIT). Proc Int IRCOBI Conf. 1986;

236. Newman J, Barr C, Beusenberg M, Fournier E, Shewchenko N, Welbourne E, et al. a New Biomechanical Assessment of Mild Traumatic Brain Injury. Proc 2000 Int Conf Biomech Impact. 1995;108(2).

237. Newman JA, Shewchenko N. A Proposed New Biomechanical Head Injury Assessment Function - The Maximum Power Index. SAE Tech Pap. 2000;2000-Novem(November).

238. Fréchède B, McIntosh AS. Numerical reconstruction of real-life concussive football impacts. Med Sci Sports Exerc. 2009;41(2).

239. Patton DA, Mcintosh AS, Kleiven S. The Biomechanical Determinants of

Concussion : Finite Element Simulations to Investigate Brain Tissue Deformations During Sporting Impacts to the Unprotected Head. J Appl Biomech. 2013;29.

240. Patton DA, McIntosh AS, Kleiven S. The biomechanical determinants of concussion: Finite element simulations to investigate brain tissue deformations during sporting impacts to the unprotected head. J Appl Biomech. 2015;31(4).

241. Tiernan S, Tiernan S, Byrne G. The effect of impact location on brain strain. Brain Inj. 2019;00(00).

242. Hernandez F, Wu L, Yip MC, Diego S, Laksari K. Six Degree-of-Freedom Measurements of Human Mild Traumatic Brain Injury. Ann Biomed Eng. 2014;

243. McAllister TW, Ford JC, Ji S, Beckwith JG, Flashman LA, Paulsen K, et al. Maximum principal strain and strain rate associated with concussion diagnosis correlates with changes in corpus callosum white matter indices. Ann Biomed Eng. 2012;40(1).

244. Viano DC, Casson IR, Pellman EJ, Zhang L, King AI, Yang KH. CONCUSSION IN PROFESSIONAL FOOTBALL : BRAIN RESPONSES BY FINITE ELEMENT ANALYSIS : PART 9. Neurosurgery. 2005;57(5).

245. Gilchrist MD, O'Donoghue D, Horgan TJ. A two-dimensional analysis of the biomechanics of frontal and occipital head impact injuries. Int J Crashworthiness. 2001;6(2).

246. Gilchrist MD. Modelling and accident reconstruction of head impact injuries. Key Eng Mater. 2003;245–246.

247. Levy ML, Ozgur BM, Berry C, Aryan HE, Apuzzo MLJ. Birth and evolution of the football helmet. Neurosurgery. 2004;55(3).

248. Clement L, Jones D. Research and Development of Hockey Protective Equipment—A Historical Perspective. Saf Ice Hockey. 2008;

249. Odelgard B. The Development of Head, Face, and Neck Protectors for Ice Hockey Players. Saf Ice Hockey. 2008;

250. D3O 2020. D3O Protection. https://www.d3o.com/. 2023.

251. 2020 K. Koroyd Impact Protection. https://koroyd.com/. 2020.

252. 2023 W. WaveCel Technology. https://wavecel.com/technology/. 2023.

253. von Holst H, Halldin P. Protective helmet (US 6,658,671 B1). Vol. 1. 2003.

254. AB M. mipsprotection [Internet]. 2023.

255. Di Landro L, Sala G, Olivieri D. Deformation mechanisms and energy absorption of polystyrene foams for protective helmets. Polym Test. 2002;21(2).

256. Pablo Casas-Rodriguez J, Camilo Calle J, Robinson V, Maranon A. Cellular sandwich composites under blast loads [Internet]. 2nd ed. Dynamic Deformation, Damage and Fracture in Composite Materials and Structures, Second Edition. Elsevier Ltd.; 2022. 361–390 p.

257. Gibson LJ, Ashby MF. The Mechanics of Three-Dimensional Cellular Materials. Proc R Soc London. 1982;382(1782).

258. Leng B, Ruan D, Tse KM. Recent bicycle helmet designs and directions for future research: A comprehensive review from material and structural mechanics aspects. Int J Impact Eng. 2022;168(July).

259. Bhudolia SK, Gohel G, Subramanyam ESB, Leong KF, Gerard P. Enhanced impact energy absorption and failure characteristics of novel fully thermoplastic and hybrid composite bicycle helmet shells. Mater Des. 2021;209.

260. Spyrou E, Pearsall DJ, Hoshizaki TB. Effect of helmet geometry and material properties on impact attenuation of ice hockey helmets. Arch Physiol Biochem. 2000;108(1–2).

261. Gilchrist A, Mills NJ. Modelling of the impact response of motorcycle helmets. Int J Impact Eng. 1994;15(3).

262. AB M. Mips Integra [Internet]. 2023.

263. Halldin P, Aare M, Kleiven S, von Holst H. Improved helmet design and test methods to reduce rotational induced brain injuries. RTO Spec Meet NATO's Res Technol Organ. 2003;

264. Holst V. United States Patent: US 6,658,671. 2004;2(12).

265. Jacques Durocher S-J. United States Patent US 9,961,952 B2. Vol. 2. 2018.

266. MIPS. mipsprotection. https://mipsprotection.com/.

267. Evans KE. Auxetic polymers: a new range of materials. Endeavour. 1991;15(4).

268. Maheo L, Viot P. Impact on multi-layered polypropylene foams. Int J Impact Eng. 2013;53.

269. Coelho RM, Alves de Sousa RJ, Fernandes FAO, Teixeira-Dias F. New composite liners for energy absorption purposes. Mater Des. 2013;43.

270. Andena L, Caimmi F, Leonardi L, Ghisi A, Mariani S, Braghin F. Towards Safer Helmets: Characterisation, Modelling and Monitoring. Procedia Eng. 2016;147.

271. Mcgillivray K, Przysucha E, Sanzo P, Liu M, Zerpa C. Comparison of Hockey Helmet Lining Technologies in Mitigating Concussion Risk During Simulated Horizontal Head Collisions. Int J Extrem Autom Connect Healthc. 2022;4(1).

272. Wei M, Lin K, Sun L. Shear thickening fluids and their applications. Mater Des. 2022;216.

273. Nakonieczna P, Wierzbicki Ł, Śladowska B, Leonowicz M, Lisiecki J, Nowakowski D. Composites With Impact Absorption Ability Based on Shear Thickening Fluids and Auxetic Foams. Compos Theory Pract. 2017;17(2).

274. Jachowicz M, Owczarek G. Analysis of selected mechanical parameters for foamed materials with non-Newtonian liquid characteristics in terms of their use in aspects of protective helmets. Int J Occup Saf Ergon. 2020;26(3).

275. Waitukaitis SR, Jaeger HM. Impact-activated solidification of dense suspensions via dynamic jamming fronts. Nature. 2012;487(7406).

276. Barchiesi E, Spagnuolo M, Placidi L. Mechanical metamaterials: a state of the art. Math Mech Solids. 2019;24(1).

277. Surjadi JU, Gao L, Du H, Li X, Xiong X, Fang NX, et al. Mechanical Metamaterials and Their Engineering Applications. Adv Eng Mater. 2019;21(3).

278. Zadpoor AA. Mechanical meta-materials. Mater Horizons. 2016;3(5).

279. Lee JH, Singer JP, Thomas EL. Micro-/nanostructured mechanical

metamaterials. Adv Mater. 2012;24(36).

280. Lakes Roderic. Foam Structures with a Negative Poisson ' s Ratio. Science (80-). 1987;235.

281. Duncan O, Shepherd T, Moroney C, Foster L, Venkatraman PD, Winwood K, et al. Review of auxetic materials for sports applications: Expanding options in comfort and protection. Appl Sci. 2018;8(6).

282. Allen T, Hewage T, Newton-Mann C, Wang W, Duncan O, Alderson A. Fabrication of Auxetic Foam Sheets for Sports Applications. Phys Status Solidi Basic Res. 2017;254(12).

283. Duncan O, Alderson A, Allen T. Fabrication, characterization and analytical modeling of gradient auxetic closed cell foams. Smart Mater Struct. 2021;30(3).

284. Duncan O, Leslie G, Moyle S, Sawtell D, Allen T. Developments on auxetic closed cell foam pressure vessel fabrications. Smart Mater Struct. 2022;31(7).

285. Fan D, Li M, Qiu J, Xing H, Jiang Z, Tang T. Novel Method for Preparing Auxetic Foam from Closed-Cell Polymer Foam Based on the Steam Penetration and Condensation Process. ACS Appl Mater Interfaces. 2018;10(26).

286. Chan N, Evans KE. Indentation Resilience of Conventional and Auxetic Foams. J Cell Plast. 1998;34.

287. Alderson KL, Pickles AP, Neale PJ, Evans KE. Auxetic polyethylene: The effect of a negative poisson's ratio on hardness. Acta Metall Mater. 1994;42(7).

288. Duncan O, Foster L, Senior T, Allen T, Alderson A. A Comparison of Novel and Conventional Fabrication Methods for Auxetic Foams for Sports Safety Applications. Procedia Eng. 2016;147.

289. Allen T, Shepherd J, Hewage TAM, Senior T, Foster L, Alderson A. Low-kinetic energy impact response of auxetic and conventional open-cell polyurethane foams. Phys Status Solidi Basic Res. 2015;252(7).

290. Tancogne-Dejean T, Spierings AB, Mohr D. Additively-manufactured metallic micro-lattice materials for high specific energy absorption under static and dynamic loading. Acta Mater. 2016;116.

291. Qiu W, Lu F, Wang G, Huang G, Zhang H, Zhang Z, et al. Evaluation of mechanical performance and optimization design for lattice girders. Tunn Undergr Sp Technol. 2019;87(February).

292. Soe S, Ryan M, McShane G, Theobald P. Energy absorption characteristics of additively manufactured TPE cellular structures. Second Int Conf Sustain Des Manuf. 2015;

293. Zheng X, Lee H, Weisgraber TH, Shusteff M, DeOtte J, Duoss EB, et al. Ultralight, ultrastiff mechanical metamaterials. Science (80-). 2014;344(6190).

294. Khosroshahi SF, Duckworth H, Galvanetto U, Ghajari M. The effects of topology and relative density of lattice liners on traumatic brain injury mitigation. J Biomech. 2019;97.

295. Bauer J, Hengsbach S, Tesari I, Schwaiger R, Kraft O. High-strength cellular ceramic composites with 3D microarchitecture. Proc Natl Acad Sci U S A. 2014;111(7).

296. Ashby MF. The properties of foams and lattices. Philos Trans R Soc A Math Phys Eng Sci. 2006;364(1838).

297. Liu Y, Schaedler TA, Chen X. Dynamic energy absorption characteristics of hollow microlattice structures. Mech Mater. 2014;77.

298. Soe S, Robinson MR, Martin PS, Jones MD, Theobald P. Feasibility of using Duraform® flex lattice structures and additive manufacturing for optimising bicycle helmet design safety. Sustain Des Manuf 2014 Part 1. 2014;

299. Soe SP, Martin P, Jones M, Robinson M, Theobald P. Feasibility of optimising bicycle helmet design safety through the use of additive manufactured TPE cellular structures. Int J Adv Manuf Technol. 2015;79(9–12).

300. Gokhale V, Tapkir P, Tovar A. Force Diverting Helmet Liner Achieved Through a Lattice of Multi-Material Compliant Mechanisms. In: Proceedings of the ASME 2017 International Design Engineering Technical Conferences & Computers and Information in Engineering Conference. 2017. p. 1–9.

301. Wang Y, Groen JP, Sigmund O. Simple optimal lattice structures for arbitrary loadings. Extrem Mech Lett. 2019;29.

302. Du Y, Li H, Luo Z, Tian Q. Topological design optimization of lattice structures to maximize shear stiffness. Adv Eng Softw. 2017;112.

303. Song J, Wang Y, Zhou W, Fan R, Yu B, Lu Y, et al. Topology optimization-guided lattice composites and their mechanical characterizations. Compos Part B Eng. 2019;160(November 2018).

304. Xiang Y, Yu T, Yang L. Comparative analysis of energy absorption capacity of polygonal tubes, multi-cell tubes and honeycombs by utilizing key performance indicators. Mater Des. 2016;89.

305. Gümrük R, Mines RAW. Compressive behaviour of stainless steel micro-lattice structures. Int J Mech Sci. 2013;68.

306. Evans AG, Hutchinson JW, Fleck NA, Ashby MF, Wadley HNG. The topological design of multifunctional cellular metals. Prog Mater Sci. 2001;46(3–4).

307. Kholoosi F, Galehdari SA. Design, optimisation and analysis of a helmet made with graded honeycomb structure under impact load. Int J Crashworthiness. 2019;24(6).

308. Caccese V, Ferguson JR, Edgecomb MA. Optimal design of honeycomb material used to mitigate head impact. Compos Struct. 2013;100.

309. Zhang Y, Lu M, Wang CH, Sun G, Li G. Out-of-plane crashworthiness of bio-inspired self-similar regular hierarchical honeycombs. Compos Struct. 2016;144.

310. Kholoosi F, Galehdari SA. Design and Analysis of a Helmet Equipped with Graded Honeycomb Structure under Impact of Flat and Hemi-spherical Anvils. Procedia Eng. 2017;173.

311. Galehdari SA, Khodarahmi H, Atrian A. Design and analysis of graded honeycomb shock absorber for increasing the safety of passengers in armored vehicles exposed to mine explosion. J Solid Mech. 2017;9(2).

312. Sun G, Jiang H, Fang J, Li G, Li Q. Crashworthiness of vertex based hierarchical honeycombs in out-of-plane impact. Mater Des. 2016;110.

313. Khosroshahi SF, Tsampas SA, Galvanetto U. Feasibility study on the use of a hierarchical lattice architecture for helmet liners. Mater Today Commun.

2018;14(February).

314. Fernandes FAO, de Sousa RJA, Ptak M, Migueis G. Helmet design based on the optimization of biocomposite energy-absorbing liners under multi-impact loading. Appl Sci. 2019;9(4).

315. Hansen K, Dau N, Feist F, Deck C, Willinger R, Madey SM, et al. Angular Impact Mitigation system for bicycle helmets to reduce head acceleration and risk of traumatic brain injury. Accid Anal Prev. 2013;59.

316. Caserta GD, Iannucci L, Galvanetto U. Shock absorption performance of a motorbike helmet with honeycomb reinforced liner. Compos Struct. 2011;93(11).

317. 2020 Carbon I. Carbon3D CCM Super Tacks X. https://www.carbon3d.com/resources/blog/ccm-super-tacks-x/. 2020.

318. Mosleh Y, Cajka M, Depreitere B, Ivens J, Sloten J Vander. Smart material and design solutions for protective headgears in linear and oblique impacts: column/matrix composite liner to mitigate rotational accelerations. Smart Mater Struct. 2023;32(1).

319. Ozdemir Z, Hernandez-Nava E, Tyas A, Warren JA, Fay SD, Goodall R, et al. Energy absorption in lattice structures in dynamics: Experiments. Int J Impact Eng. 2016;89.

320. Fleck NA, Deshpande VS, Ashby MF. Micro-architectured materials: Past, present and future. Proc R Soc A Math Phys Eng Sci. 2010;466(2121).

321. Schaedler TA, Ro CJ, Sorensen AE, Eckel Z, Yang SS, Carter WB, et al. Designing metallic microlattices for energy absorber applications. Adv Eng Mater. 2014;16(3).

322. Wang S, Xu Y, Zhang W. Low-velocity impact response of 3D-printed lattice sandwich panels. IOP Conf Ser Mater Sci Eng. 2019;531(1).

323. Gao D, Wang S, Zhang M, Zhang C. Experimental and numerical investigation on in-plane impact behaviour of chiral auxetic structure. Compos Struct. 2021;267(December 2020).

324. Lu Q, Qi D, Li Y, Xiao D, Wu W. Impact energy absorption performances of

ordinary and hierarchical chiral structures. Thin-Walled Struct. 2019;140(March).

325. Wu W, Hu W, Qian G, Liao H, Xu X, Berto F. Mechanical design and multifunctional applications of chiral mechanical metamaterials: A review. Mater Des. 2019;180(June).

326. Ye M, Gao L, Wang F, Li H. A novel design method for energy absorption property of chiral mechanical metamaterials. Materials (Basel). 2021;14(18).

327. Kai L, Xiaofei C, Peng Z, WenWang W, Ying L. Dynamic mechanical performances of enhanced anti-tetra-chiral structure with rolled cross-section ligaments under impact loading. Int J Impact Eng. 2022;166(July 2021).

328. Xiang X, Qiang W, Hou B, Tran P, Lu G. Quasi-static and dynamic mechanical properties of Miura-ori metamaterials. Thin-Walled Struct. 2020;157(May).

329. Xiang X, Fu Z, Zhang S, Lu G, Ha NS, Liang Y, et al. The mechanical characteristics of graded Miura-ori metamaterials. Mater Des. 2021;211.

330. Liu Z, Liu J, Liu J, Zeng W, Huang W. The impact responses and failure mechanism of composite gradient reentrant honeycomb structure. Thin-Walled Struct. 2023;182(October 2022).

331. Özen İ, Çava K, Gedikli H, Alver Ü, Aslan M. Low-energy impact response of composite sandwich panels with thermoplastic honeycomb and reentrant cores. Thin-Walled Struct. 2020;156(August).

332. 2020 Carbon I. Carbon3D Riddell. https://www.carbon3d.com/riddell/. 2020.

333. Heimbs S, Cichosz J, Klaus M, Kilchert S, Johnson AF. Sandwich structures with textile-reinforced composite foldcores under impact loads. Compos Struct. 2010;92(6).

334. Heimbs S, Middendorf P, Kilchert S, Johnson AF, Maier M. Experimental and numerical analysis of composite folded sandwich core structures under compression. Appl Compos Mater. 2007;14(5–6).

335. Li Z, Chen W, Hao H. Crushing behaviours of folded kirigami structure with square dome shape. Int J Impact Eng. 2018;115(February).

336. Li Z, Chen W, Hao H. Numerical study of folded dome shape aluminium structure

against flatwise crushing. In: 12th International Converence on Shock & Impact Loads on Structures. 2017.

337. Teng TL, Liang CC, Nguyen VH. Innovative design of bicycle helmet liners. Proc Inst Mech Eng Part L J Mater Des Appl. 2014;228(4).

338. Townsend S, Adams R, Robinson M, Hanna B, Theobald P. 3D printed origami honeycombs with tailored out-of-plane energy absorption behavior. Mater Des. 2020;195.

339. Li Z, Chen W, Hao H, Cui J, Shi Y. Experimental study of multi-layer folded truncated structures under dynamic crushing. Int J Impact Eng. 2019;131(May).

340. Li Z, Chen W, Hao H. Numerical study of open-top truncated pyramid folded structures with interconnected side walls against flatwise crushing. Thin-Walled Struct. 2018;132(September).

341. Li Z, Chen W, Hao H. Blast mitigation performance of cladding using square dome-shape kirigami folded structure as core. Int J Mech Sci. 2018;145(July).

342. Warrior Europe Inc. Warrior Alpha One Helmets. https://www.warrioreurope.com/alpha-one-helmets. 2020.

343. Defense 2020 Viconic. Viconic Defense. http://www.viconicdefense.com/. 2020.

344. Sporting 2023 Viconic. Viconic Sporting [Internet]. 2023.

345. Platus DL. Negative Stiffness Mechanism. In: Technology MK. 1999. p. 98–105.

346. Lakes RS, Drugan WJ. Dramatically stiffer elastic composite materials due to a negative stiffness phase? J Mech Phys Solids. 2002;50(5).

347. Churchill CB, Shahan DW, Smith SP, Keefe AC, McKnight GP. Materials Engineering: Dynamically variable negative stiffness structures. Sci Adv. 2016;2(2).

348. Hewage TAM, Alderson KL, Alderson A, Scarpa F. Double-Negative Mechanical Metamaterials Displaying Simultaneous Negative Stiffness and Negative Poisson’s Ratio Properties. Adv Mater. 2016;28(46).

349. Ha CS, Lakes RS, Plesha ME. Cubic negative stiffness lattice structure for energy absorption: Numerical and experimental studies. Int J Solids Struct.

2019;178–179.

350. Zhang K, Qi L, Zhao P, Zhao C, Deng Z. Buckling induced negative stiffness mechanical metamaterial for bandgap tuning. Compos Struct. 2023;304(P2).

351. Goldsberry BM, Haberman MR. Negative stiffness honeycombs as tunable elastic metamaterials. J Appl Phys. 2018;123(9).

352. Pan F, Li Y, Li Z, Yang J, Liu B, Chen Y. 3D Pixel Mechanical Metamaterials. Adv Mater. 2019;31(25).

353. Gibson LJ, Ashby MF. Cellular solids. Structure and properties. Cambridge: Press Syndicate of the University of Cambridge; 1997. 4, 67, 103, 106, 167–169, 176–183, 259–264, 286 p.

354. Masters IG, Evans KE. Models for the elastic deformation of honeycombs. Compos Struct. 1996;35(4).

355. Johnston R, Kazancı Z. Analysis of additively manufactured (3D printed) dual-material auxetic structures under compression. Addit Manuf. 2021;38(September 2020).

356. Wang K, Chang YH, Chen YW, Zhang C, Wang B. Designable dual-material auxetic metamaterials using three-dimensional printing. Mater Des. 2015;67.

357. Smith JO. Spectral Audio Signal Processing. W3K Publishing; 2010.

358. Shrout PE, Fleiss JL. Intraclass correlations: uses in assessing rater reliability. Psychol Bull. 1979;86(2).

359. Rankin G, Stokes M. Reliability of assessment tools in rehabilitation: An illustration of appropriate statistical analyses. Clin Rehabil. 1998;12(3).

360. Rowson S, Duma SM, Beckwith JG, Chu JJ, Greenwald RM, Crisco JJ, et al. Rotational head kinematics in football impacts: An injury risk function for concussion. Ann Biomed Eng. 2012;40(1).

361. Liu K, Aponte DI, Greencorn DJ, Robbins SM, Pearsall DJ. Are headforms a poor surrogate for helmet fit? Proc Inst Mech Eng Part P J Sport Eng Technol. 2019;234(2).

362. Timoshenko SP, Gere JM, Prager W. Theory of Elastic Stability, Second Edition.

2nd ed. Vol. 29, Journal of Applied Mechanics. McGraw Hill Book Company, Inc.; 1962. 46–51 p.

363. Petousis M, Vidakis N, Mountakis N, Karapidakis E, Moutsopoulou A. Compressive response versus power consumption of acrylonitrile butadiene styrene in material extrusion additive manufacturing: the impact of seven critical control parameters. Int J Adv Manuf Technol. 2023;

364. Shepherd T, Winwood K, Venkatraman P, Alderson A, Allen T. Validation of a Finite Element Modeling Process for Auxetic Structures under Impact. Phys Status Solidi Basic Res. 2020;257(10).

365. International Organization for Standardization. BS ISO 37:2017 - Rubber, vulcanized or thermoplastic - Determination of tensile stress-strain properties. 2017.

366. Extrudr. Technisches Datenblatt TPU Flex Medium. 2020.

367. Copper3D. MD Flex Antibacterial Nanocomposite. 2010.

368. Ultimaker. Technical data sheet TPU 95A. 2017.

369. NinjaTek. NinjaFlex® 3D Printing Filament: Flexible Polyurethane Material for FDM Printers. 2016.

370. Timoshenko S, Goodier JN. Theory Of Elasticity. 1951.

371. Pro R. Technical Document RS PRO - PLA PRO+ [Internet]. 2023.

372. Garrett SJ. Chapter 13 Introductory Numerical Methods. Introduction to Actuarial and Financial Mathematical Methods. 2015. 425–426 p.

9. Chapter - Appendices

Appendix 1 – Acceleration vs. time traces from free-fall drop tests

A.1.1: Representative linear acceleration [g] vs. time [ms] traces of all five helmets and unhelmeted impacts for flat surface, Front site impacts onto the (**A**) MEP Pad, (**B**) 24 mm foam layer, (**C**) 48 mm foam layer, (**D**) 72 mm foam layer, and (**E**) 96 mm foam layer.

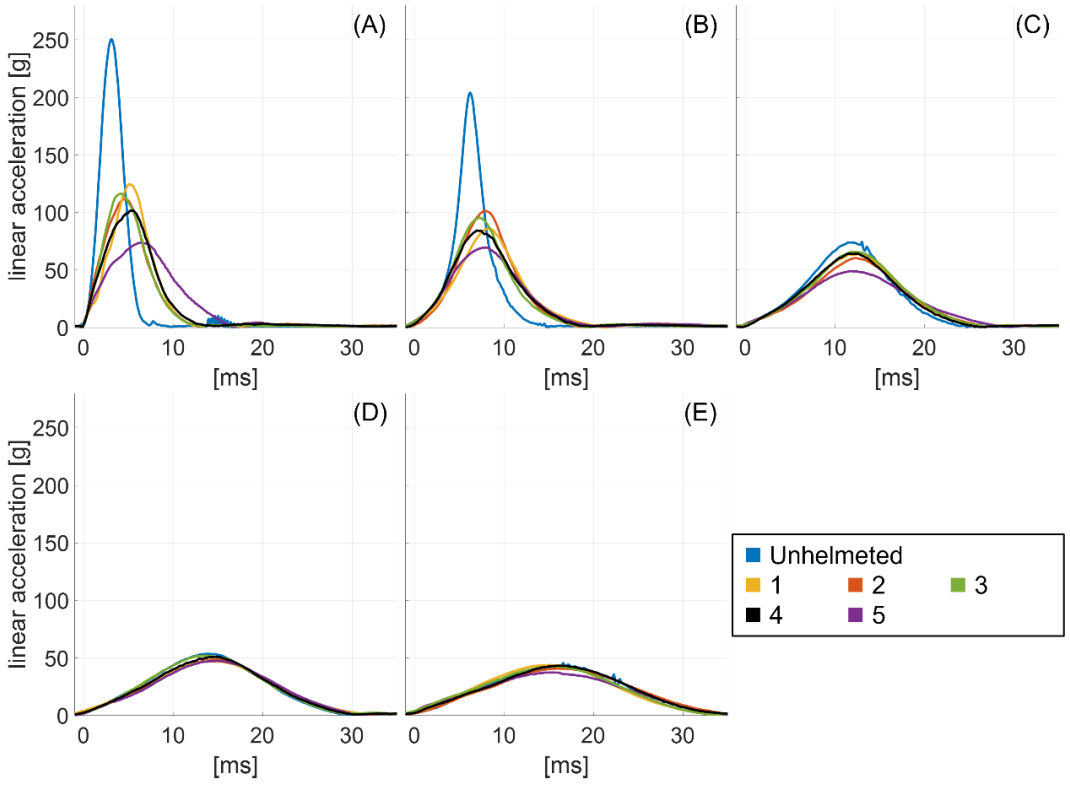

A.1.2: Representative linear acceleration [g] vs. time [ms] traces of all five helmets and unhelmeted impacts for flat surface, Rear site impacts onto the (**A**) MEP Pad, (**B**) 24 mm foam layer, (**C**) 48 mm foam layer, (**D**) 72 mm foam layer, and (**E**) 96 mm foam layer.

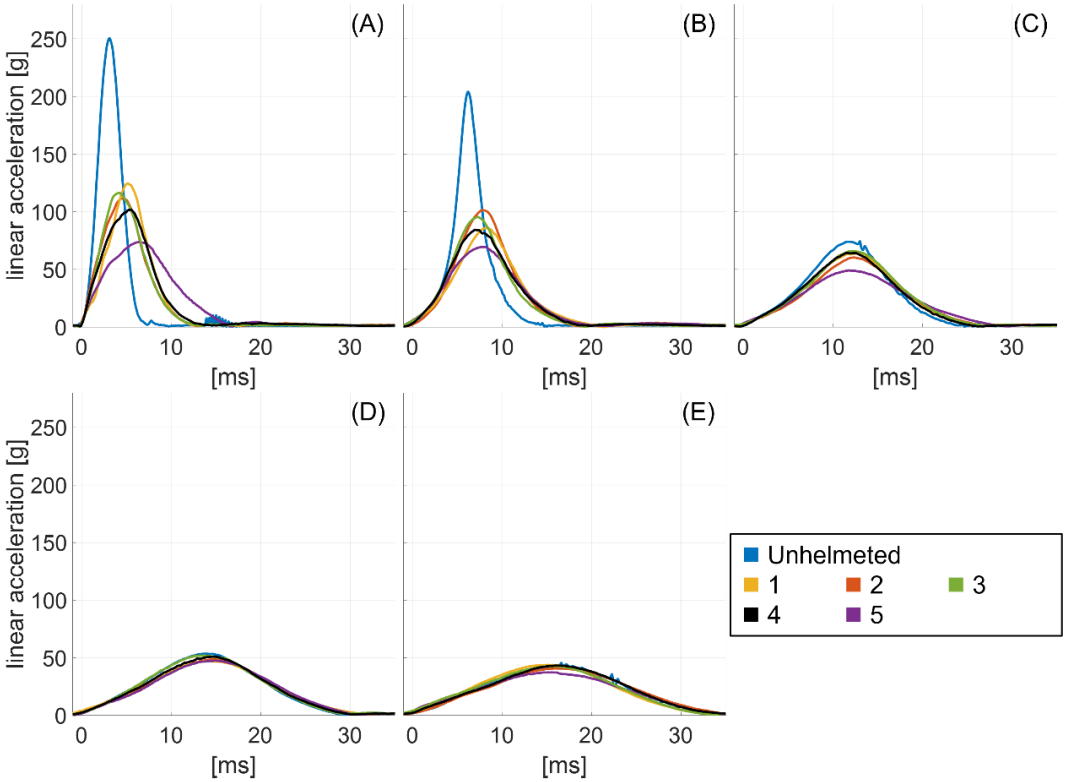

A.1.3: Representative linear acceleration [g] vs. time [ms] traces of all five helmets and unhelmeted impacts for flat surface, Side site impacts onto the (**A**) MEP Pad, (**B**) 24 mm foam layer, (**C**) 48 mm foam layer, (**D**) 72 mm foam layer, and (**E**) 96 mm foam layer.

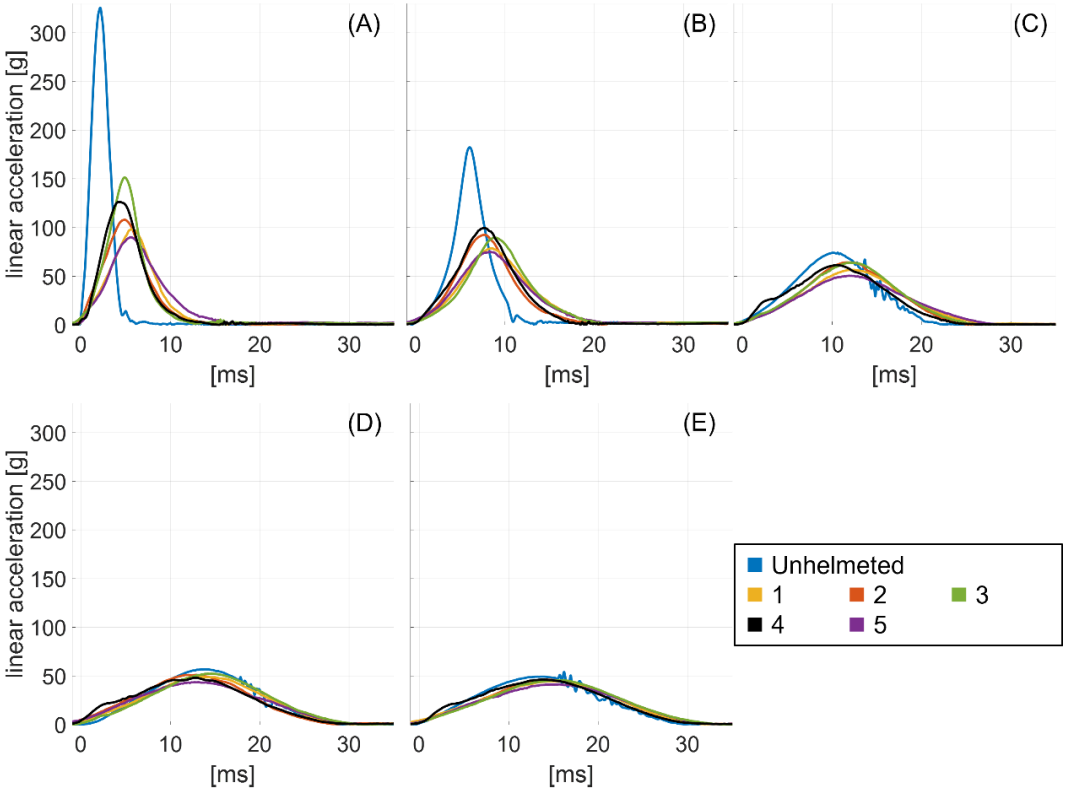

A.1.4: Representative (**A – C**) linear [g] and (**D – E**) angular [krad/s²] acceleration vs time [ms] traces of all five helmets and unhelmeted impacts for oblique surface, FrontBoss site impacts onto (**A**) & (**D**) 24 mm foam layer, (**B**) & (**E**) 48 mm foam layer, and (**C**) & (**F**) 72 mm foam layer.

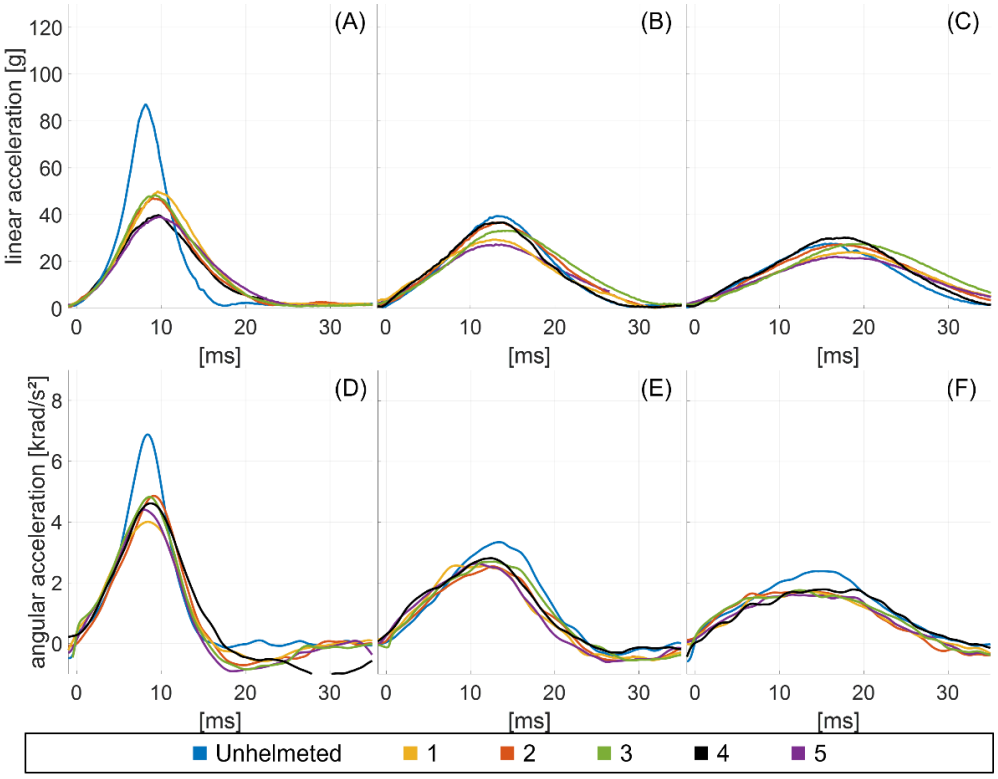

A.1.5: Representative (**A – C**) linear [g] and (**D – E**) angular [krad/s²] acceleration vs time [ms] traces of all five helmets and unhelmeted impacts for oblique surface, RearBoss site impacts onto (**A**) & (**D**) 24 mm foam layer, (**B**) & (**E**) 48 mm foam layer, and (**C**) & (**F**) 72 mm foam layer.

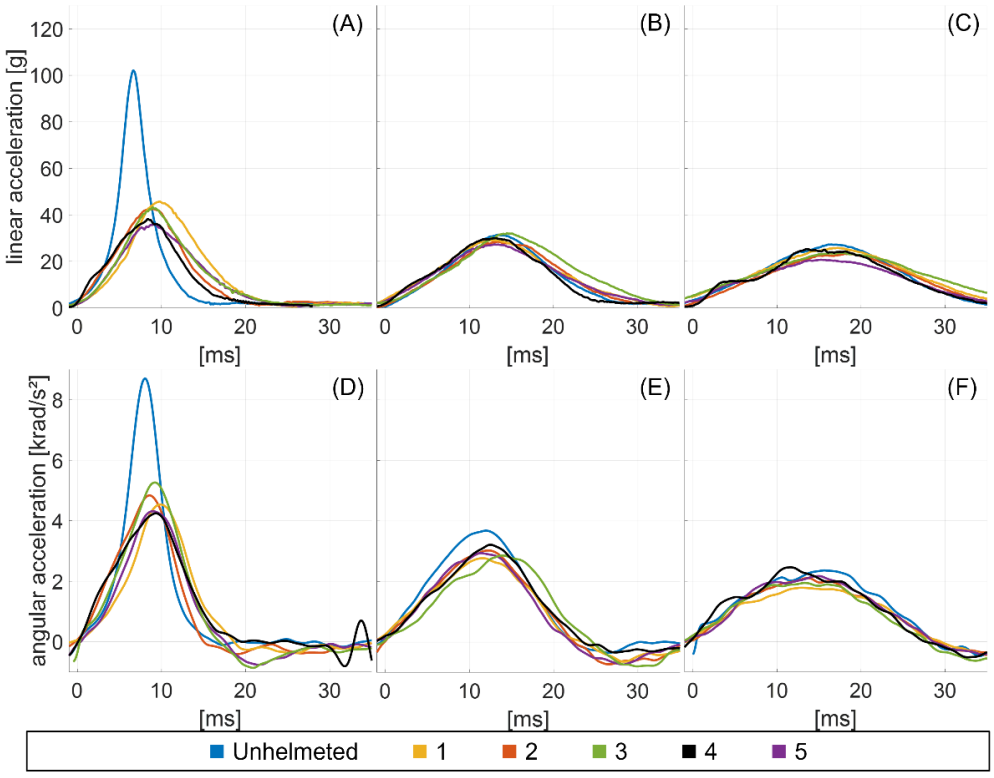

A.1.6: Representative (**A – C**) linear [g] and (**D – E**) angular [krad/s²] acceleration vs time [ms] traces of all five helmets and unhelmeted impacts for oblique surface, Rear site impacts onto (**A**) & (**D**) 24 mm foam layer, (**B**) & (**E**) 48 mm foam layer, and (**C**) & (**F**) 72 mm foam layer.

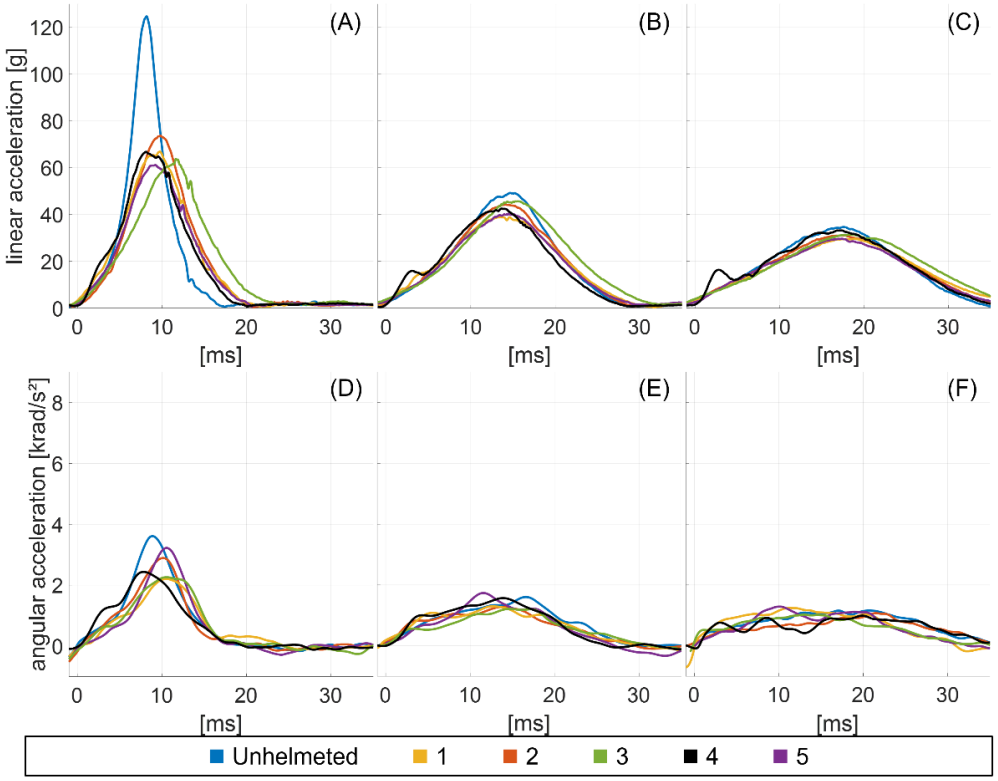

A.1.7: Representative (**A – C**) linear [g] and (**D – E**) angular [krad/s²] acceleration vs time [ms] traces of all five helmets and unhelmeted impacts for oblique surface, Side site impacts onto (**A**) & (**D**) 24 mm foam layer, (**B**) & (**E**) 48 mm foam layer, and (**C**) & (**F**) 72 mm foam layer.

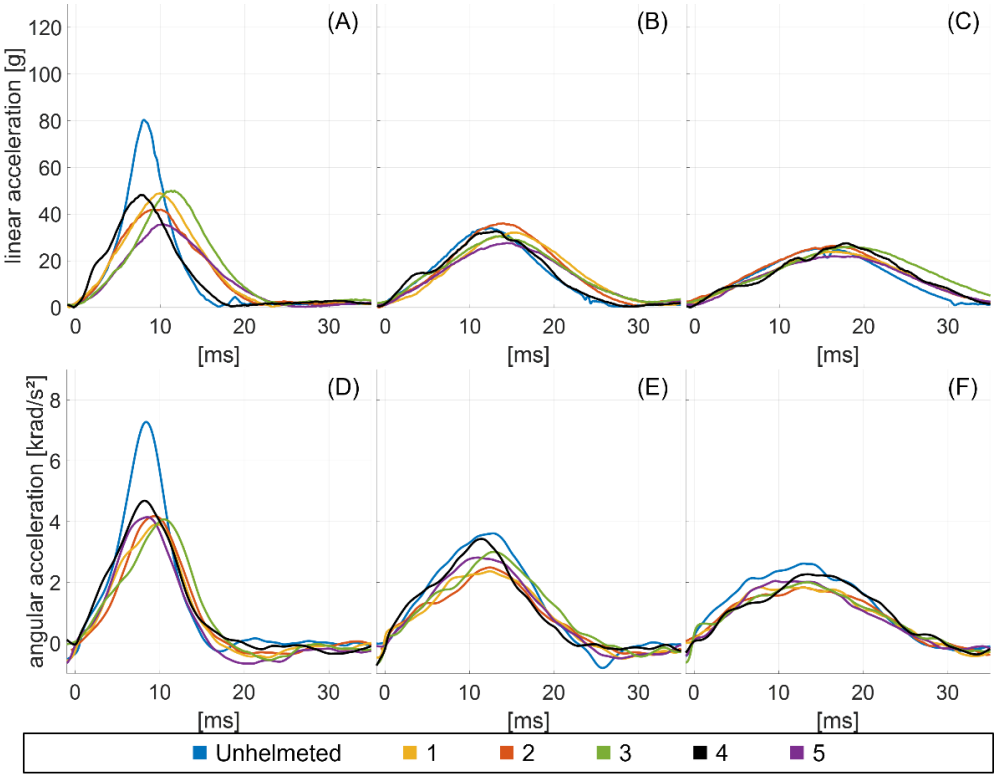

Appendix 2 – Head impact metrics from free-fall drop tests

A.2.8: Mean peak acceleration [g] with standard deviation error bars for all flat surface (**A**) Front, (**B**) Rear, and (**C**) Side site impacts.

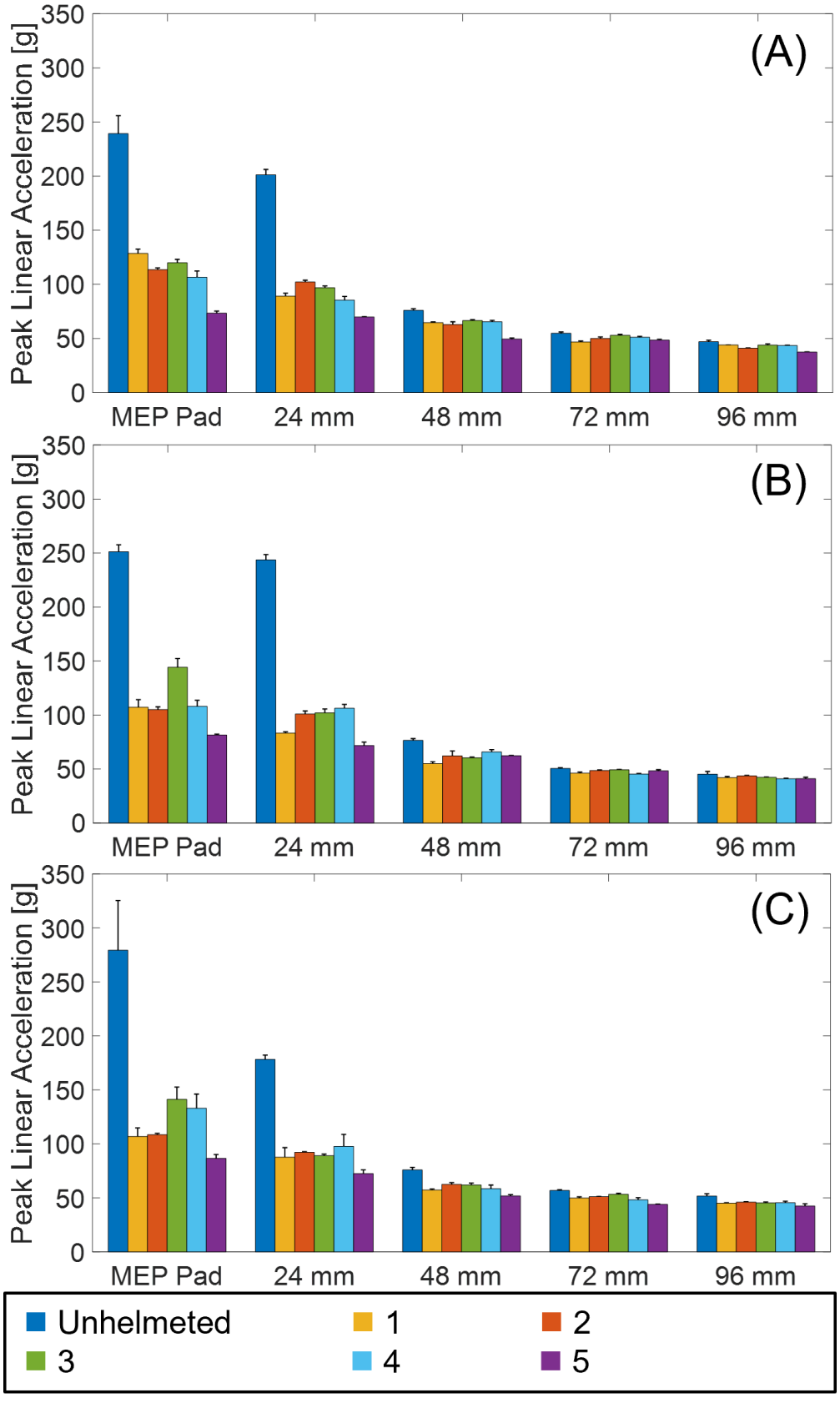

A.2.9: Mean impact duration [ms] with standard deviation error bars and horizontal bars indicating the proportion of time to peak (bottom half) and rebound time (top half) for all flat surface (**A**) Front, (**B**) Rear, and (**C**) Side site impacts.

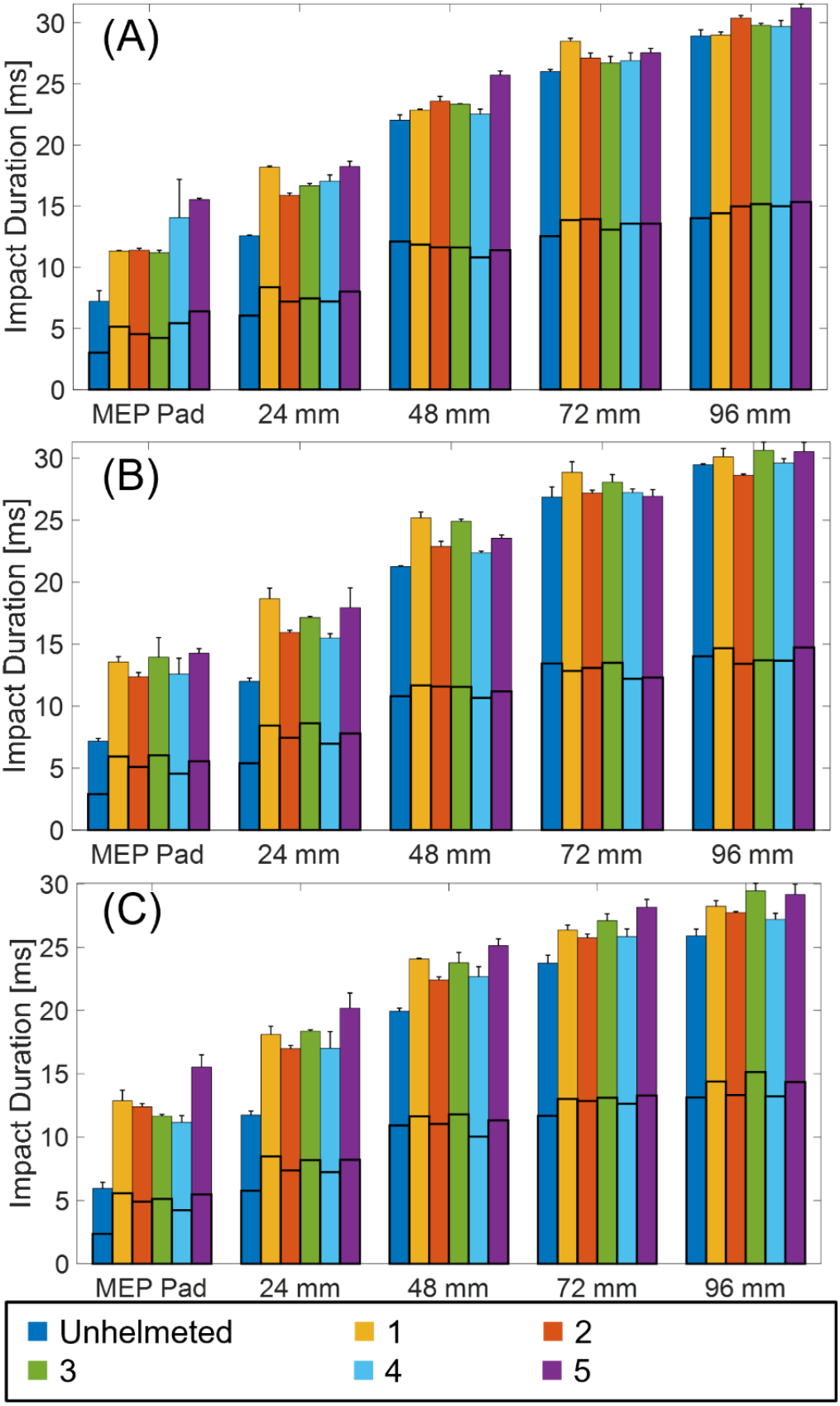

A.2.10: Mean percentage with standard deviation error bars of time to peak of the total impact duration for all flat surface (**A**) Front, (**B**) Rear, and (**C**) Side site impacts.

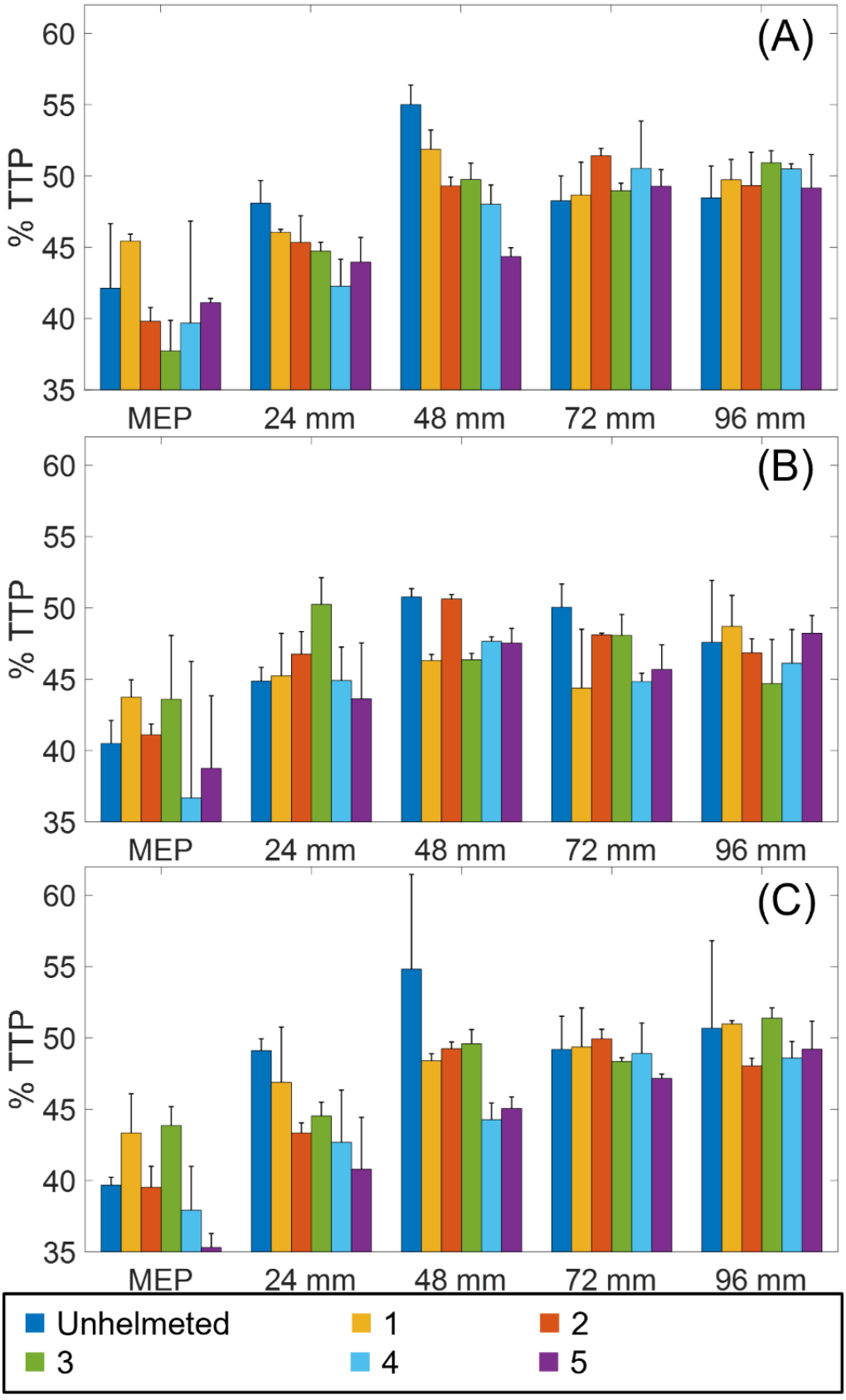

A.2.11: Mean HIC with standard deviation error bars for all flat surface (**A**) Front, (**B**) Rear, and (**C**) Side site impacts.

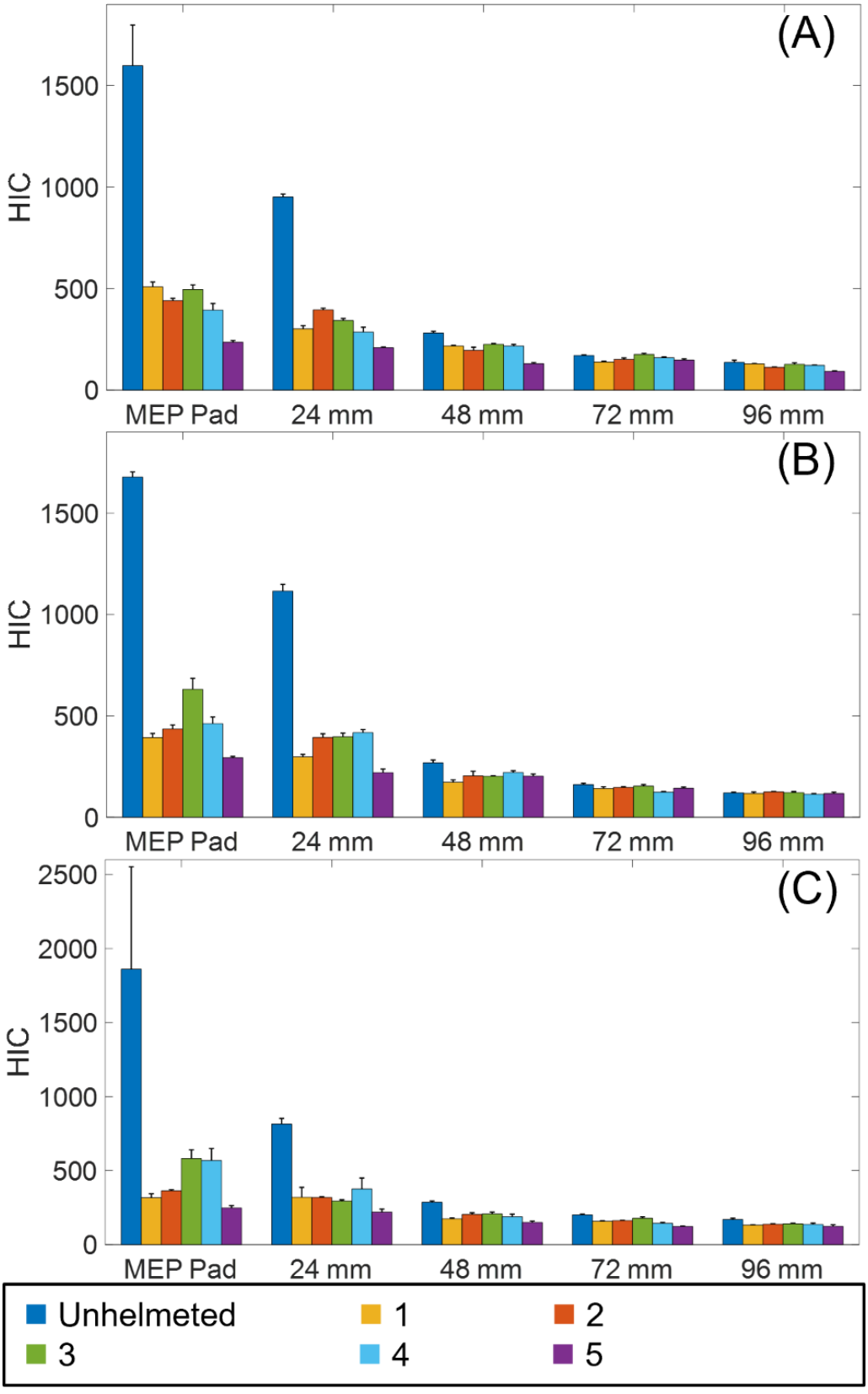

A.2.12: Mean SI with standard deviation error bars for all flat surface (**A**) Front, (**B**) Rear, and (**C**) Side site impacts.

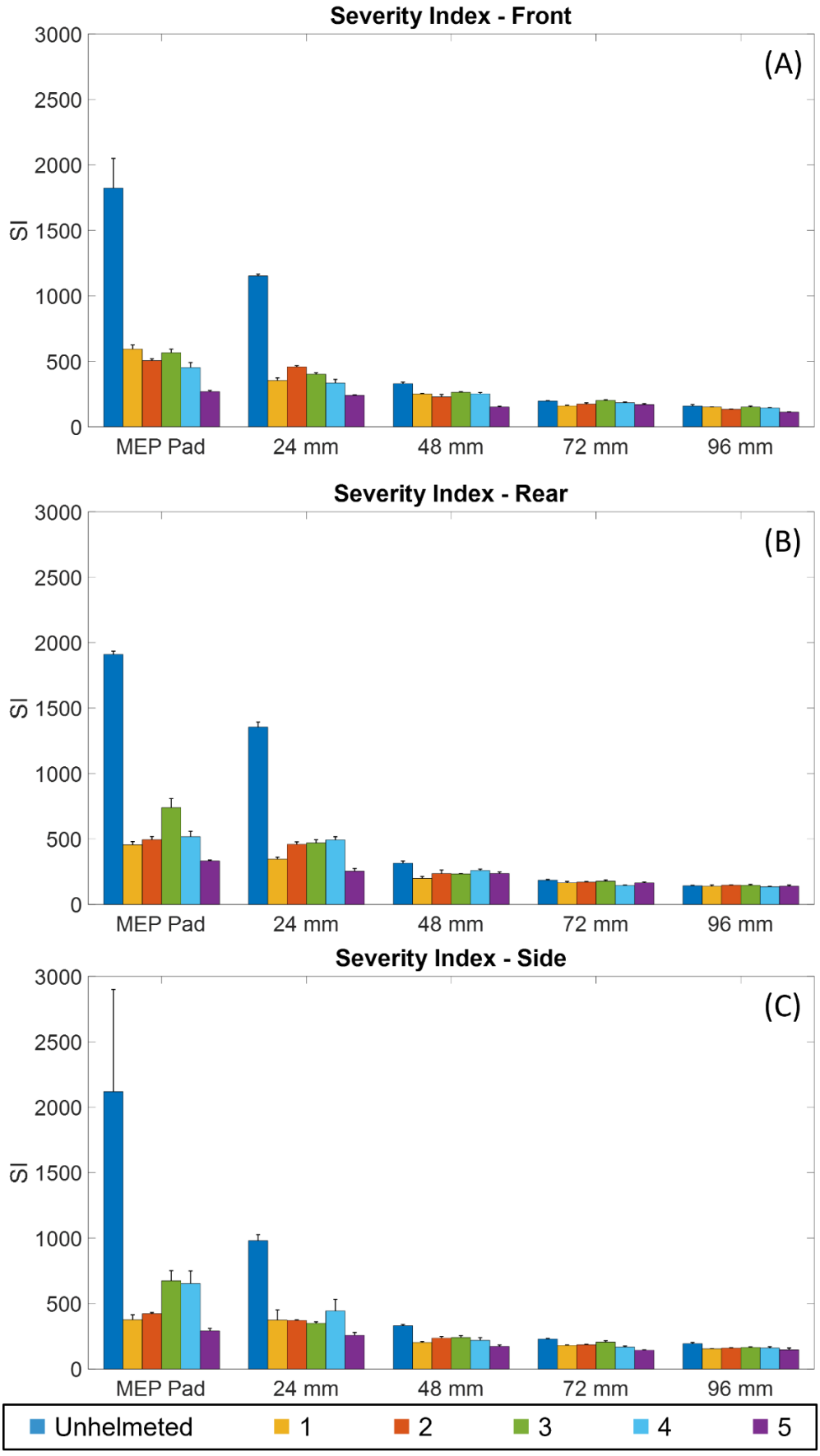

A.2.13: Mean peak linear acceleration [g] with standard deviation error bars for all oblique surface (**A**) FrontBoss, (**B**) RearBoss, (**C**) Rear, and (**D**) Side site impacts.

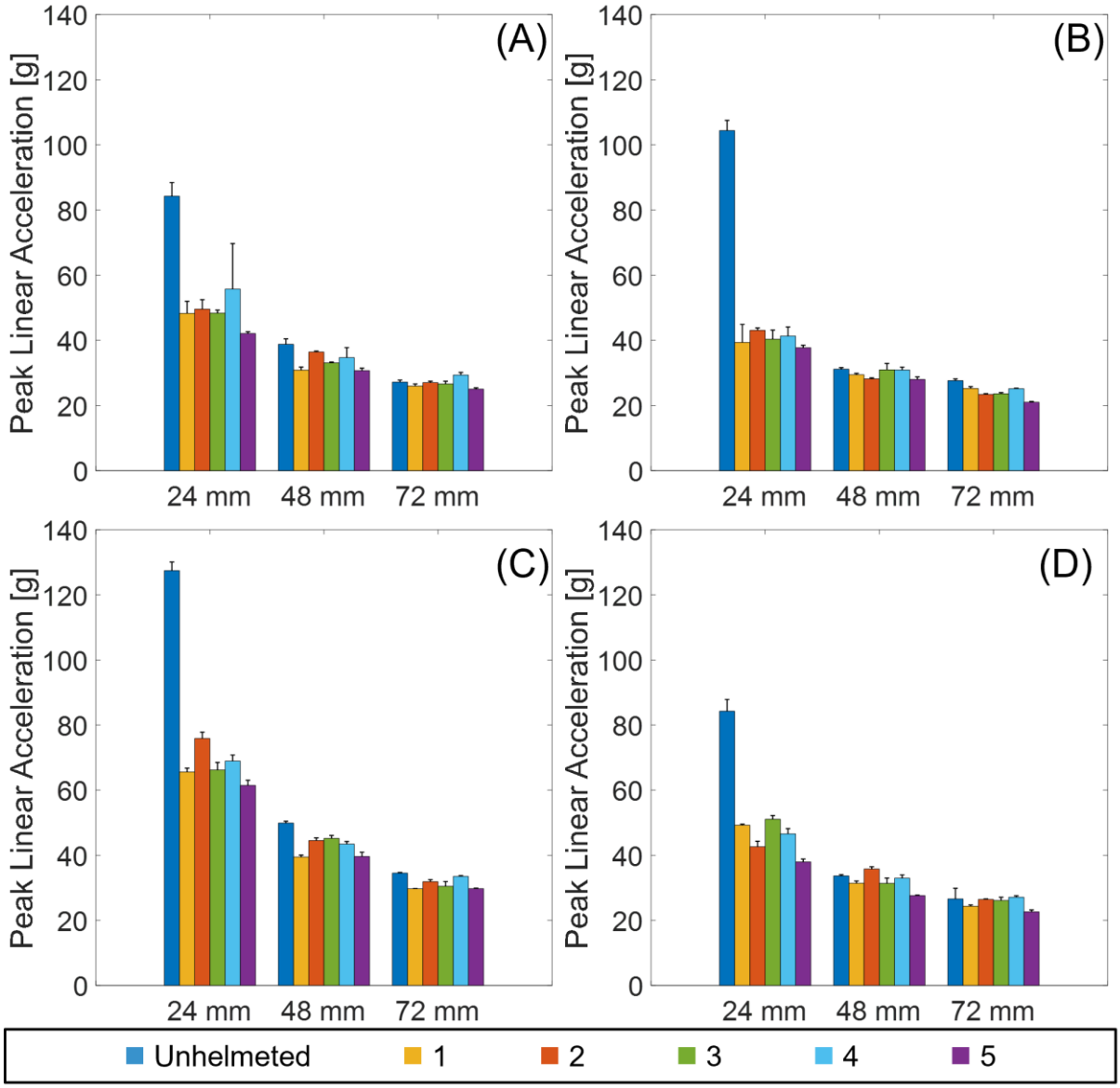

A.2.14: Mean peak angular acceleration [krad/s²] with standard deviation error bars for all oblique surface (**A**) FrontBoss, (**B**) RearBoss, (**C**) Rear, and (**D**) Side site impacts.

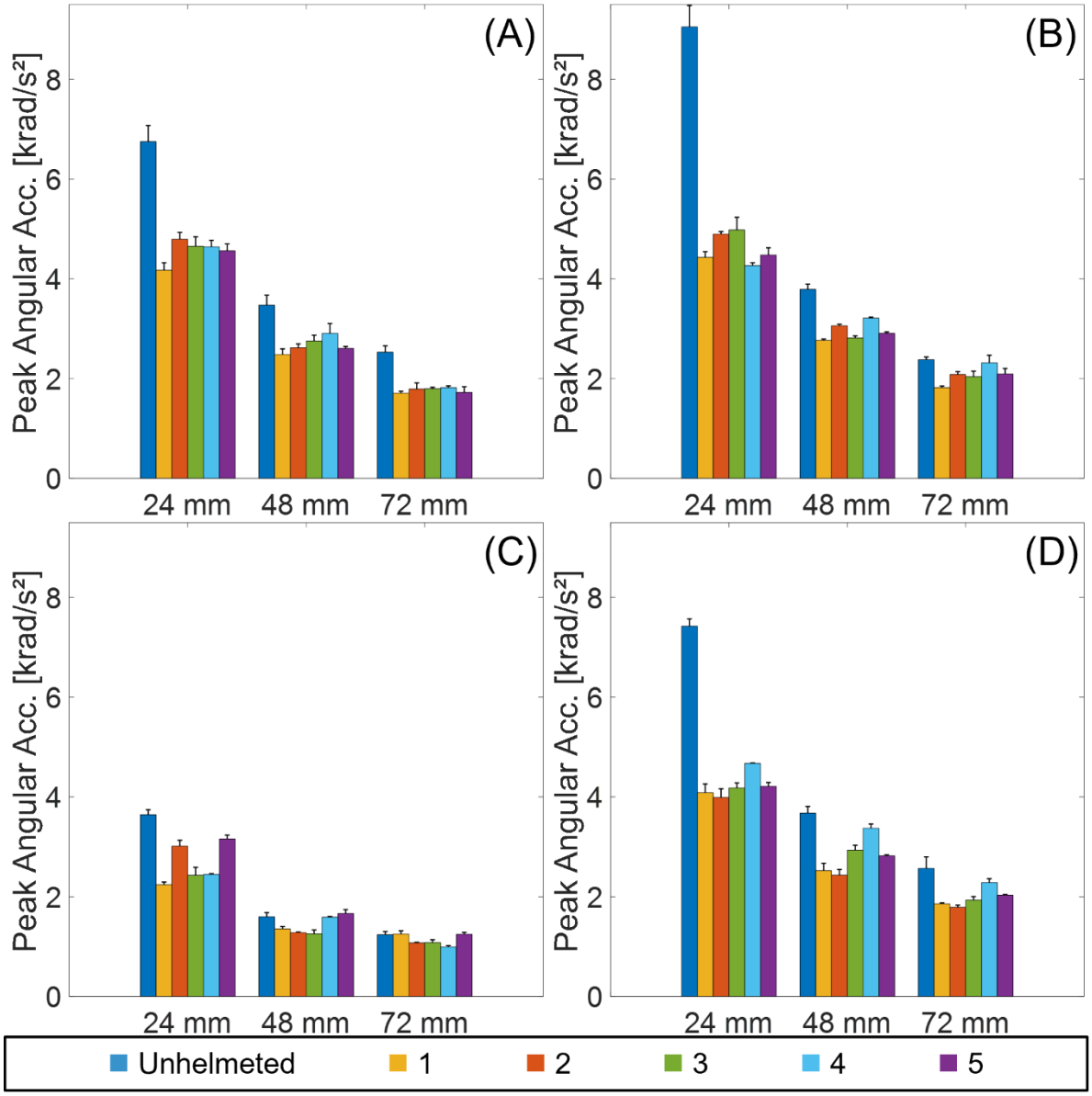

A.2.15: Mean impact durations [ms] with standard deviation error bars and horizontal bars indicating the proportion of time to peak (bottom half) and rebound time (top half) for all oblique surface (**A**) FrontBoss, (**B**) RearBoss, (**C**) Rear, and (**D**) Side site impacts.

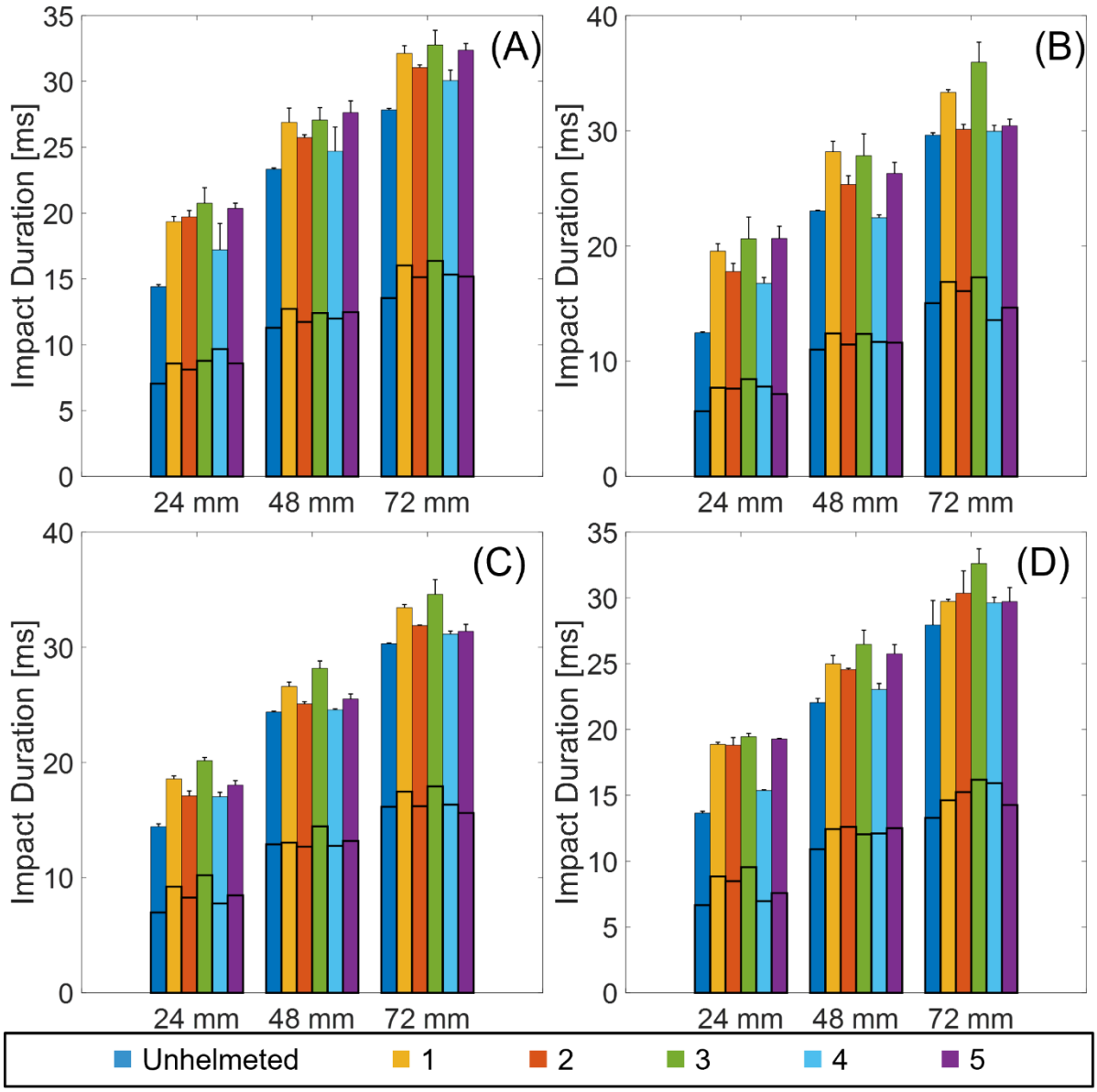

A.2.16: Mean percentage with standard deviation error bars of time to peak of the total impact duration for all oblique surface (**A**) FrontBoss, (**B**) RearBoss, (**C**) Rear, and (**D**) Side site impacts.

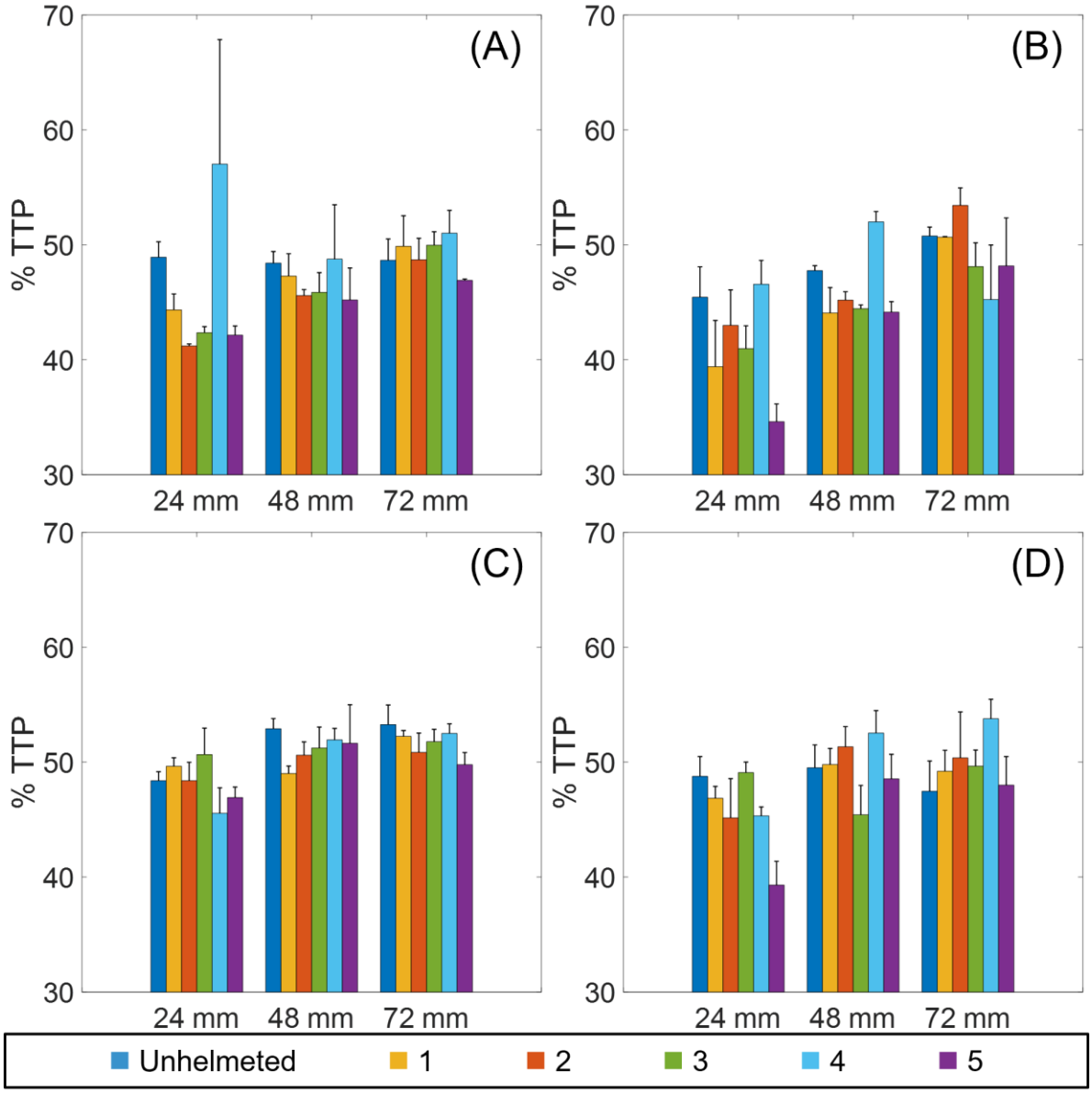

A.2.17: Mean HIC with standard deviation error bars for all oblique surface (**A**) FrontBoss, (**B**) RearBoss, (**C**) Rear, and (**D**) Side site impacts.

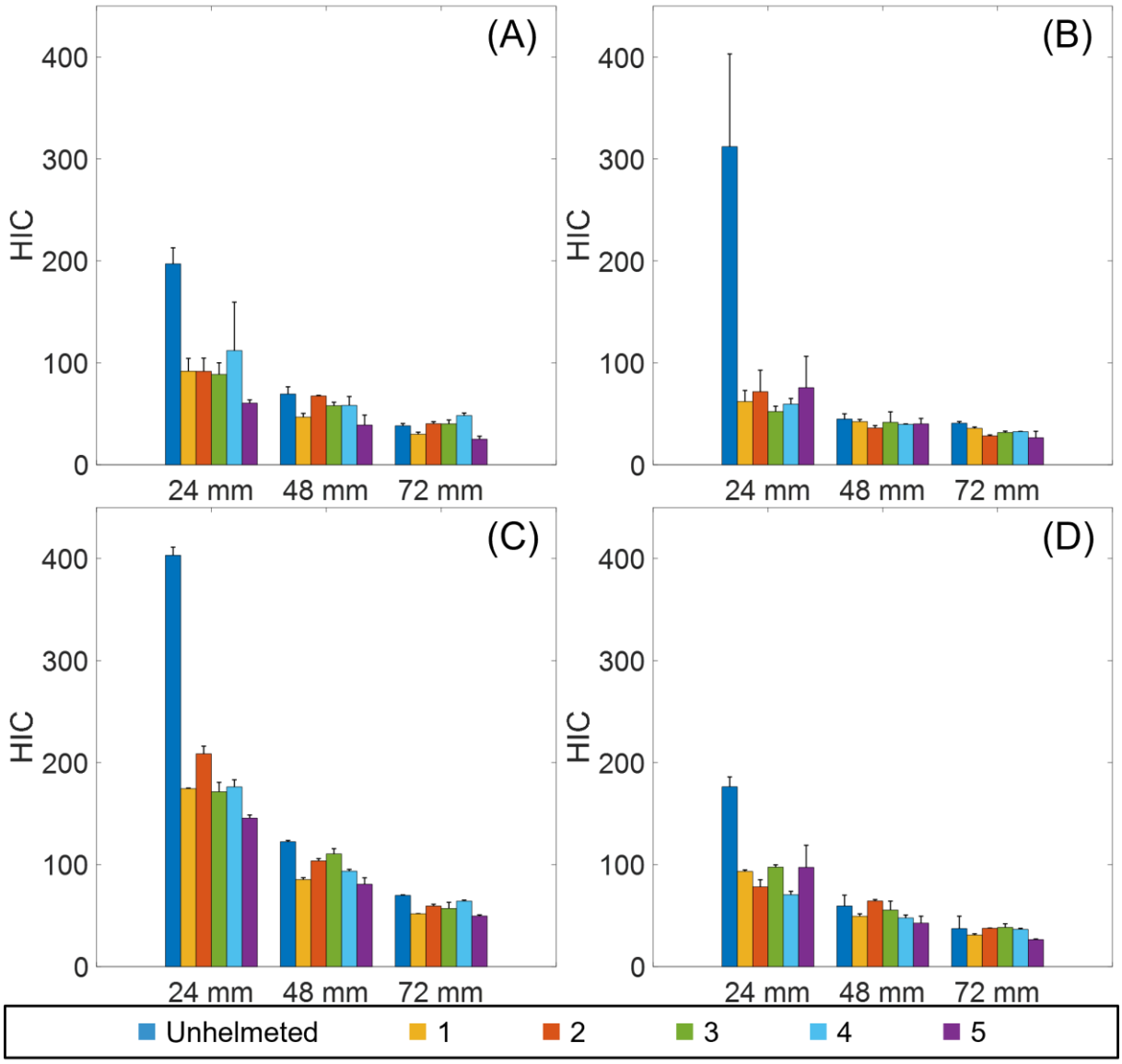

A.2.18: Mean RIC with standard deviation error bars for all oblique surface (**A**) FrontBoss, (**B**) RearBoss, (**C**) Rear, and (**D**) Side site impacts.

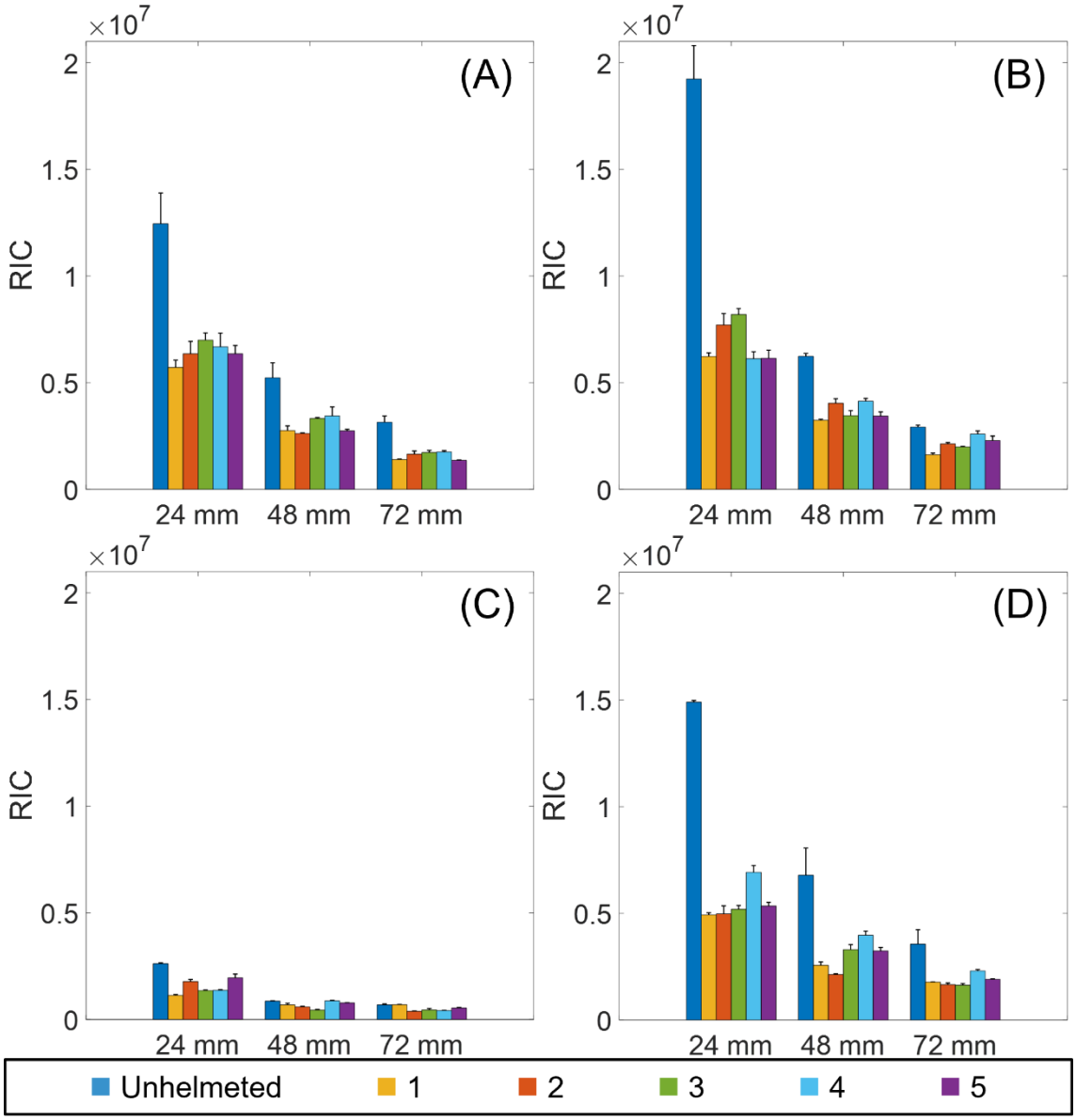

A.2.19: Mean SI with standard deviation error bars for all oblique surface (**A**) Front, (**B**) FrontBoss, (**C**) Rear, (**D**) RearBoss, and (**E**) Side site impacts.

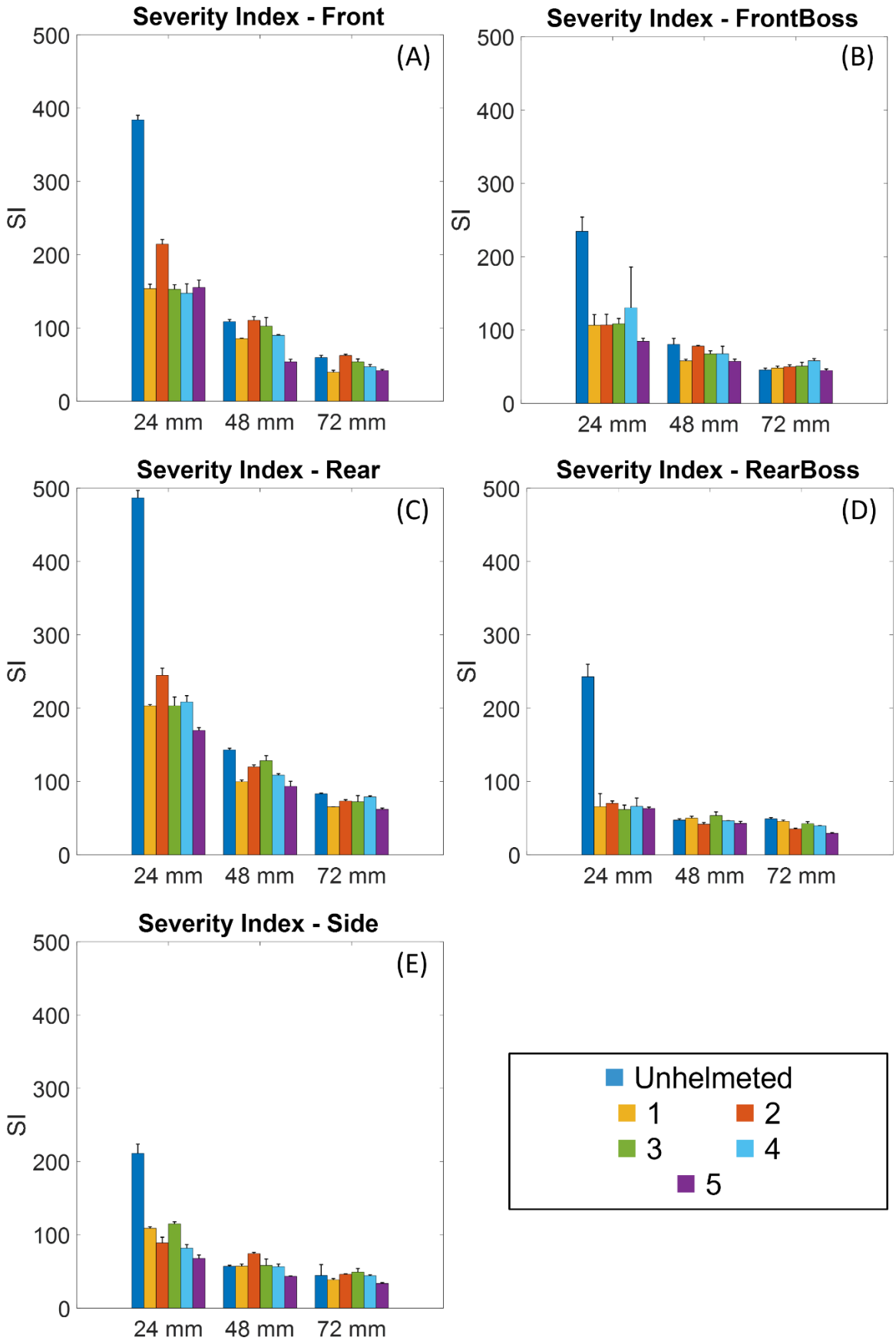

A.2.20: Mean BrIC with standard deviation error bars for all oblique surface (**A**) Front, (**B**) FrontBoss, (**C**) Rear, (**D**) Rear, and (**E**) Side site impacts.

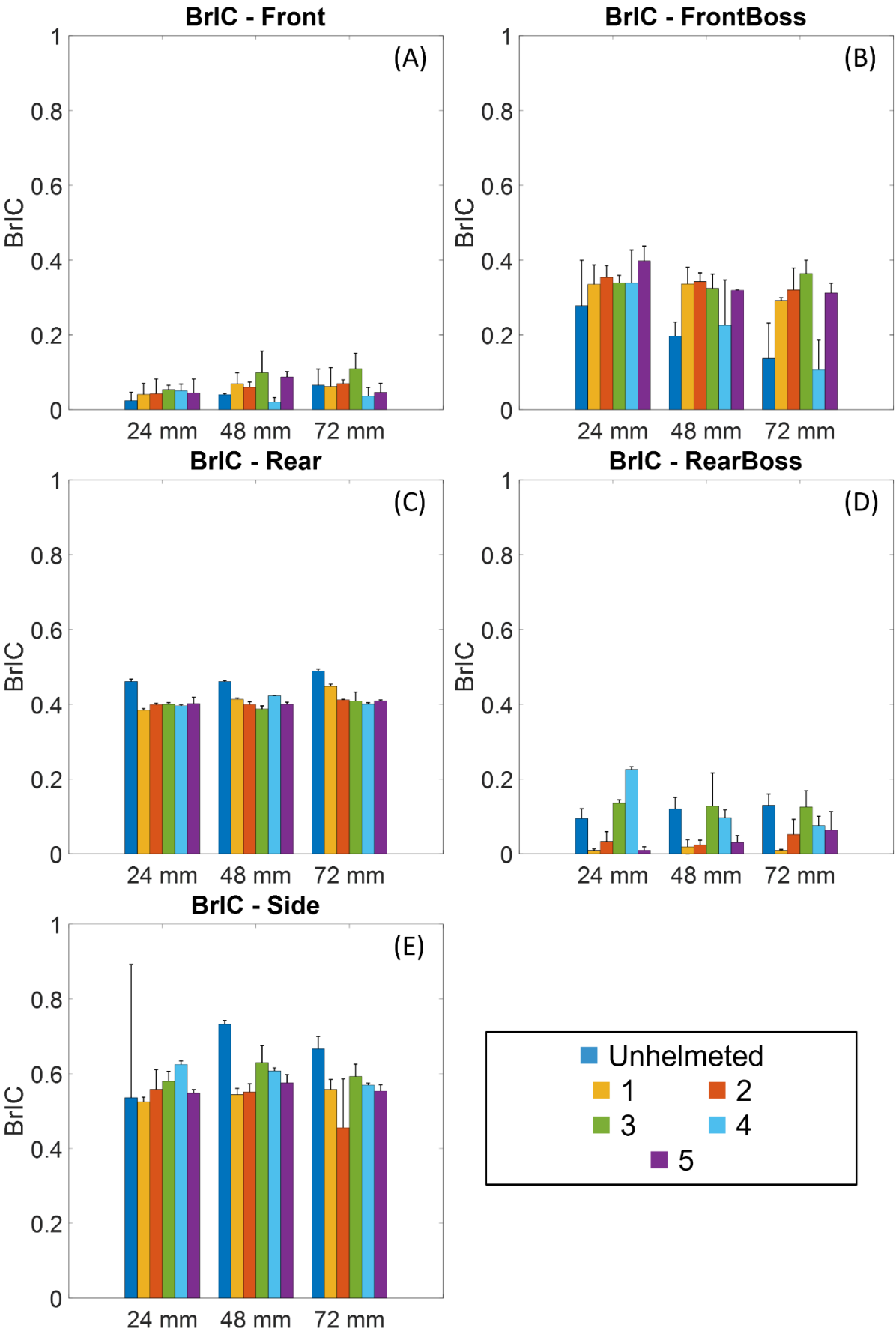

A.2.21: Mean BrIC with standard deviation error bars for all oblique surface (**A**) Front, (**B**) FrontBoss, (**C**) Rear, (**D**) RearBoss, and (**E**) Side site impacts.

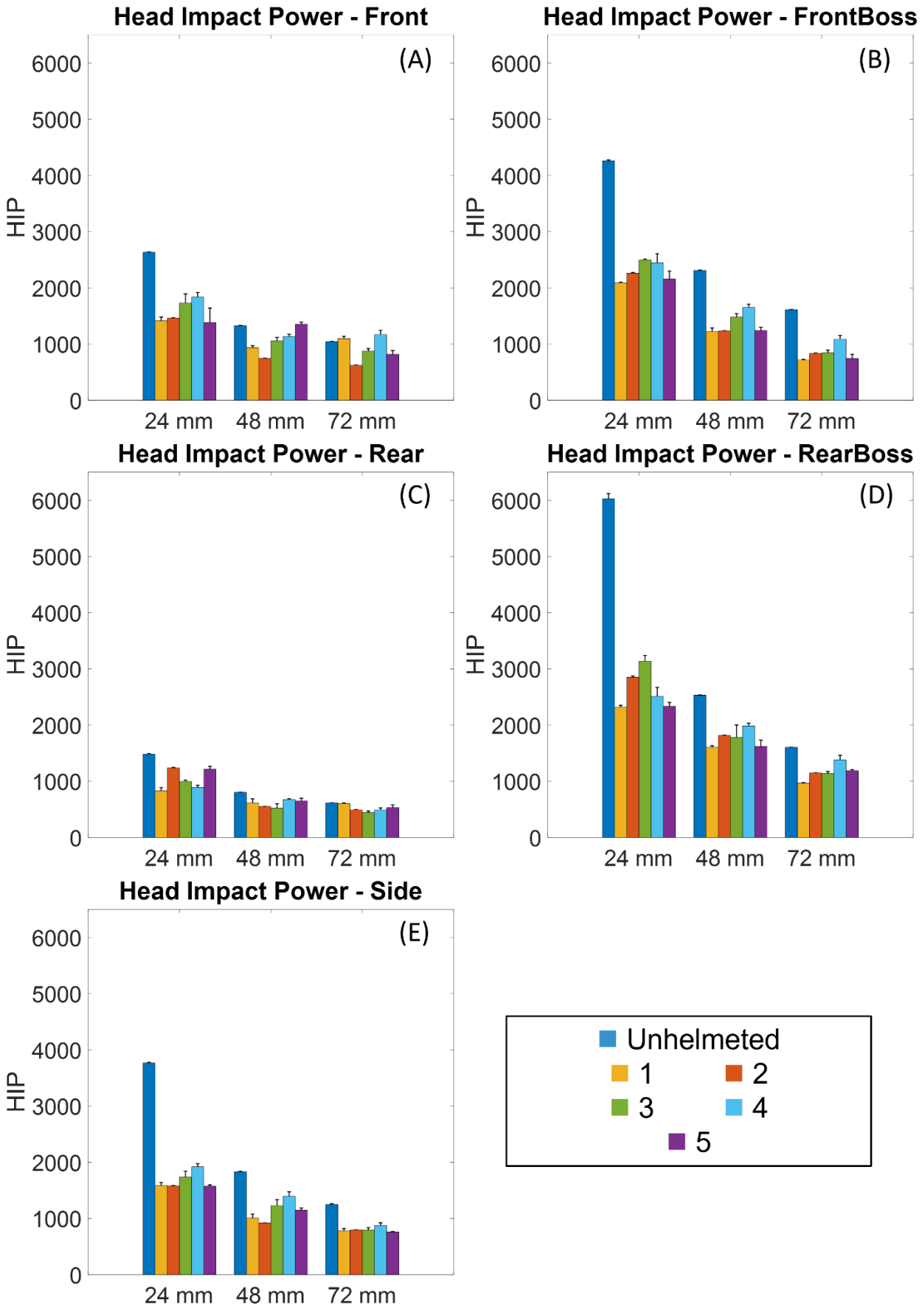

Appendix 3 – Force vs. displacement traces from bi-beam compression tests

A.3.22: Force [N] vs. displacement [mm] traces of uniaxial compression tests of individual bi-beam at (**A**) 0.83 s^{-1}, (**B**) 8.3 s^{-1}, and (**C**) 83 s^{-1} strain rate.

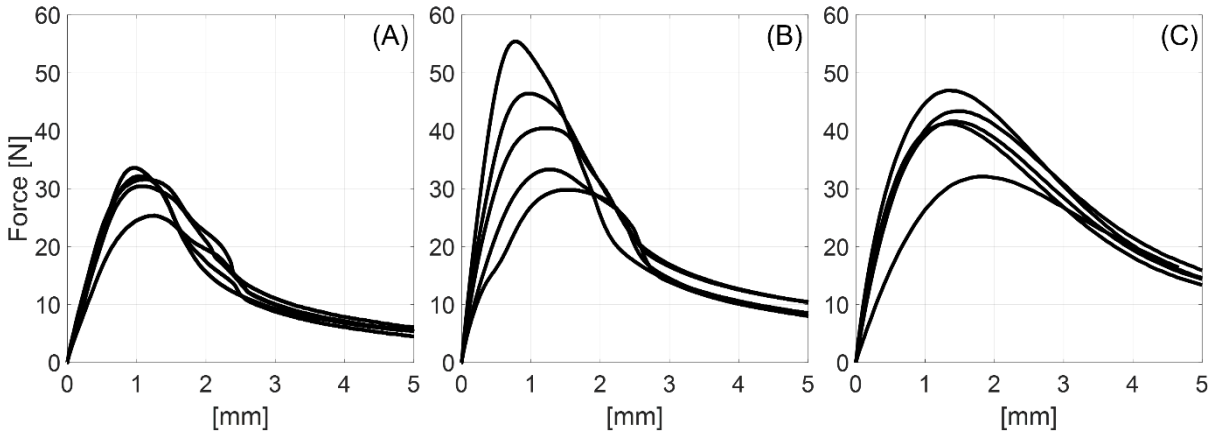

A.3.23: Force [N] vs. displacement [mm] traces of uniaxial compression tests of unit cells buckling "out" at (**A**) 0.83 s^{-1}, (**B**) 8.3 s^{-1}, and (**C**) 83 s^{-1} strain rate.

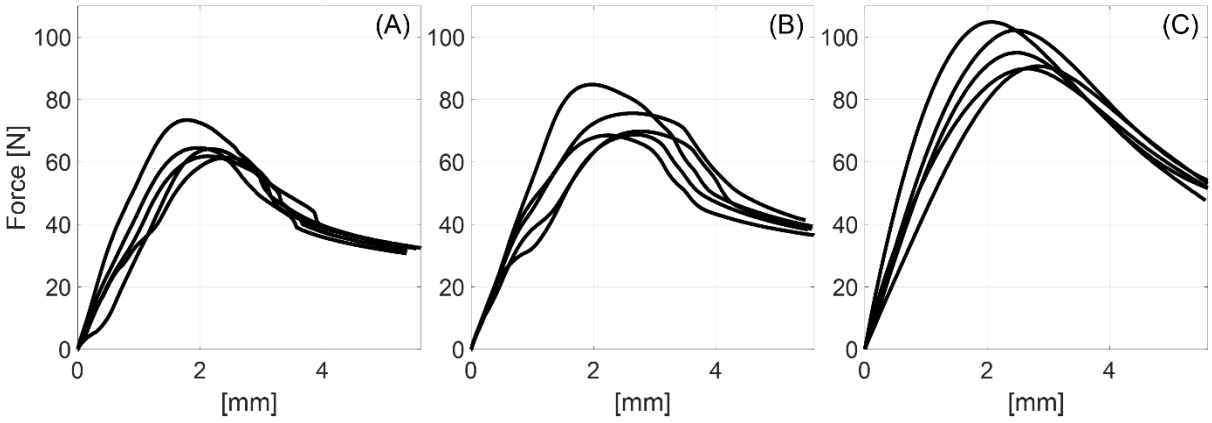

A.3.24: Force [N] vs. displacement [mm] traces of uniaxial compression tests of unit cells buckling "in" with a 2 mm gap at (**A**) 0.83 s^{-1}, (**B**) 8.3 s^{-1}, and (**C**) 83 s^{-1} strain rate.

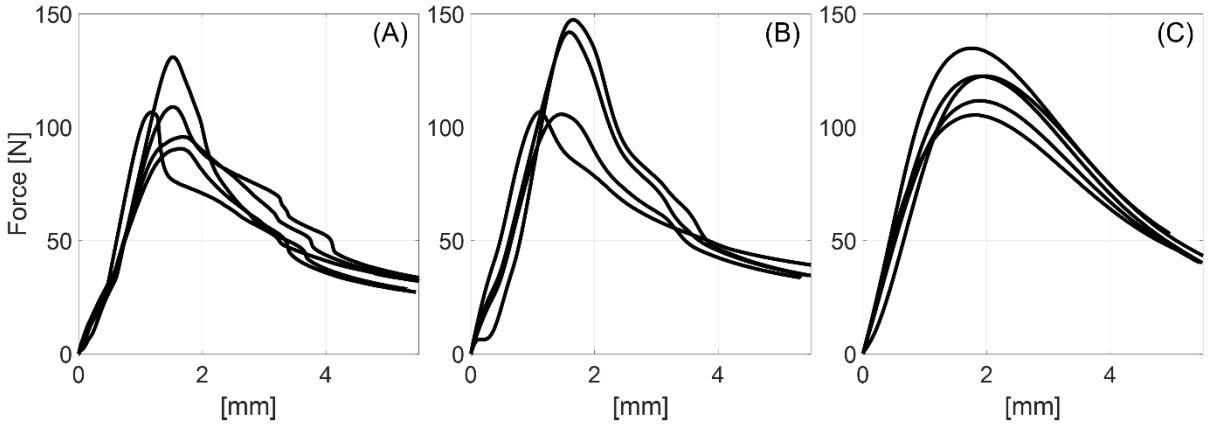

A.3.25: Force [N] vs. displacement [mm] traces of uniaxial compression tests of unit cells buckling "in" with a 10 mm gap at (**A**) 0.83 s^{-1}, (**B**) 8.3 s^{-1}, and (**C**) 83 s^{-1} strain rate.

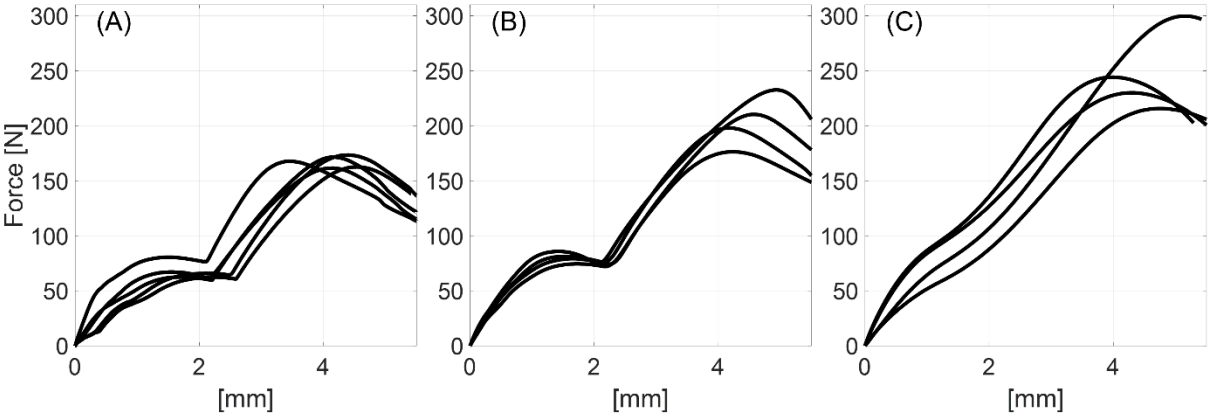

Appendix 4 – Force vs. time traces from cellular structure impact tests

A.4.26: Force [N] vs. time [ms] traces for impacts onto cellular structures consisting of four bi-beam unit cells from a drop height of (**A**) 20 cm, (**B**) 40 cm, and (**C**) 60 cm. Line colour represents the number of unit cells making contact during compression.

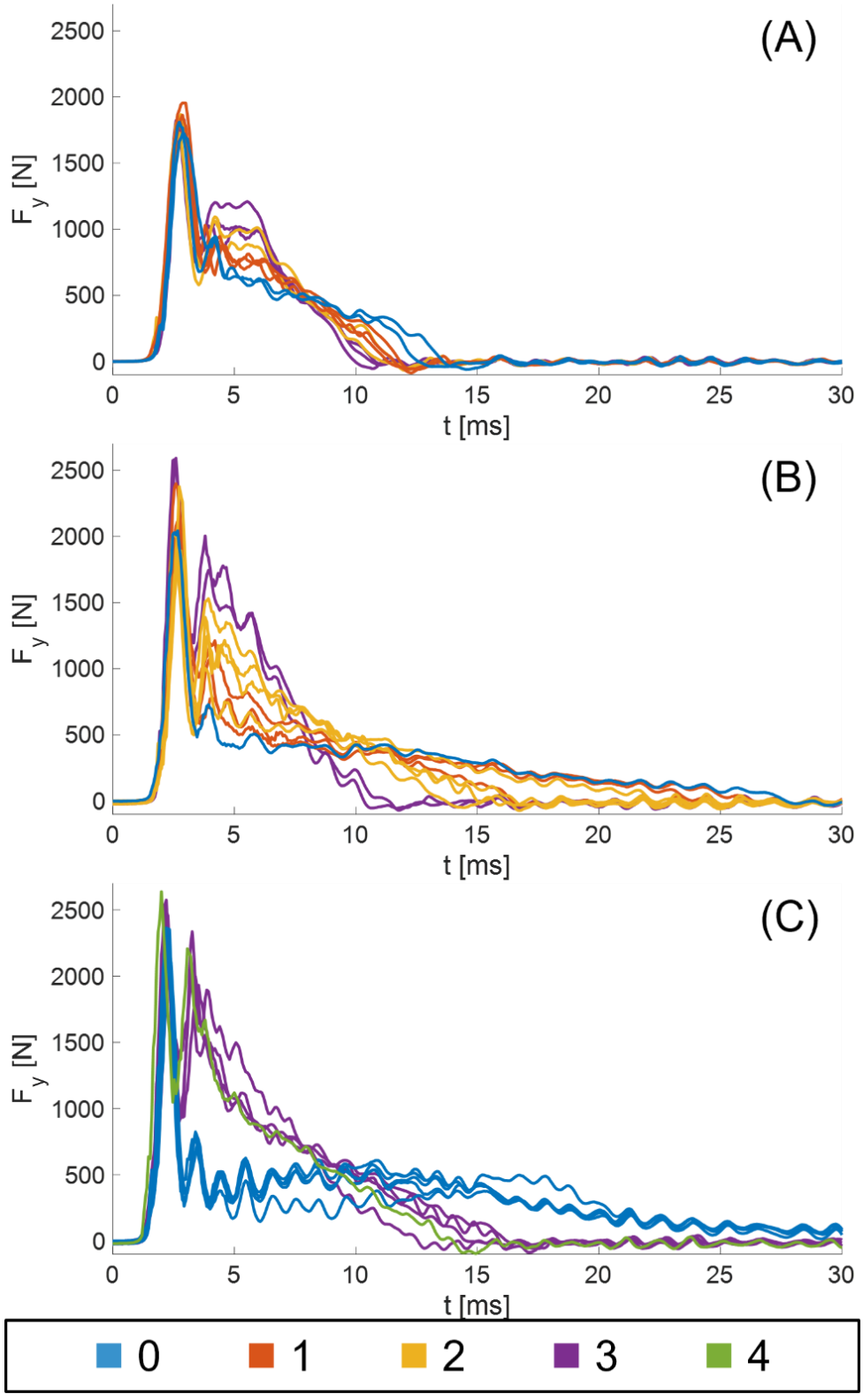

Appendix 5 – Force vs. displacement traces from buckling direction validation

A.5.27: Force [N] vs. displacement [mm] traces of uniaxial compression tests of individual bi-beams at 0.83, 8.3, and 83 s^{-1} strain rate